Chemical Fractionation in Molybdenum-rich Borosilicate Glass-ceramic and Behavior of Powellite Single Crystal under Irradiation

Xiaochun Wang

To cite this version:

Xiaochun Wang. Chemical Fractionation in Molybdenum-rich Borosilicate Glass-ceramic and Behavior of Powellite Single Crystal under Irradiation. Nuclear Experiment [nucl-ex]. Université Claude Bernard - Lyon I, 2013. English. NNT : 2013LYO10183 . tel-01172665

HAL Id: tel-01172665

https://theses.hal.science/tel-01172665

Submitted on 7 Jul 2015

N° d'ordre Année 2013

THESE

Présentée

Devant l'UNIVERSITE CLAUDE BERNARD – LYON 1
Université de Lyon

Pour l'obtention

du **DIPLOME DE DOCTORAT**
spécialité « Physique »

(arrêté du 7 août 2006 et arrêté du 6 janvier 2005)

présentée et soutenue publiquement le 10 octobre 2013

par

Xiaochun WANG

Chemical Fractionation in Molybdenum-rich Borosilicate Glass-ceramic and Behavior of Powellite Single Crystal under Irradiation

Directeur de thèse : Gérard PANCZER
Co-directeur de thèse : Jin YU and Dominique DE LIGNY

JURY:		
	M. Abdesselam ABDELOUAS (PR)	Examinateur
	M. Dirk BOSBACH (PR)	Rapporteur
	M. Jacek JAGIELSKI (PR)	Rapporteur
	Mme Nathalie MONCOFFRE (DR)	Examinateur
	M. Gérard PANCZER (PR)	Directeur de thèse
	M. Sylvain PEUGET (CR)	Examinateur
	M. David SIMEONE (CR)	Examinateur
	M. Jin YU (PR)	Co-directeur de thèse

UNIVERSITE CLAUDE BERNARD – LYON 1

Président de l'Université	**M. François-Noël GILLY**
Vice-président du Conseil d'Administration	M. le Professeur Hamda BEN HADID
Vice-président du Conseil des Etudes et de la Vie Universitaire	M. le Professeur Philippe LALLE
Vice-président du Conseil Scientifique	M. le Professeur Germain GILLET
Directeur Général des Services	M. Alain HELLEU

COMPOSANTES SANTE

Faculté de Médecine Lyon Est – Claude Bernard	Directeur : M. le Professeur J. ETIENNE
Faculté de Médecine et de Maïeutique Lyon Sud – Charles Mérieux	Directeur : Mme la Professeure C. BURILLON
Faculté d'Odontologie	Directeur : M. le Professeur D. BOURGEOIS
Institut des Sciences Pharmaceutiques et Biologiques	Directeur : Mme la Professeure C. VINCIGUERRA
Institut des Sciences et Techniques de la Réadaptation	Directeur : M. le Professeur Y. MATILLON
Département de formation et Centre de Recherche en Biologie Humaine	Directeur : M. le Professeur P. FARGE

COMPOSANTES ET DEPARTEMENTS DE SCIENCES ET TECHNOLOGIE

Faculté des Sciences et Technologies	Directeur : M. le Professeur F. De MARCHI
Département Biologie	Directeur : M. le Professeur F. FLEURY
Département Chimie Biochimie	Directeur : Mme la Professeur H. PARROT
Département GEP	Directeur : M. N. SIAUVE
Département Informatique	Directeur : M. le Professeur S. AKKOUCHE
Département Mathématiques	Directeur : M. le Professeur A. GOLDMAN
Département Mécanique	Directeur : M. le Professeur H. BEN HADID
Département Physique	Directeur : Mme S. FLECK
Département Sciences de la Terre	Directeur : Mme la Professeure I. DANIEL
UFR Sciences et Techniques des Activités Physiques et Sportives	Directeur : M. C. COLLIGNON
Observatoire des Sciences de l'Univers de Lyon	Directeur : M. B. GUIDERDONI
Polytech Lyon	Directeur : M. P. FOURNIER
Ecole Supérieure de Chimie Physique Electronique	Directeur : M. G. PIGNAULT
Institut Universitaire de Technologie de Lyon 1	Directeur : M. C. VITON
Institut Universitaire de Formation des Maîtres	Directeur : M. A. MOUGNIOTTE
Institut de Science Financière et d'Assurances	Administrateur provisoire : M. N. LEBOISNE

Acknowledgement

Time flies very fast. The journey of my study in France is about to come to an end. As we all know, life is not a bed of roses. However, difficulties vanish when faced boldly. I am sincerely grateful to everyone who has helped and supported me along this long, tough, but fulfilling road to complete my doctoral dissertation.

This thesis was accomplished at the former Laboratoire de Physico-Chimie des Matériaux Luminescent (LPCML UMR 5620) and the new Institut Lumière Matière (ILM UMR5306) of the Université Claude Bernard Lyon 1.

First and foremost I want to thank my advisor, Professor Gérard PANCZER, who provided me lots of valuable guidance, assistance, and expertise during the past three years. I appreciate all his contributions of time and ideas to make my Ph.D. experience productive and stimulating. It has been an honor to be his Ph.D. student. The enthusiasm, responsibility, and foresight he has for scientific research was and will be motivational for me in my own career pursuit.

I would like to express my heartfelt gratitude to Dominique DE LIGNY, who gave me a lot of interesting, important, and useful advices on my research and experiments. Thank him for bringing joys and humor to me and to everyone else in the team.

Thank Clément MENDOZA, Sylvain PEUGET, and Jean-Luc DUSSOSSOY at the CEA Marcoule for the borosilicate glass samples that were used in the fractionation study and elemental analysis, for the optical interference equipment to measure the swelling of irradiated powellite crystals, and especially, for sharing me their excellent knowledge and experiences in nuclear waste storage, nuclear wasteforms, and irradiation damage in materials by using charged particles.

My joint advisor Professor Jin YU and the colleagues, Vincent MOTTO-ROS, Qianli MA, Wenqi LEI, and Xueshi BAI at the PUBLI team of ILM, gave me immense help in the experimental setup and data analysis of laser-induced break down spectroscopy (LIBS). Without their help I would not be able to realize the micro-LIBS mapping and multi-element analysis on the Mo-rich borosilicate glass-ceramics. Particularly, I would like to express my appreciation to Vincent MOTTO-ROS, who contributed a lot of time on the Labview program for realizing automatic micro-LIBS mapping.

The rare earth doped powellite single crystal was grown by Julien Lejay at the Ecole Nationale Supérieure de Chimie de Paris (ENSCP, Chimie-Paristech), which constructed the most basic and essential part of this study. Thank Christophe PEAUCELLE, Clément BERNARD, Nicolas BERERD, and Nathalie MONCOFFRE at the Institute of Nuclear physics of Lyon (IPNL) for the facilities and experiments of multi-energy Ar irradiation. Thank Michel FIALIN at the CAMParis platform for the electron microprobe analyses (EMPA) of Mo-rich borosilicate glass-ceramics. Sincerely, thank Iwona JOZWIK-BIALA and Jacek JAGIELSKI at the Institute of Electronic Materials Technology of Poland for the very difficult tasks of FIB manipulations on irradiated powellite crystals and the valuable discussion on irradiation-induced damage in crystals which were indispensable for well discovering and interpreting the structure change of powellite crystal under irradiations. Moreover, thanks for the precious advices of TEM analysis from Anne-Magali SEYDOUX GUILLAUME at the Geoscience Environnement Toulouse.

I also would like express my gratitude to the director of the Physics and Astrophysics Doctoral School, Christophe DUJARDIN, to the director of ILM, Marie-France JOUBERT, and to the colleagues of the ILM. Thank Laurent GROSVALET, Yann GUILLIN, Gerald BRETON and Jean-Marc INGARGIOLA for the technical support of instrumentation and mechanical components. Thank Yannick GUYOT for his help on the site-selective excitation experiment. Thank Nicholas BLANCHARD for the transmission electron microscopy (TEM) measurement on the focused-ion-beam (FIB) lamellae of irradiated powellite. Thank Jean-Michel BENOIT for the atomic force microscopy (AFM) analyses of laser-ablated crater on the Mo-rich borosilicate glass-ceramics. Moreover, thank Ben MOULTON (University of Toronto) for his important advices on scientific writing in English, which were very helpful and useful to improve the text of this thesis.

I will never forget the nice and friendly colleagues at the SOPRANO team (Spectroscopies optique des matériaux verres, amorphes et à nanoparticules), Professor Bernard CHAMPAGNON, Professor Micheline BOUDEULLE, Julien DE BONFILS, Eric NARDOU, Dominique VOUAGNER, Camille SONNEVILLE, Valérie MARTINEZ, Simon DEGIOANNI, Assia KASSIR BODON, and Omar BENZINE, as well as Françoise CHAMPION and Rihab CHAKROUN. Thanks for sharing me your happy and enjoyable time. I really like to work and stay with all of you.

Thank my Chinese friends Jinshan XU, Dan ZHANG, Xuan HU, Wenchao YU, Yu WANG, Mingchao JI, Hui REN, Ran HAN, Shan YE, and Guoneng LU. I was so lucky to

meet you in France which is a country ten thousand kilometers far away from China. I will never forget every Chinese traditional festival that we have ever celebrated and every journey that we have ever enjoyed together. Thanks for your warm greetings in those days when I was homesick.

I would like express my appreciation to the University of Science and Technology of China (USTC) where I spent three year on my postgraduate studies (2007 to 2010) and to the China Scholarship Council (CSC) who gave me great financial support during my study in France (2010 to 2013), for providing me this precious opportunity to achieve my research and dissertation in France. I really appreciate the experience in USTC, particularly at luminescent materials laboratory. The knowledge I have acquired and the experiment skill I have learned participate to the success of this study.

Finally, I would like to thank my family for all their love and encouragement which accompanied me every day and night and led me forward in the past three years. I am so grateful to my parents who supported me in all my pursuits, to my grandmother who encouraged me with a love of life, to my sister Danxian and my brother Zepeng who brought me endless joys, and most of all to my loving, supportive, and patient husband Qinzhi. Thank you very much.

Xiaochun WANG
Institut Lumière Matière
Université Claude Bernard Lyon 1
July 26th, 2013

Contents

Appendix

General introduction

Glass and ceramic have been under investigation for decades as host for nuclear waste storage. Nowadays, with the increasing demand for the immobilization of large quantities of high level waste (HLW) from diverse sources, there is a strong incentive to develop many of the alternative types of wasteform and to identify new candidate materials, particularly, glass-ceramic materials. In most cases, fission products are vitrified as nuclear waste glass by reprocessing the spent fuel. Borosilicate glass is the most widely used wasteform in many countries that have defense waste or reprocessed high-level waste. Although many different types of glass and ceramic materials have been investigated as possible candidates for the immobilization of HLW, until now, borosilicate glass is the generally accepted as first decision and it is used as the first generation host for the immobilization of HLW. The selection of borosilicate glass is mainly based on the fact that the processing technique is easy and well demonstrated for actual radioactive waste, and the glass form can accommodate wide variations in the extremely complex waste stream compositions. Moreover, it is not susceptible to radiation-induced transformations.

During the past decades, a lot of researches have been conducted on the disposal of UMo spent fuel which contains a high amount of Mo. Due to the low stability and solubility of MoO_3 in borosilicate, a large volume of glass matrix is required during nuclear waste vitrification, and in addition, the maximum waste loading in borosilicate is limited in the range of 15 to 20 wt.%. Recent study on the crystallization of Mo-rich phases in borosilicate implies a possibility to trap Mo as crystal which can also incorporate and enrich fission products and minor actinides, resulting in their depletion in the glass matrix. A borosilicate glass-ceramic wasteform containing Mo crystalline phases can be developed for nuclear waste storage, taking advantage of the crystallinity. A primary Mo crystalline phase that forms in borosilicate during glass-ceramic processing has been found to be $CaMoO_4$ (powellite).

The aim of this research is to investigate the fractionation of fission products and minor actinides (simulated by rare-earth elements) in Mo-rich borosilicate glass-ceramic containing powellite crystallites, and to follow the behavior of powellite single crystal incorporated with rare-earth elements (minor actinide surrogates) under irradiations, in order to figure out its long term behavior in storage conditions.

The background and the purpose of this study are stated in Chapter 1. The methodology of studying the fractionation of fission products in Mo-rich borosilicate glass-ceramic and the behavior of powellite crystal after irradiation are introduced in Chapter 2, including two main sections. Section 2.1 talks about the preparation of Mo-rich borosilicate and the approaches to study the fractionation of elements by using micro-laser-induced breakdown spectroscopy (μLIBS) and electron microprobe analysis (EMPA). A μLIBS system based on a YAG: Nd nanosecond pulse laser coupled with a modified microscope was set up and optimized to perform multi-element mapping. Section 2.2 talks about the preparation of powellite single crystal doped with rare-earth elements (Eu and Nd) and the techniques that were used to investigate the behavior of oriented powellite after external Ar irradiation, including optical interferometry, micro-Raman, micro-luminescence, and transmission electron microscope (TEM).

Chapter 3 presents the results and discussion on the element fractionation of fission products in Mo-rich borosilicate glass-ceramics. Measurement protocols and mapping for detecting elements in Mo-rich borosilicate by μLIBS are stated in Section 3.1. Spatial resolution of μLIBS was characterized by using atomic force microscopy (AFM). Principal components analysis (PCA) was used to classify all the elements detected by μLIBS. Complementary quantitative analyses on Mo-rich borosilicate were conducted by using the EMPA.

Chapter 4 presents the results and discussion on the behavior of rare earth (Eu, Nd) doped powellite single crystal after irradiations. Surface topography of powellite crystal after irradiations was characterized by optical interferometry (Section 4.1). Confocal micro-Raman mapping on thin sections from irradiated powellite (prepared by focus ion beam) was used to investigate the irradiation induced medium-range-order structure modifications, including structure volume change, stress, and structural disorder (Section 4.2). Transmission electron microscopy (TEM) was employed to investigate the irradiation-induced defects in powellite structure (Section 4.3). Micro-luminescent spectra of Eu were used to study the modification of local structural environment in powellite (Section 4.4).

Chapter 1: Nuclear waste storage and long-term behavior of nuclear glass-ceramic

The background and the purpose of this study in the manuscript are introduced in this chapter which includes four sections. Section 1.1 introduces the origin of radioactive fission products and nuclear wastes as well as the risks resulted from the radioactive wastes. Section 1.2 presents the immobilization of fission products by means of several wasteforms, including glass, ceramic, and glass-ceramic forms. Section 1.3 is overviews of Mo-rich borosilicate glass-ceramic and its powellite crystalline phase, which are the materials studied in this thesis. The purpose and content of this study are stated in Section 0.

1.1 The nuclear fuel cycle and fission products

1.1.1 Nuclear reaction and the nuclear fuel cycle

Uranium is a relatively common element that is found throughout the Earth and mined in a number of countries. This element is in the actinide series of the periodic table, with symbol U and atomic number 92. Like coal, oil and natural gas, uranium is an energy resource which can be used to generate electricity by means of nuclear fission reaction. The capture of a neutron of ^{235}U generates unstable ^{236}U which later splits into two smaller nuclei (^{141}Ba and ^{92}Kr) and three neutrons, as described in Equation (1-1).

$$^{235}_{92}U + ^{1}_{0}\mathrm{n} \rightarrow ^{141}_{56}Ba + ^{92}_{36}Kr + 3^{1}_{0}\mathrm{n} + \mathrm{Energy} \qquad \textbf{(1-1)}$$

A *nuclear chain reaction* occurs when one nuclear reaction causes an average of one or more reactions, which leads to self-propagating reactions. The nuclear chain reaction is unique since it releases several million times more energy per reaction than any other chemical reaction.

Each fuel, such as coal, oil, and natural gas, has its own distinctive fuel cycle. Generally, the uranium or "nuclear fuel cycle" is more complex than the others. The nuclear fuel cycle (Figure 1-1) is a series of industrial processes which involves fuel preparation, electricity production and nuclear waste process [1]. Before using in a nuclear reactor, uranium must be processed through a series of steps to produce an efficient fuel, including mining, milling, conversion to UF$_6$, enrichment, and fuel fabrication. These steps make up the "front end" of the nuclear fuel cycle. After uranium has been spent about three years in a reactor producing electricity, the used fuel may undergo further series of steps including temporary storage, reprocessing, and recycling before eventual disposal as waste. These steps are known as the "back end" of the fuel cycle.

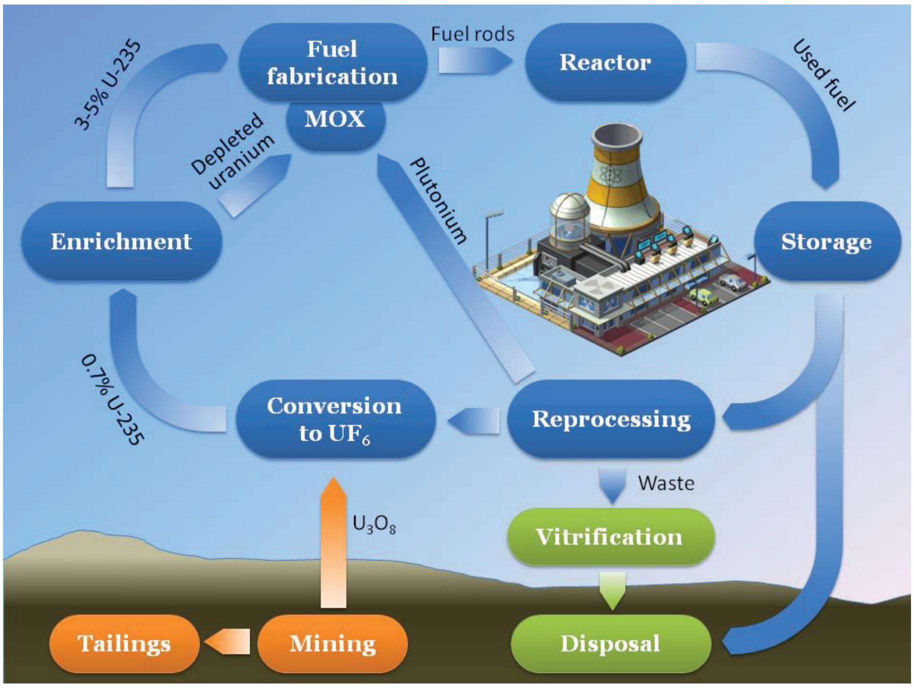

Figure 1-1: The nuclear fuel cycle [2]

1.1.2 *Fission products and nuclear waste*

During the nuclear fission reactions, atomic fragments are generated by splitting a larger atomic nucleus into two smaller atomic nuclei. These two smaller nuclei are known as "fission products", which are always unstable (radioactive) due to the fact that they are relatively neutron-rich in atomic number. They undergo beta decay rapidly, releasing additional energy in the form of beta particles, antineutrinos, and additional gamma rays which are not directly produced during the fission event itself.

Species of fission products are statistically predictable. The amount of any particular isotope produced per fission is defined as "fission product yield" which is typically expressed as percent per parent fission. The yield is dependent on the parent atom and also on the energy of the initiating neutron. Fission products include every element from zinc to the lanthanides. For the ^{235}U fission reaction, the average atomic mass of the fragments is about 118, but very few fragments near the average are found. According to statistics, *^{235}U is more probable to split into two unequal fragments, with average atomic masses of 95 and 137*, as shown in Figure 1-2

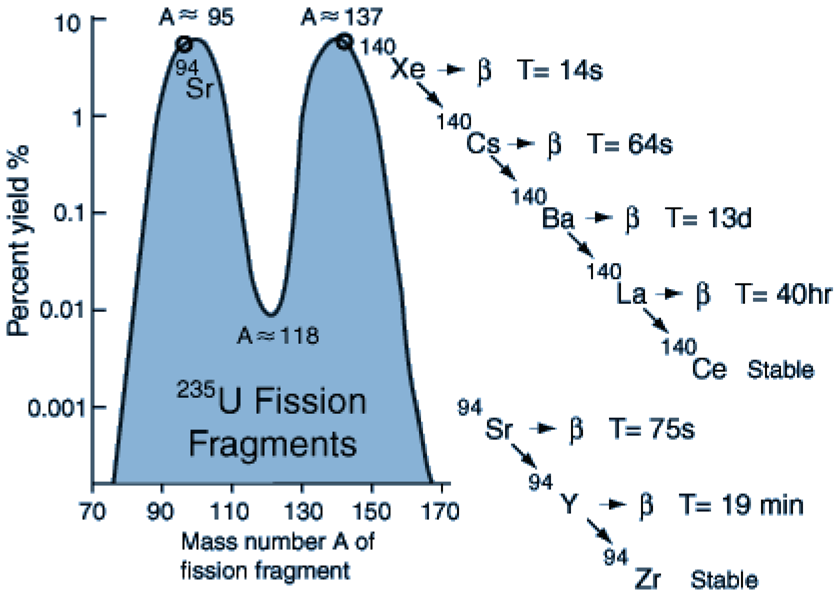

Figure 1-2: Mass distribution of fission fragments for different fission chains of $^{235}_{92}U$ [3]

After nuclear fission reactions and neutron captures in nuclear plants, radioactive fission products including minor actinides (e.g. ^{72}Ge, ^{88}Sr, ^{95}Mo, ^{139}La, ^{147}Pr and Ac, etc) are generated as nuclear waste. The chief sources of radiation in high-level nuclear waste forms are β-decay (mainly from ^{137}Cs and ^{90}Sr) and α-decay (mainly from actinide elements like U, Np, Pu, Am, and Cm), which are very dangerous for human beings, living organisms, and the environments. The radiation from fission products and minor actinides can last a long time depending on the half-life of the radioactive elements. Generally, *β-decay is the primary source of radiation during the first 500 years of storage; whereas, α-decay dominates a much longer time (more than 100 000 years)*, as it originates from the long-half-life actinides. Figure 1-3 illustrates the dpa[1] generated by β-decay and a-decay in typical ceramics containing DOE tank (243 underground tanks at U.S. Department of Energy site) waste and 10 wt. % ^{239}Pu. Thus, *it is very important to consider the safety of the long-term storage of all these radioactive fission products and minor actinides*.

---

[1] See Subsection 2.2.2

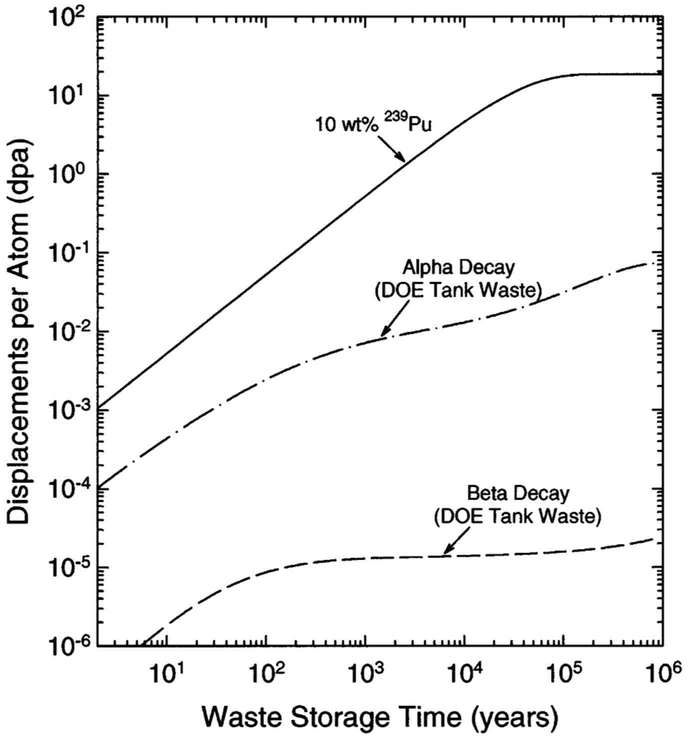

Figure 1-3: Relative number of displacements generated by *β*-decay and *a*-decay events in typical ceramics containing DOE tank (243 underground tanks at U.S. Department of Energy site) waste and by *a*-decay events in typical ceramics containing 10 wt. % ^{239}Pu [4]

1.2 Storage and immobilization of radioactive waste

Development of the materials for the long term storage or disposal of high-level radioactive nuclear waste[2] (HLW) materials [5-8] is related to the reprocessing of spent commercial reactor fuels. *The aim of immobilizing and disposing of radioactive waste is concentrated on prevention of nuclear dissemination.* Waste loading in nuclear wasteform determines the radiation dose and the thermal future of the wasteform. The final damage state is a function of the balance between accumulated damage and the kinetics of annealing of the individual phases. Nowadays, with the increasing demand for the immobilization of large quantities of HLW from plenty of additional and diverse sources, there is a strong incentive to identify new candidate materials and to develop advantageous wasteform.

---

[2] The term high-level radioactive waste (HLW) generally refers to the highly radioactive wastes requiring permanent isolation from man's environment that arise as a byproduct of nuclear power generation.

1.2.1 Nuclear wasteforms

Glasses[3], ceramics[4], and especially glass-ceramics[5] have been under investigation for decades as hosts for nuclear waste storage [9-17]. The rationale of the immobilization of radioactive waste materials in glass, ceramic or glass-ceramic wasteforms is to provide a solid, stable and durable material that can be more easily stored and disposed than the current liquid wastes. Immobilization may be accomplished either by dissolving the waste elements on an atomic scale within the host lattice, or by encapsulating the waste within an inert matrix. For the safety of long-term storage, it is required that nuclear waste hosts must possess superior thermal stability, mechanical properties and other potential performances to meet the challenges of specific applications.

1.2.1.1 Glass form

The potential use of glass as a nuclear wasteform was initially investigated in 1950s in Canada using a natural silicate mineral, nepheline syenite, as starting materials[9]. Various glass systems [10, 11, 18-20], such as silicate, borosilicate, aluminosilicate, phosphate, rare earth oxide, etc., have been shown to be suitable for producing waste glass forms that are thermally and mechanically stable and exhibit a good chemical durability. By dissolving the HLW in a suitable glass host, glass (vitreous) homogeneous product can be cast into suitable forms. Glass materials are good matrix for HLW, which can be very tolerant of variations in waste composition. Moreover, glasses exhibit reasonable chemical durability and radiation resistance [21]. The technique for preparing glass wasteforms is well established in vitrification plants operational throughout the world. Large amount of HLW immobilized in glass is currently in interim storage at various vitrification plants awaiting the construction of suitable underground repositories for their permanent disposal.

However, glass materials are metastable with respect to temperature and time [22]. Thermal stability of glass is particularly important for the immobilization of HLW. Stress induced by self-irradiation may generate cracks inside the glass during the time in storage. If serious cracking of the glass subsequently occurs, leaching rates may be significantly enhanced.

---

[3] Amorphous (non-crystalline) solid materials

[4] Inorganic polycrystalline materials

[5] Polycrystalline materials produced through controlled crystallization of base glass, containing both amorphous (glass) phase and one or more crystalline phases

1.2.1.2 *Ceramic form*

Many ceramics are known to possess superior chemical durabilities to glasses under typical repository conditions for immobilization of HLW [11]. Radionuclides may occupy specific atomic positions in the periodic structure of constituent crystalline phases, so as to form a dilute solid solution [13]. The coordination polyhedra in each phase impose specific size, charge and bonding constraints on the nuclides that can be incorporated in the structure. However, unlike vitrification, there are currently no commercial plants in operation for the immobilization of HLW employing crystalline ceramic materials. Titanate-based ceramics are the most widely studied ceramic wasteform [23]. The most widely known titanate-based ceramics are the synthetic rock (Synroc) family which was developed by Ringwood and coworkers in Australia in the 1970s [14]. Synroc is a titanate ceramic based on naturally occurring minerals, which incorporates actinide elements in nature. Synroc is usually a combination of hollandite ($BaAl_2Ti_2O_6$), perovskite ($CaTiO_3$), zirconolite ($CaZrTi_2O_7$) and rutile (TiO_2). Immobilization of radionuclides is realized by incorporating them and the other waste constituents as solid solutions in the crystal lattices of the various ceramic phases. A wide range of cations with different charges can be incorporated into these crystalline phases.

Ceramics are generally multiphase systems containing many minor phases in addition to the major crystalline phases, which can increase the difficulty to predict their long-term behavior in repository environments. Moreover, techniques associated with manufacture of crystalline ceramics are much more complex than that associated with the production of glasses (particularly with the requirement for remote handling facilities in a nuclear environment).

1.2.1.3 *Glass-ceramic form*

According to the previous statement of glass and ceramic forms, it is proposed that *glass-ceramics may offer a useful compromise between glasses and ceramics*, being easier and less expensive to prepare than conventional ceramics, but offering higher durability than glasses. Glass-ceramics are defined as polycrystalline ceramic materials prepared by the controlled bulk crystallization of base glasses [24], consisting of an amorphous (glass) phase and one or more crystalline phases. In contrast to a spontaneous crystallization which is usually not wanted in glass manufacturing, glass-ceramics are produced by a so-called “controlled crystallization” process. Crystallization of conventional glasses normally occurs by the nucleation of crystals at external surfaces. This crystallization behavior generally gives rise to a coarse microstructure with large anisotropic crystals that grow inwards from the surfaces of the glass [21]. Such materials are usually mechanically weak. To produce mechanically strong and high-quality glass-ceramic materials, there are several requirements, for example, *high crystal nucleation density within the glass bulk, dispersed and fine-grained crystallites, homogeneous crystallization, and good crystallinity* [25]. In this case, major crystalline phases can form and grow from a very large number of internal heterogeneities inside the glass bulk. This can be achieved practically by using specific nucleating agents.

Immobilization of HLW in the crystalline phases of glass-ceramics is quite similar to that in ceramic forms, by incorporating the radionuclides into the host lattice on atomic scales. By improving the vitrification process, the nuclear glasses can be subjected to an additional heat treatment procedure in order to crystallize the glass into the glass-ceramic form [21]. Further potential advantages of using glass-ceramic as HLW wasteform include easy manufacture, higher thermal stabilities than glass, superior mechanical properties, and an ability to tailor many of their properties to meet the challenges of specific applications. Moreover, glass-ceramics are more resilient to variations in waste composition than crystalline ceramics prepared by conventional routes.

1.2.2 Radiation damage on wasteform in long-term storage

Radiation (mainly from α-decay and β-decay) effects in glasses and ceramics may impact the performance of nuclear wasteforms and stabilized nuclear materials. The nuclear wasteforms will be exposed to continued radiation and thermal effects during interim storage and permanent disposal that can result in significant restructuring of the materials. Especially, radiation from α-decay of actinides will be dominant for millions of year.

Responses of solid subjected to irradiation includes: heating, localized displacement of the constituent ions, and disordering or other global rearrangements of those ions [13]. The energy from radiation can be stored in the exposed materials, resulting in heating and disruption to the structures. The combined effects of radiation and high temperatures from β- and α-decay can lead to phase instabilities, charge imbalance, redistribution of fission products and actinides, and the onset of helium bubble formation. Damages accumulated in wasteforms can mechanically weaken the materials and cause radioactive dissemination risk in long-term storage.

1.3 Mo-rich borosilicate glass-ceramic as wasteform

Nowadays, most of the fission products are vitrified as nuclear waste glass by reprocessing the spent fuel [26]. As stated previously, glasses such as borosilicate and phosphate are used as wasteforms to immobilize radioactive fission products [21, 27]. Depending on the chemical composition of the waste stream and the waste loading factor, glass or glass-ceramic conditioning matrices can be obtained [28].

Borosilicate glass is the most widely used wasteform in many countries that have defense waste or reprocessed HLW. Although many different types of glass and ceramic materials have been investigated as possible candidates for the immobilization of HLW, until now, borosilicate glass is generally accepted as the first decision and used as the first generation host for the immobilization of HLW [21]. The selection of borosilicate glass is mainly based on the fact that the processing technique is easy and well demonstrated for actual radioactive waste, and the glass form can accommodate wide variations in the extremely complex waste stream compositions. Moreover, it is not susceptible to radiation-induced transformations [13].

1.3.1 Mo-rich borosilicate glass-ceramic

During the past decades, a lot of researches have been conducted on the treatment of UMo spent fuel [29-33]. At present, one of the big troubles is the storage of Mo in the UMo spent fuel which contains a high amount of MoO_3 (10-12 wt.% [32]). Due to the low stability and solubility of MoO_3 in borosilicate, a large volume of glass matrix is required during nuclear waste vitrification, and in addition, the maximum waste loading in borosilicate is limited in the range of 15 to 20 wt.% [34, 35]. For the R7T7 type nuclear waste glass which is currently produced by La Hague in France, the content of MoO_3 is only 1.75 wt.% with a maximum waste loading of 18.5 wt.% [36]. Accordingly, it is necessary to reduce the glass volume and to better store Mo, fission products, as well as minor actinides.

The study of Chouard *et al.* shows that the solubility of Mo in borosilicate glass can be improved by controlling the Nd_2O_3 content (8 to 12 wt.%) [37, 38]. Moreover, it is shown that crystallization in the glass matrix can be avoided by controlling the composition of the matrix. However, the presence of crystals is not always detrimental. For instance, long-lived radionuclides can be partitioned into the stable crystalline phases and depleted in the glass matrix, which leads to an increase of the waste loading and a reduction of matrix volume. Most importantly, due to the presence of Mo-rich compounds, Mo crystalline phases can form inside borosilicate during processing the nuclear waste glass [35, 39]. It is a good opportunity to *use the chemically durable crystalline phases in glass-ceramics to incorporate Mo as well as fission products and minor actinides*.

Glass-ceramics form a stable phase within a glass matrix for immobilization of elements that fractionate to the crystalline phase. Recent study on glass development with combining ^{137}Cs, ^{90}Sr, and lanthanides waste stream yields high degrees of crystallization in lanthanide borosilicate with high waste loading (up to 62.5 wt. %) [40], which indicates that the possibility of developing a glass-ceramic wasteform that takes advantage of crystallinity instead of avoiding crystallization in glass. The acceptance of crystallinity in a glass-based wasteform will typically lead to higher waste loadings [34] and higher thermal stability comparing with glasses.

According to literature, crystalline phases that could potentially form in borosilicate include Mo-rich phases such as *powellite* [34, 39, 41-44]. ($CaMoO_4$) and rare earth (RE)-rich silicate phase such as *apatite* [45, 46] ($Ca_2RE_8(SiO_4)_6O_2$ or $NaRE_9(SiO_4)_6O_2$). It is reported by Chouard [37] that phase separation and crystallization in borosilicate glass can be impacted by the content of rare earth oxides (e.g. Nd_2O_3) in the composition. The primary crystalline phase in borosilicate glass is powellite when the content of rare earth oxides is controlled between 0 to 8 wt.%; whereas, the crystalline phase becomes apatite when the rare earth oxides exceed 12 wt.%. Since apatite is not a Mo-rich phase, it cannot help to accommodate Mo of the UMo spent fuel. Accordingly, the study in this thesis is focus on Mo-rich powellite phase.

Due to the self-irradiation from α-decay events, it is possible to result in a crystalline-to-amorphous transformation for the crystalline phases (e.g. apatite [4]) in glass-ceramics during long-term storage, which can mechanically weaken the materials. So far, there are not many studies on the behavior of powellite crystal under irradiations. Powellite is shown to be a stable phase in borosilicate [35, 39]. Moreover, it is suggested that powellite have a high chemical stability since it is present in the process of R7T7 glass corrosion (up to 190°C) [47].

Therefore, it is interesting to study the structure modification of powellite due to irradiation-induced damage, in order to understand and evaluate powellite as host for immobilization of radioactive fission products and minor actinides. Borosilicate glass-ceramic containing powellite crystals can be realized through partial crystallization by performing additional annealing (Subsection 1.2.1.3). Physical and chemical properties of powellite crystal are briefly introduced in the following subsections.

1.3.2 Powellite crystal phase

Powellite ($CaMoO_4$) is a well-known member of the scheelite ($CaWO_4$) type compounds. It has the same structure as $CaWO_4$ which has $I4_1/a$ space-group symmetry and C_{4h} point-group symmetry, with eight-coordinated Ca and tetrahedral Mo [48-50]. Both Ca and Mo occupy S_4 sites while the O ions occupy C_1 site in the lattice. As shown in Figure 1-4, perfect $CaMoO_4$ structure is constituted by regularly arranged MoO_4 tetrahedra and CaO_8 polyhedra. Mineral data [48, 51] for the powellite structure is shown in Table 1-1. To study the behavior of irradiated powellite, it is necessary to have a general overview of the powellite structure as well as the properties which can be characterized by Raman, photoluminescence, and TEM, etc (See Chapter 2).

Since there are two $CaMoO_4$ molecules (i.e. 12 atoms) in each primitive cell, the degree of freedom for $CaMoO_4$ is $3N = 36$. According to the Group Theory, the lattice vibrations can be divided into 26 species, i.e. $3A_g+5A_u+5B_g+3B_u+5E_g+5E_u$, where g stands for the even vibration mode which is Raman active, and u stands for the odd vibration mode which is Raman inactive. The A and B vibrations are non-degenerate, whereas the E vibrations are doubly degenerate.

The symmetry of free $[MoO_4]^{2-}$ ion is T_d while that of $[MoO_4]^{2-}$ tetrahedron in crystal is reduced to S_4 [52]. As it has been reported [49, 52, 53], the atoms are tightly bound in the $[MoO_4]^{2-}$ molecular group while the coupling between $[MoO_4]^{2-}$ and the rest of the $CaMoO_4$ lattice is relatively weak (long-range ionic forces). Hence, it is a good approximation to label vibrations as internal and external. Internal vibration refers to the motions in which the center of mass of $[MoO_4]^{2-}$ ion does not move; while external vibration refers to motion of $[MoO_4]^{2-}$ ions as rigid units. Accordingly, the 13 Raman active vibration modes of $[MoO_4]^{2-}$ can be classified as [52]: 7 internal modes (illustrated in Figure 1-5) including stretching and bending, as well as 6 external modes including rotation and translation. A summary of reported Raman frequencies of MoO_4 vibration is listed in Table 1-2.

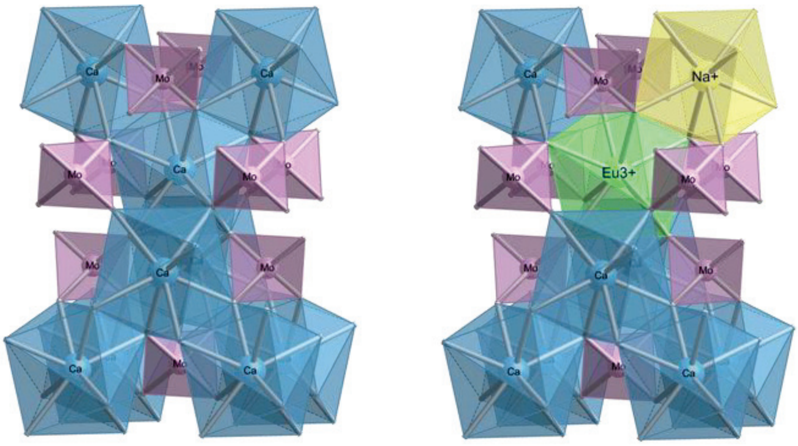

Perfect $CaMoO_4$ Doped $CaMoO_4$

Figure 1-4: Perfect and doped $CaMoO_4$ structure; MoO_4 tetrahedra is colored in purple and the CaO_8 polyhedra is colored in blue; REEs (Eu^{3+}, in green) and Na^+ (in yellow) substitute the Ca^{2+} site in the powellite structure

Table 1-1: Mineral data of powellite [48, 51]

Powellite	$CaMoO_4$
Crystal Data	
Symmetry	Tetragonal
Point group	4/*m*
Physical properties	
Cleavage	(112), (011), (001), all indistinct
Fracture	Uneven
Hardness	3.5 - 4
Density	4.26 g/cm^3
Optical properties	
Transparency	Transparent - translucent
Optical class	Uniaxial (+)
Cell data	
Space group	I (synthetic)
Cell parameters	a = 5.222 Å, c = 11.425 Å
Unit cell volume	311.55 Å^3

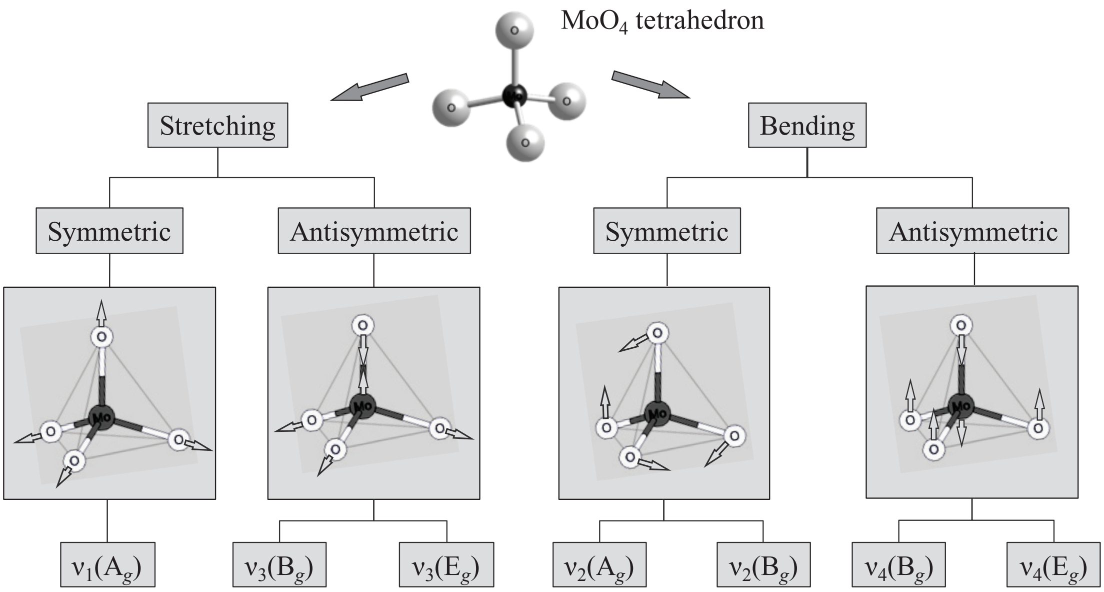

Figure 1-5: Schematic illustration of internal vibration modes of MoO_4 tetrahedron in powellite structure

Table 1-2: Comparison of reported Raman frequencies of MoO_4 vibration modes

	Reported frequency (cm^{-1})			
Vibration mode	Porto [49]	Scott [54]	L-Duyckaerts [52]	Khanna [55]
Internal				
$\nu_1(A_g)$	878	878	879	878
$\nu_3(B_g)$	844	844	848	844
$\nu_3(E_g)$	797	797	794	794
$\nu_4(E_g)$	401	401	403	404
$\nu_4(B_g)$	393	339	392	390
$\nu_2(A_g)$	333	333	323	322
$\nu_2(B_g)$	339	393	323	322
External				
$R(E_g)$	263	263	268	189
$T(B_g)$	219	219	--	--
$R(A_g)$	205	205	205	204
$T(E_g)$	189	189	191	192
$T(E_g)$	145	145	144	150
$T(B_g)$	110	110	112	115

1.3.3 Rare earth elements (REEs) as surrogate of radioactive actinides

Lanthanides, also called rare earth elements (REEs), have been the subject of intensive investigations for last several decades. For rare earth (RE) ions, a combination of partially filled $4f^{n}$-electron shell and screening effect produced by the completed filled $5s^{2}5p^{6}$-electron shell can weaken the influence of external electric and magnetic fields on the $4f$-electrons while providing a large number of possible energetic states [56]. Electron transitions between energy levels of RE ions yield emissions covering a wide spectral range, from infrared (IR) to vacuum ultraviolet (VUV). The first systematic experimental study of the RE energy level schemes was undertaken by Dieke and Crosswhite. A diagram of trivalent RE energy levels known as "Dieke diagram" [57, 58] has been established. Taking advantage of the luminescent properties, rare earth doped luminescent materials have received extensive attention for their potential applications such as phosphors [59, 60], solar cells [61], flat-panel displays [62, 63], scintillators [64], solid state lasers [65], fluorescent labels and biological probes [66], etc.

Due to the similarity in physical and chemical properties between lanthanides and actinides, *non-radioactive lanthanides are always used as surrogates to simulate the radioactive actinides in nuclear wasteform* [36]. Because of the structural variability, powellite can accommodate considerable chemical substitutions including trivalent actinides and lanthanide elements [67]. The lanthanides substitute the Ca site (S_4 symmetry) in powellite structure. It is reasonable to predict that, in the Mo-rich borosilicate glass-ceramic, lanthanides and actinides (α-decay source) fractionate in favor of the powellite phase. Therefore, the glass matrix surrounding the crystalline phase can be considered as a second-barrier to trap the radioactive actinides.

Meanwhile, luminescent properties of REEs are very sensitive to the local environment of the lattice structure. Therefore, REEs can be exploited as *optical probe* to investigate the structure modification of powellite after irradiations. Figure 1-6 shows the energy levels of Eu^{3+} which will be used to probe the local environment of irradiated powellite in this study. Figure 1-7 shows polarized steady-state emission spectra of Eu^{3+}: $^{5}D_{0} \rightarrow {}^{7}F_{J\ (J\,=\,0,\ 1)}$ transition (in the studied pristine powellite) under continuous 532 nm excitation at 300 K.

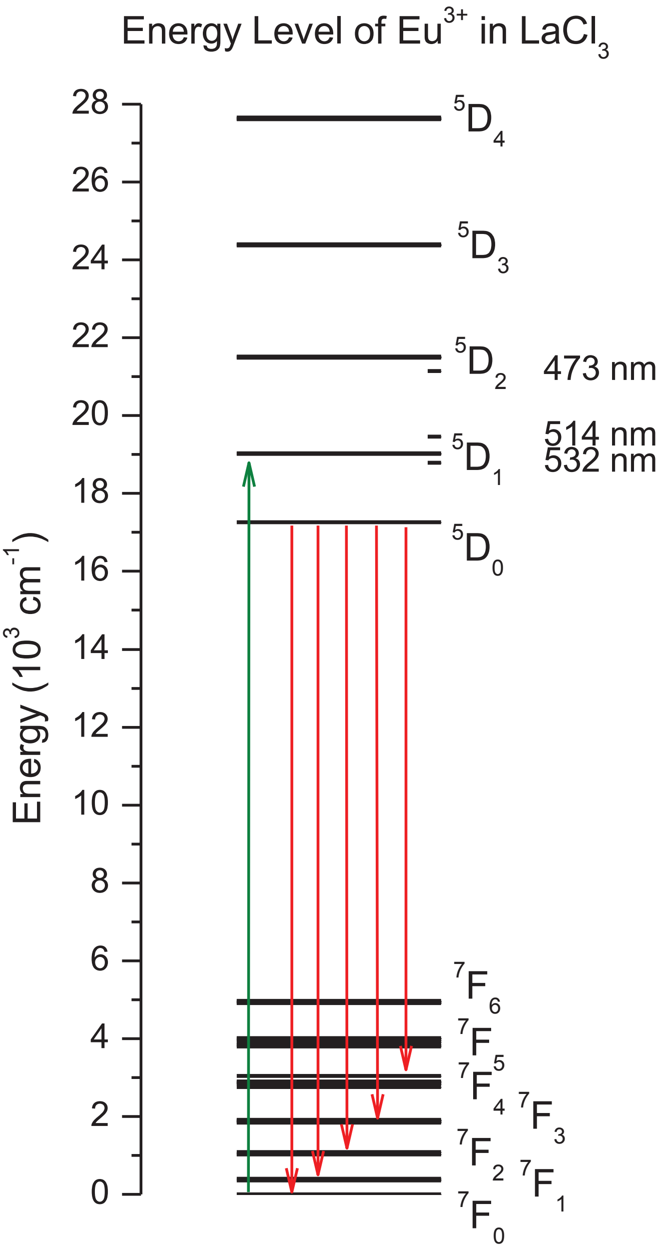

Figure 1-6: Energy levels diagram of Eu^{3+} in LaCl$_3$ [57]; wavelengths of laser that are possible to excite Eu^{3+} are marked on the right side of the figure

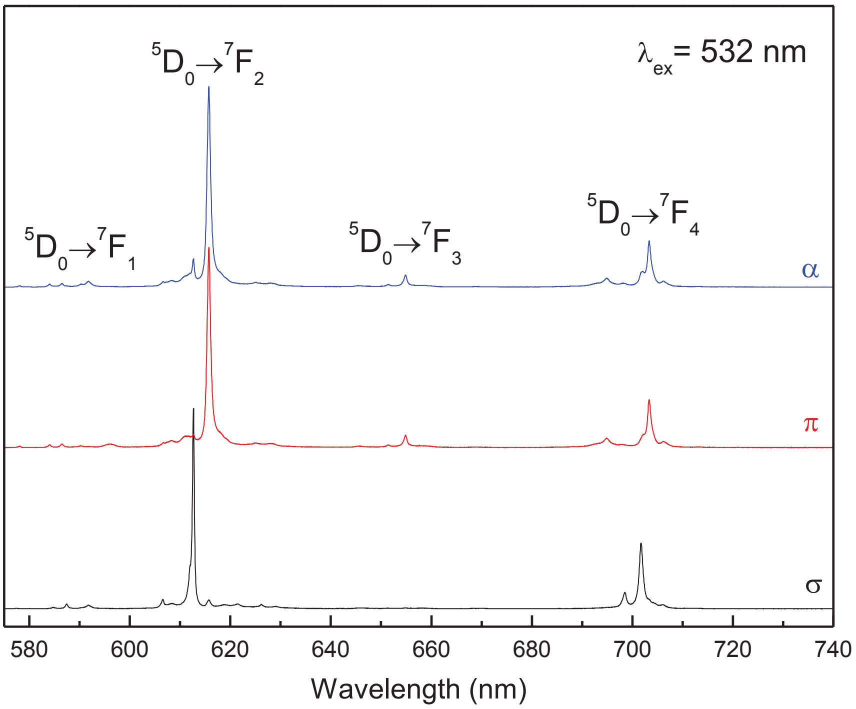

Figure 1-7: Polarized steady-state emission spectra of Eu^{3+}: $^5D_0 \rightarrow ^7F_{J\ (J = 0\text{-}4)}$ in powellite under continuous 532 nm excitation at 300 K; α, σ, and π refer to different polarized spectra[17](Page 164)

1.4 The work in this thesis

The research in this thesis is mainly focused on two aspects. The first one is the fractionation of constituent elements between glass and powellite crystalline phase in borosilicate glass-ceramics. The second one is the behavior of powellite crystal under irradiations.

1.4.1 Fractionation of radioactive elements in the Mo-rich borosilicate glass-ceramic

Minor actinides, lanthanides and the other fission products have different fractionation behavior between glass and crystalline phases in the Mo-rich borosilicate glass-ceramic. During the process of $CaMoO_4$ crystallization, some of the elements are preferentially incorporated into crystalline phase [15, 17, 27, 68, 69] while the others remain in the glass one. To take advantage of the Mo-rich crystalline phase in borosilicate to accommodate Mo as well as fission products and minor actinides, the ability of powellite to incorporate the elements in nuclear waste has to be figured out. It is therefore necessary for the nuclear industry to monitor this fractionation of elements in the glass-ceramic wasteform for controlling the immobilization of fission products and considering the long term behavior of glass-ceramic in the nuclear waste storage conditions.

The methodology to study the fractionation of constituent elements in borosilicate glass will be stated in the first section of Chapter 2, while the corresponding results and discussion will be presented in Chapter 3.

1.4.2 Behavior of powellite crystal under irradiation

Internal bombardment due to α-decay can induce damage on the structure of crystalline phases in long-term storage. The responses of the crystal structure subjected to irradiation includes heating, localized displacement of the constituent ions, and global rearrangements (e.g. disordering) [13]. Moreover, the incorporated irradiating particles in the crystal can have a significant effect on the evolution of the microstructure, through their deposition in the wasteform.

It has been demonstrated that the structure modification on crystalline phase under the high dose rates of the heavy-ion irradiation is nearly identical to that of Pu-doped zircon[70]. This suggests that heavy ion beam irradiation can be used to simulate the damage caused by α-decay events [13]. Charged-particle irradiations using electrons, protons, α-particles or heavy ions [70] have been used to study radiation damage effects, since significant doses can be reached in short periods of time (e.g. minutes or hours)[13].

Since luminescent properties of REEs are very sensitive to the local environment of the lattice structure, it can be used to probe the structure modification. In this study, non-radioactive REEs (Eu and Nd) doped in powellite single crystal were used as surrogate of fission products and optical probe of the powellite local structure after irradiations. The doped REEs in the powellite structure substitute the Ca^{2+} site (Figure 1-4). External Ar irradiation was performed on the REEs doped powellite crystal to simulate the internal bombardments from α-decays during nuclear waste storage.

Macroscopic, mesoscopic and microscopic effects of powellite single crystal under irradiations were investigated based on optical and electron microscopy techniques. Surface topography of powellite crystal[6] after irradiations was characterized by optical

---

[6] "Powellite crystal" mentioned in the manuscript refers to powellite single crystal hereafter.

interferometry. Confocal micro-Raman mapping on irradiated powellite was used to investigate the irradiation induced structure modifications in medium-range order. Transmission electron microscopy (TEM) was employed to investigate the irradiation-induced defects in powellite structure. Micro-luminescent spectra of Eu were used to study the modification of local structural environment in powellite.

The methodology to study the behavior of powellite crystal under irradiation is stated in the second section of Chapter 2, while the corresponding results and discussion are presented in Chapter 4.

Reference

1. OECD Nuclear Energy Agency., *Advanced nuclear fuel cycles and radioactive waste management*. Nuclear development2006, Paris: Nuclear Energy Agency, Organisation for Economic Co-operation and Development. 244 p.
2. World-Nuclear-Association. *The nuclear fuel cycle*. 2012; Available from: http://www.world-nuclear.org/info/Nuclear-Fuel-Cycle/Introduction/Nuclear-Fuel-Cycle-Overview/#.UeVJ66zZkw8.
3. Nave, C.R. *HyperPhysics*. Nuclear 2001; Available from: http://hyperphysics.phy-astr.gsu.edu/hbase/nucene/fisfrag.html#c3.
4. Weber, W.J., et al., *Radiation effects in crystalline ceramics for the immobilization of high-level nuclear waste and plutonium.* Journal of Materials Research, 1998. **13**(6): p. 1434-1484.
5. Girardi, F., G. Bertozzi, and M. Dalessandro, *Long-Term Risk Assessment of Radioactive-Waste Disposal in Geological Formations.* Transactions of the American Nuclear Society, 1977. **26**: p. 275-277.
6. Oszuszky, F.J.P., *General Considerations on Disposal of Radioactive-Waste Materials in Geological Formations.* Atom & Strom, 1978. **24**(3): p. 61-71.
7. Mather, J.D., et al., *The Geological Disposal of High-Level Radioactive-Waste - a Review of the Institute of Geological Sciences Research-Program.* Nuclear Energy-Journal of the British Nuclear Energy Society, 1982. **21**(3): p. 167-173.
8. Pigford, T.H., *Geological Disposal of Radioactive-Waste.* Chemical Engineering Progress, 1982. **78**(3): p. 18-26.
9. Lutze, W. and R.C. Ewing, *Radioactive waste forms for the future*, ed. W. Lutze and R.C. Ewing1988, North-Holland, Amsterdam. 712
10. Donald, I.W., *Waste immobilization in glass and ceramic based hosts : radioactive, toxic and hazardous wastes*2010, Chichester, U.K.: Wiley. xvii, 507 p.
11. Donald, I.W., B.L. Metcalfe, and R.N.J. Taylor, *The immobilization of high level radioactive wastes using ceramics and glasses.* Journal of Materials Science, 1997. **32**(22): p. 5851-5887.
12. Ewing, R.C., *Nuclear waste form glasses: The evaluation of very long-term behaviour.* Materials Technology, 2001. **16**(1): p. 30-36.
13. Ewing, R.C., W.J. Weber, and F.W. Clinard Jr, *Radiation effects in nuclear waste forms for high-level radioactive waste.* Progress in Nuclear Energy, 1995. **29**(2): p. 63-127.
14. Ringwood, A.E., et al., *Immobilization of High-Level Nuclear-Reactor Wastes in Synroc.* Nature, 1979. **278**(5701): p. 219-223.
15. Stefanovsky, S.V., et al., *Nuclear waste forms.* Geological Society, London, Special Publications, 2004. **236**(1): p. 37-63.
16. Taurines, T. and B. Boizot, *Microstructure of Powellite-Rich Glass-Ceramics: A Model System for High Level Waste Immobilization.* Journal of the American Ceramic Society, 2012. **95**(3): p. 1105-1111.

17. Yudintsev, S., *Immobilization of High-Level Waste: Analysis of Appropriate Synthetic Waste Forms*, in *An International Spent Nuclear Fuel Storage Facility: Exploring a Russian Site as a Prototype: Proceedings of an International Workshop*2005. p. 208.
18. Vance, E.R., P.J. Hayward, and I.M. George, *Crystallization of Na2o-Al2o3-Cao-Tio2-Sio2 Glasses Containing Rare-Earth-Oxides.* Physics and Chemistry of Glasses, 1986. **27**(2): p. 107-113.
19. Neeway, J., et al., *Vapor hydration of SON68 glass from 90°C to 200°C: A kinetic study and corrosion products investigation.* Journal of non-crystalline solids, 2012. **358**(21): p. 2894-2905.
20. Pinet, O., et al., *Glass matrices for immobilizing nuclear waste containing molybdenum and phosphorus.* Journal of Nuclear Materials, 2008. **377**(2): p. 307-312.
21. Donald, I., B. Metcalfe, and R.N.J. Taylor, *The immobilization of high level radioactive wastes using ceramics and glasses.* Journal of Materials Science, 1997. **32**(22): p. 5851-5887.
22. Zarzycki, J., *Glasses and the vitreous state*. Vol. 9. 1991: Cambridge University Press.
23. Deokattey, S., et al., *Borosilicate glass and synroc R&D for radioactive waste immobilization: An international perspective.* Jom-Journal of the Minerals Metals & Materials Society, 2003. **55**(10): p. 48-51.
24. McMillan, P.W., *Glass-ceramics*. 2d ed. Non-metallic solids1979, London ; New York: Academic Press. viii, 285 p.
25. Caurant, D., et al., *Glasses, glass-ceramics and ceramics for immobilization of highly radioactive nuclear wastes*2009: Nova Science Publishers.
26. Vienna, J.D., *Nuclear waste vitrification in the United States: recent developments and future options.* International Journal of Applied Glass Science, 2010. **1**(3): p. 309-321.
27. Haggerty, S.E., *Radioactive nuclear waste stabilization-Aspects of solid-state molecular engineering and applied geochemistry.* Annual Review of Earth and Planetary Sciences, 1983. **11**: p. 133-163.
28. Orlhac, X., *Etude de la stabilité thermique du verre nucléaire. Modélisation de son évolution à long terme*, 1999.
29. Auziere, P., *UMo Spent Fuel Acceptance for Treatment at La Hague Plant.* Research Reactor Fuel Management, 2004.
30. Do Quang, R., et al., *Vitrification of HLW produced by uranium/molybdenum fuel reprocessing in COGEMA's cold crucible melter.* Waste Management, 2003.
31. Do Quang, R., et al. *Review of the French vitrification program*. in *Global 2003 Conference, New Orleans, ANS/ENS Global Conference Committee*. 2004.
32. Pinet, O., et al., *Vitrification of Molybdenum-Rich High-Level Solutions by the Cold Crucible Melter Process-11502.* 2011.

33. Gruber, P., et al., *Limited Increase of Particle Entrainment in the Off-Gas System of a Cold Crucible Induction Melter Compared with a Joule-Heated Metal Melter for HLLW Vitrification-11465.* 2011.
34. Crum, J.V., et al., *Multi-Phase Glass-Ceramics as a Waste Form for Combined Fission Products: Alkalis, Alkaline Earths, Lanthanides, and Transition Metals.* Journal of the American Ceramic Society, 2012. **95**(4): p. 1297-1303.
35. Brinkman, W.M., et al., *Single versus multimodality training basic laparoscopic skills.* Surgical Endoscopy and Other Interventional Techniques, 2012. **26**(8): p. 2172-2178.
36. Mendoza, C., *Caractérisation et comportement sous irradiation de phases powellites dopées terres rares: applications au comportement à long terme de matrices de confinement de déchets nucléaires*, 2010, Université Claude Bernard-Lyon I.
37. Chouard, N., *Structure, stabilité thermique et résistance sous irradiation externe de verres aluminoborosilicatés riches en terres rares et en molybdène*, 2011, Université Pierre et Marie Curie-Paris VI.
38. Chouard, N., et al., *Effect of neodymium oxide on the solubility of MoO3 in an aluminoborosilicate glass.* Journal of non-crystalline solids, 2011. **357**(14): p. 2752-2762.
39. Henry, N., et al., *Heat treatments versus microstructure in a molybdenum-rich borosilicate.* Journal of non-crystalline solids, 2004. **333**(2): p. 199-205.
40. Crum, J.V., et al., *Baseline Glass Development for Combined Fission Products Waste Streams*, 2009, Pacific Northwest National Laboratory (PNNL), Richland, WA (US).
41. Rose, P.B., et al., *Crystallisation of a simulated borosilicate high-level waste glass produced on a full-scale vitrification line.* Journal of non-crystalline solids, 2011. **357**(15): p. 2989-3001.
42. Caurant, D., et al., *Structural investigations of borosilicate glasses containing MoO3 by MAS NMR and Raman spectroscopies.* Journal of Nuclear Materials, 2010. **396**(1): p. 94-101.
43. Caurant, D.M., Odile; Fadel, Edouard; Lenoir, Marion; Gervais, Christel; Charpentier, Thibault; Neuville, D. R., *Structural characterization of SiO2-Na2O-CaO-B2O3-MoO3 glasses.* eprint arXiv:1104.1862, 2011.
44. BRINKMAN, K., et al., *Single phase melt processed powellite (Ba,Ca)MoO[4] for the immobilization of Mo-rich nuclear waste*. Vol. 551. 2013, Kidlington, ROYAUME-UNI: Elsevier. 7.
45. Quintas, A., et al., *Crystallization of a rare earth-rich aluminoborosilicate glass with varying CaO/Na2O ratio.* Journal of the American Ceramic Society, 2007. **90**(3): p. 712-719.
46. Quintas, A., et al., *Effect of changing the rare earth cation type on the structure and crystallisation behaviour of an aluminoborosilicate glass.* Physics and Chemistry of

Glasses-European Journal of Glass Science and Technology Part B, 2008. **49**(4): p. 192-197.

47. Abdelouas, A., et al., *Formation of hydrotalcite-like compounds during R7T7 nuclear waste glass and basaltic glass alteration.* Clays and Clay Minerals, 1994. **42**(5): p. 526-533.
48. Hazen, R.M., L.W. Finger, and J.W.E. Mariathasan, *High-Pressure Crystal-Chemistry of Scheelite-Type Tungstates and Molybdates.* Journal of Physics and Chemistry of Solids, 1985. **46**(2): p. 253-263.
49. Porto, S.P.S. and J.F. Scott, *Raman Spectra of Cawo4 Srwo4 Camoo4 and Srmoo4.* Physical Review, 1967. **157**(3): p. 716-719.
50. Gurmen, E., E. Daniels, and J.S. King, *Crystal Structure Refinement of SrMoO4, SrWO4, CaMoO4, and BaWO4 by Neutron Diffraction.* The Journal of Chemical Physics, 1971. **55**(3): p. 1093-1097.
51. Anthony, J.W., et al., *Handbook of Mineralogy*1990, Tucson Arizona, USA: Mineral Data Publishing.
52. Liegeois-Duyckaerts, M. and P. Tarte, *Vibrational studies of molybdates, tungstates and related compounds—II: New Raman data and assignments for the scheelite-type compounds.* Spectrochimica Acta Part A: Molecular Spectroscopy, 1972. **28**(11): p. 2037-2051.
53. Russell, J.P. and R. Loudon, *The first-order Raman spectrum of calcium tungstate.* Proceedings of the Physical Society, 1965. **85**(5): p. 1029.
54. Scott, J.F., *Lattice Perturbations in CaWO4 and CaMoO4.* Journal of Chemical Physics, 1968. **48**(2): p. 874-&.
55. Khanna, R.K. and Lippinco.Er, *Infrared Spectra of Some Scheelite Structures.* Spectrochimica Acta Part a-Molecular Spectroscopy, 1968. **A 24**(7): p. 905-&.
56. Gschneidner Jr, K.A., J.-C. Bünzli, and V.K. Pecharsky, *Handbook on the physics and chemistry of rare earths*. Vol. 34. 2004: North Holland.
57. Dieke, G.H. and R.A. Satten, *Spectra and Energy Levels of Rare Earth Ions in Crystals.* American Journal of Physics, 1970. **38**(3): p. 399-400.
58. Carnall, W.T., et al., *A systematic analysis of the spectra of the lanthanides doped into single crystal LaF3.* The Journal of Chemical Physics, 1989. **90**(7): p. 3443-3457.
59. Li, P., Q. Peng, and Y. Li, *Dual-Mode Luminescent Colloidal Spheres from Monodisperse Rare-Earth Fluoride Nanocrystals.* Advanced Materials, 2009. **21**(19): p. 1945-1948.
60. Wang, L., et al., *Fluorescence Resonant Energy Transfer Biosensor Based on Upconversion-Luminescent Nanoparticles.* Angewandte Chemie International Edition, 2005. **44**(37): p. 6054-6057.
61. Shalav, A., B.S. Richards, and M.A. Green, *Luminescent layers for enhanced silicon solar cell performance: Up-conversion.* Solar Energy Materials and Solar Cells, 2007. **91**(9): p. 829-842.

62. Downing, E., et al., *A Three-Color, Solid-State, Three-Dimensional Display.* Science, 1996. **273**(5279): p. 1185-1189.
63. Maciel, G.S., et al., *Blue cooperative upconversion in Yb3+-doped multicomponent sol-gel-processed silica glass for three-dimensional display.* Applied Physics Letters, 2000. **76**(15): p. 1978-1980.
64. Panayiotakis, G., et al., *A study of X-ray luminescence and spectral compatibility of europium-activated yttrium-vanadate (YVO4: Eu) screens for medical imaging applications.* Applied Physics A, 1996. **62**(5): p. 483-486.
65. Heine, F., et al., *Green upconversion continuous wave Er3+: LiYF4 laser at room temperature.* Applied Physics Letters, 1994. **65**(4): p. 383-384.
66. Zhang, P., et al., *Versatile Photosensitizers for Photodynamic Therapy at Infrared Excitation.* Journal of the American Chemical Society, 2007. **129**(15): p. 4526-4527.
67. Bosbach, D., et al., *Trivalent actinide coprecipitation with powellite (CaMoO4): Secondary solid solution formation during HLW borosilicate-glass dissolution.* Radiochimica Acta, 2004. **92**(9-11-2004): p. 639-643.
68. Gieré, R. and P. Stille, *Energy, waste and the environment: a geochemical perspective*2004: Geological Society of America.
69. Paul, J. and G. Campbell, *Investigating Rare Earth Element Mine Development in EPA Region 8 and Potential Environmental Impacts.* United States Environmental Protection Agency, 2011.
70. Weber, W.J. and L.M. Wang, *Effect of Temperature and Recoil-Energy Spectra on Irradiation-Induced Amorphization in Ca2la8(Sio4)6o2.* Nuclear Instruments & Methods in Physics Research Section B-Beam Interactions with Materials and Atoms, 1994. **91**(1-4): p. 63-66.

Chapter 2: Sample preparation and methodology of the study

The methodology of studying the fractionation of elements in Mo-rich borosilicate glass-ceramic and the behavior of powellite crystal after irradiation is stated in this chapter. The first section describes the preparation of Mo-rich borosilicate glass-ceramics and the approaches to study the fractionation of fission products by using micro-laser-induced spectroscopy, laser ablation inductively coupled plasma mass spectrometry and electron microprobe analysis. The second section presents the techniques used to investigate the behavior of oriented powellite after external Ar irradiation, including optical interferometry, micro-Raman, micro-luminescence, and transmission electron microscope.

2.1 Methodology for studying the fractionation of fission products in Mo-rich borosilicate glass-ceramic

Elements in Mo-rich borosilicate have different fractionation behaviors between glassy and crystalline phases. A portion of the elements are incorporated in the precipitated $CaMoO_4$ crystallites while the others remain in the glass matrix. Location of radioactive elements in the Mo-rich borosilicate glass-ceramic is important to predict self-irradiation damage. Accordingly, mapping techniques can be employed to perform elemental analysis and monitor the fractionation behaviors of elements between the residual glass and the crystalline phase.

An inactive Mo-rich borosilicate glass which is a glass analogue of SON68[7] glass without radioactive elements was used for the study of fractionation of the constituent elements. The techniques used to realize multi-element mapping include micro laser-induced breakdown spectroscopy (μLIBS) and electron microprobe analysis (EMPA). First, a μLIBS system was set up and optimized for performing multi-element mapping automatically on the specified sample surface. Laser ablation inductively coupled plasma mass spectrometry (LA-ICP-MS) and EMPA were conducted for comparison and validation of the μLIBS measurements. Particularly, the fractionation behavior of elements in the borosilicate glass-ceramic was carefully determined by EMPA mapping.

---

[7] A non-radioactive French R7T7 type glass

2.1.1 Preparation of Mo-rich borosilicate glass-ceramic sample

2.1.1.1 The Mo-rich borosilicate glass sample

The Mo-rich borosilicate that used as precursor material of the glass-ceramic sample was prepared by Sophie Schuller from CEA Marcoule [1]. The compositions (in oxide) of the SON68 glass and its analogue are listed in Table 2-1. As shown in Table 2-1, main components of the analogue are the same as those of the SON68 glass: silicon, boron and aluminum oxides constitute the network formers of the glass, while sodium oxide acts as main modifier. To reduce the opacity of the glass for spectral measurements, Cd, Cr as well as Ni were removed since they can yield very deep colors.

Various metallic elements with relatively high concentrations (1 to 5 weight percent) are coexisting in the glass, such as Mo, Ca, Al, Fe, Cs, Zn and Zr. REEs (lanthanides) like Eu, Nd, Pr and La with very low concentration (less than 1 weight percent) are present as well. On one hand, REEs are considered as fission products and surrogates of minor actinides. On the other hand, REEs can also be applied as optical probe of local structural environment using luminescence measurements.

Table 2-1: Compositions (wt.%) of the SON68 glass and the corresponding synthetic analogue used in this study

	Weight percent (%)			Weight percent (%)	
Oxide	Analogue	SON68	Oxide	Analogue	SON68
SiO_2	46.42	45.12	BaO	0.63	0.61
B_2O_3	14.32	13.92	Y_2O_3	0.20	0.20
Na_2O	10.35	10.06	La_2O_3	0.95	0.92
Al_2O_3	5.07	4.92	Ce_2O_3	--	0.95
CaO	4.12	4.01	Nd_2O_3	1.67	1.63
Li_2O	2.02	1.96	Pr_2O_3	0.48	0.45
Fe_2O_3	3.07	2.98	Eu_2O_3	0.39	--
NiO	--	0.42	Ag_2O	0.03	0.03
Cr_2O_3	--	0.52	SnO_2	0.02	0.03
ZnO	2.56	2.49	TeO_2	0.23	0.23
P_2O_5	0.29	0.29	UO_2	--	0.06
SrO	0.35	0.34	ThO_2	--	0.31
ZrO_2	2.79	2.70	CdO	--	0.03
MoO_3	2.54	1.75	RuO_2	--	0.99
MnO_2	0.39	0.38	Pd	--	0.60
Cs_2O	1.11	1.10	Total	100	100

2.1.1.2 Preparation of Mo-rich glass-ceramic sample

Glass-ceramics are defined as polycrystalline ceramic materials [2] which have composite microstructures. An effective way to obtain glass-ceramics in laboratory preparation is precipitating a microscale crystalline phases in conventional nuclear glasses by partial crystallization during heat treatments [3-6]. In this experiment, Mo-rich borosilicate glass-ceramic sample containing needle-shaped $CaMoO_4$ crystallites was created by thermally treatmenting the Mo-rich borosilicate analogue.

According to Clément Mendoza's study [1], a long annealing time (about 150 hours) on Mo-rich borosilicate glass analogue is needed to obtain the required glass-ceramic. The annealing temperature depends on the reaction of MoO_3 and CaO and the nucleation of $CaMoO_4$ crystal in borosilicate.

Thermal treatment of Mo-rich borosilicate glass consists of two steps (Figure 2-1). First, the Mo-rich borosilicate glass was placed in a platinum crucible and annealed in air at 850^{o}C for 100 hours. During this period, $CaMoO_4$ was formed by MoO_3 and CaO combination reaction. Then, nucleation and crystal growth of $CaMoO_4$ crystallites occurred by means of slow cooling (at -5 ^{o}C/min), accompanying with fractionation of elements between glass and crystalline phases[8]. Second, the sample was reheated at 950 ^{o}C for 3 hours to increase the size of $CaMoO_4$ crystallites. During this period, $CaMoO_4$ crystal growth was initiated by contact between different crystallites which did not change the total amount of crystalline phase.

Raman spectra of $CaMoO_4$ crystallites in the sample are shown in Figure 2-2 in comparison with that of single $CaMoO_4$ crystal to provide a proof of the structure of the crystalline phase. Details of the Raman spectrum of $CaMoO_4$ will be explain in Subsection 2.2.5.

---

[8] In the manuscript, glass matrix and residual glass both refer to the glassy phase of the Mo-rich borosilicate glass-ceramic; while powellite crystallite or crystal refers to the crystalline phase.

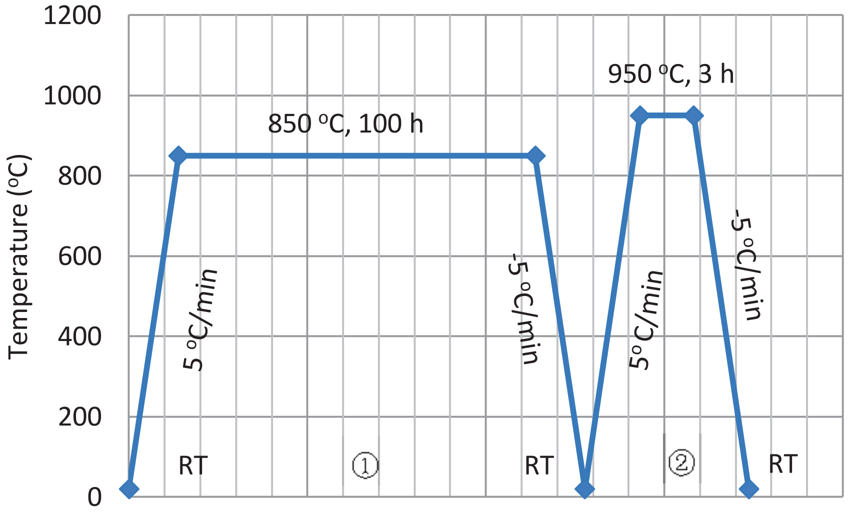

Figure 2-1: Thermal treatments on the R7T7 analogue glass to obtain the Mo-rich borosilicate glass-ceramic; step-1 corresponds to $CaMoO_4$ formation and nucleation; step-2 corresponds to $CaMoO_4$ crystal growth (RT: room temperature)

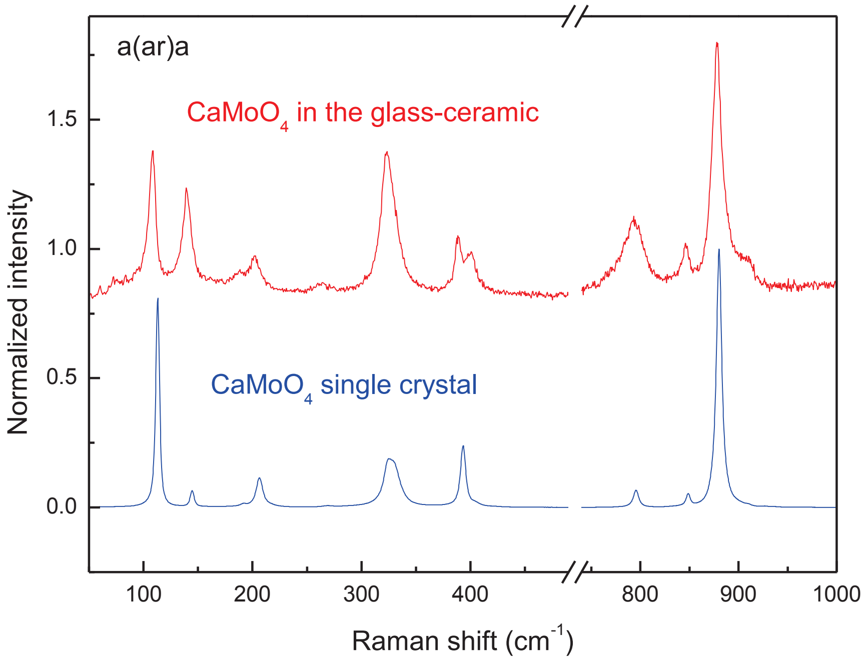

Figure 2-2: Raman spectra of $CaMoO_4$ crystallites in the Mo-rich borosilicate glass-ceramic sample (in red) and $CaMoO_4$ single crystal (in blue); a(ar)a is the Porto notation (See Subsection 2.2.5)

Figure 2-3 shows the reflective optical microscope images of Mo-rich borosilicate samples before and after thermal treatments. The initial Mo-rich borosilicate was kind of homogeneous and isotropic glass material with a brownish color observed under reflected white light (Figure 2-3-(a)), with a small amount of bubbles presenting within the glass. Figure 2-3-(b) shows an image of the sample after the first step of annealing at 850 °C for 100 hours. Numerous needle-shaped $CaMoO_4$ crystallites precipitated in the glass after undergoing the first annealing step, which grew in radial directions from one central point. The transparency of the glass phase of the sample was relatively poor in such a case. Figure 2-3-(c) and (d) are images of the samples after the second step of annealing at 950 °C for 3 hours under different magnifications. The sizes of the powellite crystallites in the borosilicate glass-ceramice were well increased for performing elemental mapping. As can be seen, both length and section diameter of the $CaMoO_4$ crystallites increased, and the transparency of the glassy phase of the sample was well improved. The needle-shaped $CaMoO_4$ crystallites can be recognized by naked eyes after the second annealing step. As shown in Figure 2-3, the powellite crystallites are well dispersed after the second step of thermal treatment. All the needle-shaped $CaMoO_4$ crystallites are isolated, discrete, and randomly embedded in the glass matrix.

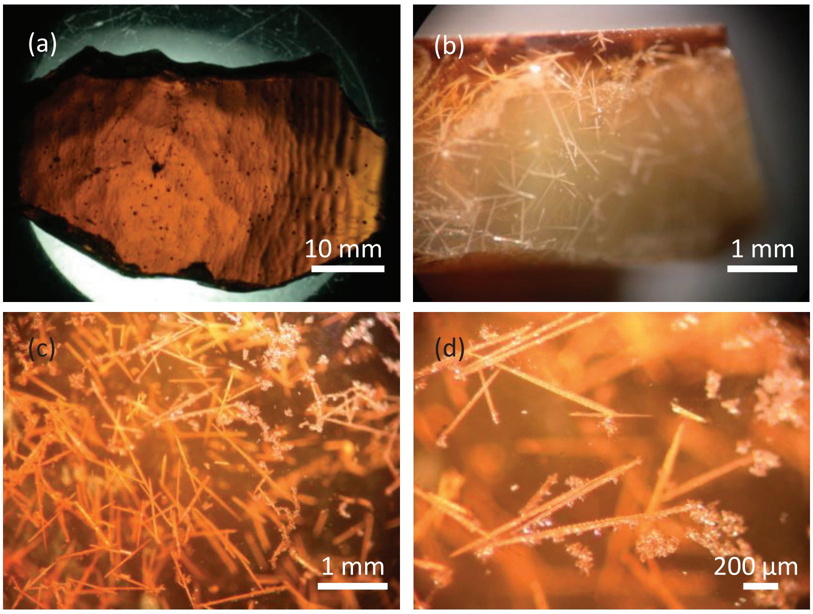

Figure 2-3: Reflective optical microscope images of Mo-rich borosilicate samples; (a) image of glass sample before thermal annealing; (b) image of sample after the first step of annealing at 850 °C (needle-shaped $CaMoO_4$ crystallites which grew in radial direction were precipitated in the glass); (c)-(d) different magnified images of samples after the second step of annealing at 950 °C with increased needle-shaped $CaMoO_4$ crystallites size and improved glass transparency

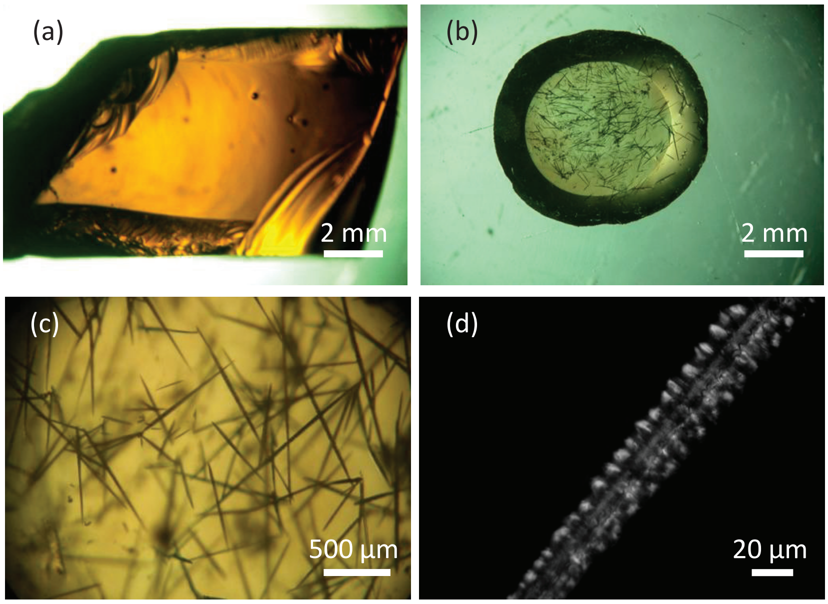

Figure 2-4: Transmitted optical microscope images of Mo-rich borosilicate samples; (a) glass sample before thermal annealing; (b-d) corresponding glass-ceramic sample containing needle-shaped $CaMoO_4$ crystallites after the second step of thermal annealing under different magnifications; (d) $CaMoO_4$ dendritic shaped crystal under a crossed polarized light

Transmitted optical microscope images of the sample before and after thermal treatments are shown in Figure 2-4. Figure 2-4-(a) shows an image of the initial Mo-rich borosilicate glass under non-polarized transmitted white light. Figure 2-4-(b) corresponds to polished glass-ceramic after the two steps of annealing. Transparency of the sample was very good. Figure 2-4-(c) and (d) are images of the Mo-rich glass-ceramic sample under larger magnifications. As shown in Figure 2-4-(c), the contrast between crystalline and glassy phases of the sample after annealing can be easily observed. *The needle-shaped dark regions correspond to* $CaMoO_4$ *crystallites, which are several hundreds of microns in length*. The white areas correspond to the glass matrix which is transparent. It is obvious that all the crystallites are randomly distributed in the glass matrix. Since the microscope was focused on the sample surface, crystallites with a blurred image are beneath the surface of the glass-ceramic. Figure 2-4-(d) is an image of the glass-ceramic under crossed polarized white light. By performing two mutually perpendicular polarizers, it is easy to see the extinction of the glass matrix (the dark area in Figure 2-4-(d)). However, due to the anisotropy of crystal, the transmitted white light cannot be totally extinct in such a configuration. Accordingly, the bright area shows clearly that *the powellite crystallite in the glass-ceramic sample has a dendritic shape with about 25 µm in section diameter.*

Summary of this subsection:

Mo-rich borosilicate glass-ceramic sample containing needle-shaped dendritic $CaMoO_4$ crystallites, which have a diameter of about 25 µm and a length of several hundred microns, was obtained by performing two-step thermal treatment on the Mo-rich borosilicate glass.

2.1.2 Technique I: Laser induced breakdown spectroscopy (LIBS)

In this study, laser-induced breakdown spectroscopy (LIBS, Subsection 2.1.2.1) was employed to perform the elemental analysis on the Mo-rich borosilicate glass-ceramic sample. A micro-LIBS (µLIBS, Subsection 2.1.2.2) system was set up (Subsection 2.1.2.3) and optimized (Subsection 2.1.2.4) based on a YAG: Nd nanosecond pulse laser coupled with a microscope to perform multi-element mapping automatically on the specified sample surface. Atomic force microscopy (AFM) was used to characterize the spactial resolution of µLIBS mapping (Subsection 2.1.2.5).

2.1.2.1 LIBS

LIBS is an established analytical technique based on spectroscopic analysis of radiation, which is emitted by a micro-plasma induced on the analyzed surface by laser pulse. Generally, plasma can be formed by focusing a laser beam which can induce breakdown on a sample surface. The principle of laser-induced breakdown process consists of three basic steps (Figure 2-5): interaction of laser and the target; removal of sample mass (ablation); plasma formation (breakdown).

Emission of the plasma is collected through an optical fiber and sent to a spectrometer. By identifying the emission lines in the plasma, it is able to analyze elements in the studied materials. The relative simplicity of the LIBS principle makes this technique very attractive for a large variety of applications [7-9]. The increasing interest of using LIBS in spectrochemical analysis can be ascribed to the unique advantages of this technique, such as easy sample preparation, capacity of non-contact and remote analysis, instantaneous response for multi-elemental identification and possibility of precisely localized (micro) surface analysis[10]. Evidently, *LIBS can be beneficial to the detection of rare earth elements* [11, 12] *and investigation of nuclear waste* [13-15].

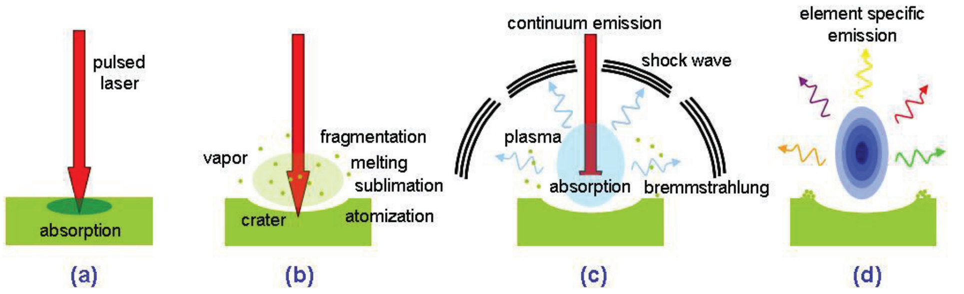

Figure 2-5: Schematic diagram of laser-induced breakdown process and plasma generation [16]; (a) the process is initiated by absorption of energy by the solid from a pulsed radiation field; (b) the absorbed energy is rapidly converted into heating, resulting in vaporization of the sample (ablation) when the temperature reaches the boiling point of the material; the removal of particulate matter from the surface leads to the formation of a vapor above the surface (c) the laser pulse continues to illuminate the vapor plume; (d) narrow atomic/ionic emissions may be identified in the spectrum approximately 1 microsecond after the ablation pulse

2.1.2.2 μLIBS mapping

μLIBS mapping allows us to establish fast spatial scanning without complicated sample preparation. Nowadays, μLIBS is a growing area of LIBS, which employs focusing microscope objective to perform μJ-energy laser pulse for the excitation of plasma [17]. Microanalysis of material surfaces is a main application of μLIBS. It can provide a convenient approach to conduct elemental analysis of inhomogeneous and heterogeneous materials, such as mineral samples [18, 19], and has been used as an elemental surface mapping tool. Compared to other elemental analysis techniques, such as Laser ablation inductively coupled plasma mass spectrometry (LA-ICP-MS) and electron microprobe analysis, LIBS or μLIBS setup is simple and cost effective [20]. μLIBS gives an instantaneous signal directly related to the location at which a single ablation event occurs. It is therefore a suitable technique to realize space-resolved elemental analysis with fast response [17, 21].

Elemental mapping consists of information about the variation of the emitted line intensity of a specific element versus one or more spatial coordinates. Images of spatial distribution are used to establish compositional interrelationships of the elemental constituents in the sample. Several studies have been reported on μLIBS mapping of metallic samples [21-23]. However, μLIBS mapping of rare earth elements in nuclear waste glass-ceramic has still not been studied. Laser-material interaction mechanism in glass-ceramic is much more complicated comparing to what happens in a metallic sample. For nuclear waste glass-ceramic, it is a challenge to conduct elemental mapping with high spatial resolution due to tiny size of crystallites (tens of microns in section diameter) which are embedded in glass matrix. Therefore, it is important to develop μLIBS system to perform mapping for this kind of samples, especially, to detect the distribution of trace rare earth elements. In this study, according to the advantages of μLIBS technique, a μLIBS mapping system was set up based on a YAG: Nd nanosecond pulse laser coupled with an improved microscope to realize multi-elemental mapping on a specified sample surface.

2.1.2.3 Experimental setup of μLIBS

The μLIBS mapping system consists of a pulsed laser and an improved microscope[9] that is combined with an XY translation stage. The experimental setup is shown in Figure 2-6 and Table 2-2. A Nd:YAG nanosecond pulse laser (Spectra-Physics) operating at 266 nm with an energy of 2 mJ per pulse was used as ablation source. The beam was attenuated to work with an adjustable energy. An iris followed by a beam expander system was used to shape the laser and to obtain a good Gaussian beam profile to gain spatial resolution. A laser power meter (Ophir) was placed in the beam path to monitor the laser energy in real time. The beam was introduced into an improved microscope (Zeiss, Axiotech) and focused on the sample surface through a × 40 UV objective (OFR) to generate a tiny plasma. Signal was collected through the same microscope system and sent to a spectrometer (Andor, Shamrock SR-303i) by fiber. The spectrometer which is equipped with a 1200-groves/mm grating has a focal length of 303 mm. Signal was finally recorded by a 1024 × 1024-pixel (13.3 × 13.3 mm) time-resolved ICCD (Andor, iStar). A CCD camera was coupled on the microscope to precisely monitor the focalization. Mapping was achieved by controlling the movement of an XY stage (Märzhäuser, Wetzlar) step by step. Software was developed to operate all the devices (beam shutter, XY stage, CCD camera, spectrometer and ICCD) and to realize automatic 2D scanning on the sample surface. Laser energy sent on the sample was maintained at several hundred μJ per pulse under the microscope objective. Single laser shot spectrum was recorded by controlling a beam shutter and synchronizing the laser shot and the CCD camera.

---

[9] Modified to support high energy pulse laser

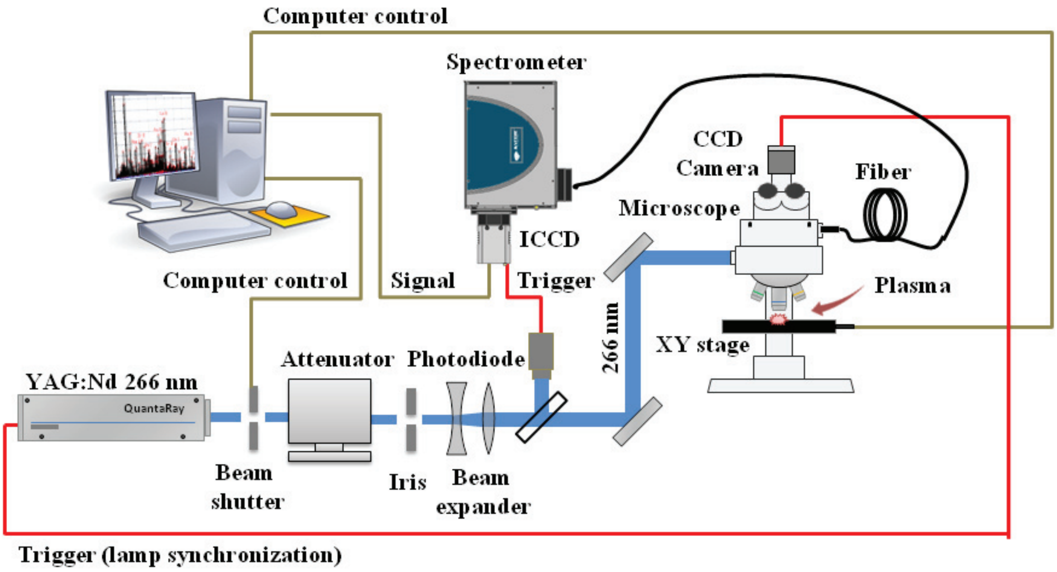

Figure 2-6: µLIBS experimental setup (blue lines: optical path; red lines: trigger; gray lines: cables for computer control; black line: optical fiber)

Table 2-2: Devices and their corresponding functions used to generate and control the laser-induced plasma in a micro-area; the labeled number indicates the positions of devices in Figure 2-8

Device	Function
YAG: Nd laser [1]	266 nm; Maximum energy ~20 mJ 355 nm; Maximum energy ~50 mJ
Microscope [2]	Focus system, × 40 UV objectives
Beam shutter [3]	To control the laser shot
Attenuator [4]	To attenuate the beam energy
Iris [5]	To control the beam shape
Beam expander [6]	To expander the beam Concave lens, f = 25 mm; Convex lens, f = 50 mm
Partial reflective lens [7]	To partial reflect the beam and trig the photodiode
Reflective mirrors [8]	To lift the optical path and introduce the beam into the microscope

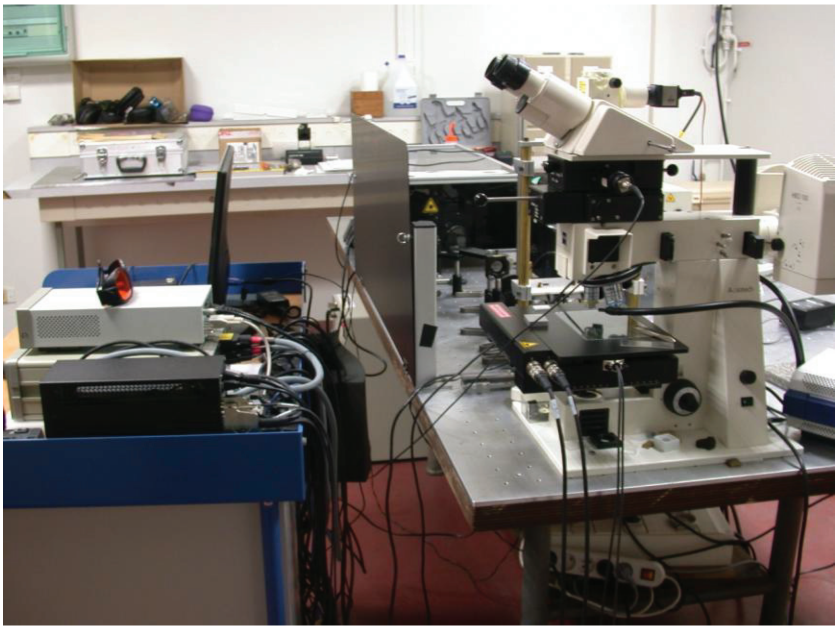

Figure 2-7: μLIBS setup (computer, ICCD, spectrometer, controls of the XY stage and the beam shutter are positioned on a table on the left, while microscope, laser and all optical devices are placed and well aligned on an optical table on the right)

Figure 2-7 is a photo of the μLIBS setup in our lab. As shown in Figure 2-7, computer, ICCD, spectrometer, controls of the XY stage and the beam shutter are positioned on a table on the left, while microscope, laser and all optical devices are placed and well aligned on an optical table. The Zeiss microscope was modified to adapt high energy pulse laser. Table 2-2 lists all the devices and their corresponding functions used to generate and control the laser-induced plasma in a micro-area. Parameters related to the setup are provided as well in this table. All the devices are labeled according to their position, as shown in Figure 2-8.

2.1.2.4 Optimization of μLIBS mapping setup

Figure 2-8 is a scheme of devices used to generate and control the laser-induced plasma in a micro-area. Before the beam is introduced in to the microscope, it is necessary to improve the beam quality. As it is shown in Figure 2-8, first, the output laser passes through an attenuator and an iris; then it is expanded by a concave-convex lens group; after, the beam is lifted by a pair of mirrors and introduced into the microscope system. A series of tests were performed to optimize the parameters of the μLIBS system.

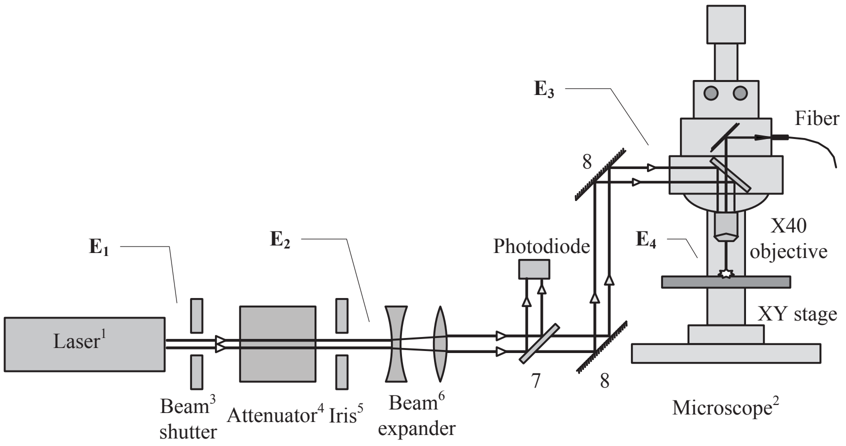

Figure 2-8: Schematic diagram of devices used to generate and control the laser-induced plasma in a micro-area (E_1: output laser energy; E_2: energy after attenuator; E_3: energy at the entrance of the microscope; E_4: energy performed on the sample surface)

First of all, *laser stability* plays a critical role in a long time mapping, which affects the emission intensity of plasma. A stable laser beam is required to obtain reliable mapping which is retrieve from intensity data. Figure 2-9 shows the laser energy variation with time for 266 nm. In the first 1.5 hours, the laser energy decreased from about 21.5 mJ to 16.5 mJ (23.2 % attenuation). It was then remained at about 16.2 mJ for more than 5 hours. It is reasonable to consider that, *the laser beam begins to be stable from 1.5 hours after starting*. Hence, mapping should be conducted after this period of time.

Secondly, it is important to use an *attenuator* to control the laser energy. For 266 nm, the maximum energy is about 20 mJ. As it has been stated in subsection 2.1.2.2, energy performed on the sample surface is micro-Joule, which is much less than the output laser energy. Generally, the output laser energy can be adjusted by the laser controller. However, laser beam is more stable when operating at around maximum energy. In this case, an attenuator can be used to reduce the laser power, based on which the laser can be maintained at a stable state but with very low energy. Table 2-3 lists the energies measured at different positions in the optical path of the μLIBS experimental setup. After passing through the attenuator, the output laser energy (E_1) reduces from 15 to 1.85 mJ (E_2), with 87.7 % of attenuation. The absolute laser energy variation with time can therefore be reduced, which is good for long-time mapping. Another reason to use attenuator is that high energy laser can induce damage to the optical system inside the microscope which should be carefully avoided.

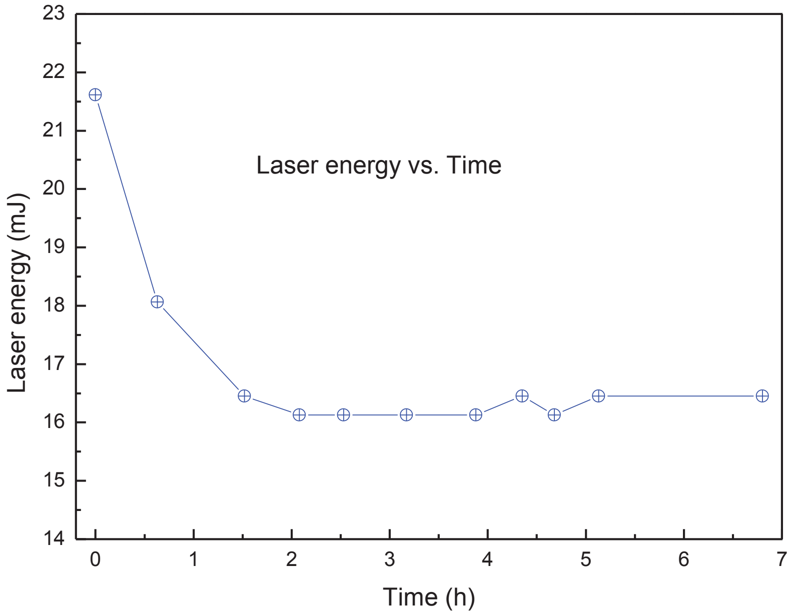

Figure 2-9: Laser (operating at 266 nm) energy (mJ) variation versus time (hour)

In addition, all optical devices can attenuate laser energy, such as optical lens, mirrors and the microscope system. As shown in Table 2-3, the laser energy is reduced from 1.6 (E_3, energy at the entrance of the microscope) to 1.0 mJ when using a ×15 objective. By comparison, *the final energy performed on sample surface* is only 0.6 mJ when using a ×40 objective. That is to say, with a ×15 objective, the total attenuation rate is about 93.3 %, while *with a ×40 objective, the total attenuation rate becomes 96 %.*

Table 2-3: Energy attenuation at different positions (see Figure 2-8, E_1 - E_4) in the optical path; E_1: output laser energy; E_2: energy after attenuator; E_3: energy at the entrance of the microscope; E4: energy performed on the sample surface (both ×15 and ×40 OFR UV objectives were used for the test)

Position	E_1	E_2	E_3	E_4 (×15)	E_4 (×40)
Energy (mJ)	15.00	1.85	1.60	1.00	0.60
Attenuation (%)	--	87.7	89.3	93.3	96.0

Thirdly, it is important to consider the relation between *spatial resolution* of the μLIBS mapping and the laser energy performed on the sample surface. As it has been reported, the *crater diameter* is related to the beam spot on the sample surface and the pulse energy [17]. To achieve high spatial resolution, small energy and tight focal spot are required. For the same focal condition, lower pulse energy leads to smaller crater. However, sufficient emission signal for detection must be considered while reducing the crater size by lowering the laser energy [24, 25]. Compromise between spatial resolution and sufficient LIBS signal is very important. It is thus important to adjust laser energy and crater size to obtain both adequate LIBS signal and high spatial resolution, particularly to detect trace rare earth elements in nuclear waste glass-ceramic sample.

A crater size versus 266-nm laser energy after attenuator (E_2) test was performed on an organic sample, polypropylene (PP), in order to measure the crater size by optical microscope easily. Each crater had undergone four laser shots. As shown in Figure 2-10, crater size reduces continuously with the decrease of laser energy (equipped with x40 objective). Sufficient spectral signal can still be detected when E_2 is reduced to 1 mJ for PP sample. For the initial glass of Mo-rich borosilicate, spectral signal is sufficient when E_2 is maintained at 1.2 to 1.8 mJ. *The final energy (E_4) performed on the sample surface is suggested to be 400 to 600 μJ.*

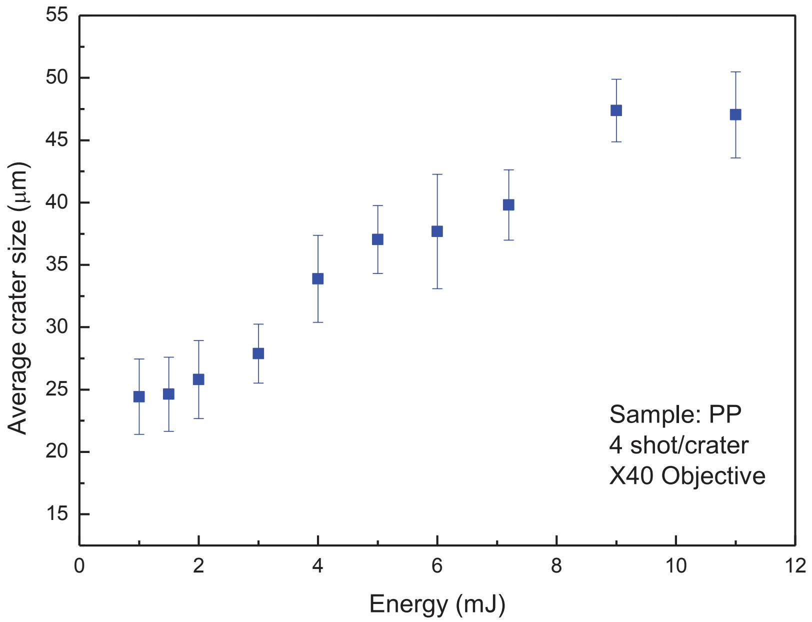

Figure 2-10: Crater size generated by the µLIBS system on polypropylene (PP) versus 266-nm laser energy after attenuator (E_2, mJ per pulse) with a x40 objective; each crater had undergone four laser shots

2.1.2.5 Characterization of µLIBS spatial resolution using atomic force microscopy (AFM)

The atomic force microscope (AFM) [26] is a kind of scanning probe microscopes (SPM) which are designed to measure local properties (such as height, friction, magnetism) of materials with a probe. The AFM consists of a cantilever with a sharp tip (probe) at its end which is used to scan the specimen surface. The cantilever is typically silicon or silicon nitride with a tip radius of curvature on the order of nanometers. When the tip is brought into proximity of a sample surface, forces between the tip and the sample lead to a deflection of the cantilever according to Hooke's law. Depending on the situation, forces that are measured in AFM include mechanical contact force, van der Waals forces, capillary forces, chemical bonding, electrostatic forces, magnetic forces, Casimir forces, solvation forces, etc. By measuring the force between the tip and the specimen surface continuously during scanning, an image of the detected surface can be acquired, which contains information of local properties of the material. In most cases, a feedback mechanism is employed to adjust the tip-to-sample distance to maintain a constant force between the tip and the sample. In such design, the tip is mounted on a vertical piezo scanner when the sample is being scanned in X and Y using another piezo block. The resulting map of the area represents the topography of the sample.

The lateral resolution µLIBS mapping can be determined by characterizing the crater size [24, 27-29]. For the study of fractionation of elements in the Mo-rich borosilicate glass-ceramic using µLIBS, AFM topography observation were performed with an AFM Nanoscope III Digital Instrument working at tapping mode condition to characterize single-laser-shot craters precisely on polished Mo-rich borosilicate glass ceramic sample.

Summary of this subsection:

A µLIBS system was set up and optimized based on a YAG: Nd nanosecond pulse laser coupled with a modified microscope to perform mapping of multi-elements automatically on the Mo-rich borosilicate glass-ceramic. AFM was used to characterize lateral resolution of µLIBS mapping on the sample surface.

2.1.3 Technique II: Laser ablation inductively coupled plasma mass spectrometry (LA-ICP-MS)

Laser ablation inductively coupled plasma mass spectrometry (LA-ICP-MS) [30] is an analytical technology that enables highly sensitive elemental and isotopic analysis to be performed directly on solid samples. It begins with a laser beam focused on the sample surface to generate fine particles – a process known as Laser Ablation (LA). The ablated particles are then transported to a secondary excitation source in which those particles are effectively ionized (or energized) by inductively heating with an electrical coil to generate inductively coupled plasma (ICP) torch. The excited ions in the plasma torch are subsequently introduced to a mass spectrometer detector for both elemental and isotopic analysis. General configuration of an LA-ICP-MS instrument consists of an LA system and ICP-MS equipment, as shown in Figure 2-11.

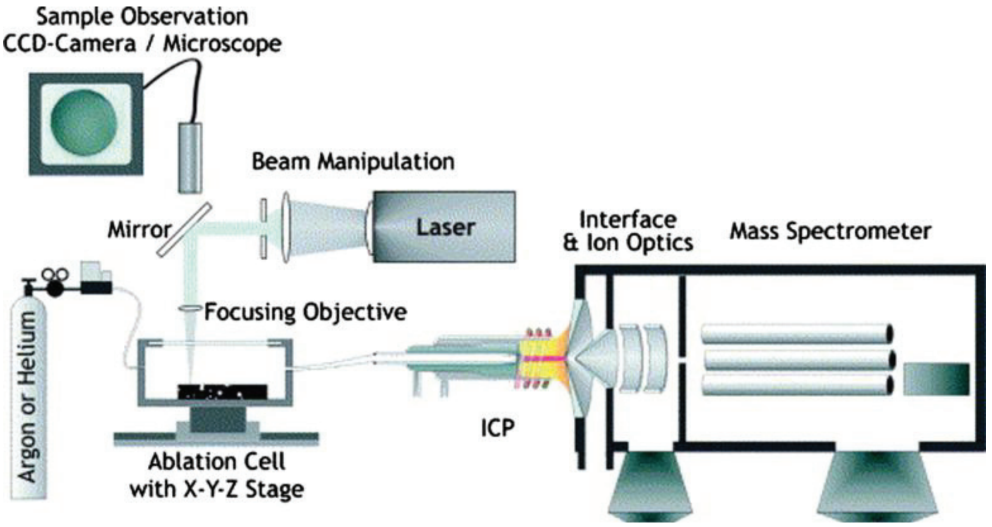

Figure 2-11: General configuration of an laser-ablation inductively-coupled plasma-mass spectrometry (LA-ICP-MS) instrument [31]

The LA-ICP-MS analysis on Mo-rich borosilicate glass-ceramic performed by C. Mendoza [1] was used as validation of the µLIBS mapping. The quantitative analyses of the Mo-rich borosilicate glass-ceramic were done with an Agilent 7500 ICP-MS spectrometer coupled with a 193 nm Resonetics M-50E excimer laser ablation device. For both glassy and crystal phases of the Mo-rich borosilicate glass-ceramic sample, ten points of measurements were performed respectively on each phase. The ablation craters have a diameter around 20 µm. Multidoped NIST 610 (400 and 500 ppm) and NIST 612 (40 to 50 ppm) standards were used as references.

2.1.4 Technique III: Electron microprobe analysis (EMPA)

Electron microprobe analysis (EMPA) [32], also known as an electron probe microanalysis (EPMA), is a technique used to determine the chemical composition of small selected areas of solid samples, in which X-rays are excited by a focused electron beam. The X-ray spectrum contains characteristic lines of the elements present in the sample that can be used for identification. Qualitative analysis is easy to obtain by identifying the lines from their wavelengths (or photon energies). By comparing their intensities with those emitted from standard samples (pure elements or compounds of known composition), it is also possible to quantitatively determine the concentrations of the elements. Generally, detection limits can be attained down to tens of parts per million (ppm). Spatial resolution is limited to about 1 μm by the spreading of the beam within the sample.

In this experiment, EMPA was used as a complementary technique for quantitative elemental analyses of the Mo-rich borosilicate glass-ceramic, and particularly for determining the fractionation behavior of the elements in the glass-ceramic sample. The quantitative elemental analyses were conducted on the CAMParis platform (Figure 2-12) using a Cameca SX FIVE instrument equipped with a versatile electron gun as well as five spectrometers. Mineral samples with known components are used as standards (listed in Table 2-4).

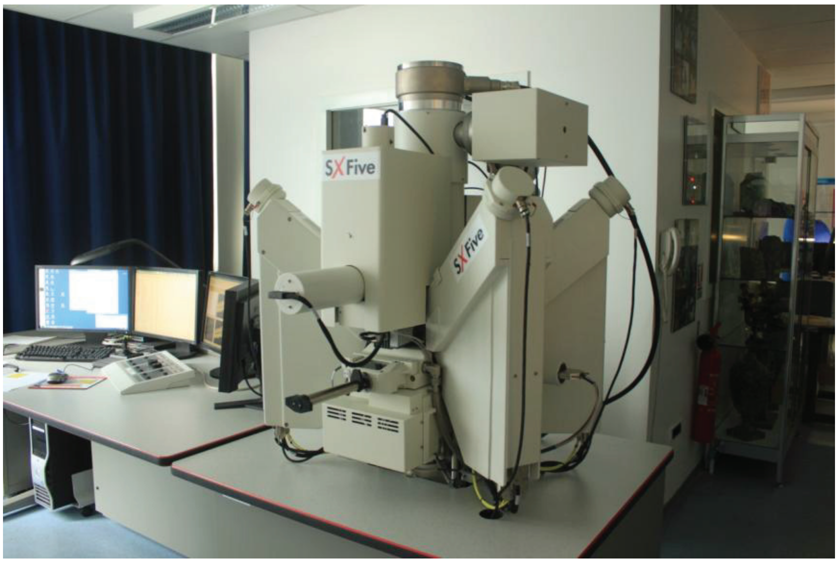

Figure 2-12: SX FIVE instrument equipped with a versatile electron gun as well as five spectrometers on the CAMParis platform

The EMPA was both performed on the initial Mo-rich borosilicate glass and its glass-ceramic sample. Mapping of the glass-ceramic sample was conducted on areas containing both glassy and crystalline phases. The working conditions of the EMPA are show in Table 2-5.

Table 2-4: Standards used for the EMPA analysis of Mo-rich borosilicate initial glass and its glass-ceramic sample

Element	Standard
B	boron nitride
Na	albite
Si, Ca	diopside
Al	orthose
Sr	glass SrSiO3
Zr	zircon
Mo	pure metal
La, Pr	REE doped glass
Nd	REE doped glass
Fe	hematite
Zn	ZnS
Cs	CsTiAsO5
Eu	REE doped glass

Table 2-5: Working conditions for EMPA measurement of the initial Mo-rich borosilicate glass and the mapping of glass-ceramic

Sample	Initial Mo-rich borosilicate glass	Glass-ceramic Mapping 1	Glass-ceramic Mapping 2
Measurement	100 points	233 × 149 points	512 × 512 points
Beam size	15 μm	0.5 to 1 μm	0.5 to 1 μm
Column Conditions	15 keV, 20 nA	15 keV, 40 nA	15 keV, 100 nA
Mapping step	--	0.5 μm	0.14 μm
Mapping area	--	116.5 × 74.5 μm^2	71.7 × 71.7μm^2

2.2 Methodology for studying the behavior of powellite single crystal under irradiations

The powellite crystal that used to incorporate minor actinides in Mo-rich borosilicate has to undergo self-irradiation in the long-term storage. It is important to know if the radioactive compounds can degrade the crystal structure by self-irradiation through internal bombardments and induce potential metamictization and amorphization. The behavior of powellite crystal under irradiations becomes crucial. For instance, irradiation induced swelling of the powellite crystal may cause cracks in the glassy matrix, resulting in an increase of the surface accessible to water and radioactive dissemination risk. This problem needs to be considered and avoided carefully in long-term nuclear waste storage.

To have an intuitive understanding of the behavior of powellite after irradiations, an oriented $CaMoO_4$ single crystal doped with Eu and Nd as FP surrogates and Na as compensator was prepared for the study (Subsection 2.1.1). External Ar-ion beam bombardment was performed on oriented sample surfaces to simulate the internal self-irradiation (Subsection 2.2.2). Optical interferometry was conducted to investigate the irradiated surface morphology (Subsection 2.2.4). Micro-Raman spectroscopy was employed to study the medium-range order modification of tetrahedral powellite structure (Subsection 2.2.5) while photoluminescence of rare-earth elements probes the local environment distortions (Subsection 2.2.6). Transmission electron microscope (TEM) was used to determine the structural defects induced by Ar irradiations (Subsection 2.2.7).

2.2.1 Preparation of REEs doped powellite ($CaMoO_4$) single crystal slices

2.2.1.1 REEs doped $CaMoO_4$ single crystal growth by Czochralski method

In this study, 2 % Eu and 0.1 % Nd were doped in $CaMoO_4$ single crystal to simulate the nuclear fission products. According to electrical neutrality, 2.1 % Na were co-doped as compensator to maintain the charge balance. Precursory oxide powder of CaO, MoO_3, Eu_2O_3, Nd_2O_3 and Na_2O in stoichiometric proportion were uniformly mixed and calcined at high temperature (temperature-time conditions shown in Figure 2-13), under which solid-state reaction occurred and $CaMoO_4$ powder was formed. Table 2-6 shows the corresponding mass and molar mass of each oxide and the expected atomic percent of each element in the powellite crystal sample. Powder X-ray diffraction (XRD) in Figure 2-14 confirms that $CaMoO_4$ phase was formed after calcination of the precursory oxide powders.

The detected XRD peaks of $CaMoO_4$ powder are identical to the $CaMoO_4$ reference (JCPDS 04-008-6868) and no complementary phases were found.

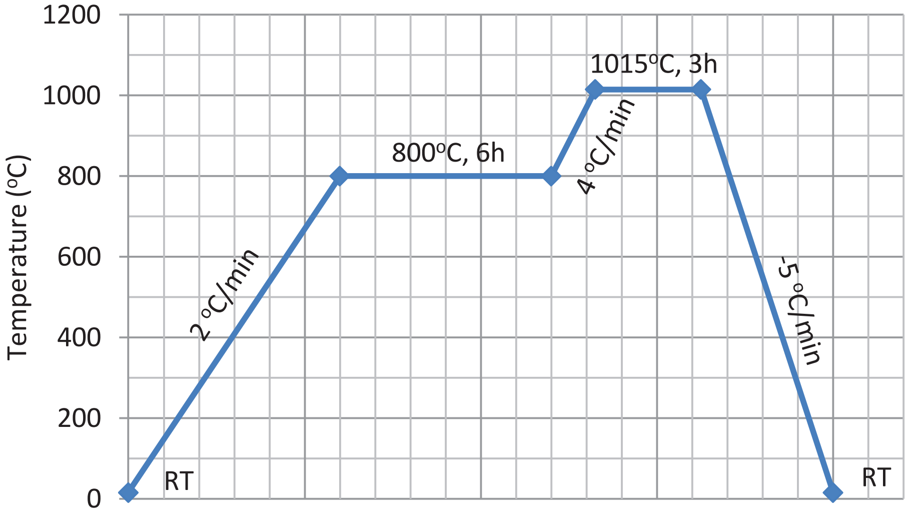

Figure 2-13: Calcination curve of CaO, MoO_3, Eu_2O_3, Nd_2O_3 and Na_2O precursory oxide power mixture, used to form $CaMoO_4$ (RT: room temperature)

Table 2-6: Atomic percent of elements in the $(Ca_{0.958}Eu_{0.02}Nd_{0.001}Na_{0.021})MoO_4$ single crystal as well as corresponding mass and molar mass of oxides for growing the crystal

Elements	Atomic percent (%)	Oxide	Molar mass (g/mol)	Mass (g)
Ca	95.8	$CaCO_3$	100.1	173.2
Eu	2	Eu_2O_3	351.9	6.4
Nd	0.1	Nd_2O_3	336.5	0.3
Na	2.1	Na_2O	106.0	2.0
Mo	100	MoO_3	144.0	260.1
O	100	--	--	--

The Eu, Nd and Na doped $CaMoO_4$ single crystal was then grown using *Czochralski* technique (at the École Nationale Supérieure de Chimie de Paris, France) by heating the $CaMoO_4$ powder to a molten state. Lattice structure and orientations of the crystal were verified using X-ray diffraction (Laue). The experimental X-ray diffraction pattern according to [001] direction is identical to the theoretical one (Figure 2-15). Images of the synthetic Eu, Nd, Na doped $CaMoO_4$ single crystal under natural light and UV lamp are presented in Figure 2-16. The crystal has an elliptical cylinder shape. The deep purple color of the crystal under natural light is due to oxygen vacancies. Red emission corresponding to Eu^{3+} can be observed when exposed to UV lamp.

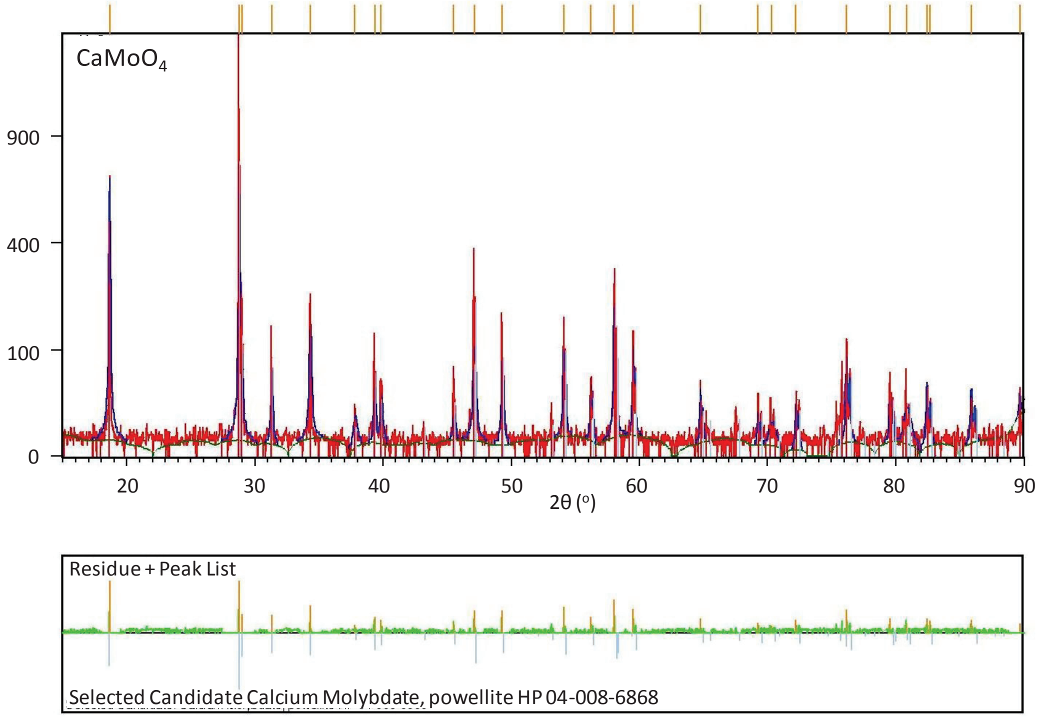

Figure 2-14: Powder X-ray different of $CaMoO_4$ (upper) as well as a comparison of the detected XRD peaks and a $CaMoO_4$ JCPDS 04-008-6868 reference (lower)

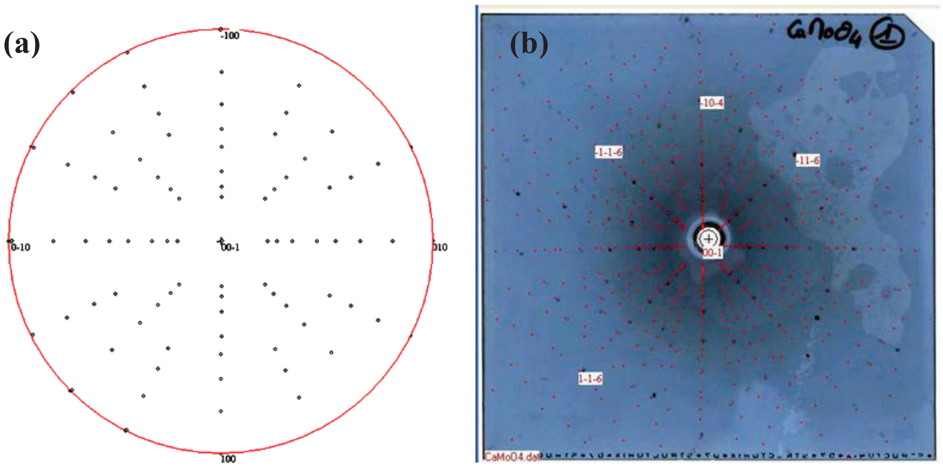

Figure 2-15: Laue X-ray diffraction pattern of single $CaMoO_4$ crystal according to $[0\ 0\ \bar{1}]$ axis (*c*-axis); (a) theoretical diffraction pattern; (b) experimental diffraction pattern

Figure 2-16: Images of the synthetic Eu, Nd, Na doped $CaMoO_4$ single crystal under natural light (left) and UV lamp (right), respectively; the crystal has a deep purple color under natural light; red emission under UV lamp (Exc. 365 nm) corresponds to Eu^{3+}; Blue emission on top of the crystal is yield by Nd^{3+} doped powellite seed crystal which was used for crystal growth.

2.2.1.2 Preparation of oriented $CaMoO_4$ crystal slices

For performing irradiation along specific orientations, the powellite crystal was cut along the crystallographic planes to get two series of slices perpendicular to *a*- and *c*- axes respectively, with a thickness of 1 mm.

Schematic diagram of powellite crystal cutting and orientations of the sample are presented in Figure 2-17. The surfaces of all the slices were well polished, up to less than 1 μm roughness. Figure 2-18 is an image of oriented powellite slices after polishing. In order to distinguish the samples, *slices perpendicular to a-axis are called a-slices, while those perpendicular to c-axis are called c-slices.* For *a*-slices, the other two axes on the plane parallel to the slice are *a*- and *c*-axes respectively; whereas, for *c*-slices, they are two identical a-axes.

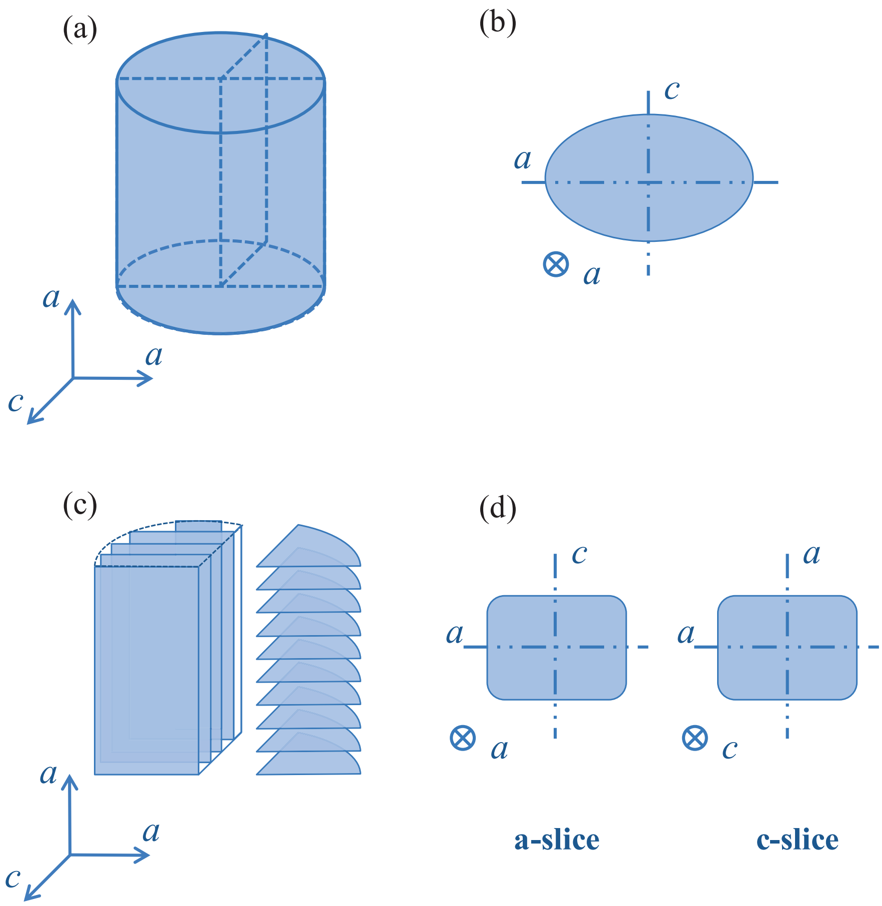

Figure 2-17: Scheme of cutting on the doped $CaMoO_4$ single crystal; (a) elliptical cylinder $CaMoO_4$ single crystal (b) sectional view (which is an ellipse) of the single crystal according to the axis of growth; (c) cutting performed on the single crystal to acquire two series of crystal slices perpendicular to *a*- and *c*-axes respectively with a thickness of 1 mm; (d) orientations of a- and c-slices

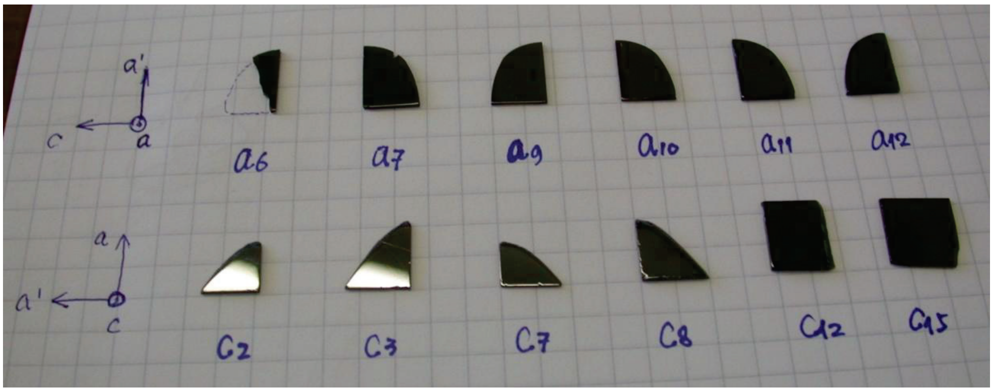

Figure 2-18: Image of some $CaMoO_4$ crystal slices after cutting and polishing; slices in the first row are perpendicular to *a*-axis; slices in the second row are perpendicular to *c*-axis

Summary of this subsection:

A Eu, Nd and Na doped calcium molybdate single crystal was grown by Czochralski technique. The phase of the synthetic powellite crystal was verified to be $CaMoO_4$ by XRD. Orientations of the powellite crystal were determined using Laue X-ray diffraction. a- and c-oriented powellite slices were prepared by cutting the bulk crystal along two different crystallographic planes.

2.2.2 Oriented Ar irradiation on doped powellite

The effects of radiation from the decay of radionuclides will accumulate over long time periods. A broad range of accelerated irradiation techniques have to be utilized to simulate and study radiation effects in nuclear waste forms (glass, glass-ceramic, and ceramic). Generally, charged-particle irradiation using electrons, protons a-particles, and heavy ions can be employed for the purpose. Based on the high dose rates of particle accelerators, very significant doses are reached in short time periods (e.g. minutes or hours). A comparison among relative damage rates in natural mineral, HLW forms, ceramics for Pu disposition and the damage rates of accelerated irradiation methods is listed in Table 2-7 [33].

In order to compare the results of charged-particle irradiations with those from actinide-decay studies, the comparable dose in displacements per atom (dpa) can be calculated based on the binary collision approximation. It is used to represent the effect of irradiation on materials properties in radiation material Science. *Displacements per atom* (dpa) is defined as the number of times that an atom is displaced from its structural site during the irradiation. Based on the induced atom displacements (D_{atom}, vacancies/A/ion) given by SRIM, dpa can be calculated depending on determined fluence of the ion beam (ψ, ion/cm^2), as shown in the following equation.

$$\text{dpa} = \frac{10^8 \times D_{\text{atom}} \times \psi}{\frac{\rho}{M} \times N_{\text{A}} \times Z} \tag{2-1}$$

Here, ρ (g/cm^3) and M (g/mol) are respectively the density and the molar mass of $CaMoO_4$, while N_{A} is the Avogadro constant and Z is the number of atoms in one $CaMoO_4$ molecular unit. For $CaMoO_4$, $\rho = 4.26$ g/cm^3, $M = 200.02$ g/mol, $Z = 6$ and $N_{\text{A}} = 6.02\times10^{23}$.

Table 2-7: Relative damage rates

Material	Damage rate (dpa/s)
HLW forms	10^{-16}-10^{-11}
10 wt.% Pu waste form	10^{-11}
Natural minerals	10^{-17}
Actinide doping	10^{-10}-10^{-8}
Neutron irradiation	10^{-7}-10^{-6}
Ion-beam irradiation	10^{-5}-10^{-2}

2.2.2.1 Simulation of Ar irradiation by SRIM

Internal self-irradiation from fission product on powellite was imitated by exposing powellite crystal under external Ar-ion radiations. In order to evaluate the damage of powellite caused by Ar implantation, the program package “SRIM 2011” developed by J. F. Ziegler [34] was used to calculate the induced atom displacements of $CaMoO_4$ and penetration depths of Ar ions.

Deposition distributions of incident ions in the target are different depending on their incident energies. In order to use optical characterization techniques (such as micro-Raman and micro-luminescence), spatial resolutions of those techniques have to be consider carefully (see Subsection 2.2.3). In this study, thickness of the irradiated domain was designed to be not less than 3 μm. During irradiation, the atomic collisions due to nuclear energy loss and the associated electronic excitations and ionizations due to electronic energy loss are not homogeneous in the depth direction of the objective material. Single-energy Ar implantation generally leads to an uneven dpa depth profile in powellite. Hence, *multi-energies Ar irradiations (0.9, 2, 3, 5 and 7 MeV) were proposed and sequentially performed on oriented powellite single crystals to realized a constant ballistic damage in a 3-μm-thick layer* (Figure 2-19). In addition, penetration depth of incident ions increases with increasing energy. Therefore, the multi-energies Ar irradiations were carried out in a descending order of energy value, to ensure that damages induced by low energy Ar irradiation are not superimposed by high energy ones.

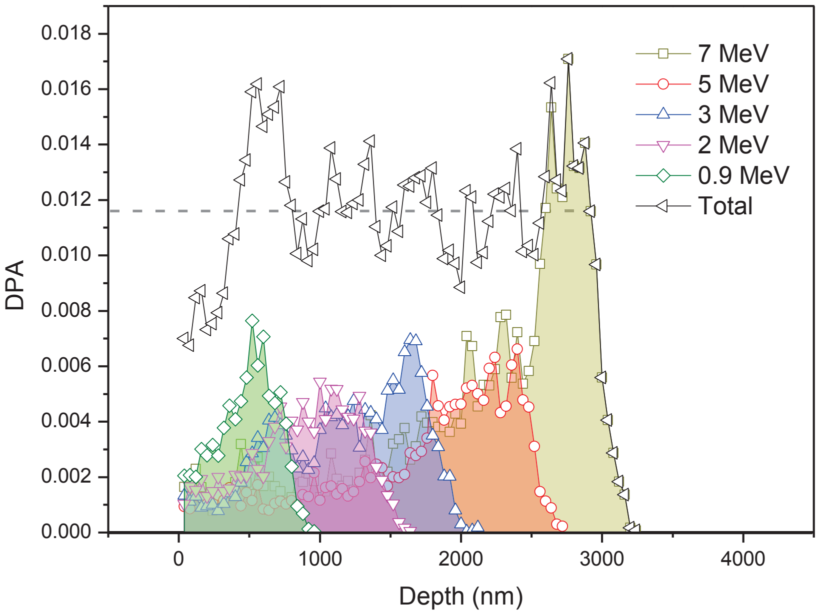

Figure 2-19: Depth profiles of dpa in powellite induced by the five Ar irradiations with energies of 7 (in gray), 5 (in red), 3 (in blue), 2 (in purple) and 0.9 MeV (in green); corresponding fluences of these five irradiations are 1.5×10^{13}, 0.8×10^{12}, 0.8×10^{12}, 0.6×10^{12} and 0.6×10^{12} ion/cm^2, respectively; total dpa generated in the 3-µm-thick lay is plotted in black, which has a average of about 0.012 dpa

The studied dpa values in powellite are predetermined to be 0.012, 0.06, 0.12, 0.6, 1.2, and 5.0 (average dpa value) to follow the structure evolution with dose. To achieve the required dpa values in the whole 3-µm-thick layer, each sample has to undergo sequentially five Ar irradiations with energies of 7, 5, 3, 2, and 0.9 MeV, respectively. For instance, Figure 2-19 presents the dpa depth profiles generated by multi-energies Ar irradiations which lead to an average dpa of 0.012 in a 3-µm-thick layer of powellite. Fluences (in ion/cm^2) of Ar irradiations to achieve 0.012 dpa are 1.5×10^{13} for 7 MeV, 8.0×10^{12} for 5 MeV, 8.0×10^{12} for 3 MeV, 6.0×10^{12} for 2 MeV, and 6.0×10^{12} for 0.9 MeV, respectively. Similarly, based on Formula (2-1), the other required dpa values can be realized by determining the Ar fluences. Figure 2-20 shows the series of flat (or even) dpa depth profiles (with averages of 0.012, 0.06, 0.12, 0.6, 1.2 and 5.0 dpa, respectively) in a 3-µm-thick lay of powellite.

Figure 2-21 is the electronic and the nuclear energy loss of Ar irradiation in powellite. The maximum electronic energy loss in this study is 4.23 MeV/µm, corresponding to the 7-MeV Ar implantation in powellite. According to Figure 2-21, the nuclear energy loss effect in powellite is negligible, except the 0.9-MeV irradiation. It can be considered that the damage in powellite is mainly due to electronic energy loss.

Table 2-8 shows the details of predetermined irradiated conditions on powellite. The first row of the table is the order of Ar irradiations that perform on each powellite crystal slice. The second to fourth rows are respectively the types, the energies, and the maximum electronic energy loss (dE/dx) of each Ar irradiation. Ar ion fluence in each irradiation to generate the required dpa value in powellite is listed from the fifth to tenth rows of the table. The rightmost column of Table 2-8 lists the estimated equivalent values of Ar fluences corresponding to each required dpa (see Appendix A.1).

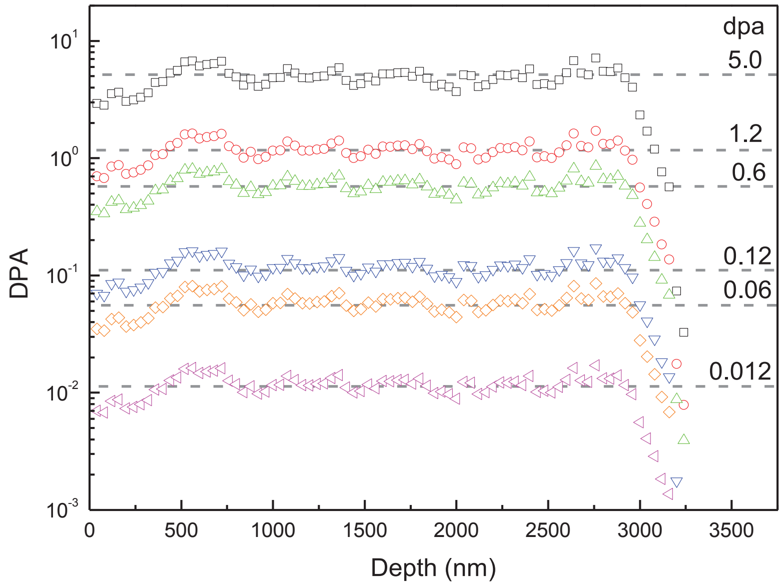

Figure 2-20: A series of dpa depth profiles in a 3-μm-thick layer of powellite induced by multi-energies Ar irradiations; average dpa values are 0.012, 0.06, 0.12, 0.6, 1.2 and 5.0 (from bottom to top), respectively

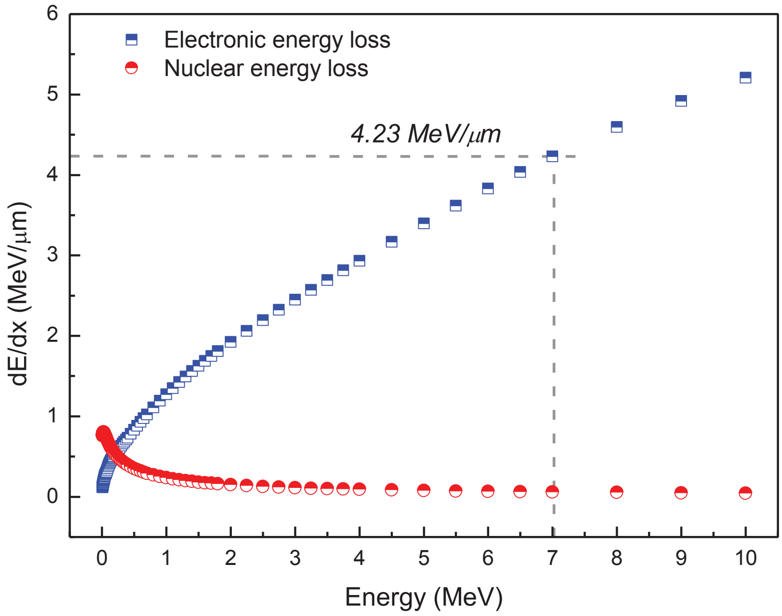

Figure 2-21: The electronic and the nuclear energy loss of Ar irradiation in powellite; maximum electronic energy loss in this study is 4.23 MeV/µm

Table 2-8: Ar multi-energies irradiations conditions used on powellite oriented single crystals, including fluence (ion/cm2), energy (MeV), and electronic energy loss dE/dx (MeV/nm) of each Ar ion beam and an estimated mean equivalent value of fluence (the rightmost column), to generate each required displacement-per-atom (dpa) in the sample

Sequences	1st	2nd	3th	4th	5th	
Ion beam	Ar^{+++}	Ar^{+++}	Ar^{++}	Ar^{++}	Ar^{+}	
Energy (MeV)	7	5	3	2	0.9	
dE/dx (MeV/µm)	4.32	3.40	2.45	1.93	1.19	
dpa	Fluence ($\times 10^{15}$ ions/cm^2)					Est. equivalent
5.0	6.250	3.133	3.133	2.500	2.500	3.635
1.2	1.500	0.750	0.750	0.600	0.600	0.872
0.6	0.750	0.375	0.375	0.300	0.300	0.436
0.12	0.150	0.075	0.075	0.060	0.060	0.087
0.06	0.075	0.038	0.038	0.030	0.030	0.044
0.012	0.015	0.008	0.008	0.006	0.006	0.009

2.2.2.2 *Ar irradiation on oriented powellite slices*

The Van de Graaf accelerator of the Institut de Physique Nucléaire de Lyon (France) was used for the Ar-ion irradiations. Figure 2-22 shows the vacuum chamber used to place the powellite crystal slices and conduct Ar irradiations. Since the maximum energy of single charge Ar ions is only 4 MeV for this facility, double charge and triple charge Ar ions were used to achieve the higher energy implantations. The currents used for the scanning ion beams (diameter of about 1 mm) were between 15 nA and 80 nA.

One *a*-slice (perpendicular to a-axis) and one *c*-slice (perpendicular to c-axis) were irradiated at the same time for each required dpa value (listed in Table 2-8) to achieve identical experimental condition. The multi-energies Ar irradiations were performed on the sample surface in a descending order of energy value as stated in Subsection 2.2.2.1.

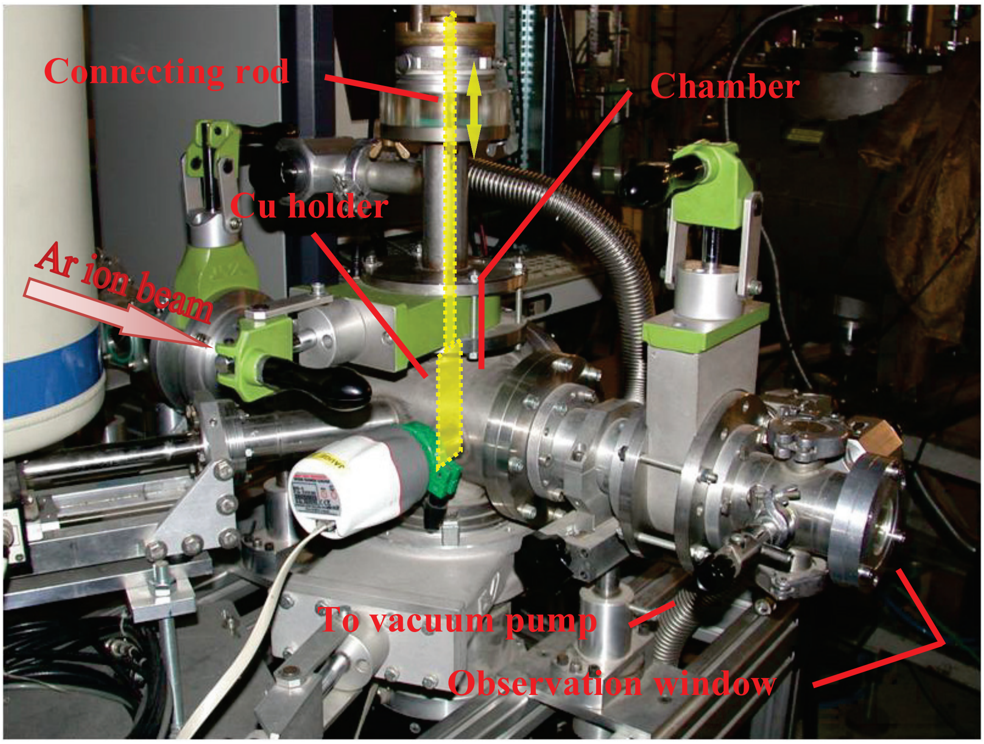

Figure 2-22: Vacuum chamber (including an observation window) used to place the powellite crystal slices and conduct Ar irradiations; position of sample holder is indicated in yellow color; direction of the Ar ion beam is drawn in pink

Samples were placed on a copper holder covered with aluminum mask, as shown in Figure 2-23. *The aluminum mask is used to stop the Ar ion beam and prevent part of the* *sample surface from irradiation, for comparing the difference of surface morphology between irradiated and non-irradiated areas.*

One *a*-slice and one *c*-slice were placed together on a square aluminum plate and then fixed on the copper holder (Figure 2-23). The copper holder which can accommodate six slices maximum was connected with a rod and inserted into the vacuum chamber. The Ar ion beam was introduced and focused on the sample surface. By moving the connecting rod, it is possible to change the focus position of Ar ion beam on the holder for performing different irradiations on different samples. The quartz on the holder is used for ion beam alignment and focalization through the observation window on the chamber.

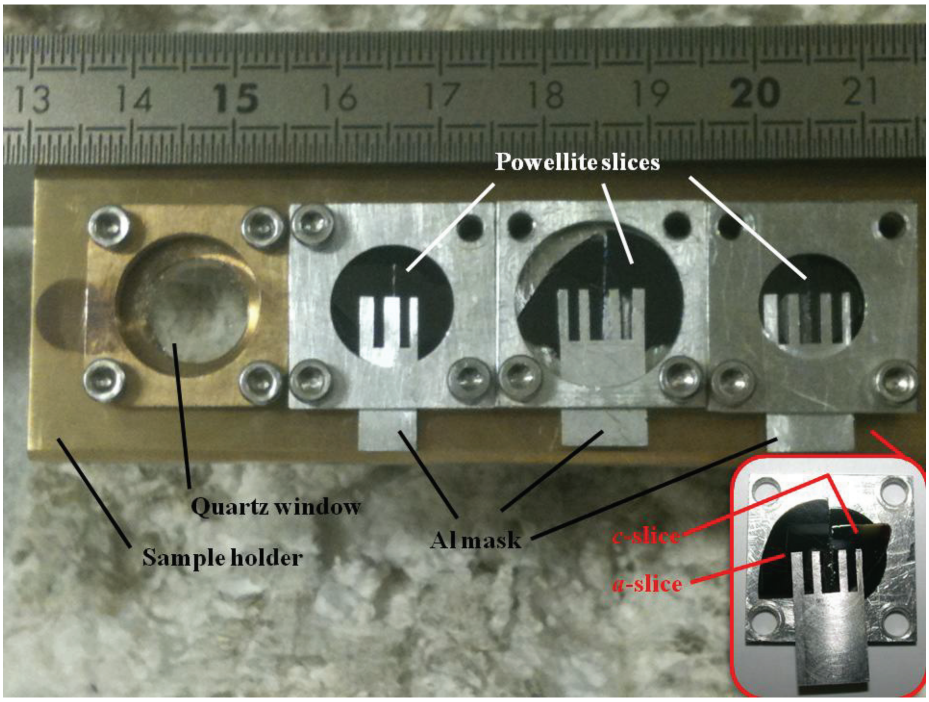

Figure 2-23: One a-slice and one c-slice were placed together on a square aluminum plate covered with aluminum masks (the figure inserted in the low right corner) and then fixed on a copper holder; one copper holder can accommodate six slices maximum; the quartz window on the holder is used for ion beam alignment and focalization

Summary of this subsection:

Internal self-irradiation from fission products (minor actinides) in powellite was simulated by exposing powellite crystal under external Ar-ion radiations. According to the SRIM simulation, multi-energies (7, 5, 3, 2, 0.9 MeV) Ar irradiations were performed successively on oriented powellite crystal slices in order to generate even dpa profiles in a 3-μm-thick damaged layer inside the sample.

2.2.3 Preparation of lamellae from irradiated powellite samples using focused ion beam (FIB)

As it has been discussed by Nasdala *et. al* [35, 36], spatial resolutions of optical characterizations technique (i.e. micro-Raman and micro luminescence) have to be considered carefully before performing measurements on the irradiated samples. When performing analyses perpendicular to the irradiated surface, depth resolution of the equipment becomes very crucial. Real analyzed volume can exceed the thickness of irradiated layer, from which spectrum is mixed by information from the non-irradiated layer just below the irradiated one.

The achievable spatial resolution (consisting of lateral and depth resolution) is primarily dependent on the laser wavelength and microscope objective being used. The maximal depth resolution of a confocal Raman [37] spectrometer can be estimated [38, 39] as $4\lambda/(NA)^2$, whereas the corresponding lateral resolutions (laser waists) is about $1.22\lambda/NA$. Here, λ is the incident laser wavelength and NA is the numerical aperture of the objective. For example, when equipped with a x100 objective (NA=0.95), depth resolutions of 473 nm and 633 nm laser are 2.1 μm and 2.8 μm, respectively, while their lateral resolutions reach as high as 0.6 μm and 0.8 μm, respectively. A comparison of Raman resolution (with 633-nm-laser exictation) between theoretical prediction and experimental estimation is shown in Appendix A.7.

According to SRIM simulation in Subsection 2.2.2, thickness of the damage layer in powellite induced by Ar irradiation is 3 μm in this study, which is very close to the estimated depth resolution of confocal Raman stated above (2.1 μm for 473-nm laser, and 2.8 μm for 633-nm laser). The principal relation of analyzed volume and irradiation-damaged layer is shown in Figure 2-24. It suggests that the actual analyzed volume can extend below the irradiation damaged layer for bulk sample.

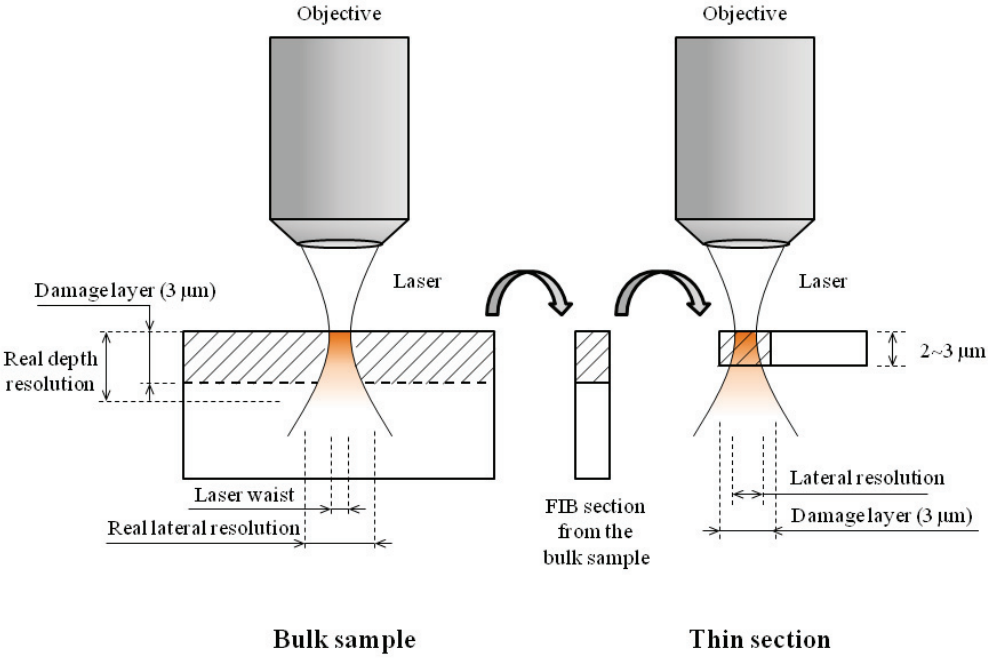

Figure 2-24: Simplified sketches of the beam path of a confocal Raman spectrometer near the focused surface of bulk sample and thin section, respectively; the analyzed volume is shown in orange, which extends below the irradiation-damaged layer (hatched)

By comparison, based on the view that lateral resolution of confocal Raman spectrometers is much better than the depth resolution, *effective spatial resolution of conventional Raman analyses of thin layers may be improved by applying lateral scanning on a cross-section prepared perpendicular to the surface*, as illustrated in Figure 2-24. Therefore, to retrieve reliable information from the irradiated layer, Focus Ion Beam (FIB) [40] can be used to prepare such a thin section for optical characterizations (micro-Raman and micro-luminescence).

A series of FIB lamellae were prepared from some of the irradiated powellite slices (with both a- and c-orientations) using a scanning electron microscope (SEM) equipped with FIB (Carl Zeiss AURIGA CrossBeam Workstation) at Institute of Electronic Materials Technology (Poland). The SEM equipment is shown in Figure 2-25. FIB sections were taken from powellite slices with damage levels of 0.012, 0.12, 1.2 and 5.0 dpa. To distinguish the samples, FIB sections from *a*- and *c*-slices are called a- and c-lamellae, respectively. Figure 2-26 shows the orientations of irradiated powellite slices and their corresponding FIB sections.

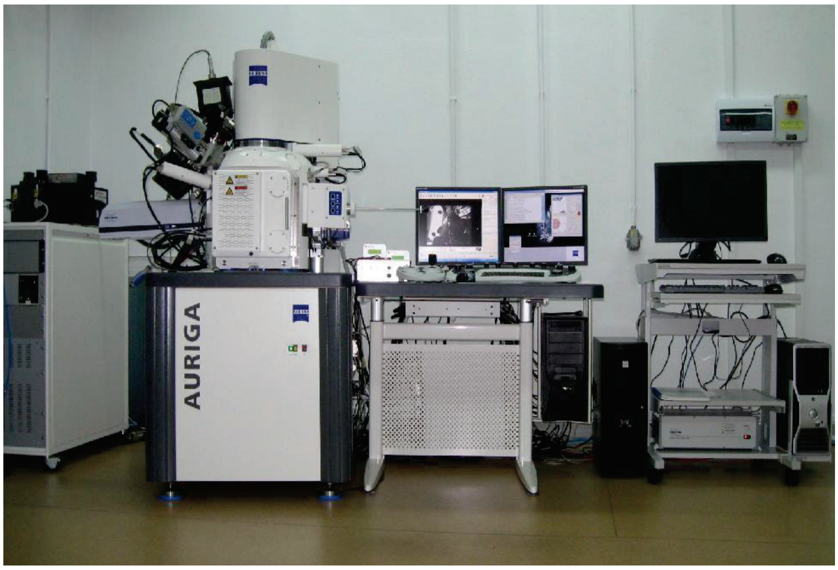

Figure 2-25: AURIGA CrossBeam Workstation (FIB-SEM) from Carl Zeiss [41] for the preparation of FIB sections from irradiated powellite single crystals

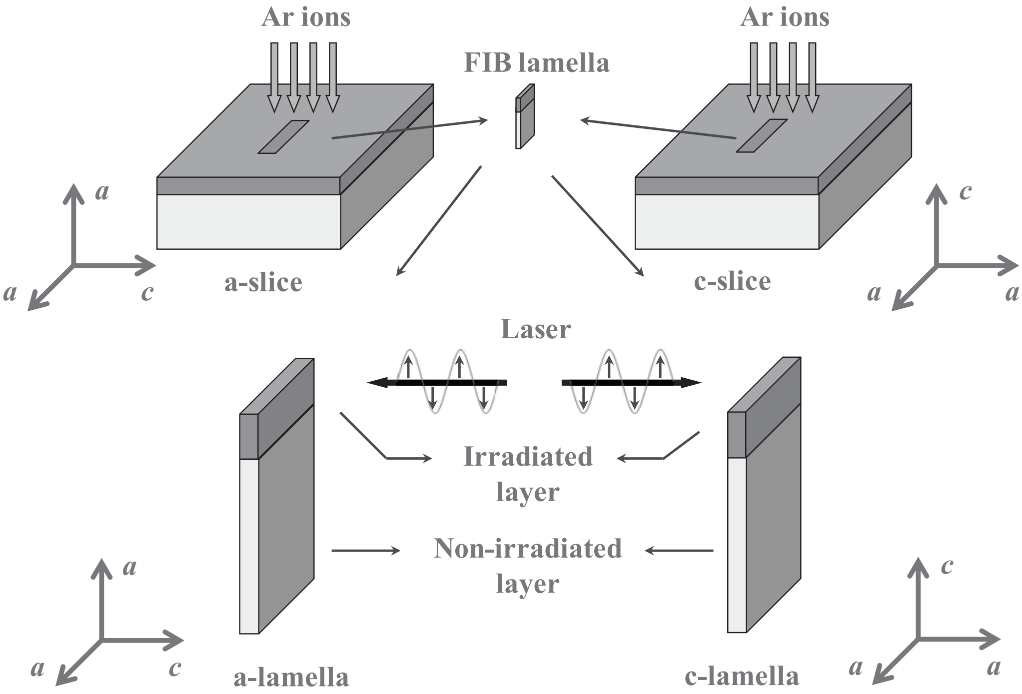

Figure 2-26: Orientation scheme of powellite slices used in Ar irradiation and their corresponding FIB lamellae (3 µm in thickness) for Raman and luminescent measurements; dark gray stands for irradiation-damaged layer and light gray stands for healthy layer in powellite

Secondary electron images of the lamella preparation procedure using FIB-SEM are shown in Figure 2-27. Two prismatic trenches (Figure 2-27-(b)) were milled by 30-kV gallium (Ga) ion beam to prepare a thin lamella cut perpendicular to the surface of the irradiated area (Figure 2-27-(a)). The lamella was lifted out from the bulk using a micromanipulator tip attached to the surface of the powellite sample, then transferred to a special holder (lift-out copper grid) and followed by final thinning to 3 µm using Ga^+ beam.

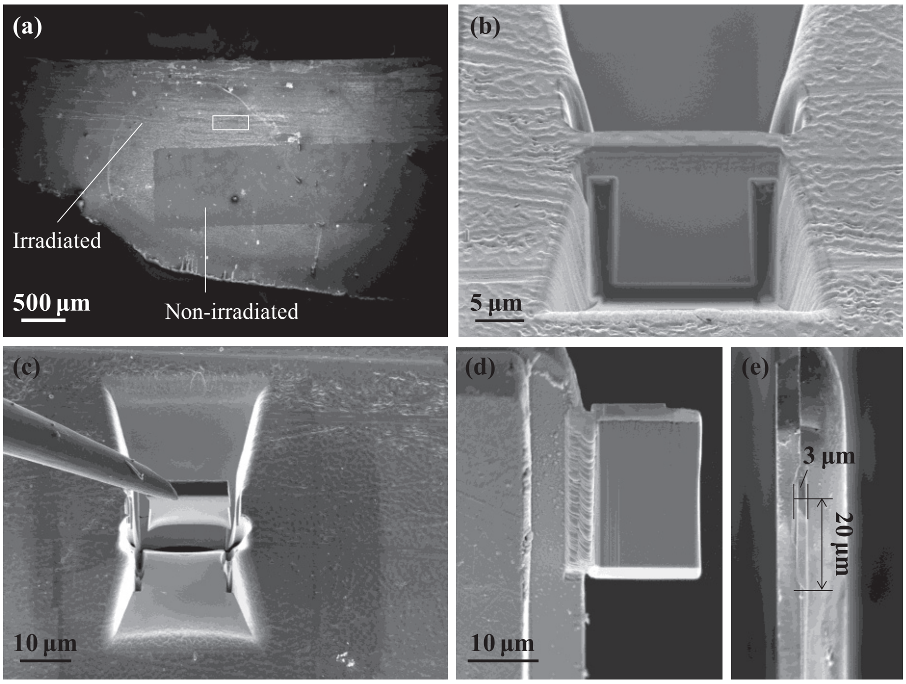

Figure 2-27: Scanning electron microscope images (secondary electron images) of the lamella preparation procedure; (a) surface of powellite crystal slice including irradiated and non-irradiated areas (stage tilted at 0°); the white rectangle indicates the origin place of the lamella; (b) prismatic trenches milled by focus ion beam on the irradiated area to prepare a thin section (FIB lamella) perpendicular to the surface (stage tilted at 10°); (c) lift-out of the lamella from the powellite slice (stage tilted at 10°); (d) the lamella attached to a TEM copper grid after final ion beam thinning(stage tilted at 55°); (e) side-view of the lamella (stage tilted at 55°)

Summary of this subsection:

By using a FIB-SEM equipment, a series of oriented FIB sections with an average thickness of 3 µm were prepared from irradiated powellite slices which have 0.012, 0.12, 1.2, and 5.0 dpa (for both a- and c-orientations).

2.2.4 Technique I: Optical interferometry — Macroscopic investigation

Optical interferometry is a technique of combining light from multiple sources in an optical instrument in order to make various precise measurements. This technique has been applied to characterize surface topography, surface profile, and surface roughness [42-44]. In this study, surface optical topography of all irradiated samples was measured using a Microsurf 3D profiler (Fogale Nanotech) built on microscope with a vertical resolution down to 1 nm, to investigate the *macroscopic swelling* of *a*- and *c*-orientated irradiated powellite.

2.2.5 Technique II: Raman spectroscopy — Mesoscopic investigation

Raman spectroscopy is a spectroscopic technique used to observe vibrational, rotational, and other low-frequency modes in materials, which relies on Raman scattering (inelastic scattering) of monochromatic light (laser) [45, 46]. Interaction between laser beam and the molecular vibrations (phonons) or other excitations in the materials results in the energy of the incident laser photons being shifted down (Stokes Raman scattering) or up (anti-Stokes Raman scattering). The shift in energy gives information about the vibrational modes in the system. An energy-level diagram of Rayleigh and Raman scattering is presented in Figure 2-28.

In this study, Raman spectroscopy was used to characterize the *modification of powellite medium-range-order structure with damage level in the irradiated layer.* Raman spectra of all the studied samples were collected at room temperature on a LabRAM ARAMIS (Horiba Jobin-Yvon, France) micro-Raman spectrometer equipped with a CCD detector under confocal condition. A 633-nm laser was used as the excitation source in order to avoid the luminescence of Eu in the Raman spectra range. All the measurements were carried out with a 100× Olympus MIR Plan objective (NA = 0.95), and each Raman spectrum was recorded using an 1800 l/mm grating (high resolution) and a 75 μm confocal pinhole.

As it is known, polarizations of the incident laser can affect the active vibration modes of $[MoO_4]^{2-}$ tetrahedra of the powellite due to selection rules [47, 48]. For Raman measurement on FIB lamellae, the laser beam was perpendicular to the section. Directions and polarizations of the laser beam are indicated in Figure 2-26. Raman Porto notation[49] are used to indicate the direction and polarization of Raman measurements on the samples, as illustrated in Figure 2-29. Therefore, notations of measurements are “c(ar)c” on a-lamella (FIB section from a-oriented powellite) and “a(cr)a” on c-lamella (FIB section from c-oriented powellite).

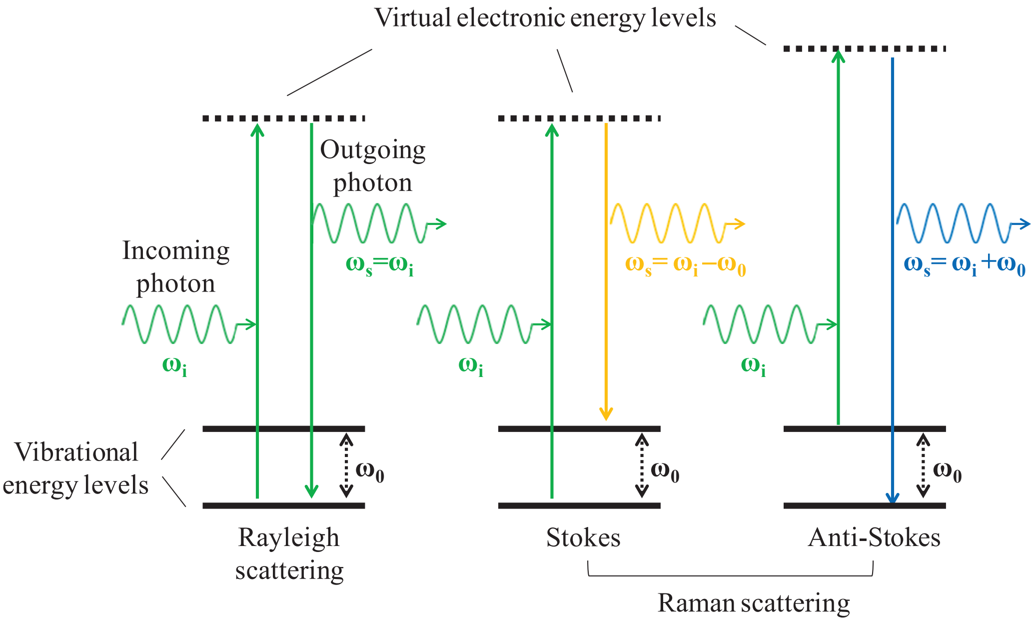

Figure 2-28: Energy-level diagram of Rayleigh and Raman scattering (Stokes and anti-Stokes); ω_i: frequency of incoming photon; ω_s: frequency of scattering photon; ω0: frequency corresponding to energy difference of two vibration levels

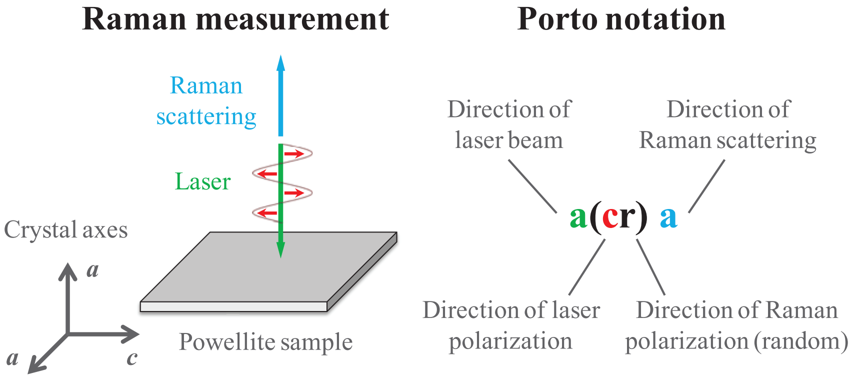

Figure 2-29: Porto notation[49] in Raman measurement

Figure 2-30 shows how mapping was perform on the FIB lamellae. Confocal Raman scanning was carried out in the white rectangle area with a step of 0.2 µm under confocal condition stated above. All spectra were background subtracted and fitted using Lorentzian profile. Parameters including peak area, linewidth (full-width at half-maximum, FWHM) and peak position (frequency) were extracted to construct map for each lamella, in order to follow structure modification according to depth and to compare the different irradiation damage due to orientations and dpa values.

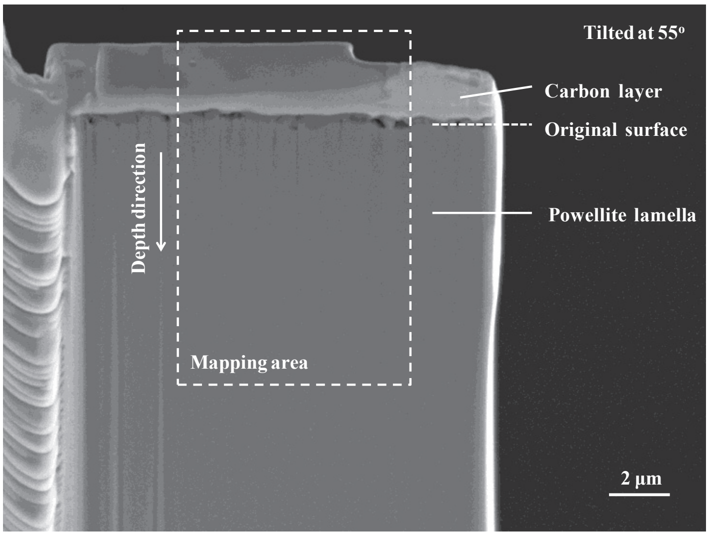

Figure 2-30: Mapping area on the FIB lamella (white rectangle); original surface of the powellite slice is indicated in the figure (SEM image, stage tilted at 55°)

2.2.6 Technique III: Luminescent spectroscopy — Local order investigation

Emission of RE ions [50, 51].can be easily recorded and it is very sensitive to local crystal environment, which can be used as optical probe to monitor the local structure of materials.

A tunable Nd: YAG laser system (NT342B-SHG/SFG, EKSPLA) is used to achieve the site-selective excitation experiments. The YAG:Nd (NL300) pumped OPO (optical parametric oscillator) followed by a second harmonic generator (SHG) crystal provided the laser exitation with a range of wavelength from 400 to 700 nm, which covers the Eu^{3+}: $^7F_0 \rightarrow {}^5D_{0\text{-}2}$ absorption bands. The laser beam was horizontally polarized with a pulse duration of 5 ns, and it is focused on sample surface by optical lens. The selectively excited Eu^{3+} emission spectra are recorded without any polarization.

Polarized emission spectra of pristine powellite are conducted on a RM 1000 micro-spectrometer (Renishaw) at room temperature with an continuous excitation of 532 nm of diode CW laser (300 mW maximum). All the measurements were carried out with a 100X Olympus objective (NA = 0.95), and each spectrum was recorded using a 1800 l/mm grating (High resolution) and a 50 μm slit.

Photoluminescence mapping is performed on FIB lamellae (similar to Raman mapping) to follow the changes of powellite structure induced by Ar irradiations. Mapping of steady-state emission spectra Eu^{3+} were conducted on a LabRAM ARAMIS Horiba equipment[10] (the same as for Raman experiment), using a continuous laser source of 473 nm and a 1800 l/mm grating (high resolution). Each luminescent spectrum was recorded from 578 nm to 620 nm which corresponds to emission of Eu^{3+}: $^5D_0 \rightarrow {}^7F_{0,1}$ transitions.

2.2.7 Technique IV: Transmission electron microscopy (TEM) — Induced defects investigation

Transmission electron microscopy (TEM) is a microscopy technique based on interaction of ultra-thin specimen and the electron beam that passes through the specimen. Alternate working modes allow TEM to observe modulations in chemical identity, crystal orientation, electronic structure and sample induced electron phase shift as well as the regular absorption based imaging [52]. It has been used to explore the atomic structure of crystalline and amorphous materials.

Accordingly, *defects* in the powellite structure induced by Ar irradiations were characterized using a TOPCON EM002B TEM equipment (Figure 2-31) working at 200 kV with a point-to-point resolution of 0.19nm and a double-tilt specimen holder. Ultra-thin FIB lamellae (as shown in Figure 2-31) were prepared particularly for the TEM measurements.

---

[10] The xy stage equipped on the ARAMIS is better than the one on RENISHAW, which is good for mapping.

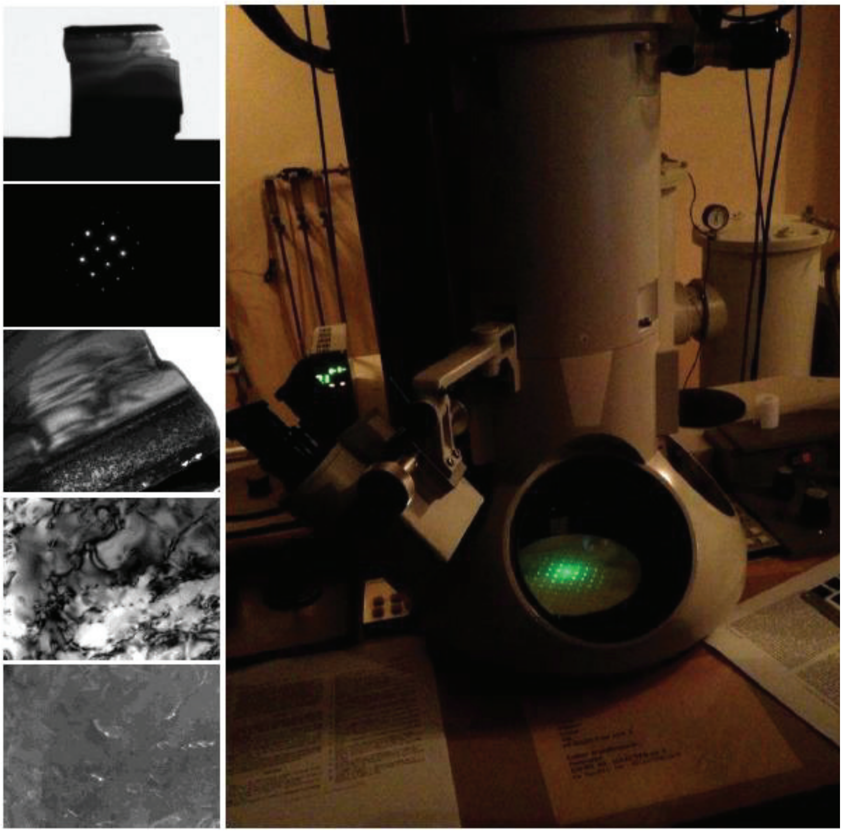

Figure 2-31: TOPCON EM002B transmission electron microscope used for characterization of defects in powellite induced by Ar irradiations; image of an ultra-thin FIB section used for TEM measurements is shown on the upper left corner

2.3 Summary

Methodology for studying the fractionation of fission products in Mo-rich borosilicate and the behavior of powellite single crystal under irradiation are described in this chapter.

Firstly, for the study on fractionation of fission products in Mo-rich borosilicate:

Mo-rich borosilicate glass-ceramic sample containing needle-shaped dendritic $CaMoO_4$ crystallites which have a diameter of about 25 microns and a length of several hundred microns was obtained by performing two-steps thermal treatment on the Mo-rich borosilicate analogue. A μLIBS system was set up based on a YAG: Nd nanosecond pulse laser coupled with a microscope modified to support high energy pulse laser for performing mapping of multi-elements automatically on the specified sample surface. AFM was used to characterize precisely the laser-ablated craters on the sample surface. LA-ICP-MS was used to validate the μLIBS measurements. EMPA was used as supplementary technique to illustrate the distribution of multi-elements in the Mo-rich borosilicate glass-ceramic sample, and particularly to determine the fractionation behavior of elements in the borosilicate glass-ceramic. Results and discussion of the fractionation of fission products in Mo-rich borosilicate glass-ceramics will be presented in Chapter 3.

Secondly, for the study on behavior of powellite single crystal under irradiation:

An Eu, Nd and Na doped calcium molybdate single crystal was grown by Czochralski technique. The phase of the synthetic powellite crystal was verified to be $CaMoO_4$. Orientations of the powellite crystal were determined using XRD. A series of oriented powellite slices were prepared by cutting the bulk crystal along two different crystallographic planes. Internal self-irradiation from minor actinides on powellite was simulated by exposing powellite crystal under external Ar-ion radiations. According to the SRIM simulation, multi-energies (7, 5, 3, 2, 0.9 MeV) Ar irradiations were performed successively on oriented powellite crystal slices in order to generate even dpa profiles in a 3-μm-thick damaged layer inside the sample. By using a SEM equipment, a series of oriented FIB sections with an average thickness of 3 μm were prepared from irradiated powellite slices which have 0.012, 0.12, 1.2, and 5.0 dpa (for both a- and c-orientations). Surface optical topography of all irradiated samples was measured using optical interferometry. Modifications on powellite structural properties in medium-range-order after irradiation were characterized by Raman spectroscopy. Confocal Raman mapping was conducted on FIB sections to follow the evolution behavior of the powellite structure. Modifications on local crystal environment were probed by measuring the emission spectra of Eu^{3+}. Lattice defects induced by irradiations were characterized by TEM. Results and discussion of the behavior of powellite single crystal under irradiations will be presented in Chapter 4.

Reference

1. Mendoza, C., *Caractérisation et comportement sous irradiation de phases powellites dopées terres rares: applications au comportement à long terme de matrices de confinement de déchets nucléaires*, 2010, Université Claude Bernard-Lyon I.
2. McMillan, P.W., *Glass-ceramics*. 2d ed. Non-metallic solids1979, London ; New York: Academic Press. viii, 285 p.
3. Henry, N., et al., *Heat treatments versus microstructure in a molybdenum-rich borosilicate.* Journal of non-crystalline solids, 2004. **333**(2): p. 199-205.
4. Cantor, B., *Novel nanocrystalline alloys and magnetic nanomaterials : an Oxford-Kobe materials text*. Series in materials science and engineering2005, Bristol ; Philadelphia: Institute of Physics Pub. xiii, 325 p.
5. Hulsenberg, D., *Microstructuring of glasses*2008, New York: Springer.
6. Donald, I.W., *Waste immobilization in glass and ceramic based hosts : radioactive, toxic and hazardous wastes*2010, Chichester, U.K.: Wiley. xvii, 507 p.
7. Cremers, D.A. and L.J. Radziemski, *Handbook of laser-induced breakdown spectroscopy*, 2006, John Wiley & Sons: Chichester, West Sussex, England ; Hoboken, NJ. p. xviii, 283 p., 10 p. of plates.
8. Miziolek, A.W., V. Palleschi, and I. Schechter, *Laser-induced breakdown spectroscopy (LIBS) : fundamentals and applications*2006, Cambridge, UK ; New York: Cambridge University Press. xvii, 620 p.
9. Thakur, S.N. and J.P. Singh, *Laser-induced breakdown spectroscopy*. 1st ed2007, Amsterdam ; Boston: Elsevier. xxiv, 429 p.
10. Yu, J., et al., *Generation and expansion of laser-induced plasma as a spectroscopic emission source.* Frontiers of Physics, 2012: p. 1-21.
11. Dwivedi, Y., S. Thakur, and S. Rai, *Laser induced breakdown spectroscopy diagnosis of rare earth doped optical glasses.* Applied Optics, 2010. **49**(13): p. C42-C48.
12. Smith, P.M., *High-Purity Rare Earth Oxides Produced via Precipitation Stripping.* Metallurgical and Materials Transactions B, 2007. **38**(5): p. 763-768.
13. Ayyalasomayajula, K.K., et al., *Quantitative analysis of slurry sample by laser-induced breakdown spectroscopy.* Analytical and bioanalytical chemistry, 2011. **400**(10): p. 3315-3322.
14. Menut, D., et al., *Heavy metals migration in argilaceous rocks: on the use of micro laser-induced breakdown spectroscopy (micro LIBS) as a microanalysis tool*, in *Scientific Basis for Nuclear Waste Management XXIX*2005, MRS Fall Meeting: Ghent, Belgique. p. v. 932, pp. 913-918.
15. Sarkar, A., et al., *Laser induced breakdown spectroscopic quantification of platinum group metals in simulated high level nuclear waste.* Journal of Analytical Atomic Spectrometry, 2009. **24**(11): p. 1545-1550.

16. *What is LIBS?* 2013; Available from: http://www.uwindsor.ca/people/rehse/15/what-is-libs.
17. Thakur, S.N. and J.P. Singh, *Laser-induced breakdown spectroscopy*, 2007, Elsevier: Amsterdam ; Boston. p. xxiv, 429 p.
18. Ma, Q., et al., *Toward quantitative analysis of trace element in speleothems using laser-induced breakdown spectroscopy*, in *Conference on Lasers and Electro-Optics/Pacific Rim*2009.
19. Hark, R.R., et al., *Geographical analysis of "conflict minerals" utilizing laser-induced breakdown spectroscopy.* Spectrochimica Acta Part B-Atomic Spectroscopy, 2012. **74-75**: p. 131-136.
20. Kaiser, J., et al., *Trace elemental analysis by laser-induced breakdown spectroscopy-Biological applications.* Surface Science Reports, 2012. **67**(11-12): p. 233-243.
21. Menut, D., et al., *Micro-Laser-Induced Breakdown Spectroscopy Technique: A Powerful Method for Performing Quantitative Surface Mapping on Conductive and Nonconductive Samples.* Appl. Opt., 2003. **42**(30): p. 6063-6071.
22. Godwal, Y., et al., *Development of laser-induced breakdown spectroscopy for microanalysis applications.* Laser and Particle Beams-Pulse Power and High Energy Densities, 2008. **26**(1): p. 95-104.
23. Boue-Bigne, F., *Laser-induced breakdown spectroscopy applications in the steel industry: Rapid analysis of segregation and decarburization.* Spectrochimica Acta Part B-Atomic Spectroscopy, 2008. **63**(10): p. 1122-1129.
24. Cravetchi, I.V., et al., *Spectrochemical microanalysis of aluminum alloys by laser-induced breakdown spectroscopy: identification of precipitates.* Applied Optics, 2003. **42**(30): p. 6138-6147.
25. Kossakovski, D. and J.L. Beauchamp, *Topographical and chemical microanalysis of surfaces with a scanning probe microscope and laser-induced breakdown spectroscopy.* Analytical Chemistry, 2000. **72**(19): p. 4731-4737.
26. Maganov, S.N. and M.-H. Whangbo, *Surface analysis with STM and AFM: experimental and theoretical aspects of image analysis.* VHC, Verlagsgessellschaft, 1996.
27. Geertsen, C., et al., *Evaluation of laser ablation optical emission spectrometry for microanalysis in aluminium samples.* Spectrochimica Acta Part B-Atomic Spectroscopy, 1996. **51**(11): p. 1403-1416.
28. Gornushkin, I.B., et al., *Microchip laser-induced breakdown spectroscopy: A preliminary feasibility investigation.* Applied Spectroscopy, 2004. **58**(7): p. 762-769.
29. Salle, B., et al., *Laser ablation efficiency of metal samples with UV laser nanosecond pulses.* Applied Surface Science, 1999. **138**: p. 302-305.
30. Taylor, H.E., *Inductively coupled plasma-mass spectrometry : practices and techniques*, 2001, Academic Press: San Diego. p. xi, 294 p.

31. Orellana, F.A., et al., *Applications of laser-ablation-inductively-coupled plasma-mass spectrometry in chemical analysis of forensic evidence.* TrAC Trends in Analytical Chemistry, 2013. **42**(0): p. 1-34.
32. Reed, S.J.B., *Electron microprobe analysis and scanning electron microscopy in geology*, 2005, Cambridge University Press: Cambridge. p. xiii, 189 p., 8 p. of plates.
33. Weber, W.J., et al., *Radiation effects in crystalline ceramics for the immobilization of high-level nuclear waste and plutonium.* Journal of Materials Research, 1998. **13**(6): p. 1434-1484.
34. Ziegler, J.F., M. Ziegler, and J. Biersack, *SRIM–The stopping and range of ions in matter (2010).* Nuclear Instruments and Methods in Physics Research Section B: Beam Interactions with Materials and Atoms, 2010. **268**(11): p. 1818-1823.
35. NASDALA, L., et al., *Raman spectroscopy: Analytical perspectives in mineralogical research*, in *Spectroscopic Methods in Mineralogy* A. Beran and E. Libowitzky, Editors. 2004, EMU Notes in Mineralogy: European Mineralogical Union and the Mineralogical Society of Great Britain and Ireland. p. 662.
36. Nasdala, L., et al., *Irradiation damage in monazite-(Ce): an example to establish the limits of Raman confocality and depth resolution.* The Canadian Mineralogist, 2010. **48**(2): p. 351-359.
37. Puppels, G.J., *Chapter twenty-nine - Confocal Raman Microspectroscopy*, in *Fluorescent and Luminescent Probes for Biological Activity (Second Edition)*, W.T. Mason, Editor 1999, Academic Press: London. p. 377-406.
38. Everall, N.J., *Modeling and Measuring the Effect of Refraction on the Depth Resolution of Confocal Raman Microscopy.* Appl. Spectrosc., 2000. **54**(6): p. 773-782.
39. Baldwin, K.J. and D.N. Batchelder, *Confocal Raman Microspectroscopy through a Planar Interface.* Applied Spectroscopy, 2001. **55**(5): p. 517-524.
40. Edinger, K., *Chapter 12 - Focused Ion Beams for Direct Writing*, in *Direct-Write Technologies for Rapid Prototyping*2002, Academic Press: San Diego. p. 347-383.
41. 2010; Available from: http://www.itme.edu.pl/equipment-449.html.
42. Hariharan, P., *Chapter 6 - Electronic Phase Measurements*, in *Optical Interferometry (Second Edition)*2003, Academic Press: San Diego. p. 93-104.
43. Groot, P., *Phase Shifting Interferometry*, in *Optical Measurement of Surface Topography*, R. Leach, Editor 2011, Springer Berlin Heidelberg. p. 167-186.
44. Artigas, R., *Imaging Confocal Microscopy*, in *Optical Measurement of Surface Topography*, R. Leach, Editor 2011, Springer Berlin Heidelberg. p. 237-286.
45. Ferraro, J.R., K. Nakamoto, and C.W. Brown, *Chapter 1 - Basic Theory*, in *Introductory Raman Spectroscopy (Second Edition)*2003, Academic Press: San Diego. p. 1-94.
46. Ferraro, J.R., K. Nakamoto, and C.W. Brown, *Chapter 2 - Instrumentation and Experimental Techniques*, in *Introductory Raman Spectroscopy (Second Edition)*2003, Academic Press: San Diego. p. 95-146.

47. Kiel, A. and S.P.S. Porto, *Selection rules for the electronic Raman effect.* Journal of Molecular Spectroscopy, 1969. **32**(3): p. 458-468.
48. Porto, S.P.S. and J.F. Scott, *Raman Spectra of Cawo4 Srwo4 Camoo4 and Srmoo4.* Physical Review, 1967. **157**(3): p. 716-719.
49. Damen, T.C., S.P.S. Porto, and B. Tell, *Raman Effect in Zinc Oxide.* Physical Review, 1966. **142**(2): p. 570-574.
50. Gaft, M., R. Reisfeld, and G. Panczer, *Interpretation of Luminescence Centers*, in *Modern Luminescence Spectroscopy of Minerals and Materials*2005, Springer Berlin Heidelberg. p. 119-251.
51. Shinde, K., et al., *Basic Mechanisms of Photoluminescence*, in *Phosphate Phosphors for Solid-State Lighting*2012, Springer Berlin Heidelberg. p. 41-59.
52. Reimer, L. and H. Kohl, *Electron-Diffraction Modes and Applications*, in *Transmission Electron Microscopy*2008, Springer New York.

Chapter 3: Mapping of multi-element in Mo- rich borosilicate glass-ceramic

Fractionation behavior of elements between glassy and crystalline phases in the Mo-rich borosilicate glass-ceramic is studied in this chapter by using elemental mapping techniques based on micro laser-induced breakdown spectroscopy (µLIBS) and electron microprobe analysis (EMPA). Section One is focused on µLIBS mapping of Mo-rich borosilicate glass-ceramics, while Section Two talks about elemental mapping of Mo-rich borosilicate glass-ceramic and fractionation of the elements by using commercial EMPA equipment. A discussion on fractionation behavior of fission products is presented in Section Three.

3.1 µLIBS mapping on Mo-rich borosilicate

In this Section, µLIBS mapping was realized on the surface of a Mo-rich borosilicate glass-ceramic using a µLIBS system which consists of a nanosecond pulse laser and an optical microscope. Details of the glass-ceramic and the µLIBS setup sample have been described in Chapter 2, Section 2.1. The µLIBS mapping protocols are stated in Subsection 3.1.1. The details of multi-element mapping (i.e. Mo, Ca, Sr, rare earth elemets, Na, Al, Fe, and Zr) following the measurement protocols are presented in Subsection 3.1.2. AFM is employed to characterize the spatial resolution of µLIBS mapping. Laser-ablation inductively coupled plasma mass spectrometry (LA-ICP-MS) is used to validate the µLIBS mapping results. The fractionation behavior of detected elements in the Mo-rich borosilicate glass-ceramic is preliminarily discussed based on PCA in Subsection 3.1.3.

3.1.1 µLIBS mapping protocols

Spectral length of the spectrometer (Shamrock 303i) in the µLIBS system is about 34 nm when using a high resolution grating (1200 l/mm). Since characteristic atomic or ionic lines of different elements are in different spectral ranges, it is less likely to detect all the elements of the sample within a spectral length of 34 nm, although it is not necessary. Spectra acquisition range has to be adjusted according to the detection of specific elements (Appendix A.2 shows a full-range LIBS spectrum of initial Mo-rich borosilicate glass). LIBS spectra in two different spectral ranges from the same mapping area are shown to be correlated, which suggests the validity of µLIBS mapping for multiple scanning the same sample area with different spectral ranges (See Appendix A.3).

The priority of detection is rare earth elements (REEs) in the Mo-rich borosilicate glass-ceramic which simulate the radioactive minor actinides. Considering the fact that concentration of REEs is relatively low in the sample, the intensities of emission lines from REEs species may be weak. One advantage of using Shamrock 303i spectrometer is that it is designed for working with demanding low-light applications. Before conducting mapping on the Mo-rich borosilicate glass-ceramic, it is very important and necessary to find suitable spectral ranges for detecting REEs in the sample. The μLIBS mapping protocols in this subsection include the approach to conduct large-size mapping and the spectral lines used for elemental mapping.

3.1.1.1 Large-scale mapping

In this experiment, each spectrum was recorded with single laser shot. A sequence of single-laser shots was designed and performed on a small square area on the sample surface, as illustrated in Figure 3-1-(a). Size of the square depends on interval between two laser shots. Accordingly, large-scale mapping can be realized by conducting a series of such square units, as shown in Figure 3-1-(b). Sequences of single-laser-shots covering the expected mapping area can be designed based on the software, by which successive single-shots can scan all over the area automatically.

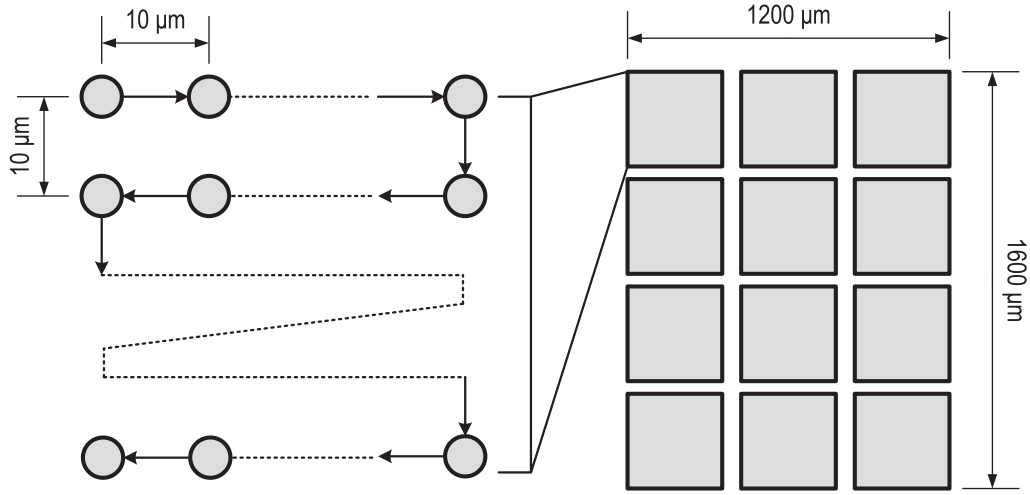

(a) One area: 40 X 40 points (b) 3 X 4 areas

Figure 3-1: Schematic diagram of performing μLIBS mapping on a large area; (a) one square unit of mapping area scanning by single-laser-shots; circles stand for single-shot craters and arrows indicate the direction of single-laser-shot series; (b) a large mapping area consisting of several one square units shown in (a)

3.1.1.2 LIBS Spectra of the glassy and crystalline phases of the Mo-rich glass-ceramic sample

To conduct efficient mapping, it is essential to detect as many elements as possible in a given spectral range, especially for the trace rare earth elements. Figure 3-2 shows LIBS spectra of the glassy phase and crystalline phase of the Mo-rich glass-ceramic sample in the range of 364 nm to 398 nm recorded with a gate delay of 150 ns and a gate width of 1 μs (atomic emission lines are labeled with “I” and ionic emission lines are labeled with “II”). According to Figure 3-2, Mo, Ca, Sr, REEs Al, Fe and Zr emission lines were found in the spectral range from 364 nm to 398 nm. All the detected elements were validated by LA-ICP-MS (which is discussed in Subsection 3.1.2.3). Emission lines of the detected elements are listed in Table 3-1, which are assigned according to the NIST database[1].

In Figure 3-2, for strong lines such as Mo I 379.8 nm, 386.4 nm and 390.3 nm, Ca II 393.3 nm and 396.9 nm, and Al I 394.4 nm and 396.2 nm, the spectral intensities change dramatically from glassy phase to crystalline one. Line intensities of Mo I and Ca II are much higher for crystal spectrum than for glass. By comparison, Al I 394.4 nm and 396.2 nm lines are very intense in the glass spectrum but almost disappear in the crystal one. This observation indicates that Mo and Ca are mainly located in the crystal while Al remains in the glass phase. This result is consistent with the previous statement that partial crystallization occurs in the Mo-rich borosilicate during thermal treatment and precipitates the $CaMoO_4$ crystallite.

According to Figure 3-2, Eu II 390.7 nm, Nd II 384.7 nm, La II 394.8 nm and Pr II 391.8 nm as well as Sr I 394.1 nm lines are present in the spectrum from the crystal whereas Fe I 372.0 nm, 373.5 nm, 373.7 nm and 374.5 nm, and Zr I 388.5 nm and 389.1 nm lines are well observed in the glass. It can be preliminary inferred that REEs (Eu, Nd, La and Pr) and Sr are preferentially incorporated into the $CaMoO_4$ crystal while Fe and Zr prefer to stay in the glass. Spectral line intensities of REEs (Eu, Nd, La and Pr), Sr, Fe and Zr were relatively weak. However, the intensity variation of these species between crystal and glass was still large enough to obtain elemental maps. Lines selected for multi-elemental mapping are indicated in Table 3-1.

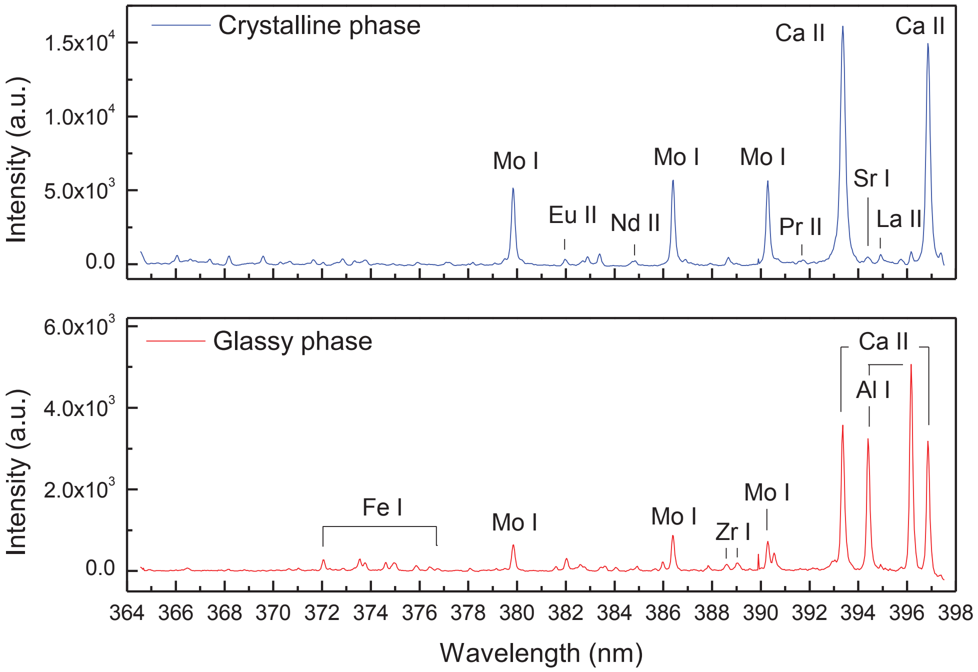

Figure 3-2: Highly resolved LIBS spectra of glassy and crystalline phases of a Mo-rich borosilicate glass-ceramic in the near UV range (364 - 398 nm); atomic lines are labeled with "I" and ionic lines are labeled with "II"

Table 3-1: Spectral lines of detected elements in the range of 364 to 398 nm (atomic lines are labeled with "I" and ionic lines are labeled with "II")

Species	Line position (nm)				
Mo I	379.8*	386.4	390.3		
Ca II	393.3*	396.8			
Sr I	394.1*				
Eu II	390.7*				
La II	394.8*				
Nd II	384.7*				
Pr II	391.8*				
Al I	394.4*	396.2			
Fe I	372.1	373.6	373.8	374.5*	374.9
Zr I	388.6	389.1*			

* Lines selected for μLIBS mapping

Summary of this subsection:

Successive single shots were designed to perform on the expected mapping area automatically. Mo, Ca, Sr, REEs, Al, Fe and Zr emission lines were found in the spectral range from 364 nm to 398 nm. The intensity variation of these species between crystal and glass was large enough to obtain elemental maps. Lines selected for multi-elemental mapping are Mo I 379.8 nm, Ca II 393.3 nm, Sr I 394.1 nm, Eu II 390.7 nm, Nd II 384.7 nm, La II 394.8 nm, Pr II 391.8 nm, Al I 394.4 nm, Fe I 374.5 nm, and Zr I 389.1 nm.

3.1.2 Multi-element mapping of Mo-rich glass-ceramic

A 1200 × 1600 μm^2 (i.e. 1.2 × 1.6 mm^2) rectangular area on the polished surface containing both residual glass and crystallites was selected to conduct µLIBS mapping, as illustrated in Figure 3-1. Sequences of single-laser-shots covering the expected scanning area were defined by the software based on Labview program. Successive single-shot ablations were performed point by point with a step of 10 µm between neighboring craters. Consequently, the total mapping area consists of 120 × 160 points, which requires a duration of about 1 hour.

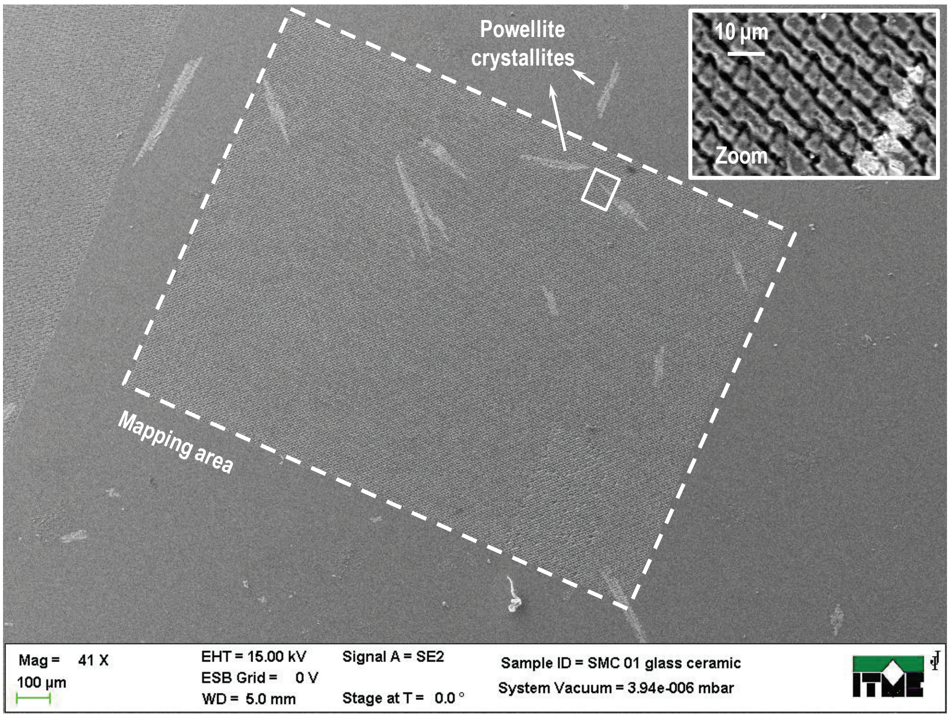

Figure 3-3: Secondary electron (SE) Image of the mapping area (enclosed by white dash rectangle) on Mo-rich borosilicate glass-ceramic sample; the inset figure is a backscattered electron (BSE) image of the area enclosed by whit solid rectangle

3.1.2.1 Laser-ablated crater characterization by AFM

Characterization of single-laser-shot craters [2-5] to determine the spatial resolution of µLIBS mapping were conducted based on AFM. Sufficient emission signal for detection must be considered while reducing the crater size by lowering the laser energy [3, 6]. It is therefore very important to find a compromise between spatial resolution and sufficient LIBS signal (stated in Subsection 2.1.2), in order to obtain both adequate LIBS signal and high spatial resolution for the detection of trace rare earth elements in the nuclear waste glass-ceramic sample.

For µLIBS mapping in this study, energy performed on the sample surface was 400 to 600 µJ. The Mo-rich borosilicate glass ceramic sample consists of glassy and crystalline phases, according to the optical microscope images (Figure 2-3 and 2-4, Chapter 2). First of all, it is interesting to investigate the difference in crater morphologies between glass and crystal. Since $CaMoO_4$ crystal has completely different structure and density from those of glass matrix, laser-material interaction may result in different crater size.

As shown in Figure 3-4, craters formed on the surface by a single laser shot were characterized by AFM. Figure 3-4-(a)-(b) and (d)-(e) provide the topography of craters on glass and on crystal, respectively. Bright regions correspond to the sample surface while dark ones to the bottom of the craters. Apparently, crater on the crystal is smaller than that on glass, which can be probably linked to the difference in laser-material interactions between the two phases. Characterizations of binding energy and chemical bond strength in both glassy and crystalline phases are necessary for further explanation of crater sizes.

Depth profiles of the craters were extracted from the AFM data and presented in Figure 3-4-(c) and (f). Crater on glass has a depth of about 1.2 µm and a diameter of about 7 µm; while crater on crystal has a similar depth as that on glass but a diameter of about 5 µm. By fitting the depth profiles with a two-dimension Gaussian function[11], it is able to calculate the integration of this curved surface which gives an estimated volume[12] of the crater by single-laser-shot. Thereby, the estimated ablated volumes of crater are 20.5 μm^3 on the glass and 10.3 μm^3 on the crystal. Related parameters are listed in Table 3-2.

---

[11] Two-dimension Gaussian function: $I(x) = I_0 \exp\left(-(x-x_0)^2/2\sigma_x{}^2 - (y-y_0)^2/2\sigma_y{}^2\right)$

[12] Estimated volume enclosed by a two-dimension Gaussian function: $V = 2\pi I_0 \sigma^2$, $(\sigma_x = \sigma_y = \sigma)$

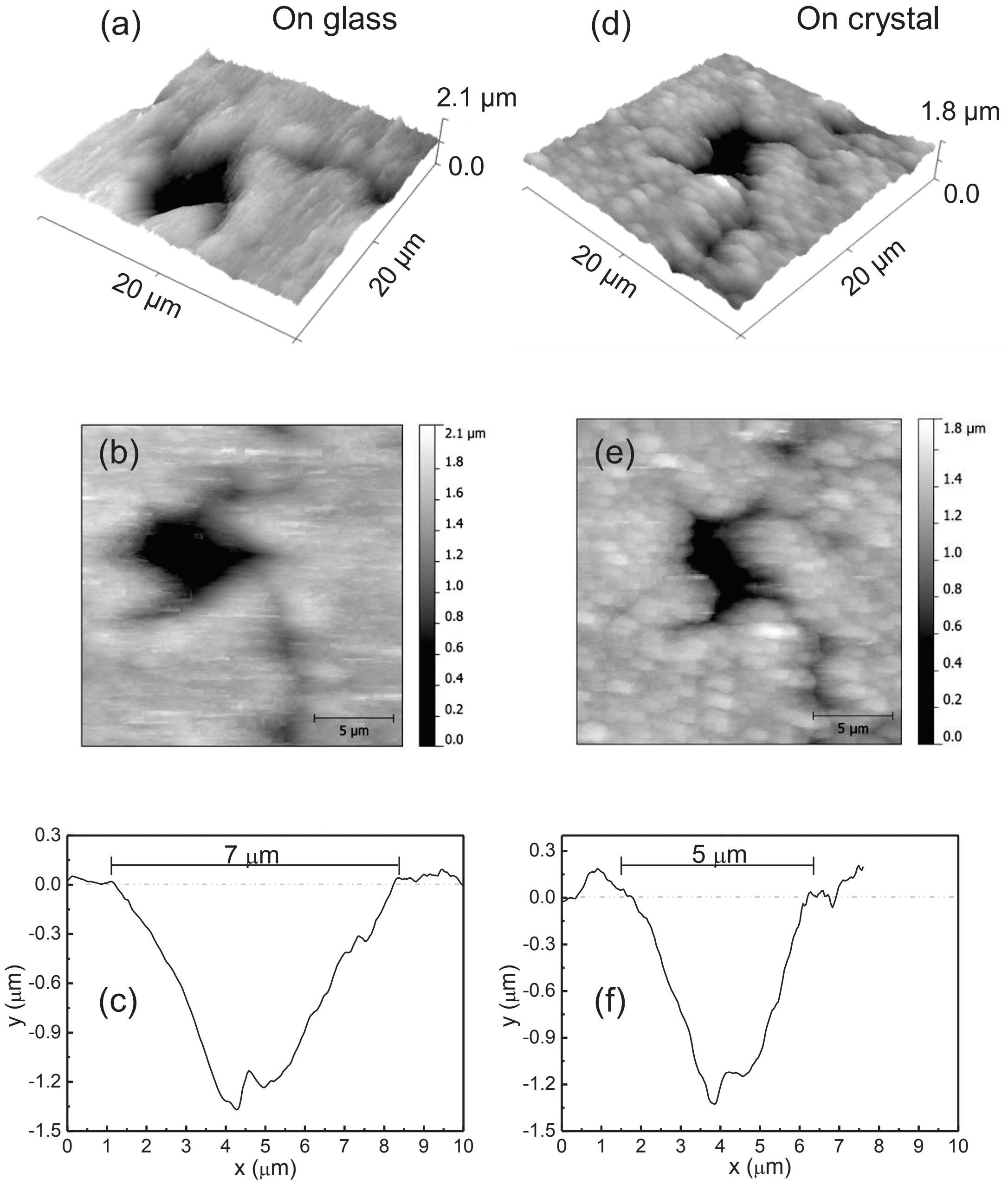

Figure 3-4: Topographies of single-laser-shot craters and depth profiles on glass (a-c) and crystal (d-f) obtained using AFM (tapping mode)

A series of single-shots were performed for AFM measurement to investigate the pulse-to-pulse variation in crater depth and width. Based on statistic calculation of measurements on eight craters, the average diameter and depth of crater on glass are 6.9 ± 0.5 µm and 1.3 ± 0.2 µm, and those on crystal are 5.2 ± 0.4 µm and 1.2 ± 0.1 µm (Table 3-3). According to the crater characterization by AFM, it is possible to perform µLIBS 2D surface scanning with a *resolution of 10 μm*, taking into account the re-deposition of material around the crater after the laser ablation.

Table 3-2: Crater sizes (diameter and depth) and the corresponding fitting parameters12, including the linewidth (σ), the amplitude (I_0), and the volume (V) of the Gaussian profiles

	Measured		Fitted		
Phase	Diameter (μm)	Depth (μm)	σ (μm)	I_0 (μm)	V (μm^3)
Glass	7.0	1.2	3.88	1.2	20.5
Crystalline	5.0	1.2	2.64	1.3	10.3

Table 3-3: Average diameter and depth of single-laser-shot crater on glassy and crystalline phases (powellite) of Mo-rich borosilicate glass-ceramics

Phase	Diameter (μm)	Depth (μm)
Glass	6.9 ± 0.5	1.3 ± 0.2
Crystalline	5.2 ± 0.4	1.2 ± 0.1

3.1.2.2 μLIBS mapping of Mo-rich glass-ceramic

Optical microscope image of the mapping area on the sample surface under a transmitted white light is shown in Figure 3-5. The needle-shaped crystallites which are randomly located in the glass matrix can be clearly distinguished from glass. Since the glass matrix is almost transparent, crystallites beneath the sample surface are always observable under transmitted white light.

For each point in the scanned area, the corresponding line intensity of every species (marked with "*") in Table 3-1 was retrieved from the spectra with background subtracted. Intensity maps of each element were therefore constructed, as shown in Figure 3-5.

Maps of Mo and Ca are full-sized images which correspond exactly to the scanned area on the sample surface. Bright zones in these two maps present very intense emission from Mo I 379.8 nm and Ca II 393.3 nm lines, which indicate the regions rich in Mo and Ca on the sample surface. Dark areas correspond to small amount of Mo and Ca. *Distributions of Mo and Ca coincide well with the localizations of the crystallites shown in the optical microscope image*. It is important to know that only crystallites exposed at the sample surface can be detected by μLIBS. Since crystallites are randomly located in the glass matrix with various tilt angles with respect to the surface, only certain part of some crystallites was exposed after polishing. Nevertheless, most of the crystallites are deeply embedded inside the glass matrix. Taking into account the result of AFM measurement on crater depth, this part of crystallites locates at least 1.2 μm below the sample surface and was not detected by μLIBS mapping. Consequently, all the bright areas correspond to crystallites lying on the surface and the dark areas to glassy surface. As shown in the Mo and Ca maps, surface crystallites distribute on the right side of the scanned area.

The white rectangle in the optical microscope image (Figure 3-5) shows an area rich in crystals on the scanned sample surface. Zoomed maps in this area for Sr, REEs (Eu, La, Nd and Pr), Al, Fe and Zr are displayed in Figure 3-5. All the spectral lines which were used to extract the elemental map of each element are listed in Table 3-1. According to these multi-elemental maps, distributions of elements are very clear. *Sr and REEs are concentrated in powellite crystallites since their maps are similar to those of Mo and Ca.* However, Al, Fe and Zr are barely observed in the crystallite areas. They have a complementary distribution with respect to REEs, which indicates that *Al, Fe and Zr prefer to locate in glass* rather than in crystallites. The green and yellow spots on the Al, Fe and Zr maps are artifact due to the increase of image contrast. These results confirm that Sr and REEs (La, Nd, Eu and Pr) preferentially incorporate $CaMoO_4$ crystal during its crystallization while Al, Fe and Zr remain in the glass matrix. Such distribution of the elements between glassy and crystalline phases can also be illustrated easily by plotting the intensity correlations between Mo I 379.8 nm and the other species, as shown in Figure 3-6. It indicates that Mo is correlated to Ca, Sr and REEs but anti-correlated to Al, Fe and Zr.

Signal from the border of crystallites and glass can be influenced by both crystalline and glassy phases. Thus, the size of crystallites shown in the multi-elemental maps is more or less different from the real one. The determination of the real size of a crystallite is affected by space resolution of the mapping system. However, the distributions of all detected elements are clear enough to show us the information about their fractionation behaviors after the nuclear glass thermal treatment. Such information provides moreover a clue for investigations of the other nuclear waste glass systems or minerals which contain micro-structures.

It has to be noticed here that quantitative elemental analysis by μLIBS is still on progress for the moment. The images in Figure 3-5 are only normalized intensity maps of multi elements. The intensity variation of element in the crystalline phase and in the residual glass is due to the increase of image contrast, which is less likely linked to inhomogeneous element distribution of in each phase (see the EMPA analysis in Section 3.2). To further improve the ability of quantitative analysis by LIBS, more experiments are required, including calibration of element concentrations and determination of analyzed sample volume, etc. However, it is still worth taking advantage of LIBS for the detection and analysis of nuclear materials, since it is sensitive to most of the elements (particularly to low-content REEs) and can response to multi-elements fast and instantaneously.

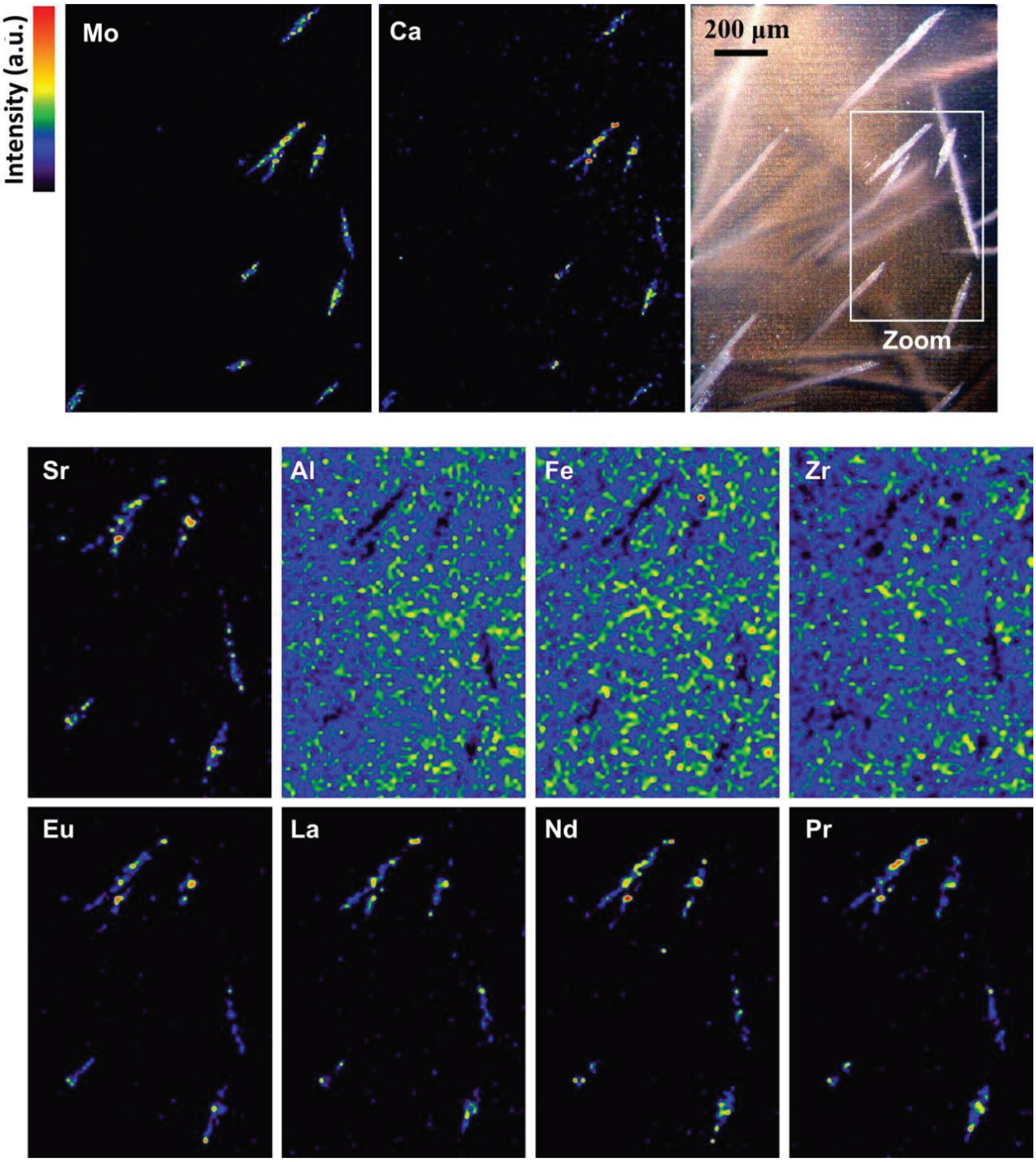

Figure 3-5: Mapping of multi-element of the Mo-rich borosilicate glass-ceramic sample and a optical microscope image of the mapping area; Mo and Ca mappings are full-sized images of the scanned area while all other mappings are images of the area enclosed by the white rectangle in the optical microscope image

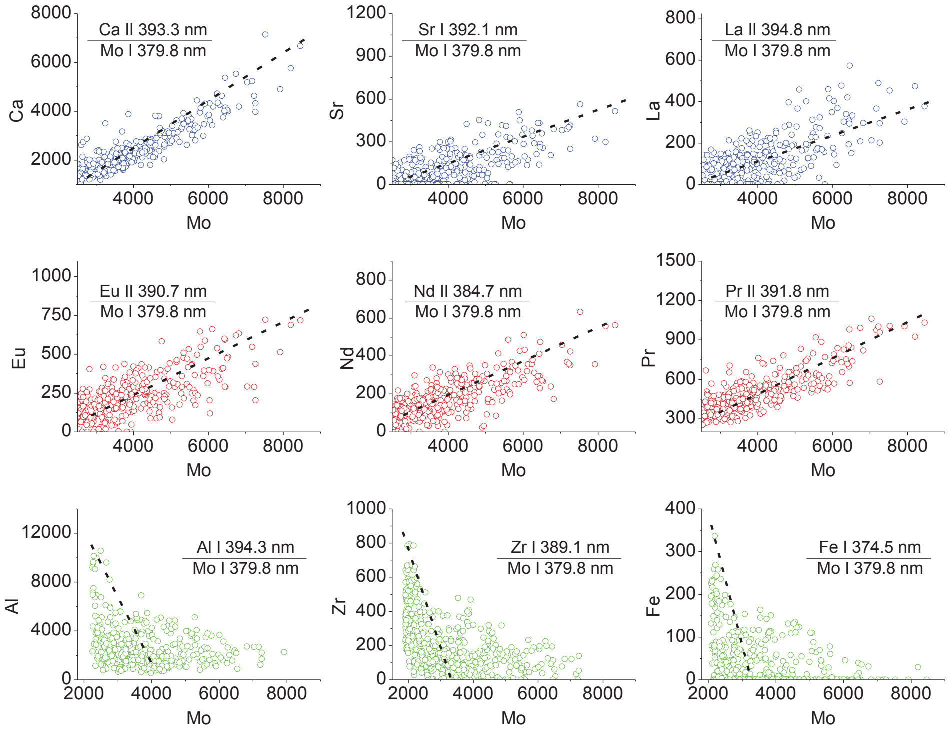

Figure 3-6: Line intensity correlation between Mo I 379.8 nm line and the lines of other species in the mapping area of Mo-rich borosilicate glass-ceramic (around 300 points for each figure)

3.1.2.3 Validation of LIBS analysis by LA-ICP-MS

So far, quantitative analysis on Mo-rich borosilicate glass-ceramics using µLIBS is still on progress. Here, the quantitative analyses on the Mo-rich borosilicate glass-ceramics conducted previously by C. Mendoza [7] is used to provide a validation for the µLIBS mapping results. Average concentrations of elements based on ten-point measurements in both glass and crystal were determined by LA-ICP-MS and are listed in Table 3-4. The ablation craters have a diameter around 20 µm. B, Si, Na, Zn and Cs were not analyzed by LIBS since lines from these elements were not found within the studied spectral range. As can be seen, nearly all the Mo (99 %) are located in crystallites. Concentrations of Ca, Sr and REEs are higher in crystallites then in glass. By comparison, Si, Al, Fe and Zr have much higher concentrations in glass. It is worth noting that, as an important member of the fission products, *Cs is prone to remain in the glassy phase*. Complementary analysis of the elements in Mo-rich borosilicate will be conducted using electron microprobe analysis (EMPA).

Table 3-4: Weight concentrations of the elements detected in Mo-rich glass-ceramic using LA-ICP-MS (average of 10-point measurements) [7]

	Crystal		Glass	
Element	wt.%	Std.	wt.%	Std.
Mo	36.60	2.04	0.48	0.09
Ca	14.48	0.52	2.79	0.06
Sr	4.82	0.44	0.15	0.22
B*	2.57	0.30	4.12	0.27
Nd	2.08	0.18	1.23	0.07
Pr	1.78	0.18	1.12	0.05
La	1.59	0.16	0.72	0.07
Eu	0.56	0.03	0.45	0.02
Na*	0.86	0.43	8.30	0.55
Si*	0.65	1.28	23.15	0.11
Zn*	0.32	0.13	2.18	0.06
Cs*	0.04	0.03	1.13	0.06
Al	0.11	0.19	3.30	0.03
Fe	0.23	0.15	2.30	0.08
Zr	0.11	0.10	1.97	0.04
Ba*	0.10	0.04	0.61	0.04
P*	0.03	0.01	0.09	0.01
O*	33.07	1.01	45.90	0.62

*Not analyzed by LIBS

Summary of this subsection:

For single-laser-shot, crater on glass are about 7 μm in diameter and 1.2 μm in depth, while crater on crystal are about 5 μm in diameter and 1.2 μm in depth. According to the crater characterization by AFM, it is possible to perform μLIBS 2D surface scanning with a resolution of 10 μm. Multi-element mapping by μLIBS suggests that REEs and Sr incorporates into $CaMoO_4$ crystallites, while Al, Fe and Zr remain in the glass. Measurements by LA-ICP-MS provide a validation of the μLIBS mapping results.

3.1.3 Data treatment with principal components analysis (PCA)

Principal components analysis (PCA) was used to classify all the elements detected in this sample by LIBS. The data from an area with 35 × 40 points in the mapping zone which contains three crystallites was extracted and used for PCA calculation (inset of Figure 3-7).

The wavelengths of each line used for mapping (Table 3-1) were considered as variables and measurements from each point were set as observables. An intensity matrix in function of line positions and measuring points was therefore established. The corresponding dataset for each variable (line position of the species) includes 35 × 40 intensity values. Covariances of every two variables were calculated to build a covariance matrix and the eigenvalues as well as eigenvectors of this covariance matrix were figured out. The first and second largest eigenvalues correspond to two most important factors revealed by the data, namely, two principal components. Based on the eigenvalues and eigenvectors, it was able to calculate the contribution of each component to the variables. Detailed procedure of the PCA calculation is shown in Appendix A.4.

Correlations between all spectral lines used for mapping and the first two principal components are plotted in Figure 3-7. According to the PCA calculation, the first principal component (PC1) and the second principal component (PC2) explain respectively 56.95 % and 41.72 % of the behavior of all those lines. Elements located in crystallites according to the μLIBS mapping, such as Mo, Ca, Sr and REEs, were well separated from Al, Fe and Zr which are located in glass. Mo, Ca, Sr and REEs are mostly associated with PC2 while Al, Fe and Zr are mostly associated with PC1. It is thus reasonable to consider that PC1 represents the performance of the glass and PC2 represents that of the crystal.

The points representing Mo, Ca and Al locate on a unit circle which centers at the origin of the PC1-PC2 coordinates. Behaviors of these three elements can be completely explained by PC1 and PC2 considering the contribution of the two principal components to each element. Mo is nearly at (0, 1) on the PC1-PC2 coordinates. It can be inferred that the glass performance (PC1) has nearly no contribution to this species and Mo is located in the crystal. Behaviors of the Ca and Al take more or less into account the other component than the major one. However, for Ca, an important reason has to be considered. During crystallization, Ca and Mo follow strictly the stoichiometric ratio of the formula in precipitating $CaMoO_4$ crystallites. Exceeded amount of Ca is left in the glass matrix. As shown by LA-ICP-MS analysis, low amount of Ca was detected in the glass. Hence, on the PC1-PC2 coordinates, PC2 shows a certain percent of contribution to Ca, which is normal and expected.

Due to the relatively low signal-to-noise-ratio in the μLIBS spectra, variables corresponding to Sr, REEs, Fe and Zn have small amount of contribution from the other components besides PC1 and PC2. However, it is still able to figure out the relation among elements by PCA calculation. Figure 3-7 clearly indicates that Sr and REEs follow the behavior of Mo and Ca which is associated with the performance of crystallization while Fe and Zr follow that of Al. This correlation of elements confirms that Sr and REEs are prone to incorporate with the precipitated $CaMoO_4$ crystallites.

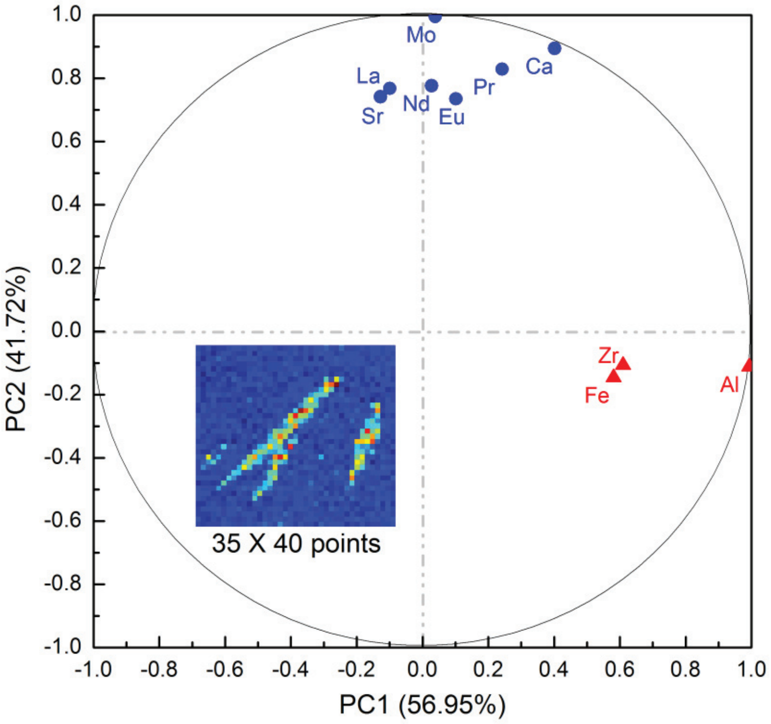

Figure 3-7: Correlation of all the species shown in Table 1 with PCA; PC1 and PC2 represent respectively the performance of glassy and crystalline phases

Summary of this subsection:

By PCA calculation, Sr and REEs (Eu, Nd, Pr, and La) follow the behavior of Mo and Ca which is associated with the performance of crystallization, while Fe and Zr follow the behavior of Al which remains in the glassy matrix.

3.2 Mapping using EMPA

As a complementary technique, quantitative elemental analyses were conducted on the Mo-rich borosilicate glass-ceramic using electron microprobe analysis (EMPA). Mineral samples with known components were used as references. Subsection 3.2.1 presents the multi-element (Si, Al, Na, Mo, Ca, Eu, Nd, La, Pr, Sr, Cs, Zr, Zn, and Fe) mapping of a small area containing both glassy and crystalline phases on the polished surface of Mo-rich borosilicate. Subsection 3.2.3 is the comparison between of µLIBS and EMPA for multi-element mapping.

3.2.1 Multi-element mapping by EMPA

Figure 3-8 to Figure 3-10 show the EMPA mapping of multi-elements, including Si, Al, Na, Mo, Ca, Eu, Nd, La, Pr, Sr, Cs, Zr, Zn, and Fe. The colorbar on the right side of each map indicates the weight percent of the corresponding element. The mapping area is 71.7 × 71.7 µm^2 (512 × 512 pixels) with an interval of 0.14 µm. It has to be noticed that the spatial resolution of EMPA in this experiment is 0.5 to 1 µm, which is larger than the mapping interval. Hence, there is an overlap between neighboring points. Weight percents of the detected elements in the Mo-rich borosilicate glass-ceramic by EMPA are listed in Table 3-5.

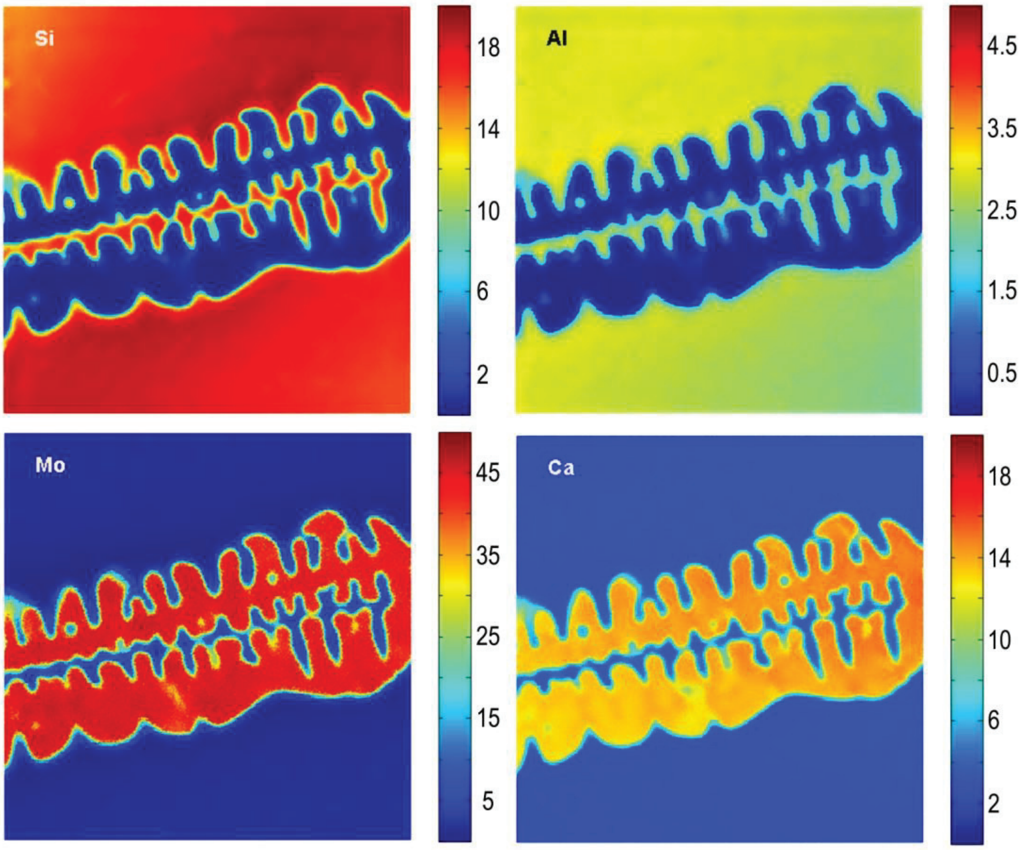

Figure 3-8: EMAP mapping (71.7 × 71.7 µm^2) of major elements, i.e. Si, Al, Mo, and Ca, in Mo-rich borosilicate glass-ceramic; the dendritic part on the maps is the powellite crystallite; colorbar on the right side of each figure indicates the weight percent of each element

As mentioned in Chapter 2, silicon, boron and aluminum oxides constitute the network formers of the borosilicate glass. Due to the experimental constraints, boron was not analyzed. Figure 3-8 shows the EMPA mapping of four major elements of the sample, i.e., Si, Al, Mo, and Ca, which have relatively high concentration in the Mo-rich borosilicate glass-ceramic. According to Figure 3-8, almost all Si and Al distribute in the glassy phase while most of the Mo and Ca fractionated to the crystalline phase and constitute the dendritic powellite crystallite, as observed in Section 3.1. Due to the high contrast between glassy and crystalline phases, the dendritic shaped powellite crystallite can be well recognized.

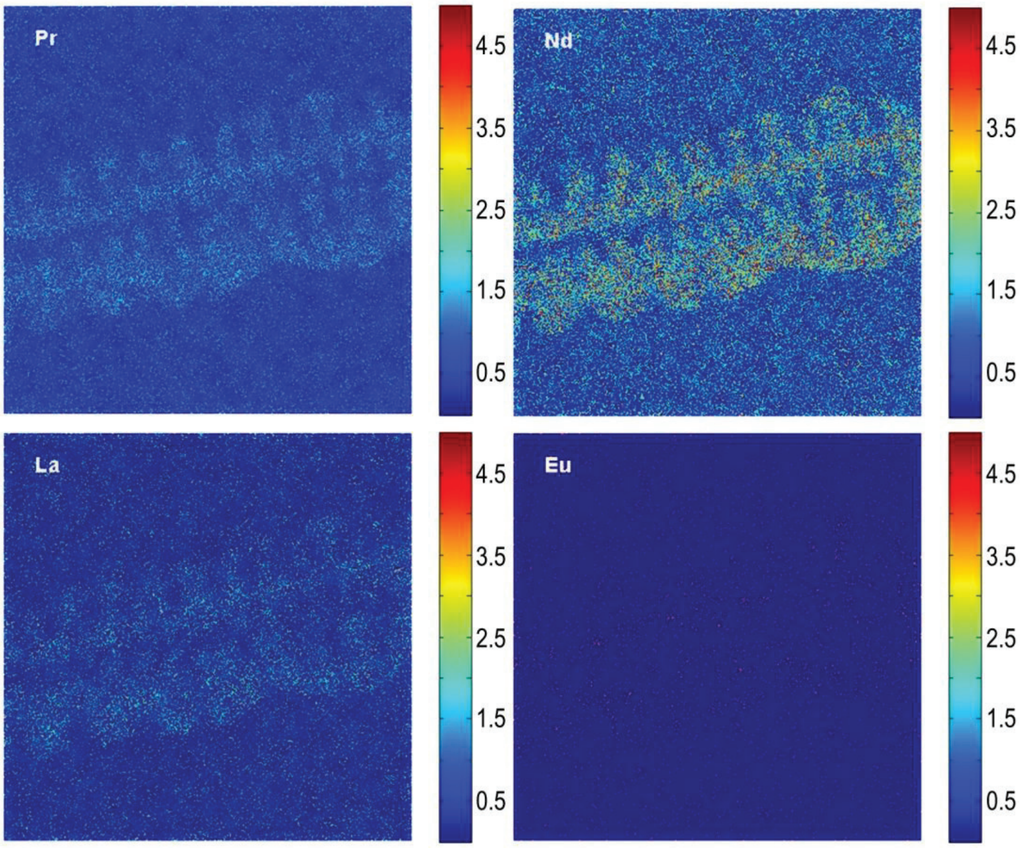

Figure 3-9: EMAP mapping (71.7 × 71.7 µm^2) of REEs (Pr, Nd, La, and Eu) in Mo-rich borosilicate glass-ceramic; the dendritic part on the maps is the powellite crystallite; colorbar on the right side of each figure indicates the weight percent of each element

Concentrations of REEs in the Mo-rich borosilicate sample are very low (as listed in Table 3-4), which may increase the technical difficulty of detection. EMPA mapping of REEs (Eu, Nd, La, and Pr) are shown in Figure 3-9. As can be seen, Nd, La, and Pr concentrate in the powellite crystalline phase, although the signal to noise ratio is very low. However, the detection of Eu is completely disappointed. According to the La-ICP-MS measurements, weight percent of Eu in the Mo-rich borosilicate is extremely low (0.56 % in crystalline phase and 0.45 % in glassy phase). Considering that the size of electron beam for EMPA mapping on the glass-ceramic sample is 0.5 μm, the analyzed volume of the beam is much less than the one in La-ICP-MS analysis (which is about 20 μm). In this case, the EMPA mapping cannot provide useful information on the distribution of very low-content Eu.

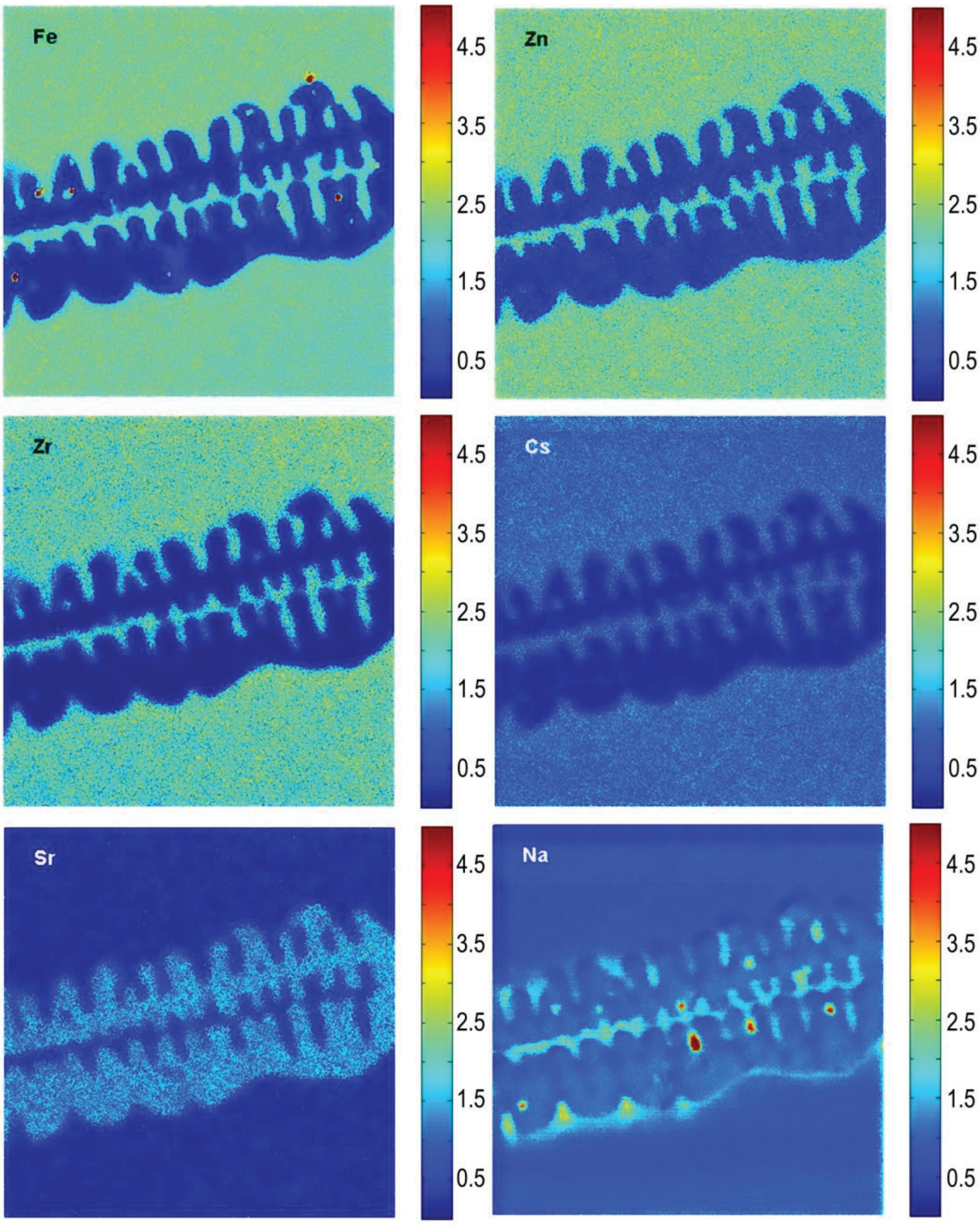

Figure 3-10: EMAP mapping (71.7 × 71.7 μm^2) of Fe, Zn, Zr, Cs, Sr and Na in Mo-rich borosilicate glass-ceramic; the dendritic part on the maps is the powellite crystallite; colorbar on the right side of each figure indicates the weight percent of each element

Figure 3-10 shows the EMPA mapping of Cs, Zr, Zn, Fe, Na, and Sr. As observed by µLIBS mapping, the same result is suggested by EMPA mapping that Fe and Zr are prone to remain in the glassy phase while Sr incorporates to powellite crystallites. The red spots on the Fe map which indicate unusually high concentration are due to pollution in the mapping area. It is worth noting that, as important fission products, Cs and Zn fractionate to the glassy phase instead of the crystalline one.

Distribution of Na is also interesting since it can act as a modifier of the glass matrix and a charge compensator in the powellite crystal. The Na map in Figure 3-10 shows a very low contrast between the glass matrix and powellite crystal as well as an enrichment of Na on the border of the powellite crystallites. It is suggested that Na does not have a preferential fractionation phase in Mo-rich borosilicate glass-ceramic. However, that is an artifact resulted from the migration/evaporation effect of Na in the glass matrix under the electron beam [8]. Since the spatial interval of mapping in Figure 3-8 to Figure 3-10 is only 0.14 µm, there is a very strong overlap between two neighboring points. Accordingly, the detected concentration of Na in the analyzed volume is much less than real amount. In such case, the detected result of Na in the glass matrix is controversial by EMPA detection. Although this artifact is depended on the current density of the electron beam, it can be simply reduced by increasing the spatial mapping interval. As shown in Figure 3-11, the distribution of Na concentration is more reliable with 0.5-µm mapping step, which indicates a higher amount of Na in the glass phase than in the crystalline one. Moreover, the enrichment of Na in the residual glass implies that Na_2MoO_4, which is also a potential Mo-rich crystalline phase, is less likely to form and crystallize in the glass-ceramic. Na_2MoO_4 is not an expected crystalline phase, since the solubility of Na_2MoO_4 in water is more than three orders of magnitude higher than that of $CaMoO_4$ [9]. The analysis by electron microprobe suggests that *$CaMoO_4$ is the most preferred crystalline phase for the studied Mo-rich borosilicate.*

Furthermore, two possible reasons can be used to interpret the enrichment of Na on the border of the powellite crystallites. First of all, due to the migration/evaporation effect, Na can be mobilized in the glass matrix under the electron beam. It is likely to induce Na enrichment on the border of powellite crystallites when the Na migration is stop by the crystal. Secondly, considering the fact that the REEs (trivalent) incorporated to powellite substitute the Ca (divalent) site, Na (monovalent) is possible to migrate from the glassy phase to the crystalline phase in order to compensate the change balance in powellite during the crystal growth. Therefore, an enrichment of Na may also occur on the border of powellite crystallites which stops the Na migration. Moreover, it is important to point out that the Na migration or evaporation is less likely to occur in the crystalline phase since Na is confined in an ordered crystal structure.

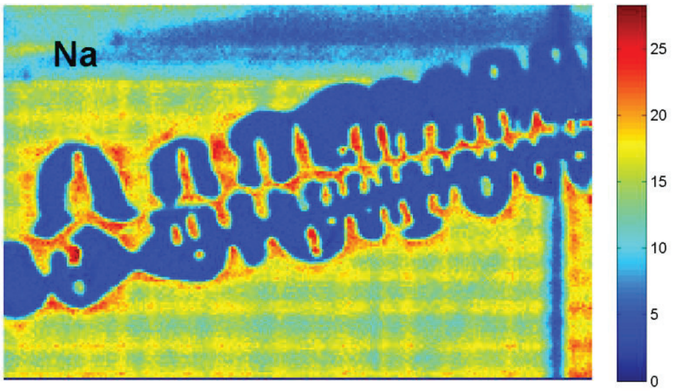

Figure 3-11: EMAP mapping (116.5 × 74.5 μm^2) of Na in Mo-rich borosilicate glass-ceramic with a step of 0.5 μm

Summary of this subsection:

EMPA was used as a complementary technique for quantitative elemental analyses on the Mo-rich borosilicate glass-ceramic, which confirms the results of μLIBS mapping: Most of Mo are trapped as $CaMoO_4$. Nd, Pr, La, and Sr incorporate into $CaMoO_4$ crystallites, while Al, Fe and Zr remain in the glass. However, mapping of REEs (especially Eu) by EMPA with a 0.5 μm beam size is unsatisfactory. Cs and Zn fractionate to the glassy phase instead of the crystalline one. Na has a very strong migration/evaporation effect under the electron beam.

3.2.2 Fractionation of the elements of Mo-rich borosilicate glass-ceramic between crystalline and glassy phases

So far, the EMPA mapping illustrates well the preferential fractionation phases of the elements in the Mo-rich borosilicate glass-ceramic. To further evaluate the glass-ceramic for nuclear waste storage, it is important to know the ability of powellite to incorporate fission products and minor actinides.

First, the partition coefficients of the detected elements between crystalline and glassy phases are employed to investigate the fractionation behavior of the elements in the Mo-rich borosilicate glass-ceramic. In this context, a partition coefficient ($P_{E,c/g}$) refers to the ratio of concentrations of an element (*E*) in the crystalline phase and the residual glass (the glass matrix) at equilibrium.

$$P_{E,c/g} = C(E_c) / C(E_g) \tag{3-1}$$

Here, $C(E_c)$ and $C(E_g)$ are the atom concentrations (at.%) of element *E* in the crystalline and the glassy phases, respectively. The atom ratio can be calculated according to the mass concentrations (wt.%) of the elements of Mo-rich borosilicate glass-ceramic (Table 3-5).

Table 3-5: Element concentrations (in weight percent and atomic percent) of the initial Mo-rich borosilicate glass and the corresponding glass-ceramic by using EMPA (average of 100-to-500-point measurements)

	Initial glass			Mo-rich borosilicate glass-ceramic					
				Glassy phase			Crystalline phase		
	wt. %	std.	**at.%**	wt. %	std.	**at.%**	wt. %	std.	**at.%**
Al	2.80	0.05	**2.14**	2.91	0.12	**2.16**	0.05	0.03	**0.07**
B	5.54	0.62	**10.58**	5.63*		**10.46**	0.00*		**0.00**
Ca	2.96	0.04	**1.53**	2.97	0.16	**1.49**	14.53	0.52	**12.33**
Cs	1.05	0.04	**0.16**	1.21	0.28	**0.18**	0.12	0.16	**0.03**
Eu	0.50	0.11	**0.07**						
Fe	2.31	0.06	**0.85**	2.34	0.40	**0.84**	0.09	0.12	**0.05**
La	0.67	0.08	**0.10**	0.15	0.42	**0.02**	1.55	0.72	**0.38**
Mo	1.67	0.08	**0.36**	0.73	0.16	**0.15**	45.38	2.50	**16.09**
Na	7.58	0.20	**6.81**	8.88	2.40	**7.76**	3.62	0.35	**5.36**
Nd	1.42	0.11	**0.20**	0.71	0.46	**0.10**	1.95	0.58	**0.46**
O	46.69		**60.27**	47.59	0.46	**59.75**	30.14	1.28	**64.05**
Pr	0.36	0.09	**0.05**	0.13	0.18	**0.02**	0.73	0.51	**0.18**
Si	21.49	0.29	**15.80**	22.17	0.29	**15.85**	0.23	0.09	**0.27**
Sr	0.20	0.05	**0.05**	0.08	0.13	**0.02**	1.47	0.48	**0.57**
Zn	1.67	0.09	**0.53**	2.30	0.43	**0.71**	0.23	0.17	**0.12**
Zr	2.19	0.09	**0.50**	2.20	0.58	**0.49**	0.13	0.04	**0.05**

*Estimated value

The partition coefficient $P_{E,c/g}$ is normally independent on the absolute concentration of the element *E*, since the concentration of *E* in the crystalline phase is normalize to that in the glassy phase (Equation (3-1),). However, $P_{E,c/g}$ depends on the thermodynamic conditions (temperature and pressure) of the system. Figure 3-12 shows the partition coefficients of the elements of Mo-rich borosilicate glass-ceramic between crystalline and glassy phases at 850 ^{o}C in air (the annealing temperature for the glass-ceramic sample). The affinity of elements with the two phases in the glass-ceramic sample can be evident by determining of their partition coefficients. According to Equation (3-1), a $P_{E,c/g}$ of greater than 1 corresponds to the element enriched in the crystalline phase (Ca, Nd, Pr, La, Sr, and Mo), while a $P_{E,c/g}$ of less than 1 implies the element concentrated in the glassy phase (Si, Al, Fe, Zr, Cs, Zn, and Na). For the element which is equally distributed between the two phases (O), it has a $P_{E,c/g}$ of 1.

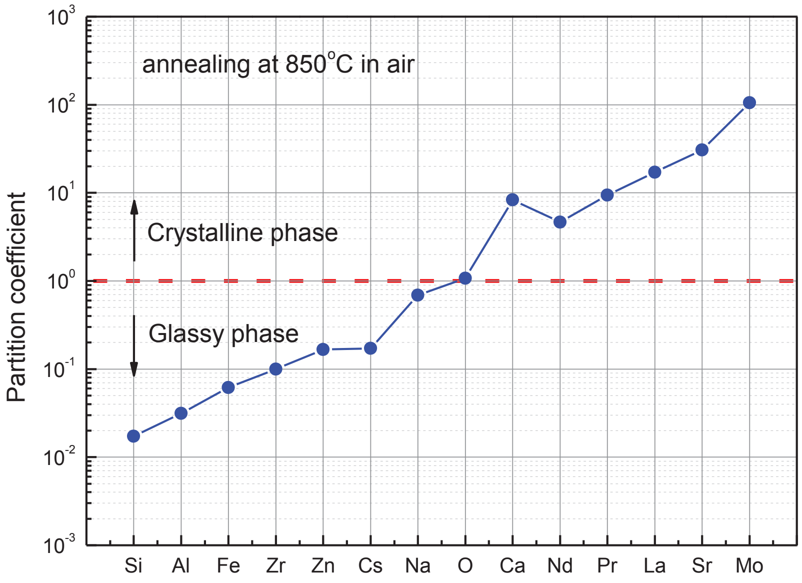

Figure 3-12: Partition coefficient of the elements of Mo-rich borosilicate glass-ceramic between crystalline and glassy phases (by EMPA)

Additionally, it can be noticed that the quantitative analysis of major elements of Mo-rich borosilicate glass-ceramic by LA-ICP-MS (Table 3-4) has some differences from the EMPA measurement (Table 3-5). This problem is probably resulted from the low spatial resolution of LA-ICP-MS (~ 20 μm). As shown by the optical images (Figure 2-4) and the EMPA maps, the section diameter of the powellite crystallites is around 25 μm (maximum), which is more or less the same as the resolution of LA-ICP-MS. Therefore, the measurements on the crystallites by LA-ICP-MS are partly mixed by the signal from the glass matrix. For instance, the amount of Mo in the crystalline phase is only 36.6 %, which gives a Mo-O stoichiometric ratio less than 1:4. However, for the EMPA measurement, a stoichiometric ratio of 0.77:1:3.98 among Ca (12.33 at.%), Mo (16.09 at.%), and O (64.09 at.%) can be determined from the composition of the powellite crystallite (Table 3-5) which is basically in agreement with the formula of $CaMoO_4$, taking into account the substitution of Ca by the incorporated elements. In this case, the EMPA results are more reliable. It has to be noticed that different working conditions of the instruments may provide difference results. The experimental errors have to be carefully considered when performing quantitative analyses on the sample.

Second, in order to figure out the ability of powellite crystallite to incorporate the constituent elements (fission products and minor actinides) of the initial glass, the fractions of the crystalline phase (x_c) and the residual glass (x_g) has to be calculated. As shown in Equation (3-2), the atom concentration of element E in the initial glass, $C(E_i)$, is equal to the sum of its concentration in each individual phase times the respective phase fraction.

$$C(E_i) = x_c C(E_c) + x_g C(E_g) \tag{3-2}$$

Here, $C(E_i)$, $C(E_c)$, and $C(E_g)$ are one-dimensional vector constituted by the known atom concentration of each element in the initial glass, the crystalline phase, and the residual glass, respectively. These three concentrations of each element were detected by EMPA (Table 3-5). The fractions of the crystalline phase (x_c) and the residual glass (x_g) can be calculated by solving Equation (3-2) which gives a value of $x_c = 0.01$ and $x_g = 0.99$ (see Appendix A.5). Due to the large volume of the glass matrix, it is reasonable that the glass phase has a much higher fraction than the crystalline one. Thus, the fractions of each element in the crystalline phase ($F(E_c)$) and in the residual glass ($F(E_g)$) can be determined according to Equation (3-3), which represents the amount of each element in both of the phases. Most importantly, $F(E_c)$ indicates the ability of powellite crystallite to incorporate elements of the initial glass.

$$F(E_c) = \frac{x_c C(E_c)}{C(E_i)}, \quad F(E_g) = \frac{x_g C(E_g)}{C(E_i)} \tag{3-3}$$

As shown in Figure 3-13, about 55 % Mo and 10 % Ca of the initial glass are crystallized as powellite. 10 % Pr, 17 % La, and 26 % Sr are incorporated into the crystallite, while 0.8 % Na is used as compensator. By comparison, Si, Al, Fe, Zr, Zn, and Cs completely remain in the residual glass.

Since the volume of the residual glass is relatively huge comparing to that of the crystallites, there is still a certain amount of REEs and Sr in the glassy phase. However, the enrichment of REEs and Sr in the crystal phase results in a depletion of those elements in residual glass, which participate the reduction of self-irradiation in the glass matrix during long-term storage. Moreover, by improving the crystallization of powellite in the Mo-rich borosilicate, more REEs (minor actinides surrogates) and Sr (fission product) can be incorporated into the crystalline phase and immobilized within a double-barrier environment. Accordingly, the matrix volume for nuclear waste storage can be effectively reduced.

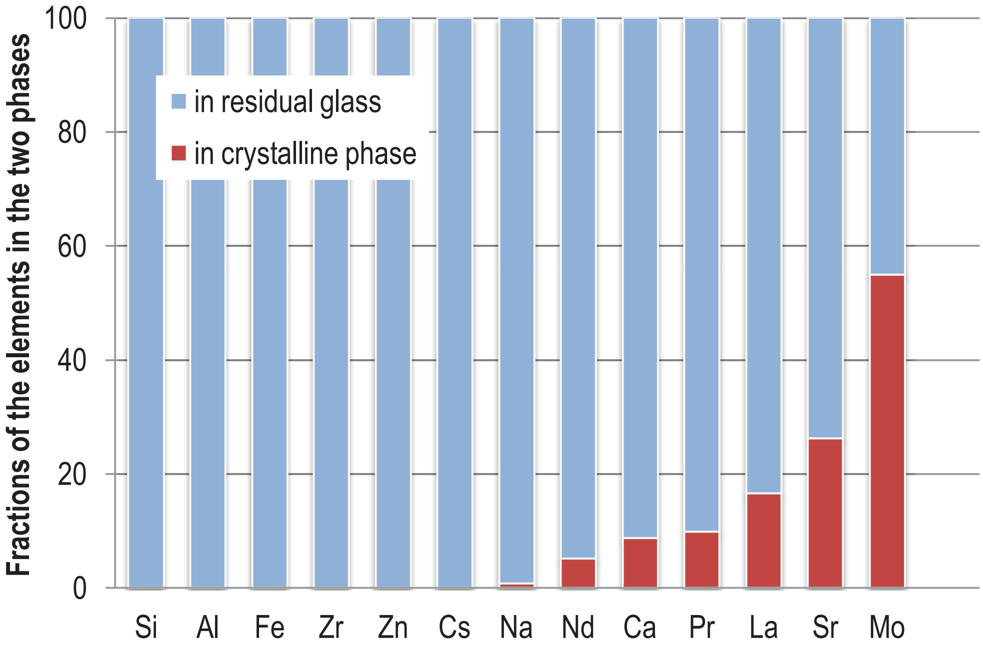

Figure 3-13: Normalized fractions of the elements segregated in the residual glass and in the powellite crystalline phase of the Mo-rich borosilicate glass-ceramic

Summary of this subsection:

Sr (β-decay source) and REEs (minor actinides surrogates, α-decay sources) are enriched in the crystalline phase. About 55 % Mo and 10 % Ca of the initial glass are crystallized as powellite with an incorporation of 10 % Pr, 17 % La, and 26 % Sr. By comparison, Cs (another β-decay source) completely remains in the residual glass. By improving the crystallization of powellite in the Mo-rich borosilicate, more REEs and Sr can be incorporated into the crystalline phase and immobilized within a double-barrier environment. Accordingly, the matrix volume for nuclear waste storage can be effectively reduced.

3.2.3 Comparison of the three techniques for elemental analysis

The main purpose of performing elemental mapping on glass-ceramic nuclear wasteform is to follow the fractionation of fission products between glassy and crystalline phases. It is therefore important and necessary to develop an efficient and convenient elemental analysis technique that can be widespread for industry application. Table 3-6 lists some features μLIBS system in our lab, as well as commercial LA-ICP-MS and EMPA. LA-ICP-MS and EMPA are both well established techniques for quantitative elemental analysis, whereas, *quantitative elemental analysis by LIBS needs to be improved*. However, taking advantages of LIBS, it is still a wonderful solution to perform fast and convenient multi-element mapping on nuclear waste glass systems or minerals containing micro-structures by using LIBS or μLIBS.

Firstly, the *procedure* of μLIBS is very easy without special sample preparation and complex equipments. The main components of the μLIBS system are laser, optics, microscope, spectrometer, and detector, which cost much less than LA-ICP-MS and EMPA instruments. Moreover, neither reference specimens nor specific ambient environment (gas or vacuum) are required during μLIBS measurements.

Secondly, the *spatial resolution* of μLIBS currently reaches less than 10 μm for the Mo-rich borosilicate glass-ceramic sample. Comparing with EMPA (3 to 5 μm), the spatial resolution of μLIBS is still not very sufficient. It has to been noted that the size of laser-ablated crater which determines the lateral resolution is related to analyzed material. For metallic sample, spatial resolution has been reported to be less than 5 μm. By comparison, the laser-material interaction is more complicated for nuclear waste glass-ceramic which can restrict the spatial resolution. However, there is still much room for improvement of μLIBS mapping for precisely localized (micro) surface analysis.

Thirdly, for LIBS, the ability of *instantaneous response for multi-element identification* is definitely attractive, which is much better than LA-ICP-MS and EMPA. For elemental mapping using a Cameca SX FIVE instrument with five detectors, only five specific elements can be analyzed for one time. However, for the μLIBS system in this study, ten elements were analyzed simultaneously using one detector. Especially, LIBS can be beneficial to the detection of rare earth elements in comparison with the sensibility of EMPA on low-content REEs. μLIBS mapping of multi-element in the Mo-rich borosilicate glass-ceramic sample illustrates straightforward the distribution of the detected elements.

Moreover, by employing one more spectrometer and detector, an alternative spectral range can be fixed to detect more elements in the sample simultaneously.

Fourthly, as a very favorable advantage, the *mapping duration* µLIBS is extremely short comparing with LA-ICP-MS and EMPA. For mapping with 10^6 scanning points, µLIBS mapping duration (< 1 hour) is less than one-twentieth of duration (~ days) of LA-ICP-MS and EMPA.

Table 3-6: Some features of the three elemental analysis techniques: µLIBS (in our lab), LA-ICP-MS (commercial), and EMPA (commercial)

Feature	µLIBS	LA-ICP-MS	EMPA
Sample damage	Ablated crater	Ablated crater	Electron irradiation
Spatial resolution	5~10 µm	~20 µm	3~5 µm
Mapping duration (/10^6 pixels)	< 1 h (1 detector)	~ days (1 detector)	> 2 days (5 detectors)
Sensibility of REEs	☺	😐	☹
Ability to detect light elements	☺	☺	☹
Ability to detect heavy elements	☺	☺	☺
Quantitative analysis	☹ (on progress)	☺	☺

For further applications, it is worth developing µLIBS technique for the application of rapid and convenient multi-elemental mapping. It can be used on elemental analysis of materials which have small and complex heterogeneous structure, such as minerals, polymetallic nodules and nuclear waste glass systems, etc. By following the distribution and fractionation behavior of elements, it is able to investigate structure formation of those complex materials.

Summary of this subsection:

Due to easy sample preparation and measurement procedure, possibility of precisely localized (micro) surface analysis, instantaneous response for multi-elemental identification, ability to detect low-content REEs, and extremely short mapping duration, µLIBS can be a suitable technique to perform multi-element mapping for nuclear wasteform and to follow the fractionation behavior of fission products in multi-phases material. Quantitative elemental analysis by using µLIBS is still on progress.

3.3 Discussion on fractionation behavior of fission products in the glass-ceramic wasteform

3.3.1 Fractionation behavior of fission products

According to the μLIBS, LA-ICP-MS, and EMPA measurements, Ca, Mo, Sr, Na, and REEs (Eu, Nd, Pr, and La) are able to be incorporated into the powellite crystalline phase, while Si, Al, Fe, Zr, Zn, and Cs remain in the glass. This fractionation behavior of elements between glass and crystal can be simply explained through their effective ionic radii which are related to the structural properties of $CaMoO_4$ crystal. The incorporated Sr and REEs in $CaMoO_4$ crystal substitute the Ca site [3, 10]. Table 3-7 lists the effective ionic radii and ion valences of the detected elements for eight-oxygen coordination.

In a $CaMoO_4$ structure, each Ca^{2+} has a coordination of 8 oxygen atoms, which forms a CaO_8 polyhedra. *Effective ionic radius* [11] of 8-coordinated Ca^{2+} is 112 pm. In the 8-coordination environment, Sr^{2+} (126 pm), Na^+ (118 pm), La^{3+} (116 pm), Eu^{3+} (107 pm), Nd^{3+} (111 pm), Pr^{3+} (113 pm) have very similar effective ionic radii as Ca^{2+}, which increases the possibility of substitution. As shown in Table 3-7, the ionic radii deviations of REEs from Ca are very small (less than 5 %), especially Nd and Pr (less than 1 %). Since REEs are considered as minor actinides surrogates, it is inferred that trivalent minor actinides can also be incorporated in $CaMoO_4$. Moreover, it has to be pointed out that the tetravalent and pentavalent actinides (e.g. Np^{4+}, Np^{5+}) are less likely to substitute Ca^{2+}.

Here, the monovalent Na plays an important role in the electroneutrality of the powellite crystalline phase, since it compensates the charge imbalance result from the substitution of divalent Ca by the trivalent rare earth ions. Ionic radius deviation of Sr from Ca is relatively high among those elements that fractionate to powellite crystalline phase. However, since Sr and Ca are congeners which both belong to alkaline earth metals, substitution of Ca by Sr is possible due to their similarities of chemical properties.

By comparison, effective ionic radii of 8-coordinated Zr^{4+} (84 pm), Fe^{3+} (78 pm), Zn^{2+} (90 pm), and Cs^+ (174 pm) are quite different from that of Ca^{2+}. Particularly, the ionic radius deviation of Cs from Ca reaches as much as 55.36 %, which suggests that Cs is too big to stay in an 8-coordinated Ca site. By comparison, Zr, Fe, and Zn are too small to maintain themselves stably with such a coordination number. Moreover, Si^{4+} and Al^{3+} do not support an 8-oxygen-coordination. Considering the structural stability, it is difficult for

Zr, Fe, Al, Zn, and Cs to show their affinity to the $CaMoO_4$ structure. Therefore, it is reasonable that these three elements remain in the glass during $CaMoO_4$ crystallization.

Table 3-7: Effective ionic radii and ion valences of multi-elements for eight-oxygen coordination [11]; the last column lists the ionic radii deviations of detected elements from Ca, with "+" standing for increase of ionic radius and "-" for decrease of ionic radius

Ion	valence	Ionic radius (pm)	Deviation (%)
Ca	+2	112	0
Sr	+2	126	+12.50
Na	+1	118	+5.36
La	+3	116	+3.57
Eu	+3	107	-4.46
Nd	+3	111	-0.89
Pr	+3	113	+0.89
Zr	+4	84	-25.00
Fe	+3	78	-30.36
Al	+3	--	--
Cs	+1	174	+55.36
Zn	+2	90	-19.64
Si	+4	--	--

3.3.2 Self-irradiation in the fission products bearing phase

It is illustrated by both uLIBS and EMPA mapping that Sr (one of the main β-decay source) and REEs (minor actinides surrogates, α-decay sources) are all prone to fractionate to the powellite crystalline phase. Therefore, powellite has to undergo self-irradiation for a very longer time. As mentioned in Chapter 1, minor actinides (U, Np, Pu, Am, and Cm) are the principal sources of α-decay in the nuclear wasteform in long-term storage (more than 100 000 years). Penetration depth of α-particles (with energy of 4 to 6 MeV) is about 20 µm while that of α-recoil nuclei (with energy of 0.1 MeV) is about 30 nm [12]. *The α-particles dissipate most of their energy by ionization processes over a range of 16 to 23 µm* (Figure 3-14), but undergo enough elastic collisions along their path to produce several hundred isolated atomic displacements [13]. The more massive but lower energy *α-recoil nuclei account for most of the total number of displacements produced by ballistic processes in the nuclear wasteform*. The α-recoil nuclei lose nearly all of their energy in elastic collisions over a very short range (*30 to 50 nm*, Figure 3-14) [13]. In this study, the powellite crystallites obtained in the Mo-rich borosilicate is about 25 μm in diameter and several hundred μm in length. Penetration depth of α-particles irradiation is on the same scale as the size of powellite crystallites. Ballistic process of α-particles and α-recoil nuclei on the crystalline phase can cause direct atomic displacements through elastic scattering collisions and induce atomic-scale rearrangement of the structure, which results in an overall macroscopic effect on the powellite crystallites. Therefore, the ability of the host crystalline phase to bear long-term α-decay from the accommodated minor actinides is very critical. Behavior of powellite crystal under irradiation will be discussed in Chapter 4, which shows that powellite is able to bear very high level damage without amorphization and can be used as a stable host structure to accommodate minor actinides for long-term storage.

β-decay from Cs and Sr is also principal radiation source in the nuclear wasteform for the first 500-year storage, which has a penetration depth of several millimeters covering almost all the wasteform [12]. Because of the low mass of β-particles, they do not transfer kinetic energy to atomic nuclei efficiently. The β-recoil nuclei are almost never energetic enough to be permanently displaced. However, β-decay of ^{137}Cs and ^{90}Sr in the nuclear wasteform is the *principal transmutation source*. Transmutation of radioactive parent nuclei into different chemical elements may significantly impact the chemical properties of the crystalline wasteform, accompanying with changes in both ionic radius and valence of the nuclei. Cs^+ (half-life 30.23 years) decays to Ba^{2+} with a decrease in ionic radius of 20 %, and Sr^{2+} (half-life 28.9 years) decays to Y^{3+}, which in turn decays to Zr^{4+} with a final ionic radius decrease of 29 % [14].

According to the mapping results, Cs remains in the glassy phase which has nearly no effect on the powellite crystalline phase. However, the main problem may come from the transmutation of Sr^{2+} to Zr^{4+}, which is prone to incorporate in the powellite crystal. From Table 3-7, for 8-oxygen coordination of CaO_8 in powellite structure, the effective ionic radius of Sr^{2+} is 12.5 % larger than that of Ca^{2+}, whereas, Zr^{4+} is 25 % smaller. For β-decay of ^{90}Sr, Sr^{2+} transmutes first to Y^{3+} (102 pm in ionic radius for 8-oxygen coordination [11]) and then to stable Zr^{4+}, which results in a ionic radius decrease of 21.4 % followed by 16.1 %. The total ionic radius change reaches as much as 37.5 % by the transmutation of Sr^{2+} to Zr^{4+}. The effect of transmutation on powellite structure is not discussed in this thesis.

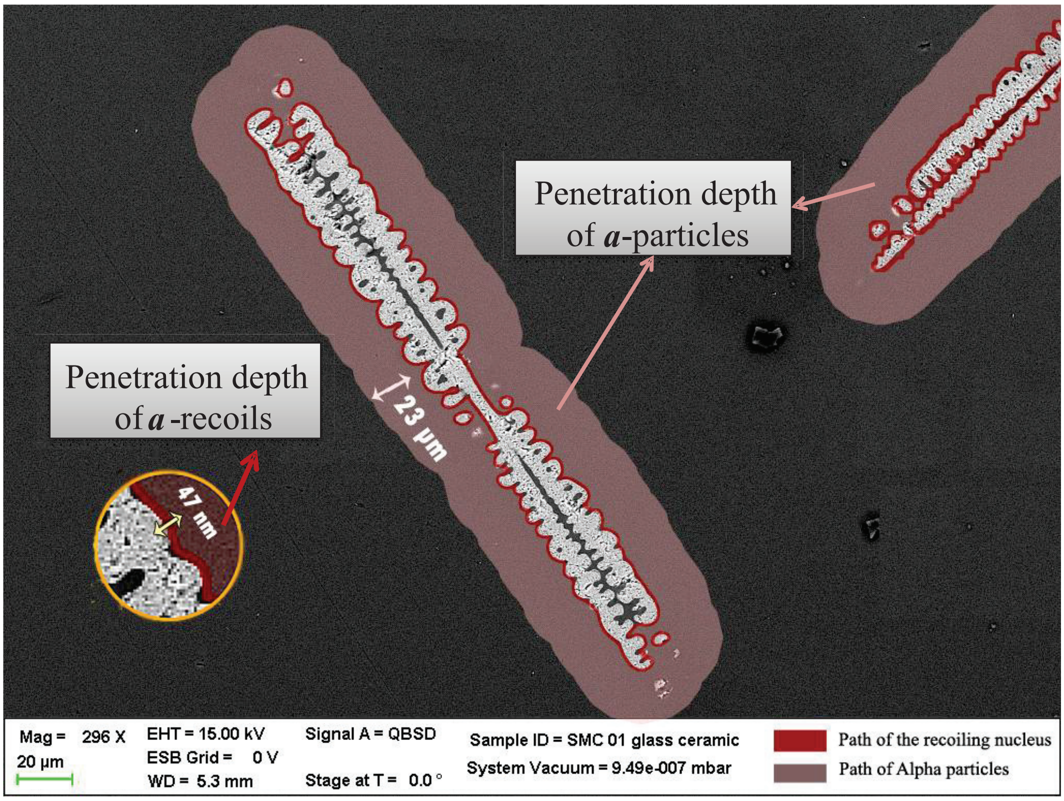

Figure 3-14: Irradiation range of α-decay from MA incorporated in powellite crystallites

3.3.3 Crystalline phase in the glass-ceramic wasteform

Here is a brief discussion of powellite crystallization in Mo-rich borosilicate glass-ceramic.

Generally, crystallization of conventional glasses occurs by the nucleation of crystals at external surfaces. However, the success of producing mechanically strong glass-ceramic material depends on inducing a high crystal nucleation density within the bulk of the glass by providing a very large number of internal heterogeneities from which the major crystalline phases can form and grow [15, 16].

In this study, powellite crystallites were generated inside the Mo-rich borosilicate glass by performing additional heat treatments. As MoO_3 and CaO are existing constituents of the Mo-rich borosilicate glass, $CaMoO_4$ is formed via high-temperature solid-state reaction of MoO_3 and CaO during thermal annealing the initial glass. Many small heterogeneities are therefore produced in the glass, onto which the powellite crystalline phases can nucleate and grow. By means of crystallization and crystal growth, MoO_3 is easily trapped as

$CaMoO_4$, which solves the Mo-storage problem arising from the UMo spent fuel. Meanwhile, the Mo-rich powellite crystalline phase can be used to enrich minor actinides and Sr, which provides a double-barrier to accommodate the irradiation sources.

3.4 Conclusion

According to the elemental analysis techniques (μLIBS, LA-ICP-MS, and EMPA), it is demonstrated that, by means of crystallization in borosilicate, Mo is easily trapped as $CaMoO_4$ which can also enrich REEs (surrogates of radioactive minor actinides) and Sr from the initial glass. About 55 % Mo and 10 % Ca of the initial glass are crystallized as powellite with an incorporation of 10 % Pr, 17 % La, and 26 % Sr. The similarity in effective ionic radii of Sr and REEs to Ca allows them to substitute the Ca site and be incorporated in powellite. On the contrary, Cs (another radioactive source) completely remains in the residual glass due to the mismatch of ionic radii.

The ability of powellite to incorporate Sr and REEs can be improved by increasing the crystallization in borosilicate. It is suggested that irradiation sources like Sr and minor actinides can be enriched using the Mo-rich powellite crystalline phase and be immobilized within a double-barrier environment. Accordingly, borosilicate glass-ceramic form provides a solution for both the Mo-storage problem arising from the UMo spent fuel and the reduction of matrix volume for accommodation of radioactive nuclear waste.

Moreover, due to the advantages of LIBS, such as easy sample preparation and measurement procedure, instantaneous response for multi-elements, ability to detect low-content REEs, and extremely short mapping duration, it can be employed in future for the detection and analysis of nuclear materials.

Reference

1. Sansonetti, J.E., W.C. Martin, and S. Young, *Handbook of basic atomic spectroscopic data*2005: National Institute of Standards and Technology Gaithersburg, MD.
2. Geertsen, C., et al., *Evaluation of laser ablation optical emission spectrometry for microanalysis in aluminium samples.* Spectrochimica Acta Part B-Atomic Spectroscopy, 1996. **51**(11): p. 1403-1416.
3. Cravetchi, I.V., et al., *Spectrochemical microanalysis of aluminum alloys by laser-induced breakdown spectroscopy: identification of precipitates.* Applied Optics, 2003. **42**(30): p. 6138-6147.
4. Gornushkin, I.B., et al., *Microchip laser-induced breakdown spectroscopy: A preliminary feasibility investigation.* Applied Spectroscopy, 2004. **58**(7): p. 762-769.
5. Salle, B., et al., *Laser ablation efficiency of metal samples with UV laser nanosecond pulses.* Applied Surface Science, 1999. **138**: p. 302-305.
6. Kossakovski, D. and J.L. Beauchamp, *Topographical and chemical microanalysis of surfaces with a scanning probe microscope and laser-induced breakdown spectroscopy.* Analytical Chemistry, 2000. **72**(19): p. 4731-4737.
7. Mendoza, C., *Caractérisation et comportement sous irradiation de phases powellites dopées terres rares: applications au comportement à long terme de matrices de confinement de déchets nucl é aires*, 2010, Université Claude Bernard-Lyon I.
8. Morgan, G.B. and D. London, *Effect of current density on the electron microprobe analysis of alkali aluminosilicate glasses.* American Mineralogist, 2005. **90**(7): p. 1131-1138.
9. Caurant, D., et al., *Effect of molybdenum on the structure and on the crystallization of SiO2–Na2O–CaO–B2O3 glasses.* Journal of the American Ceramic Society, 2007. **90**(3): p. 774-783.
10. Parchur, A.K., et al., *Luminescence properties of Eu3+ doped CaMoO4 nanoparticles.* Dalton Transactions, 2011. **40**(29): p. 7595-7601.
11. Shannon, R., *Revised effective ionic radii and systematic studies of interatomic distances in halides and chalcogenides.* Acta Crystallographica Section A: Crystal Physics, Diffraction, Theoretical and General Crystallography, 1976. **32**(5): p. 751-767.
12. GIN, S., et al., *Le comportement à long terme des verres*, 2012, Département d'études du traitement et du conditionnement des déchets, CEA, France: Le conditionnement des déchets nucléaires.
13. Weber, W.J., et al., *Radiation effects in crystalline ceramics for the immobilization of high-level nuclear waste and plutonium.* Journal of Materials Research, 1998. **13**(6): p. 1434-1484.

14. Gray, W.J., *Fission-Product Transmutation Effects on High-Level Radioactive-Waste Forms.* Nature, 1982. **296**(5857): p. 547-549.
15. Donald, I., B. Metcalfe, and R.N.J. Taylor, *The immobilization of high level radioactive wastes using ceramics and glasses.* Journal of Materials Science, 1997. **32**(22): p. 5851-5887.
16. McMillan, P.W., *Glass-ceramics*, 1979, Academic Press: London.

Chapter 4: Behavior of powellite crystal under Ar irradiations

Behaviors of powellite crystal under Ar irradiations in macroscopic, mesoscopic and microscopic scale are investigated in this chapter. It includes four sections. Section 4.1 talks about the macroscopic effect of powellite after irradiation by using optical interferometry; Raman spectroscopy is used in the Section 4.2 to investigate the medium-ranged order structure properties; irradiation-induced defects is investigated in Section 4.3 by using transmission electronic microscopy; Section 4.4 talks about the luminescent properties of rare earth elements (Eu^{3+}) as probes of local lattice environment in powellite structure.

4.1 Irradiation-induced macroscopic swelling of irradiated powellite by optical interferometry

It has been reported that radiation effects in actinide-doped simulated nuclear waste glass-ceramic can result in macroscopic volume changes of the crystalline phase [1, 2]. This macroscopic volume changes can be connected to lattice defects, solid-state phase transformations (e.g. crystalline to amorphous), or the evolution of extended defect within microstructure (such as gas bubbles, voids, dislocation and micracks). In this section, topography of sample surface containing both irradiated and non-irradiated areas was measured using optical interferometry, to investigate changes on the surface of bulk powellite single crystal after different Ar irradiations. Effect of oriented irradiation can be figured out by comparing the surface topography of *a*-slices and *c*-slices.

4.1.1 Swelling on powellite surface under oriented-irradiation

Aluminum masks were used to prevent part of the surface from the Ar irradiations, in order to investigate the difference between irradiated and non-irradiated areas. It was found that surface of powellite crystal swelled after exposure under Ar irradiations. As it is presented in Figure 4-1, an increasing surface swelling with Ar-ion dose on irradiated area was observed for both *a*- and *c*-slices by calculating the step height between irradiated and non-irradiated area (protected by aluminum mask). Left axis of Figure 4-1 indicates the absolute swelling of the irradiated surface. Bottom axis shows the irradiation dose in dpa while top axis shows the estimated Ar fluence. Based on the estimated damage depth ($3\ \mu m$)

determined by SRIM, the irradiation-induced volume changes in powellite single crystal were calculated and displayed on the right axis of the figure.

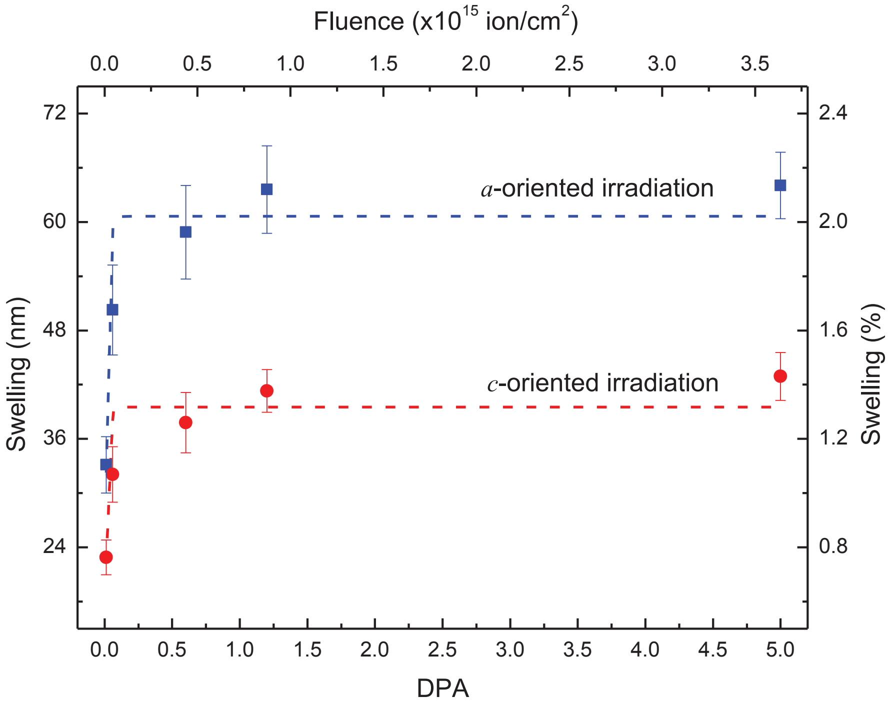

Figure 4-1: Swellings on the irradiated surface of *a*- and *c*-slices of $CaMoO_4$ respectively, measuring by optical interferometry; left axis indicates the absolute swelling value while right axis presents the corresponding estimated volume change

For *a*-oriented irradiations (on *a*-slices), surface swelling increases first strongly in very low dose range (from about 33 nm for 0.012 dpa to about 50 nm for 0.06 dpa), and then it keeps increasing with a much less slop from about 50 nm for 0.06 dpa up to about 64 nm for 1.2 dpa, after which it reaches saturation (swelling of *a*-slices with 5.0 dpa is about 64 nm.). By comparison, similar behavior of swelling can be found in powellite with *c*-oriented irradiation. The swelling rises from about 23 nm to 32 nm when the dpa varies from 0.012 to 0.6. Saturation value of swelling in this direction is about 42 nm.

As can be seen, after undergoing the same dose of Ar irradiation, the swelling of *a*-oriented powellite is always stronger than that of the *c*-oriented one. It suggests that *irradiation induced lattice expansion is more effective along a-axis than along c-axis of powellite crystal.* Since the structure of powellite is anisotropic, the reactions of powellite under oriented Ar implantation are different, depending on the structural properties (such as surface binding energy, chemical bond strength, etc.) and the ion stopping along the specific crystal axis.

Evolution behaviors of surface swelling on both *a*- and *c*-slices indicate that the powellite structure changes strongly in low dose range comparing with healthy sample. As irradiation dose increases, such structural change continues but with a weaker effect. According to Figure 4-1, swelling of powellite reaches saturation at around 1.2 dpa for both *a*- and *c*-oriented irradiation. The saturations of lattice swelling are 2.0 % along *a*-axis and 1.3 % along *c*-axis.

Summary of this subsection:

Swelling was observed on the powellite surface after exposure under Ar irradiations. The irradiation-induced swelling of powellite crystal increases with dpa (from 0.012 to 1.2) at first and reaches saturation after 1.2 dpa. The swelling is more effective along a-axis than along c-axis of powellite crystal. The saturation values of swelling are 2.0 % along a-axis and 1.3 % along c-axis (over a 3-μm thickness), respectively.

4.1.2 Irradiation induce volume change in powellite structure

The macroscopic volume change is a total effect contributed by an accumulation of lattice strain and defects in the irradiation-damaged layer. Generally, unit-cell expansion, amorphous regions and extended defects (such as dislocation loops or networks, voids, bubbles and microcracks, etc) all contribute to macroscopic swelling. The total macroscopic swelling, $\Delta V_m/V_0$, can be expressed as [2]:

$$\Delta V_m / V_0 = f_c \Delta V_{uc} / V_0 + f_a \Delta V_a / V_0 + F_{ex} \qquad \textbf{(4-1)}$$

where f_c is the mass fraction of crystalline phase; f_a is the mass fraction of amorphous phase; $\Delta V_{uc}/V_0$ is the unit-cell volume change of the crystalline phase; $\Delta V_a/V_0$ is the volume change associated with the amorphized state; and F_{ex} is the volume fraction of extended microstructures (e.g., bubbles, voids, microcracks, etc).

As it will be stated in *Subsection 4.2.2* and *4.3.2*, amorphization does not occur in the powellite structure. Hence, mass fraction of amorphous phase is zero (f_a = 0). If F_{ex} is assumed to be negligible, the macroscopic swelling is therefore dominated by the unit-cell expansion induced by the accumulation of point defects.

The unit-cell volume expansion ($\Delta V_{uc}/V_{uc}$) follows the characteristic exponential behavior predicted by Weber [3], for the accumulation of isolated structural defects. It is expressed as:

$$\Delta V_{uc} / V_{uc} = A_{uc}\left[1 - \exp\left(-B_{uc}D\right)\right] \tag{4-2}$$

where A_{uc} is the relative unit-cell volume expansion at saturation; B_{uc} is the rate constant for the simultaneous recombination of structural defects during irradiation; and D is the dose (in dpa). For non-cubic structures, the unit-cell expansion is obviously anisotropic. The unit-cell volume of powellite can be expressed as: $V_{uc} = a^2c$ (a and c are lattice parameters of powellite). Therefore, the change of unit-cell volume is deduced to be[13]:

$$\Delta V_{uc} / V_{uc} = 2\Delta a / a + \Delta c / c \tag{4-3}$$

Based on Equation (4-3), the unit-cell volume change can be estimated, as shown in Figure 4-2. Equation (4-2) is used to fit the unit-cell volume change in Figure 4-2. The fitting curves are shown in dash lines. As can been seen, the evolution of powellite volume change with irradiation dose follows basically an exponential behavior. The estimated average saturation value of unit-cell expansion is about 5.4 % at 5.0 dpa. This is quite a comparable result to the measurement performed by C. Mendoza [4] on powellite ceramic which has a swelling of 3 to 5 % after irradiated by 7-MeV silicon (3-µm damaged depth). The saturation swelling of powellite is quite small comparing with the other crystalline phases in literature [2]. For example, saturation swelling of monazite reaches as much as about 20 %, and that of zircon and quartz are 18.4 % and 17.5 %, respectively. It is reported that those crystalline phases which have large value of swelling can reach irradiation-induced amorphization [2]. Since powellite has a small saturation swelling value, it is expected that the structure of powellite could be more stable and less likely to become amorphous. Detail information of the irradiation-induced structure modification will be presented in Section 4.2 and 4.3. Based on the characterization by Raman and TEM, it is shown that no amorphizaiton was observed in irradiated powellite at 5.0 dpa.

---

[13] $V = a^2c \Rightarrow \Delta V = \Delta(a^2c) = 2\Delta a \cdot ac + \Delta c \cdot a^2 \Rightarrow \Delta V/V = 2\Delta a/a + \Delta c/c$

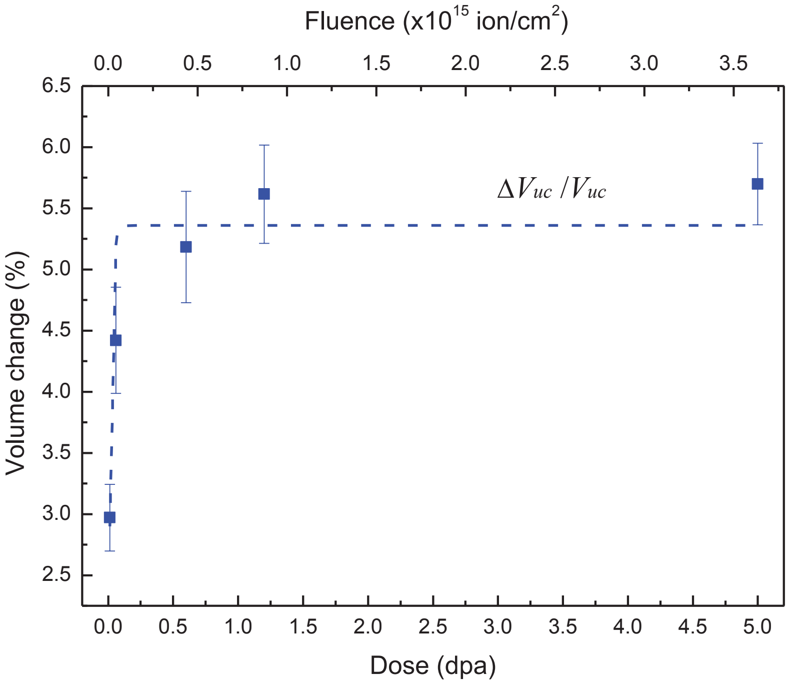

Figure 4-2: Estimation of unit-cell volume change in powellite single crystal after irradiation; dash lines are the fitting curves

Summary of this subsection:

The unit-cell volume change of powellite single crystal after irradiation was estimated based on the swelling along a- and c-axes, which shows a low saturation value of about 5.4 %.

4.1.3 Influence of powellite swelling in the glass-ceramic system

It has to be noticed that the powellite slices were free to swell under Ar irradiation in this investigation, whereas powellite crystallites in real nuclear waste glass-ceramic stay in a confined environment. Since the irradiation induced lattice strain is orientation dependent, it is important to consider the swelling or volume expansion situation of powellite crystallites in real nuclear waste glass-ceramic system caused by self-irradiation. For Mo-rich borosilicate glass-ceramic, powellite crystallites are formed by means of precipitation (refer to Chapter 2 and Chapter 3). Radionuclides which preferentially incorporate into powellite are therefore trapped inside crystallites. Structure deformation can occur on powellite crystallites after it undergoes long-term internal bombardments nuclei transmutation from radioactive elements, which can induce stress inside the glass-ceramic. Generally, the main concern with volume changes, particularly large differential changes, is that it may lead to high internal stresses that could cause micro-cracking, segregation, and increased dissolution rates [2]. In addition, the large volume changes significantly affect atomic bonding, local coordination, and the pathway for ion exchange, all of which can impact the release rates of radionuclides. It is consequently a potential risk for nuclear waste storage.

In Mo-rich borosilicate glass-ceramic, glass matrix (borosilicate) surrounding powellite crystallites are isotropic material. It is important to consider the effect of crystal swelling that can impact the glass matrix. Due to the different swelling along *a*- and *c*-axes of powellite, the generated stress inside the glass matrix varies according to orientations. Based on the Hooke's law, it is possible to estimate the stress in the borosilicate glass matrix induced by the swelling of powellite crystal. Relationship of the stresses (σ) and strains (ε) inside materials can be expressed as:

$$\sigma = -c\varepsilon \qquad \textbf{(4-4)}$$

Here, c is the elasticity tensor (or called stiffness tensor). Table 4-1 list the mechanical parameters of borosilicate glass (isotropic material), which are needed for the stress calculation. It is necessary to point out here that irradiation can induce stress inside the powellite crystal. However, the stress at (or near) the surface of the crystal is released by means of dislocation, as it will be stated in *Section 4.2* and *4.3*.

Table 4-1: Bulk, shear, and elastic moduli (in GPa) as well as fracture toughness (in MPa·m$^{1/2}$) of borosilicate glass [5]

Bulk modulus	Shear modulus	Young's modulus	fracture toughness
35-45	31-40	63-81	0.8

The generated stress in the glass matrix to confine swelling of powellite is estimated in Appendix A.6. Figure 4-3 shows the generated stress versus dpa (of powellite) inside the borosilicate glass matrix surrounding powellite crystallite resulting from crystal swelling. *Stresses along a- and c-orientations of powellite are different due to anisotropic swelling the crystal, which is always higher in a-axis than that in the c-one*. The maximum estimated stresses are 1.96 GPa in *a*-axis and 1.12 in *c*-axis.

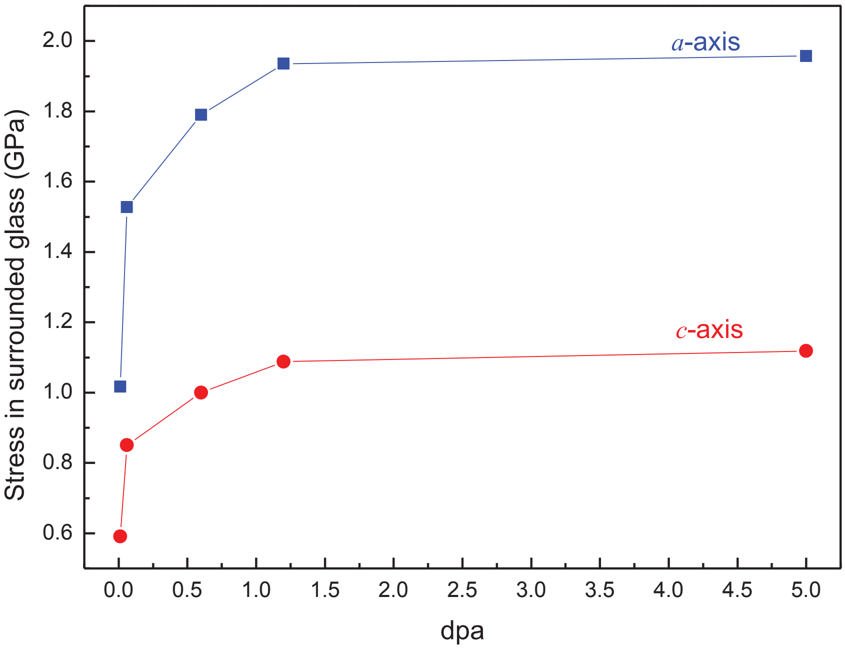

Figure 4-3: Generated stress (GPa) versus dpa (of powellite) in the surrounding glass matrix due to crystal swelling along *a*-axis (blue) and *c*-axis (red)

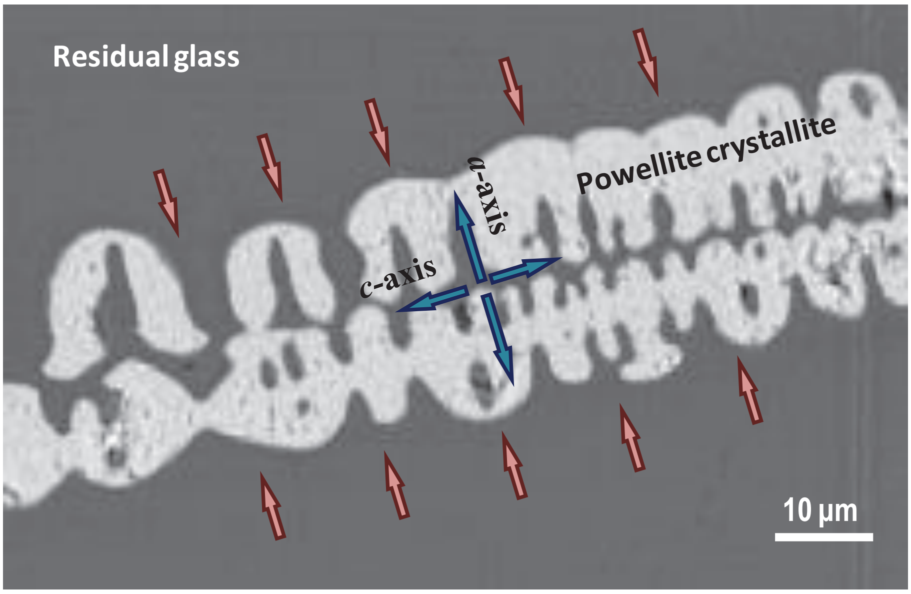

Figure 4-4: Schematic diagram of swelling-induced stress in the borosilicate glass matrix surrounding a powellite crystallite; blue arrows indicate the direction of crystal swelling, while red arrows denote the confinement of the glass matrix.

Figure 4-4 illustrates the relation between swelling-induced stress in the surrounded glass matrix and the powellite crystallite. In practical situations of α-decay in nuclear waste glass-ceramic, energies is about 4 to 6 MeV for the α particle and about 0.1 MeV for the recoil nuclei. It takes a long time (~ 10^5 years, refer to Chapter 2) to reach similar irradiation level as much as 5.0 dpa through internal bombardments. According to Figure 4-3, the most important information is that stresses generated inside the glass matrix are estimated to be less than 2 GPa, which are in the range of elastic region of borosilicate glass [6]. It is suggested that this moderate stress can be possibly tolerated by borosilicate glass.

Summary of this subsection:

The stress in the glass matrix of Mo-rich borosilicate induced by the swelling of powellite crystal was estimated based on the Hooke's law for continuous media. It is shown that stresses in the surrounded glass matrix of powellite crystal are higher in a-axis than in the c-one. Powellite swelling only induces moderate stress in the surrounded glass matrix which is in the range of elastic region of borosilicate and can possibly be tolerated.

4.1.4 Anisotropic surface topography of powellite crystal after Ar irradiations

In this subsection, the powellite slices with 1.2 dpa are used as examples to show the surface topography after oriented irradiation. Figure 4-5 shows surface topography of powellite crystal slice after *a*-oriented (a) and *c*-oriented (b) irradiations (with 1.2 dpa), as well as the corresponding surface profiles ((c) and (d), respectively). It is found that ion-beam-induced delamination occurred on powellite during *a*-oriented irradiation, superimposing to swelling phenomenon. Material was ejected from the powellite sample after Ar bombardment, which results in a series of imprints extending along *a*-axis on the surface, as shown in Figure 4-5 (a). Figure 4-5 (b) shows the surface profile of powellite after *a*-oriented irradiation. In the irradiated area, delamination occurs at a depth of around 1.4 μm. Comparing with the delamination depth (in micrometers), surface swelling (in nanometers) of *a*-oriented irradiated powellite is very small. As shown in the inset of Figure 4-5 (c), the step height between irradiated and non-irradiated area is about 64.5 nm for 1.2 dpa sample. However, delamination never occurs on the *c*-oriented irradiated powellite (Figure 4-5 (b)). Flat elevated steps were always obtained on the surface of *c*-oriented irradiated powellite. At 1.2 dpa, the swelling for *c*-oriented irradiated powellite is about 40.5 nm (Figure 4-5 (d)).

Considering this special phenomenon on the *a*-oriented irradiated powellite, the concave imprints extending along *a*-axis suggests that fracture (or delamination) is most likely to take place on (001) crystal plane of powellite. This can be ascribed to the fact that cleavage can occur on (001) plane of powellite [7]. Accordingly, when the stress in the structure exceeds its mechanical resistance, cracks is preferentially formed on (001) plane, resulting in the delamination on *a*-oriented irradiated powellite. The delamination effect associated with stress in powellite is further discussed in Subsection 4.2.4.2.

In addition, it has to be noticed that the preferred ejection on the *a*-oriented powellite is an additional effect introduced by external irradiation, which is unlikely to occur on nuclear glass-ceramics through internal self-irradiation.

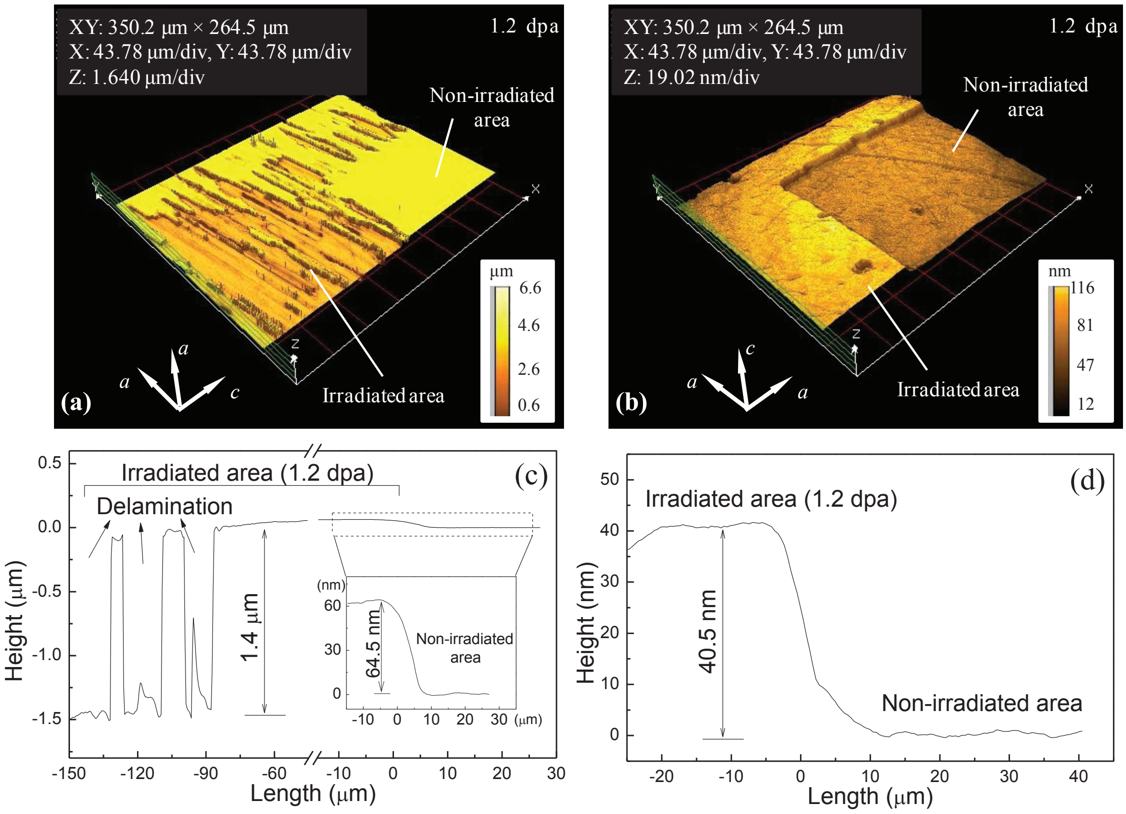

Figure 4-5: Surface topography of powellite crystal slice after *a*-oriented (a) and *c*-oriented (b) irradiations (with 1.2 dpa), as well as their corresponding surface profile ((c) and (d), respectively); the inset in (c) is a zoom of the region enclosed by dash rectangle which indicates the swellings on *a*-oriented irradiated powellite; the ion-beam-induced delamination occurs at about 1.4 µm deep inside the *a*-oriented irradiated powellite

Summary of this subsection:

Ion-beam-induced delamination was found on the a-oriented irradiated powellite, which is an additional effect for powellite under external irradiation and unlikely to happen under internal self-irradiation. This phenomenon can be ascribed to the cleavage on the (001) plane due to the excess of stress for the corresponding mechanical resistance of powellite structure.

4.2 Irradiation-induced modification on powellite structure in medium-range order by Raman spectroscopy

For the nuclear waste ceramic or glass-ceramic form, both self-irradiation damage from α-decay events and ion-irradiation damage are possible to result in a crystalline-to-amorphous transformation in most of the actinide-bearing crystalline phase, such as zircon and apatite [2]. It is reported that the fluorite-related structures (ZrO_2, PuO_2 and UO_2) appear to be not susceptible to radiation-induced amorphization.

In order to understand whether powellite can become a useful host for radioactive actinides, it is important to study the structure modification of powellite due to irradiation-induced damage. In this section, high resolved confocal Raman scanning was performed on thin FIB section (See Chapter 2) from powellite single crystals with oriented irradiations, to follow the evolution behavior of powellite medium-range order structure.

4.2.1 Raman spectra of powellite before oriented irradiations

Figure 4-6 shows Raman spectra of pristine (non-irradiated) powellite under measurements of *c*(*ar*)*c* and *a*(*cr*)*a* with 633-nm excitation. Here, "*r*" stands for random collection (refer to Porto notation in Chapter 2). Relations of orientations among the bulk crystal slice, FIB section and the incident laser are listed in Table 4-2. The *a*- and *c*-oriented powellite slices for Ar irradiation are noted as "*a*-slice" and "*c*-slice". Their corresponding FIB sections are called respectively "*a*-lamellae" and "*c*-lamellae". As can be seen from Figure 4-6, $\nu_1(A_g)$ internal symmetric stretching mode (at 879 cm^{-1}) is always active in both of the cases while $\nu_3(E_g)$ internal antisymmetric stretching mode (at 794 cm^{-1}) is only active in *a*(*cr*)*a* measurements, namely, the measurements on sections from *c*-oriented powellite. All the observed vibration modes in the range of 50 cm^{-1} to 1000 cm^{-1} are labeled [8-10] in the figure. $\nu_1(A_g)$ and $\nu_3(E_g)$ are selected as representative to follow the structural evolution behavior in medium-range-order under Ar irradiation.

Table 4-2: Orientation of the powellite samples in Ar implantations and Raman measurements (refer to Figure 2-27)

Bulk sample	Ar implantation	FIB sample	Laser incidence	Porto notation	$\nu_1(A_g)$	$\nu_3(E_g)$
a-slice	//*a*	*a*-lamella	//*c*	*c*(*ar*)*c*	active	--
c-slice	//*c*	*c*-lamella	//*a*	*a*(*cr*)*a*	active	active

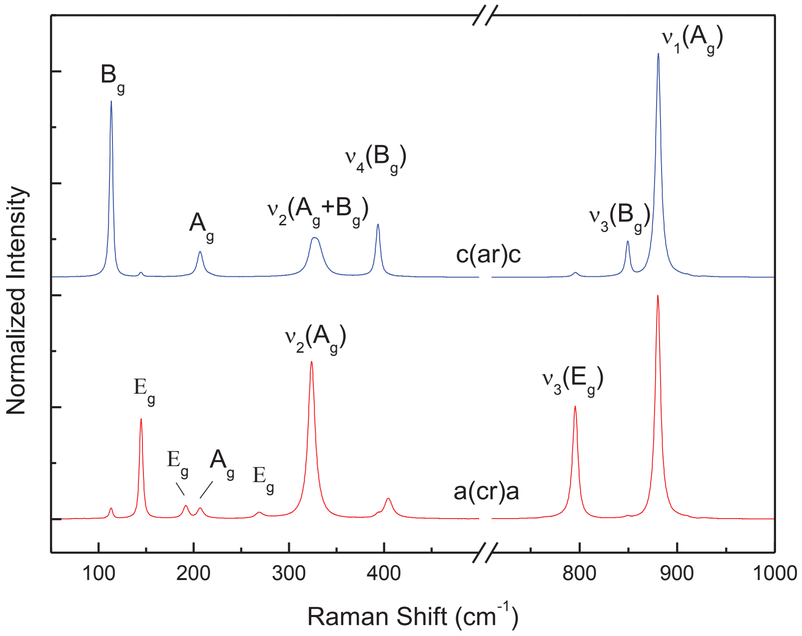

Figure 4-6: Raman spectra of non-irradiated healthy powellite under measurements of c(ar)c and a(cr)a (Porto notation) with an excitation of 633 nm

4.2.2 Evolution of Raman spectra in depth direction of powellite after oriented irradiations

A decrease in peak area (intensity) and a broadening in linewidth of powellite $\nu_1(A_g)$ *and* $\nu_3(E_g)$ *modes in the irradiation-damaged layer was observed, accompanying with shift in center frequencies (peak positions).* The shifts to higher and lower directions in frequency of Raman $\nu_1(A_g)$ and $\nu_3(E_g)$ mode were both found in the irradiation-damaged layer of each FIB section. Here, Figure 4-7 presents Raman spectra (Exc. 633 nm) of irradiated powellite (with 0.012, 0.12, 1.2 and 5.0 dpa) from different depth of the FIB sections, including one spectrum from the irradiated surface with the most peak shift in the lower-frequency direction, one from the interior of irradiation-damaged layer with the most peak shift in the higher-frequency direction and one from non-damaged layer. Each spectrum was normalized by its $\nu_1(A_g)$ peak. The depth at which the spectrum has most peak shift in the higher-frequency direction is noted in Figure 4-7. By comparison with spectra from non-damaged powellite, the shift of $\nu_1(A_g)$ peak position from the interior of irradiation-damaged layer of *c*-oriented irradiated powellites (*c*-lamellae) is higher than that of the *a*-oriented one. Linewidths of $\nu_1(A_g)$ and $\nu_3(E_g)$ modes broadened gradually from non-damaged layer to the irradiated surface. It is important to notice that *spectrum observed in the irradiated surface has the most broadened linewidth*.

Moreover, according to the Raman spectra in Figure 4-7, no matter which direction Ar irradiation comes from (*a*- or *c*-orientations), *no amorphization was observed in powellite single crystal up to 5.0 dpa.*

Summary of this subsection:

A decrease in peak area (intensity) and a broadening in linewidth of powellite $v_1(A_g)$ and $v_3(E_g)$ Raman modes in the irradiation-damaged layer was observed, accompanying with shift in center frequencies (peak positions). No amorphization was found in powellite single crystal up to 5.0 dpa.

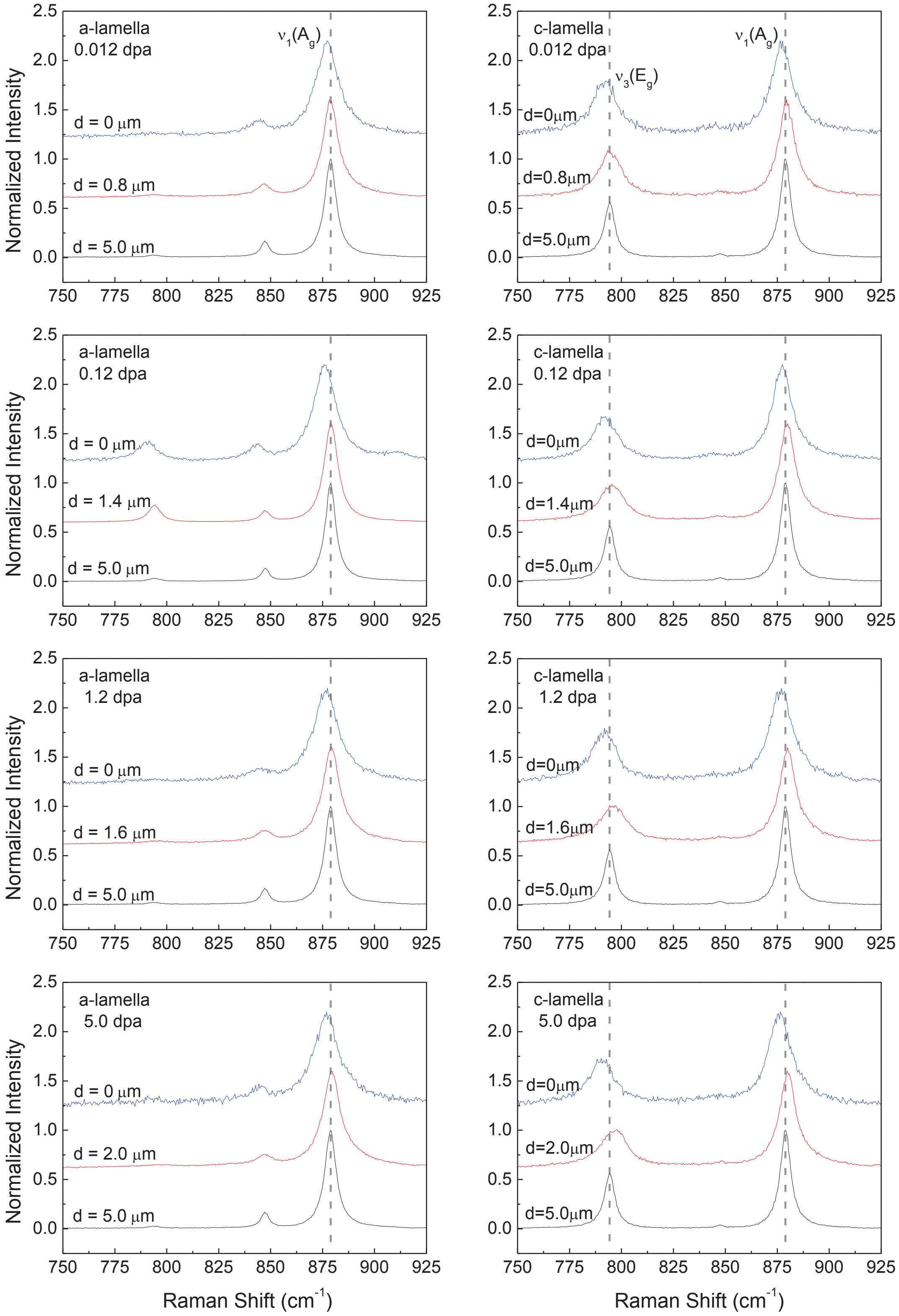

Figure 4-7: Raman spectra (Exc. 633 nm) of irradiated powellite (0.012, 0.12, 1.2 and 5.0 dpa) at different depth from FIB sections; each spectrum is normalized by the $\nu_1(A_g)$ peak

4.2.3 Mapping of Raman $\nu_1(A_g)$ and $\nu_3(E_g)$ modes of powellite in depth direction after oriented irradiations

As described in Subsection 2.2.3, Chapter 2, lateral resolution of 633-nm laser equipped with a ×100 objective (NA = 0.95) is 0.8 μm. Confocal Raman lateral scanning with a 633-nm laser was carried out on the FIB thin sections (0.012, 0.12, 1.2, 5.0 dpa) from both *a*- and *c*-oriented powellite crystal slices, to follow the evolution of medium-range-order structure of powellite after oriented irradiations. The Raman scanning area starts from irradiation-damaged layer up to non-damaged layer (as shown in Figure 2-32, Subsection 2.2.5). All spectra were background subtracted and very well fitted using Lorentzian profile which indicates a homogeneous broadening mechanism. Peak area, linewidth (full-width at half-maximum, FWHM) and peak position (frequency) of Raman spectra can provide different information about the structure. Hence, *parameters of Raman* $\nu_1(A_g)$ *and* $\nu_3(E_g)$ *modes including peak area (Subsection 4.2.3.1 and 4.2.3.2), peak position (Subsection 4.2.3.3), and linewidth (Subsection 4.2.3.4) were extracted from the spectra to construct maps of each FIB section, in order to visualized the structure evolution inside the irradiation-damaged layer*. To make a distinction among the mappings, different colormaps were used. *Profiles of the Raman mapping is present in Subsection 4.2.4 for detail discussion*. Some supplementary Raman analyses are shown in Appendix A.7 - A.10.

4.2.3.1 Area mapping and structure damage

Figure 4-8 is peak area mapping of $\nu_1(A_g)$ vibration mode on the FIB sections. Maps in the first raw correspond to *a*-oriented irradiated powellite with 0.012, 0.12, 1.2 and 5.0 dpa, respectively; while maps in the second raw correspond to *c*-oriented irradiated ones. Scales on the left side of the figure indicate the distance in depth direction from the original irradiated surface (which is 0 μm) to the non-damaged region (up to 5 μm). According to SRIM simulation, estimated thickness of irradiation-damaged layer is about 3 μm. It can be considered that structure with a depth not smaller than 4.5 μm is in the range of non-damaged region, from which spectra can be used as reference for each lamella. Consequently, *each map in Figure 4-8 was respectively normalized by the mean peak area value from the corresponding non-damaged region on each FIB section.* Colorbar on the right side of the figure indicates the normalized peak area value. Light color in Figure 4-8 represents high value of peak area, while dark color means the contrary. In such case, it is therefore easy to have a general idea about how the peak area evaluates with depth in powellite crystal after different dose of irradiations.

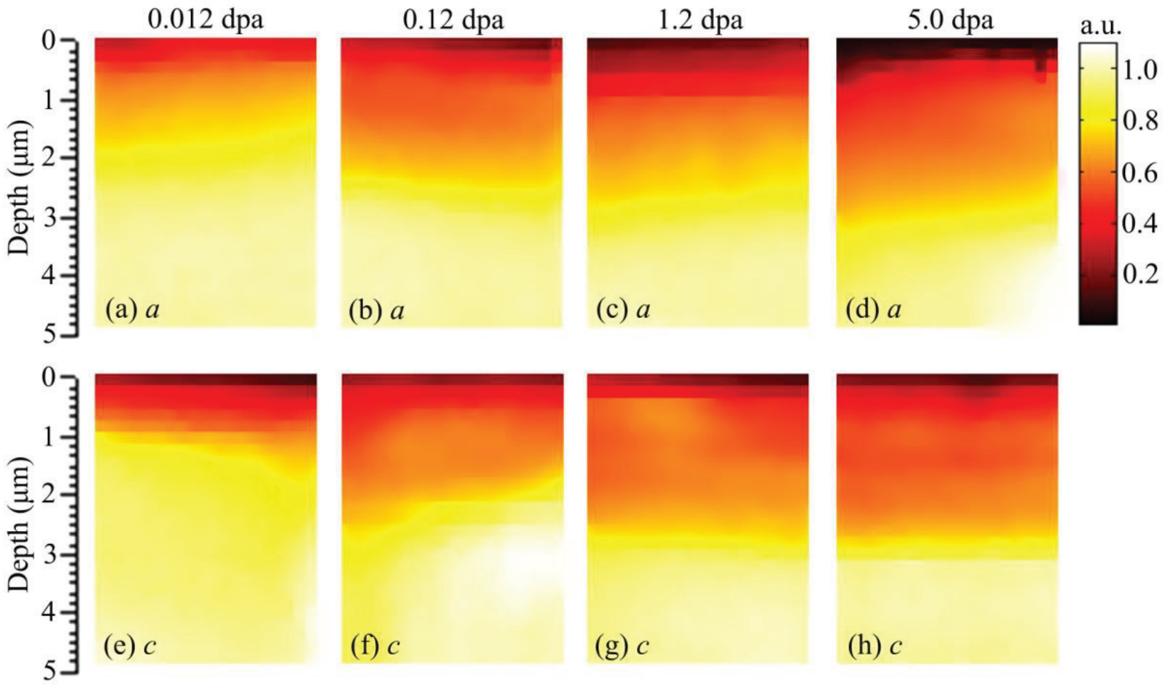

Figure 4-8: Normalized Raman peak area maps of $\nu_1(A_g)$ mode (Exc. 633 nm) in depth direction from the irradiated surface on FIB *a*-lamellae ((a)-(d)) and *c*-lamellae ((e)-(h)) with 0.012, 0.12, 1.2 and 5.0 dpa; scale on the left indicates the depth from the original irradiated surface (labeled 0 μm); color bar on the right indicates the normalized peak area value (1 a.u. for pristine powellite on the FIB section)

As can be seen in Figure 4-8, a gradual decrease in $\nu_1(A_g)$ peak area was observed from non-damaged region to the surface (depth = 0 μm) for each FIB section. A layer on each FIB section which has lower peak area than the corresponding non-damaged region can be recognized easily. Peak areas from the near-surface region are less than 15% comparing with that from non-damaged region. The lowest peak area was always found on the surface of each sample. From the maps in Figure 4-8, the evolution behaviors of $\nu_1(A_g)$ peak area according to dose (dpa) are quite similar for both *a*- and *c*-oriented irradiated powellite. *The thickness of irradiation-damaged layer increases as the Ar irradiation dose rises from 0.012 to 1.2 dpa, which indicates an expansion of the affected layer in bulk powellite crystal*. The thickness of the irradiation-damaged layer becomes constant (saturated) after 1.2 dpa.

Similar evolutions behavior with depth and irradiation dose were found in $\nu_3(E_g)$ (internal antisymmetric stretching) area maps on *c*-lamellae of powellite, as shown in Figure 4-9. First, it illustrates again that the peak area of the internal stretching mode decreases in the irradiation-damaged layer, with the lowest peak area appearing on the original irradiated surface of powellite. Second, it confirms that thickness of the irradiation-damaged layer increases with dose from 0.012 dpa to 1.2 dpa and then reaches saturation after 1.2 dpa.

Due to the structure damage and modification by irradiation, defects were created inside the lattice, resulting in the decrease of Raman vibration intensity. *The decrease in peak area provides an intuitive view of an increase in structure damage within the irradiation-affected layer.* The weakest peak area observed at the surface of each FIB section suggests that the most damaged region appears to be the surface. However, for the Raman measurements at the surface, it is important to point out that a decrease in peak area (or intensity) can be always observed at the surface even for pristine sample due to the spatial resolution of Raman. Therefore, to verify the structure damage and modification of powellite by irradiation, it is necessary to investigate the other parameters in Raman spectra which are independent on intensity, such as peak position and linewidth (Subsection 4.2.3.3 and 4.2.3.4).

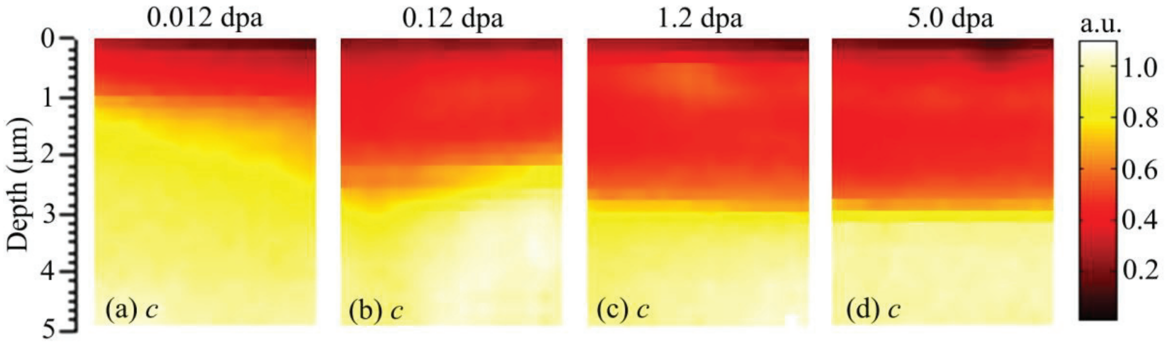

Figure 4-9: Normalized Raman peak area maps of $\nu_3(E_g)$ mode (Exc. 633 nm) in depth direction from the irradiated surface on FIB *c*-lamellae ((a)-(d)) with 0.012, 0.12, 1.2 and 5.0 dpa; scale on the left indicates the depth from the original irradiated surface (labeled 0 μm); color bar on the right indicates the normalized peak area value

4.2.3.2 Area ratio mapping

As mentioned previously, active Raman vibration modes of crystal are generally orientation dependent. For instance, $\nu_3(E_g)$ of powellite can be observed using a(cr)a measurement (laser incidence parallel to *a*-axis) but not c(ar)c one (laser incidence parallel to *c*-axis), as shown in Figure 4-6. Since $\nu_3(E_g)$ vibration mode is very sensitive to the orientation of powellite structure, the peak area ratio of $\nu_1(A_g)$ and $\nu_3(E_g)$ can therefore be used to probe the lattice modification of the powellite crystal structure after irradiation. According to variation of ratio of $\nu_1(A_g)$ and $\nu_3(E_g)$ peak areas, it is possible to extract information about how the structure evolutes with irradiation fluence. Figure 4-10 is ratio mapping of $\nu_1(A_g)$ and $\nu_3(E_g)$ peak areas from FIB section of powellite with different *c*-oriented irradiations (0.012, 0.12, 1.2 and 5.0 dpa). Colorbar shown on the right side of the figure indicates the values of the peak area ratio, with blue color for low ratio and red color for the high one.

Although peak areas of both $\nu_1(A_g)$ and $\nu_3(E_g)$ modes decrease in the irradiation-damaged layer of powellite, it can still be determined that the evolution of $\nu_1(A_g)$ and $\nu_3(E_g)$ are not exactly the same in this layer. For each FIB section from *c*-oriented irradiated powellites, the ratio of $\nu_1(A_g)$ and $\nu_3(E_g)$ peak areas changes in depth direction from non-damaged layer to the original surface, which suggests a modification of powellite structure in the damaged layer after irradiation, as shown in Figure 4-10. It can be noticed clearly that a region beneath the surface with higher value of $\nu_1(A_g)/\nu_3(E_g)$ area ratio exists in the irradiation-damaged layer, which appears at an increasing depth with increasing dpa values. Detailed discussion of the structure modification of powellite will be discussed in the next section.

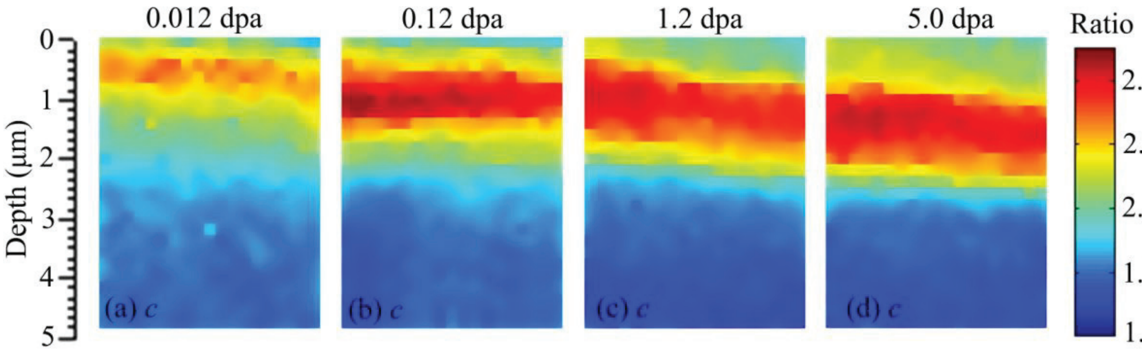

Figure 4-10: Peak area ratio maps of $\nu_1(A_g)/\nu_3(E_g)$ modes (Exc. 633 nm) in depth direction from the irradiated surface on FIB *c*-lamellae ((a)-(d)) with 0.012, 0.12, 1.2 and 5.0 dpa; scale on the left indicates the depth from the original irradiated surface (labeled 0 μm); color bar on the right indicates the ratio value

4.2.3.3 Peak position mapping and stress

To illustrate an overview of how Raman peak position and linewidth vary in depth direction for different damaged powellite, peak position and linewidth maps were constructed in the same way as that for peak area maps.

Figure 4-11 shows peak center position (frequency) mapping of $\nu_1(A_g)$ vibration mode on the FIB sections of both *a*- and *c*-lamellae with of 0.012, 0.12, 1.2 and 5.0 dpa, which were extracted from the same spectral data used in Figure 4-8. According to the colorbar in Figure 4-11, light color stands for high frequency while dark color stands for low frequency. The evolution of powellite $\nu_1(A_g)$ peak position with depth has already been described according to Raman spectra in Subsection 4.2.2. By frequency mapping, it is much easier to follow how the peak position of powellite $\nu_1(A_g)$ mode varies with depth in the irradiation-damaged layer of each FIB section. From Figure 4-11, layers which have frequency shift in $\nu_1(A_g)$ peak position can be well recognized, with shifts towards both higher and lower frequency directions.

As it is known, frequency of Raman peak depends on parameters of the lattice and properties of the corresponding molecule. By comparison with Raman spectra from non-damaged layer, *a shift of peak position towards the higher frequency can reveal a reduction in lattice parameters which is related to compressive stress; on the contrary, a shift towards lower frequency can reveal an increase of lattice parameters that indicates equivalent tensile stress.* [11, 12]. Therefore, according to the variation of Raman peak positions, it is able to figure out the irradiation-induced lattice modifications and stresses in the powellite structure.

For non-damaged layer, $\nu_1(A_g)$ mode of powellite is observed at 878.9 cm^{-1}. From non-damaged layer up to the original irradiated surface, center frequency of $\nu_1(A_g)$ increases continuously to a maximum value before it decreases in the near-surface region. It is suggested that *a region with compressive stress exist within the irradiation-damaged layer.* The lowest frequency of $\nu_1(A_g)$ always appears on the irradiation surface of powellite. According to variation of $\nu_1(A_g)$ in the FIB sections, it can be noticed that, under the same irradiation condition, maximums of $\nu_1(A_g)$ mode center frequency are higher in *c*-oriented irradiated powellite then that in *a*- oriented irradiated one. It is suggested that *irradiation-induced lattice volume (or lattice parameters) change on powellite structure is dependent on orientation.*

The depth at which the maximal center frequency was found on the FIB section increases with dpa. It reveals again an expansion behavior of affected layer in depth direction with irradiation dose, which is coincident with the result from peak area mapping in Subsection 4.2.3.1.

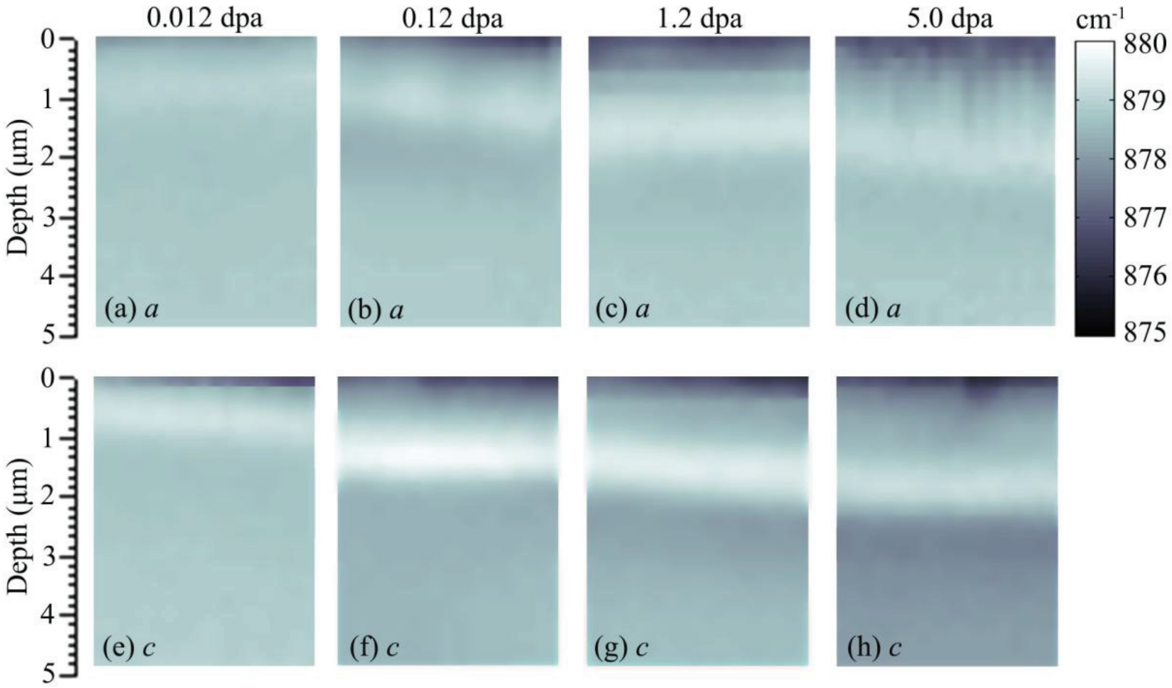

Figure 4-11: Raman peak position maps of $\nu_1(A_g)$ mode (Exc. 633 nm) in depth direction from the irradiated surface on FIB *a*-lamellae ((a)-(d)) and *c*-lamellae ((e)-(h)) with 0.012, 0.12, 1.2 and 5.0 dpa; scale on the left indicates the depth from the original irradiated surface (labeled 0 μm); color bar on the right indicates the value of peak center frequency

Very similar evolutions of peak position with depth and irradiation dose can be found in $\nu_3(E_g)$ mapping on FIB sections from *c*-oriented irradiated powellite, as presented in Figure 4-12. Peak position of $\nu_3(E_g)$ found in the non-damaged layer is 794.0 cm^{-1}. From non-damaged region to the original irradiated surface, $\nu_3(E_g)$ peak position shift first towards the higher frequency direction then to the lower one, which provides similar information about the structure variation inside the irradiation-damaged layer of powellite to what is observed from the $\nu_1(A_g)$ mapping. In addition, it can be noticed that the layer which has high frequency in $\nu_3(E_g)$ mode becomes deeper and deeper as dpa increases, as the behavior of $\nu_1(A_g)$.

Detail discussion of the peak position evolution and irradiation-induced stress are presented in Subsection 4.2.4.1 to 0.

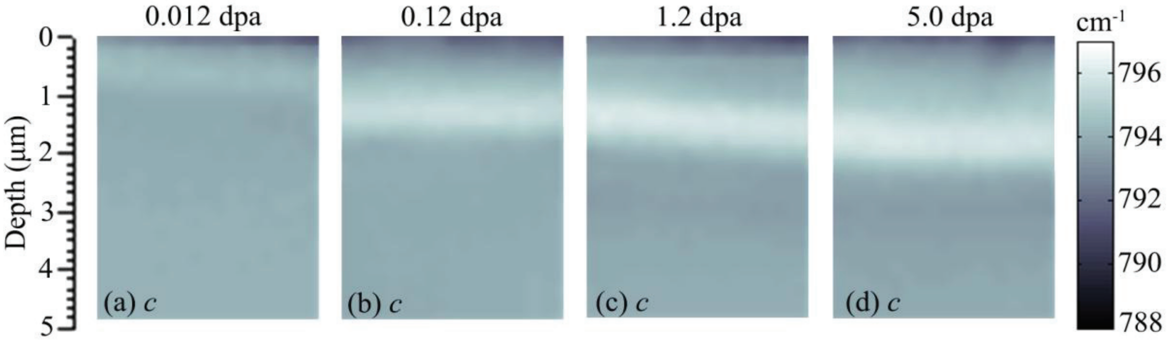

Figure 4-12: Raman peak position maps of $\nu_3(E_g)$ mode (Exc. 633 nm) in depth direction from the irradiated surface on FIB *c*-lamellae ((a)-(d)) with 0.012, 0.12, 1.2 and 5.0 dpa; scale on the left indicates the depth from the original irradiated surface (labeled 0 μm); color bar on the right indicates the value of peak center frequency

4.2.3.4 Linewidth mapping and structural disorder

Figure 4-13 presents the corresponding linewidth (FWHM) mapping of $\nu_1(A_g)$ vibration mode on the FIB sections of both *a*- and *c*-lamellae with of 0.012, 0.12, 1.2 and 5.0 dpa. For maps in Figure 4-13, an increasing linewidth is indicated by changing the map color from blue to red.

As another important parameter, the linewidth of Raman peak can provide information of the disorder of powellite structure after irradiations. Generally, each peak in Raman spectrum represents a specific collective vibration mode of elastic, periodically arranged atoms or molecules in condensed matter. In a perfect crystal which has long-range order structure, the intrinsic linewidth of one certain vibration mode is only determined by its interaction with other elementary excitations in the structure [13]. Irradiation-induced damage can result in lack of correlations on both long-range translation and orientations, which are properly referred as topologically disordered [2]. As crystal is modified or damaged, the long-range order of lattice structure are destroyed and replaced by varies of short-range orders in the structure. Vibrations of the lattice are therefore more or less changed, accompanying with linewidth broadening. When crystal structure damage increases, the short-range order decreases which results in a continuous linewidth broadening. Therefore, *by determining the linewidth of Raman vibration modes, it is possible to retrieve information about disorder and damage of the lattice structure.*

According to Figure 4-13, a layer on top of each FIB section with broadened linewidth (colored by light blue to red) of $\nu_1(A_g)$ mode can be distinguished from the non-damaged layer on the bottom which has narrower linewidth value (deep blue). As can be seen, for each FIB section, linewidth of $\nu_1(A_g)$ mode broadens gradually from non-damaged layer to the original irradiated surface, indicating *an increase in structural disorder*. Linewidth values from non-damaged layers are about 6.7 cm^{-1}, while those from the near-surfaces regions of powellite are larger than 12 cm^{-1}. The maximum linewidth value appears on the irradiated surface of powellite for all irradiated samples, which suggests that *the most disordered structure is at the surface.* Moreover, as irradiation dose increases from 0.012 to 5.0 dpa, the thickness of the affected layer with broadened linewidth increases in the depth direction of powellite bulk crystal.

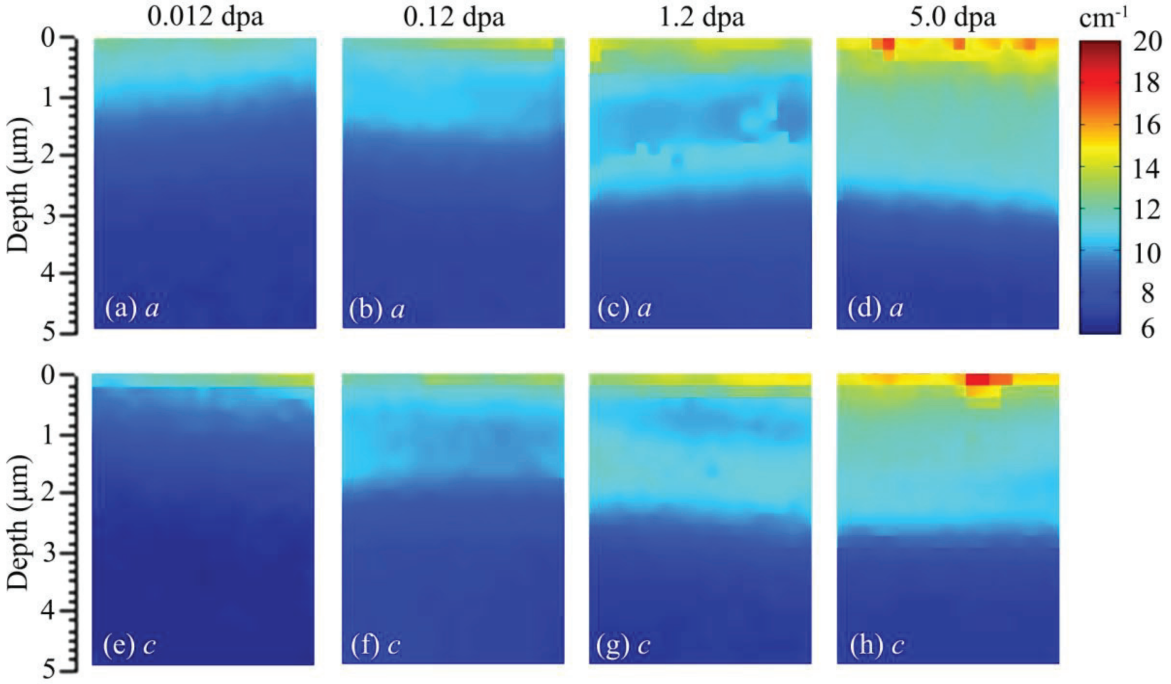

Figure 4-13: Raman linewidth maps of $\nu_1(A_g)$ mode (Exc. 633 nm) in depth direction from the irradiated surface on FIB *a*-lamellae ((a)-(d)) and *c*-lamellae ((e)-(h)) with 0.012, 0.12, 1.2 and 5.0 dpa; scale on the left indicates the depth from the original irradiated surface (labeled 0 μm); color bar on the right indicates the linewidth value

Mapping of $\nu_3(E_g)$ linewidth on FIB section of *c*-oriented irradiated powellite was shown in Figure 4-14. Linewidth of $\nu_3(E_g)$ from non-damaged layer is similar to that of $\nu_1(A_g)$, which has a value of about 6.3 cm^{-1}. Evolution behavior of the damaged layer with irradiation dose is coincident with the previous result from $\nu_1(A_g)$ linewidth mapping. However, comparing with that of $\nu_1(A_g)$,the broadening of the $\nu_3(E_g)$ linewidth with Ar irradiation dose is much more effective, which suggests that $\nu_3(E_g)$ mode is more sensitive to structural modification.

Detail discussion of the linewidth evolution and irradiation-induced disorder are presented in Subsection 4.2.4.4.

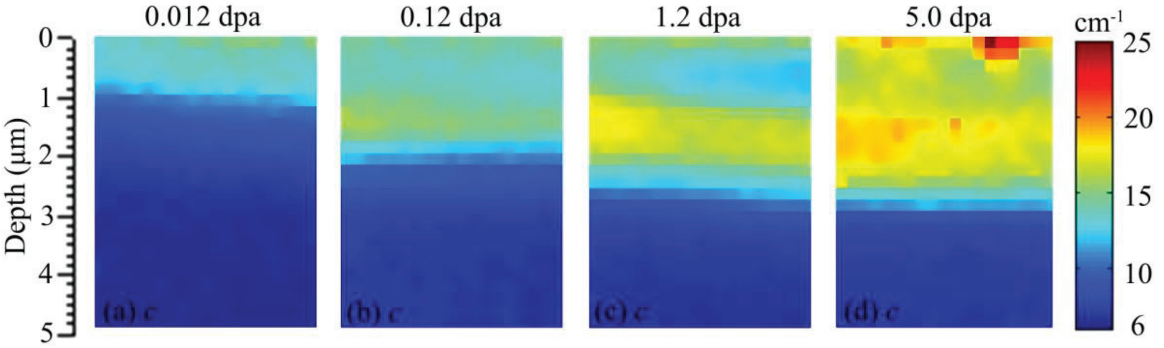

Figure 4-14: Raman linewidth maps of ν$_3$(E$_g$) mode (Exc. 633 nm) in depth direction from the irradiated surface on FIB *c*-lamellae ((a)-(d)) with 0.012, 0.12, 1.2 and 5.0 dpa; scale on the left indicates the depth from the original irradiated surface (labeled 0 µm); color bar on the right indicates the linewidth value

Summary of this subsection:

Peak area, peak position and linewidth of ν$_1$(A$_g$) and ν$_3$(E$_g$) Raman modes were extracted from the spectra to construct maps of each FIB section from different irradiated powellite samples, to visualized the structure evolution inside the irradiation-damaged layer. The decrease in Raman peak area indicates the damage of the powellite structure. Position shift of Raman peak towards higher frequency reveals compressive stress. Raman linewidth broadening indicates the structural disorder. Peak area mapping implies very similar results to the linewidth mapping.

A layer which is damaged by irradiation can be found beneath the surface of both a- and c-oriented irradiated powellite. The thickness of irradiation-damaged layer increases as the Ar irradiation dose rises from 0.012 to 1.2 dpa, which indicates an expansion of the affected layer in bulk powellite crystal. The thickness of the irradiation-damaged layer becomes constant (saturated) after 1.2 dpa. Structure damage and disorder were observed in the irradiation-affected layer due to the decrease of peak area and the broadening of linewidth, respectively. Both expansion and compression of the structure were found in the irradiation-affected layer according to the shift of peak position. The most disordered structure is shown to be at the irradiated surface of powellite due to the most broaden linewidth.

4.2.4 Evolution of the structure and the induced stress of powellite after oriented irradiations according to the Raman depth profiles

Based on the mapping of peak position and linewidth, a statistic calculation was carried out to illustrate the evolution profiles of $\nu_1(A_g)$ and $\nu_3(E_g)$ modes with depth for both *a*- and *c*-oriented irradiation on powellite at 0.012, 0.12, 1.2 and 5.0 dpa.

4.2.4.1 Depth profile of $\nu_1(A_g)$ and $\nu_3(E_g)$ peak position in the irradiated powellites

Figure 4-15 shows the evolution profiles of peak position and linewidth in depth direction of oriented irradiated powellites with 0.012, 0.12, 1.2, and 5.0 dpa. Evolutions in *a*-oriented irradiated powellites are present on the left column of Figure 4-15, while those in *c*-oriented ones are on the right column. Left axes and right axes of Figure 4-15 stand respectively for the peak center frequency and linewidth of $\nu_1(A_g)$ mode. Figure 4-16 shows comparisons of $\nu_1(A_g)$ depth profiles of peak position as well as linewidth between *a*- and *c*-oriented powellites under each irradiation conditions (0.012, 0.12, 1.2 and 5.0 dpa).

As mentioned previously, frequency of Raman peak relates to parameters of the lattice and properties of the corresponding molecule. Shift of Raman peak position (vibration frequency) consequently provides information of the change in lattice structure. A shift of peak position towards the higher-frequency direction can be related to the compression of lattice, while position shifts towards the lower-frequency direction can be conversely related to the expansion of lattice. Therefore, several regions can be defined based on the $\nu_1(A_g)$ peak position value, in order to distinguish the different irradiation induced effects on powellite structure.

In the whole irradiation-damaged layer, the near-surface region where frequency of $\nu_1(A_g)$ vibration mode has lower-frequency shift can be defined as "*expansion region* (or layer)", and the neighboring region where $\nu_1(A_g)$ has higher-frequency shift is defined as "*compression region* (or layer)"; while the one which connects the compaction region and the non-damaged layer could be "*transition region* (or layer)". Ranges of estimated regions are drawn in different colors in Figure 4-15. Related data is listed in Table 4-4. It is necessary to point out that the spatial resolution of Raman spectroscopy in this study is around 0.8 μm (as mentioned in Chapter 2) whereas the step of the Raman profiles is 0.2 μm, which means that each Raman measurement provide an average results of information from a region with a radius of about 0.4 μm. However, the most important thing is that the evolution of the structure can be represented definitely by determine the evolution of Raman spectra.

a) Depth profile of $\nu_1(A_g)$ peak position in each irradiation-damaged layer

For each oriented irradiated powellite single crystal, evolution of $\nu_1(A_g)$ frequency from non-damaged to damaged layers are illustrated clearly in Figure 4-15. As it has been already shown in the peak position mapping (Subsection 4.2.3.3), the $\nu_1(A_g)$ frequency first has a slight decrease in the transition region and then it rises to a maximum value in the compression region, after which it continues to decrease until reaching the surface. Minimum peak position of $\nu_1(A_g)$ always appears on the irradiated surface for each powellite.

b) Comparison of depth profile of $\nu_1(A_g)$ peak position between *a*- and *c*-oriented powellite under the identical irradiation condition (anisotropic effects)

Comparing the depth profiles of $\nu_1(A_g)$ peak position in the two oriented irradiated powellite in Figure 4-16, it can be seen that for the same dpa value, peak position of $\nu_1(A_g)$ shifts more towards the lower-frequency direction in the expansion region of *a*-oriented irradiated powellite than that of the *c*-oriented one. It suggests that, after undergoing the same irradiation, powellite lattice was more expanded when Ar ions come along *a*-axis.

Conversely, effect in the compression region follows the other way around. Central peak position of $\nu_1(A_g)$ in the compression region of powellite with *c*-oriented irradiation always shift more towards the higher-frequency direction than the one with *a*-oriented irradiation, which indicates that this region is more compressed when irradiation comes along *c*-axis.

Modifications on powellite structure can be different according to the irradiated directions since the physical properties of powellite along *a*- and *c*-axes are not the same. For each irradiation condition, *a*-oriented powellites always have more shifts towards the lower-frequency direction in the expansion region but less shifts towards the higher-frequency direction in the compression region, comparing with the *c*-oriented powellites. Considering the macroscopic swelling of powellite after irradiations by optical interferometry in Section 4.1.2, it is therefore reasonable that *a*-oriented powellite have more surface swelling than the *c*-oriented one after undergoing the same dose of irradiation, since *the irradiation-damaged layer is less compressed in the compression region and more expanded in the expansion region for powellite with a-oriented irradiation*.

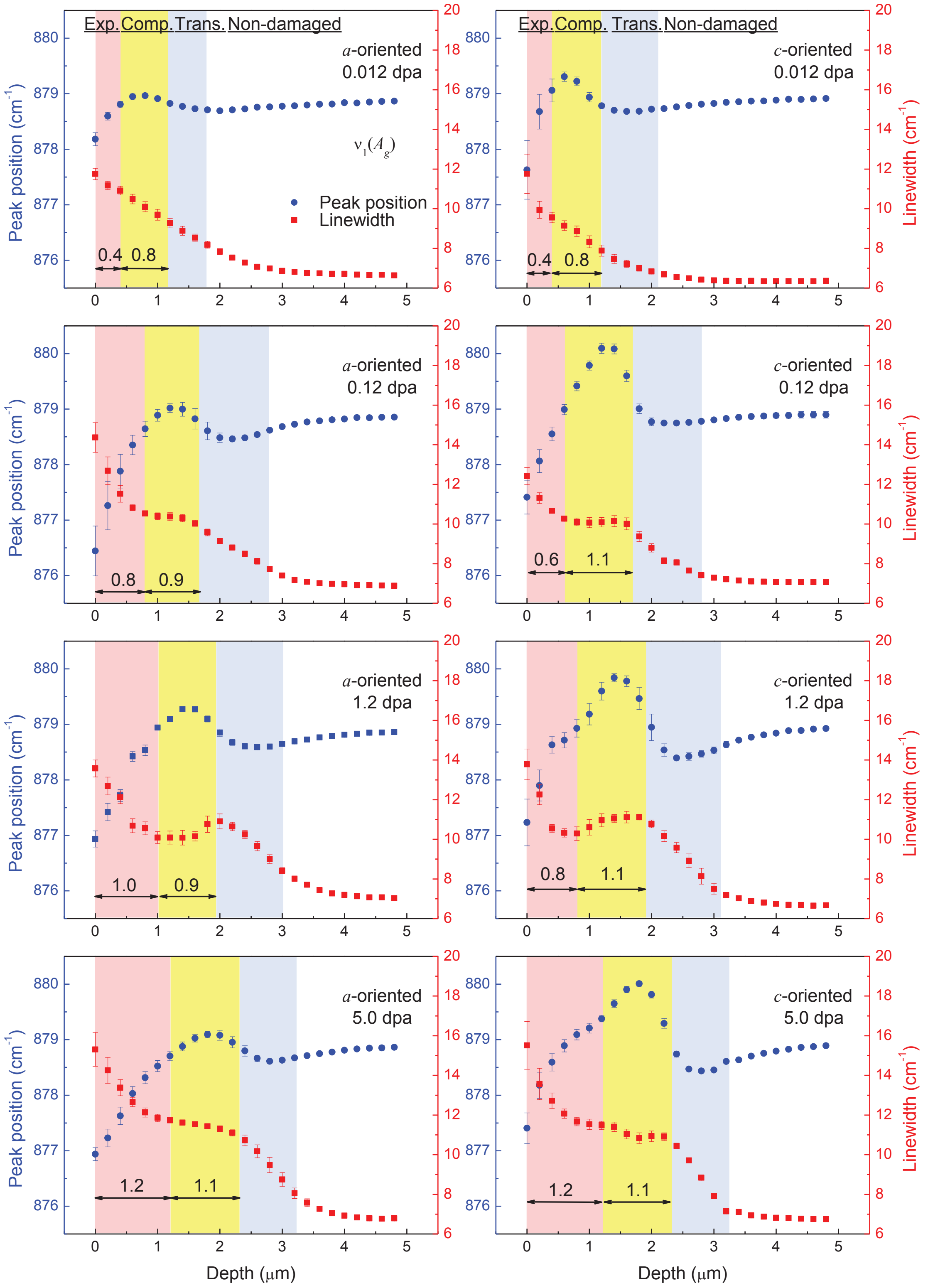

Figure 4-15: Depth profile of Raman $\nu_1(A_g)$ peak position (blue circle) and linewidth (red square) on FIB sections of both *a*-oriented (left column) and *c*-oriented (righ column) irradiated powellite at 0.012, 0.12, 1.2 and 5.0 dpa; left axes represent peak position while righ axes indicate the linewidth; expansion (exp.), compaction (comp.) and transition (trans.) layers are colored in red, yellow and blue, respectively, whereas, non-damaged layer is colored in white

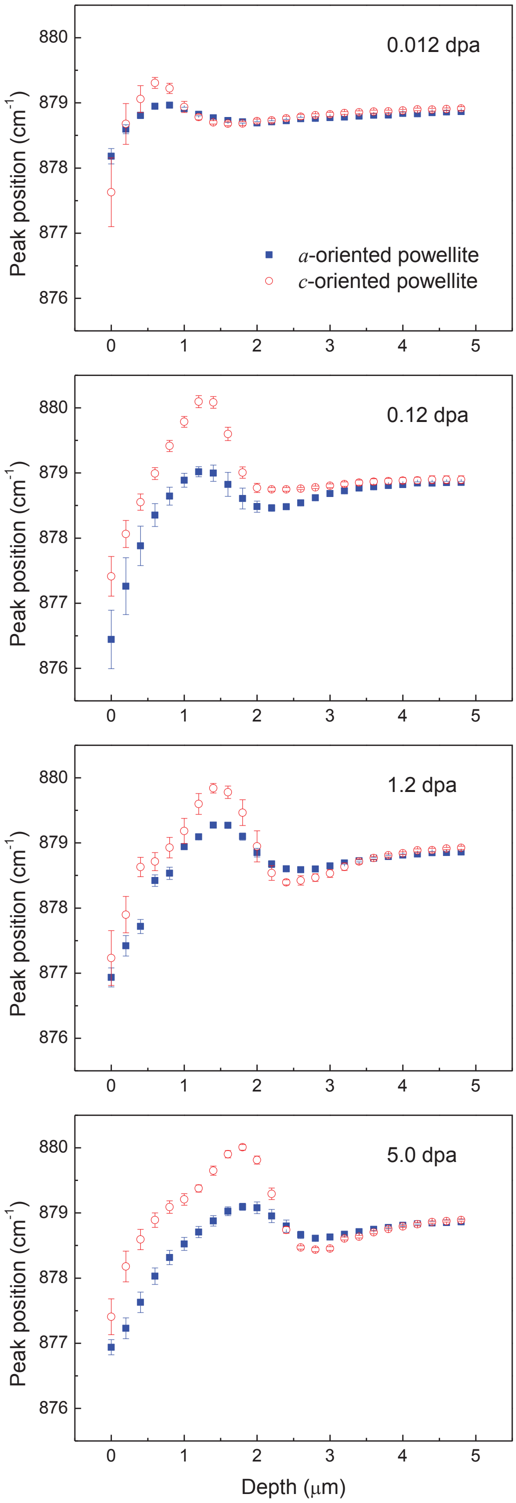

Figure 4-16: Comparison of $\nu_1(A_g)$ peak position evolution in depth direction between *a*- and *c*-oriented irradiated powellite

c) Evolution of depth profile of $\nu_1(A_g)$ peak position with increasing dpa

Although the depth profiles of $\nu_1(A_g)$ peak positions in the irradiation-damaged layer are similar to each other for different irradiated powellite, the depth corresponding to the maximal frequency of $\nu_1(A_g)$ peak position increases with irradiation dose (dpa). It suggests that *the compression region goes deeper and deeper when Ar irradiation dose increases*, as illustrated in Figure 4-15 and Figure 4-16. The maximal peak position and its corresponding depth for each irradiated powellite are listed in Table 4-4.

According to the SRIM simulation (see Subsection 2.2.2), the predetermined damaged depth in powellite by Ar irradiation is 3 μm. However, the irradiation-affected layers presented by Raman mapping are not the same for powellite at different dpa. Particularly, the thickness of the affected layer for 0.012-dpa sample is much less than 3 μm. It is shown that there may be some theoretical error for SRIM simulation of single crystal, since SRIM is designed for isotropic materials. More discussion on the damage depth in powellite is presented in Section 4.3.

d) Depth profile of $\nu_3(E_g)$ peak position

To further confirm the information of structure modification from Raman $\nu_1(A_g)$ mode, it is interesting to investigate the $\nu_3(E_g)$ mode of powellite. As mention previously (Subsection 4.1.1), $\nu_3(E_g)$ vibration mode can be observed only in an a(cr)a Raman measurement on FIB sections from *c*-oriented powellite slices in this study. Evolutions of $\nu_3(E_g)$ peak position in irradiated powellite with 0.012, 0.12, 1.2 and 5.0 dpa are presented in Figure 4-17. As can be seen, the evolution behaviors of $\nu_3(E_g)$ mode are very similar to that of $\nu_1(A_g)$. The same regions corresponding respectively to expansion, compression and transition in FIB section of *c*-oriented irradiated powellite (*c*-lamellae) can be found from $\nu_3(E_g)$ evolution data by determining the shift of peak position. Similarly, the depth that corresponds to the maximal frequency of $\nu_3(E_g)$ peak position increases with irradiation dose (dpa).

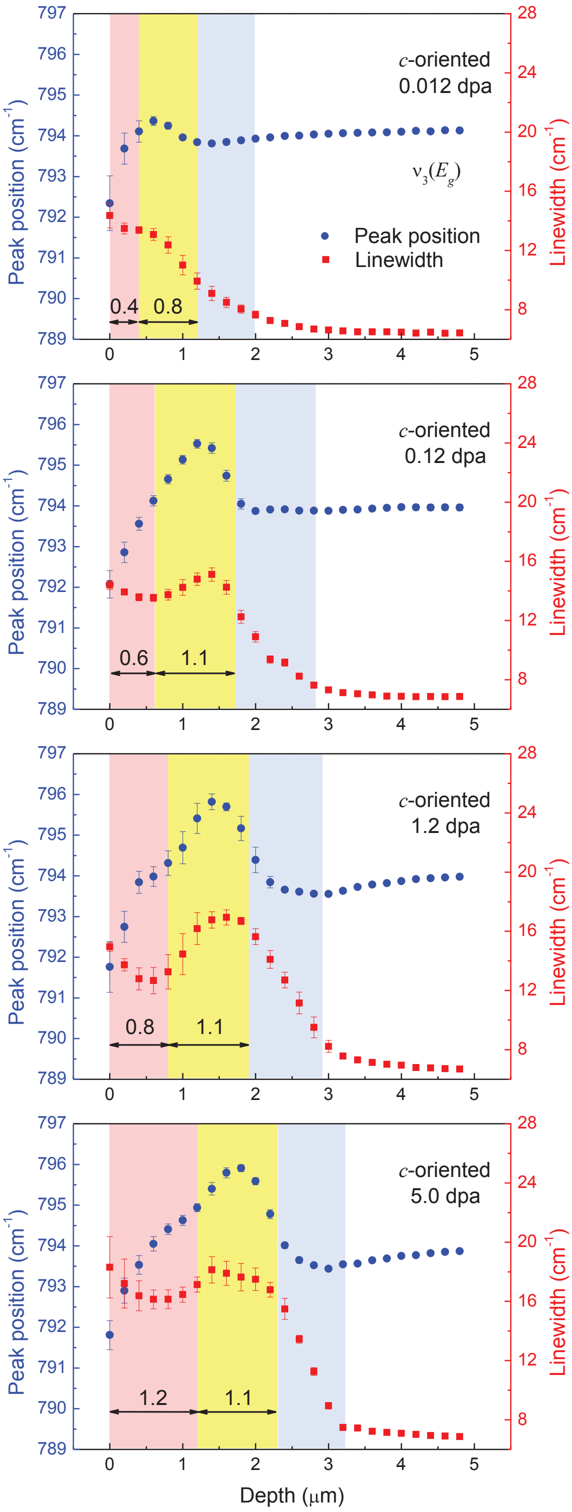

Figure 4-17: Depth profile of Raman ν3(Eg) peak position (blue circle) and linewidth (red square) on FIB sections of *c*-oriented irradiated powellite at 0.012, 0.12, 1.2 and 5.0 dpa; left axes represent peak position while righ axes indicate the linewidth; expansion (exp.), compaction (comp.) and transition (trans.) layers are colored in red, yellow and blue, respectively; whereas, non-damaged layer is colored in white (the same as Figure 4-15).

4.2.4.2 Discussion of irradiation-induced compressive stress in powellite

It is reported that all Raman modes (except the 113 cm^{-1} B_g translation mode) of the powellite structure exhibit a linear pressure dependence with positive slopes before phase transition occurs at 8.2 GPa [11, 12]. According to the pressure dependence of the Raman modes of powellite in Figure 4-18 [11], frequencies of $\nu_1(A_g)$ and $\nu_3(E_g)$ increase linearly with the increasing pressure performed on the sample in the 0 to 8.2 GPa range.

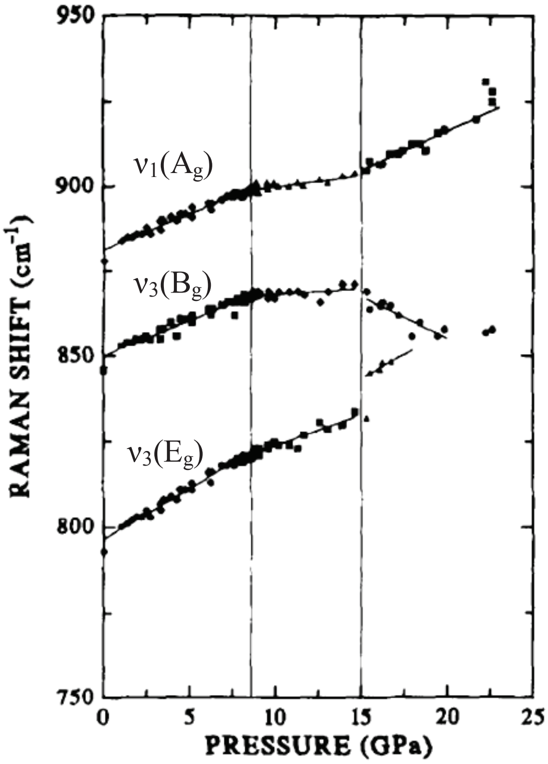

Figure 4-18: Pressure dependence of the Raman modes of powellite in the high frequency region ($\nu_1(A_g)$, $\nu_3(B_g)$, and $\nu_3(E_g)$); Phase transitions were observed at 8.2 and 15 GPa (marked with the vertical lines) according to the change in slopes of the phonon lines [11]

Accordingly, *peak shift towards the higher-frequency direction reveals the generation of compressive stress in the irradiation-damaged layer of powellite, associated with lattice compression*. On the contrary, peak shift towards the lower frequency can indicate the tensile stress in the structure. However, since the expansion region of irradiated powellite is on the surface which is free to swell, this tensile stress is released. Here, it is more interesting to investigate the irradiation-induced compressive stresses inside the damaged layer of powellite single crystal, especially to determine the anisotropic stresses along the two crystal axes (*a*- and *c*-axes). Based on the pressure coefficient ($d\omega/dp$) of $\nu_1(A_g)$ and

$\nu_3(E_g)$ (listed in Table 4-3) [11] and the difference in peak position ($\Delta\omega$), it is possible to evaluate the compressive stress (Δp) in the compression region of powellite through Equation (4-5).

$$\Delta p = \frac{\Delta\omega}{d\omega / dp} \qquad \textbf{(4-5)}$$

Figure 4-19 presents the evaluation of anisotropic compressive stresses in function of dpa within the compression region of irradiation-damaged layer inside powellites, according to the peak position shift of both $\nu_1(A_g)$ and $\nu_3(E_g)$. The difference between the maximal peak position and the peak position from non-damaged layer of each FIB section is used for the calculation of maximal compressive stress. As can be seen clearly in Figure 4-19, evolution of stresses follows basically an increasing behavior according to irradiation damage levels (dpa) in both orientations.

For powellite under *c*-oriented irradiations, it can be notice that the shift of $\nu_3(E_g)$ is always larger than that of $\nu_1(A_g)$, according to the depth profiles of peak positions from *c*-oriented irradiated powellites in Figure 4-15 and Figure 4-17. It is a predictable result due to the fact that the pressure coefficient ($d\omega/dp$) of $\nu_3(E_g)$ is higher than that of $\nu_1(A_g)$.

Stresses in powellite induced by *a*- and *c*-oriented irradiations are significantly different. From Figure 4-19, both the shifts of $\nu_1(A_g)$ and $\nu_3(E_g)$ modes give similar values of stresses (from 0.12 to 0.64 GPa) in the *c*-oriented irradiated powellite. By comparison, *a*-oriented irradiations generate much less stresses in powellite (from 0.05 to 0.20 GPa). For *a*-oriented irradiated powellite, only the shifts of $\nu_1(A_g)$ are used for the calculation since $\nu_3(E_g)$ mode is not active. According to the pressure dependence of the Raman vibration frequencies of powellite in Figure 4-18, the irradiation- induced stresses in powellite are not enough to give rise to phase transition.

The anisotropic performances along the two crystal axes suggest that *the powellite structure endure more stress under c-oriented irradiations.* Considering the fact that linear compressibility of the *c*-axis is larger than that of the *a*-axis [12] in the powellite structure, it is reasonable that *the structure can bear more stress along c-axis.*

In addition, as shown by optical interferometry in Subsection 4.1.4, delamination effect was observed in *a*-oriented irradiated powellite. This delamination effect can be linked to the compressive stress in the damaged layer. It is shown by Figure 4-20 that the depth at which delamination occurs is close to the location of maximum compressive stress in the damaged layer of *a*-oriented irradiated powellite at different dpa. It is reasonable that when the increasing induced stress cannot be endured by powellite, delamination takes place near the most compressed structure to release part of the stress in the damaged layer.

Table 4-3: Peak positions ($\omega(0)$) of $\nu_1(A_g)$ and $\nu_3(E_g)$ modes from non-irradiated region of FIB sections, as well as their pressure coeffecient ($d\omega/dp$) and the mode Grüneisen parameters[14] (γ) [11]

Vibration mode	$\omega(0)$ (cm^{-1})	$d\omega/dp$ (cm^{-1}/GPa)	γ
$\nu_1(A_g)$	878.9	2.1	0.20
$\nu_3(E_g)$	794.0	3.0	0.32

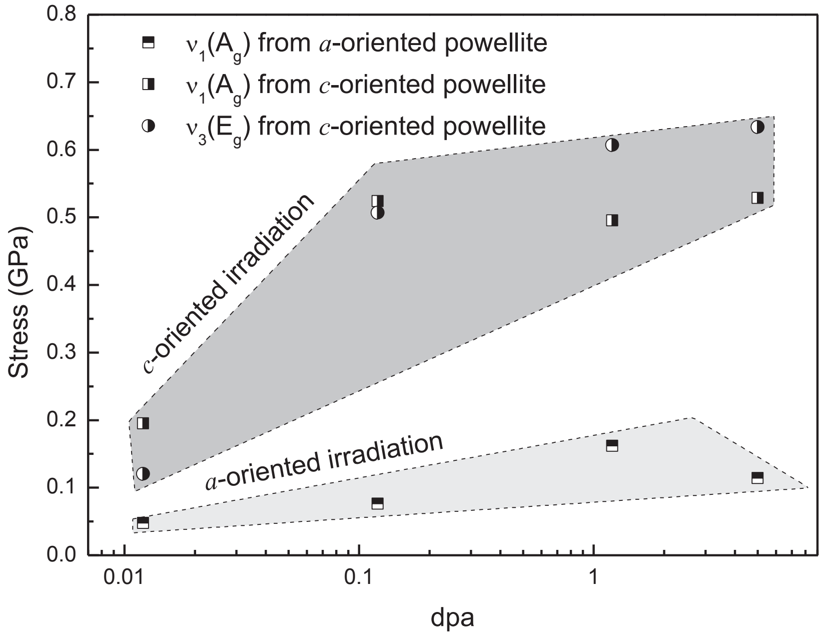

Figure 4-19: Evaluation of anisotropic compressive stresses (maximum) in the compression region of irradiation-damaged layer inside powellites through frequency-pressure dependence; the light gray region is the stress in *a*-oriented irradiated powellite while the dark gray region is the stress in the *c*-oriented one

---

[14] The Grüneisen parameter (γ) is a term used to describe the response of the lattice vibrations to the change of lattice volume

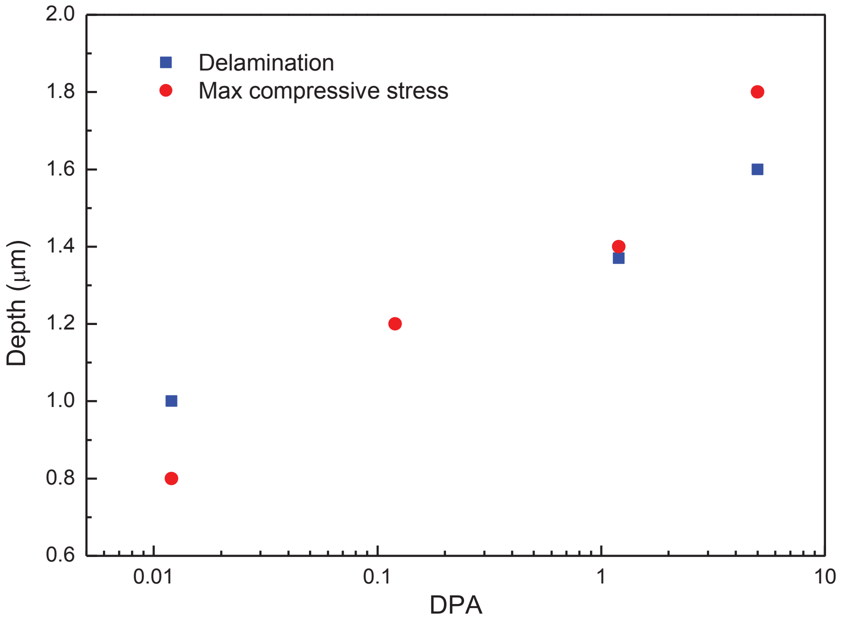

Figure 4-20: Depth values of the delamination and the maximum compressive stress in the damaged layer of *a*-oriented irradiated powellite at different dpa

4.2.4.3 Discussion of irradiation-induced lattice volume change

As observed by optical interferometry in Section 4.1, irradiation induces swelling in powellites. Considering the fact that the frequency shift of Raman vibration modes can provide information of the lattice volume change, it is interesting to find a connection between macroscopic swelling and frequency shift of Raman vibration modes of powellite.

The Grüneisen parameter (γ) [14] is a term used to describe the response of the lattice vibrations to the change of lattice volume in a thermodynamic process. According to the relation of the frequency of a specific vibration mode (ω_i) and the corresponding Grüneisen parameter Correlation (γ_i) in Equation (4-6) [14, 15], the thermodynamic volume change can be calculated by determining the shift of Raman vibration frequencies.

$$\gamma_i = \left(\frac{\partial \ln \omega_i}{\partial \ln V} \right)_T \tag{4-6}$$

Here, ω_i is the frequency of a specific Raman vibration mode (phonon); V is the volume; the subscript T means isothermal process. The Grüneisen parameters for $\nu_1(A_g)$ and $\nu_3(E_g)$

of powellite are listed in Table 4-3. Equation (4-7) can be deduced from Equation (4-6), which illustrate the relation between the change of volume (ΔV) and the frequency of Raman mode. $\omega_i(0)$ is the initial frequency.

$$\left(\frac{V_0+\Delta V}{V_0}\right)_T=\left(\frac{\omega_i}{\omega_i(0)}\right)^{1/\gamma_i} \tag{4-7}$$

Accordingly, the ranges of volume change and stress in both a- and c-oriented irradiated powellite can be calculated based on the Raman peak position shift, as shown in Figure 4-21 which is obtained by determining the peak position shift of $\nu_1(A_g)$. Data on Figure 4-21 comes from the depth profiles of $\nu_1(A_g)$ peak position. Obviously, the red regions in the coordinates of Figure 4-21 indicate the expansion behavior while the yellow ones indicate the compression behavior. The maximum volume changes of expansion and compression are marked in the figure. For each irradiated powellite, *the expansion effect is more significant than the compression ones* according to the maximum changes, which can explain why swelling is always observed for each irradiated powellite. Based on the distribution of points, it is shown that *both expansion and compression effects in the powellite structure increase with dpa*. Moreover, the anisotropy in irradiation-induced stress and volume change are well demonstrated in Figure 4-21. *a-oriented irradiated powellites always have more expansion and less compression than the c-oriented ones under identical irradiation condition*, which helps to understand the larger swelling in a-oriented irradiated powellites.

This is simply a qualitative evaluation of the relation between lattice volume change and macroscopic swelling. The real situation in the damaged layer of powellite is more complex. Besides lattice volume change, the formation of defects induced by irradiation can also contribute to the swelling of powellite. The effect of powellite swelling associated to defect accumulation in the structure is further discussed in Section 4.3

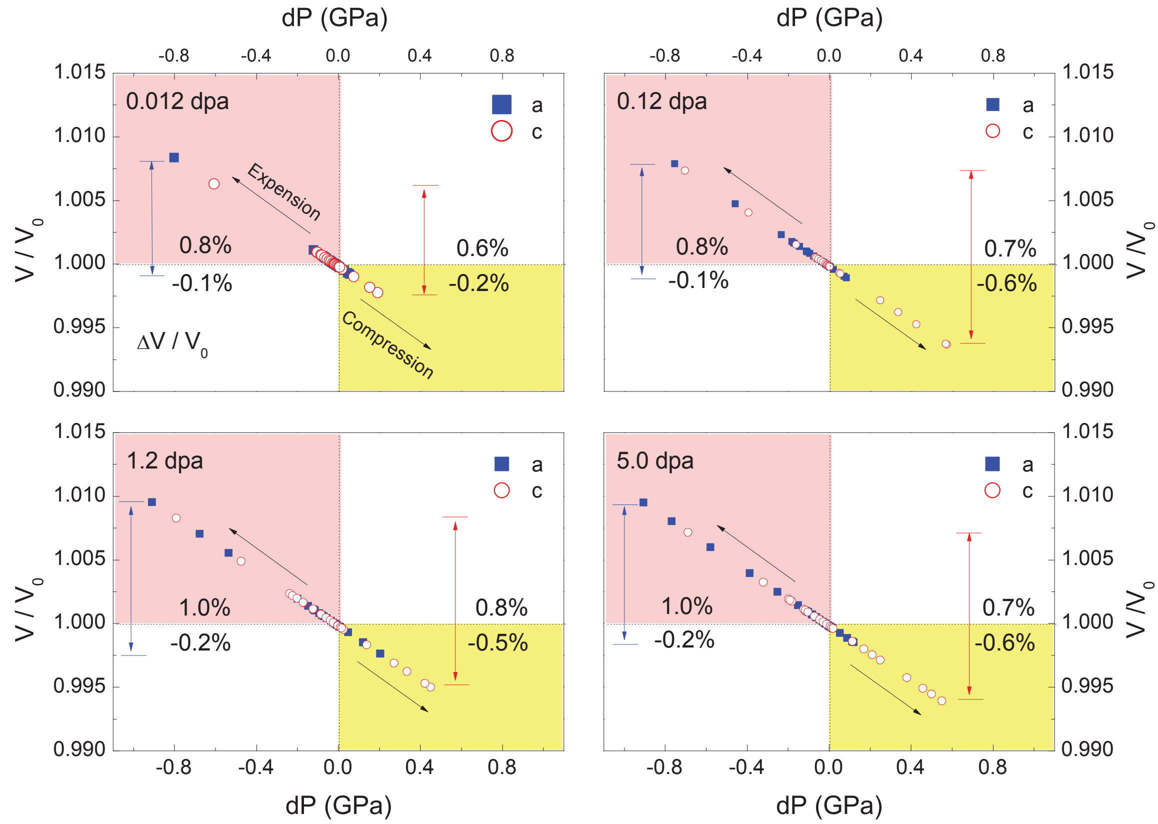

Figure 4-21: Ranges of the volume change and pressure (stress) in *a*-oriented (blue square) and c-oriented (red circle) irradiated powellite (calculated from the peak position shift of $\nu_1(A_g)$); red regions in the coordinates indicate the expansion behavior while the yellow ones indicate the compression behavior

4.2.4.4 Discussion of irradiation-induced structural disorder in powellite by determining the depth profile of linewidths

As stated in linewidth mapping section (4.2.3.4), linewidth broadening can be used to study the structural disorder of powellite induced by irradiation. Depth profiles of $\nu_1(A_g)$ linewidth in oriented irradiated powellites with 0.012, 0.12, 1.2 and 5.0 dpa are presented in Figure 4-15, together with the depth profile of peak position. Linewidth values are shown in the right axis of each figure.

a) Depth profile of $\nu_1(A_g)$ linewidth in each irradiation-damaged layer

Linewidth broadening was observed in the irradiation-damaged layer of each irradiated powellite, indicating the presence of structure disorder. As shown by the linewidth mapping in Subsection 4.2.3.4, the most broadened linewidth always appears on the irradiated surface, indicating that *the most disordered structure is at the surface*. According to Figure

4-15, the linewidth of $\nu_1(A_g)$ mode decreases gradually from the surface down to the interior of the irradiation-damaged layer. It means that the disorder of structure in the irradiation-damaged layer decrease in the depth direction of irradiated powellites.

For *a*-oriented irradiation, linewidth of $\nu_1(A_g)$ mode at the irradiated surface of powellite (corresponding to 0-μm on the FIB sections of *a*-lamellae) are 11.8, 14.4, 13.5, 15.3 cm^{-1} for 0.012, 0.12, 1.2 and 5.0 dpa, respectively. By comparison, linewidth from irradiated surface of *c*-oriented powellite are 11.8, 12.4, 13.8, 15.5 cm^{-1} for 0.012, 0.12, 1.2 and 5.0 dpa. The linewidth from non-damaged region of each FIB section is about 6.8 cm^{-1}. It is proposed that the surface acts as a sink to accommodate defects in the damage layer [16], resulting in more structural disorder on the surface than the other regions.

b) Comparison of depth profile of $\nu_1(A_g)$ linewidth between *a*- and *c*-oriented powellite under the same irradiation

Figure 4-22 shows a comparison of depth profiles of $\nu_1(A_g)$ mode between *a*- and *c*-oriented irradiated powellites. As can be seen from the figure, there is no significant difference in linewidth profiles between *a*- and *c*-oriented irradiated powellites, except the 0.012-dpa one which exhibits more linewidth broadening under *a*-oriented irradiation. It suggests that *the irradiation-induced structural disorder in powellite structure is not depended on crystal orientation*, which is different from the anisotropic stress effects.

c) Evolution of linewidth broadening of $\nu_1(A_g)$ mode with increasing dpa

In the irradiation-damaged layer of 0.012-dpa powellite, linewidth decreases continuously with depth before reaching the non-damaged region for both *a*- and *c*-oriented irradiate powellites. However, as dpa increases (from 0.12 to 5.0), the depth profiles of $\nu_1(A_g)$ linewidth become different from the 0.012-dpa one. After a dramatic decrease in the near-surface region, the linewidth of $\nu_1(A_g)$ mode is then maintained in a certain level in the compression region. A plateau on the depth profiles can be well recognized in Figure 4-15 for irradiated powellite with 0.12, 1.2 and 5.0 dpa in both *a*- and *c*-orientations. It can be inferred that the irradiation-induced disorder in powellite structure tends to be stabilized in this region. Therefore, the mean linewidth of $\nu_1(A_g)$ mode in the plateau region of each irradiated powellite were calculated to determine the average structural disorder inside the damaged layer, as shown in Figure 4-23.

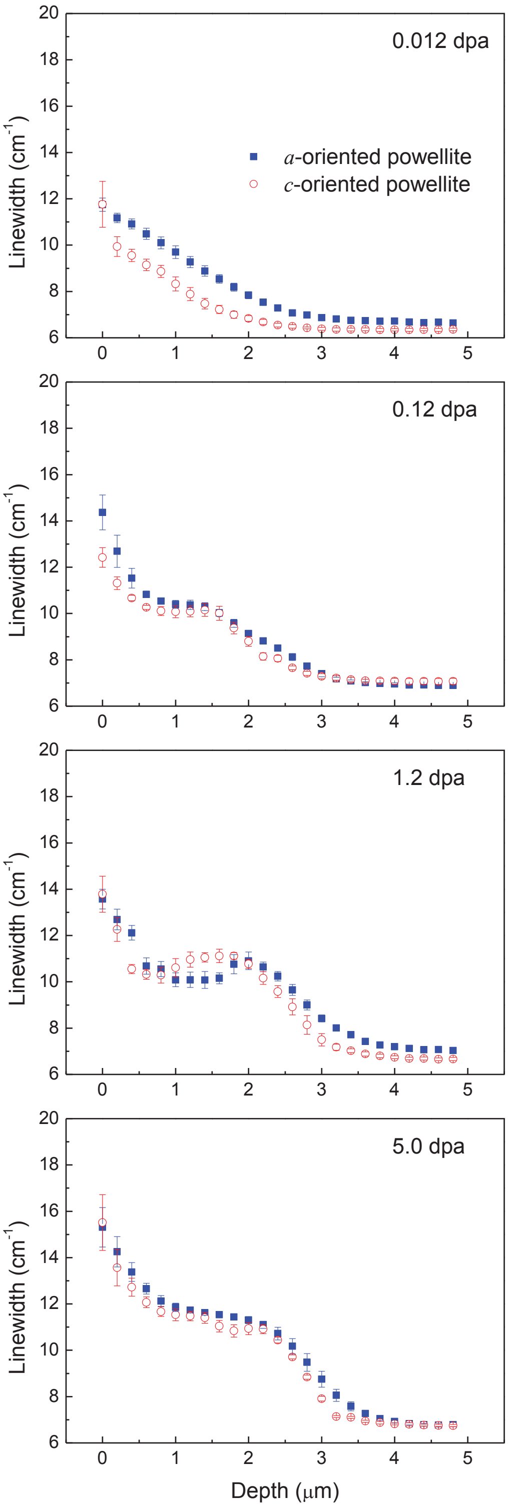

Figure 4-22: A comparison of ν$_1$(A$_g$) linewidth evolution in depth direction between *a*- and *c*-oriented irradiated powellite

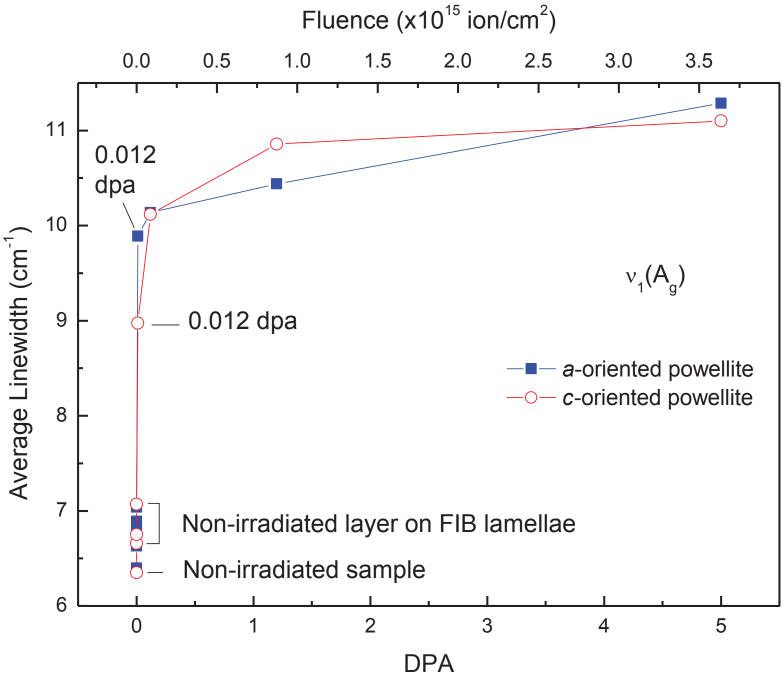

Figure 4-23: Evolution of $\nu_1(A_g)$ average linewidth with Ar irradiation dose (dpa) in the compression region of both *a*- and *c*-oriented irradiated powellite; slight broadening in linewidth due to the Ga ion beam during the FIB manipulation can be observed

According to Figure 4-23, for powellite at very low dpa, the mean linewidth of $\nu_1(A_g)$ in the compression region is higher in the *a*-oriented irradiated powellite. The mean linewidth increases basically with the increasing irradiation level, which indicates *an increase of structural disorder (or damage) in powellite*. Evolutions of the mean linewidth of $\nu_1(A_g)$ mode of the compression region versus dpa of the compression region are quite similar for both *a*- and *c*-oriented irradiated powellite.

First, a significant irradiation-induced disorder effect on pristine powellite structure is inferred since the linewidth rises dramatically in very low dpa range (from 0 to 0.012). As irradiation increases (from 0.12 to 5.0 dpa), the powellite structure becomes more and more disordered but with a much less effect, according to the continuous linewidth broadening. It is important to note that the $\nu_1(A_g)$ linewidth tends to become saturated instead of immoderately broadened with the increasing dpa. According to the Raman spectra 5.0-dpa powellite (Figure 4-7), vibration modes of MoO_4 tetrahedra can be well recognized, which suggests that *the powellite structure still remains crystallized at 5.0 dpa.* No amorphization was observed by Raman spectroscopy. It can be inferred that the *irradiation-induced* *structural disorder in powellite crystal can be maintained in a certain level* without resulting in amorphizaiton.

By the way, the $\nu_1(A_g)$ linewidth observed in the non-damaged region of FIB sections has a slight broadening, comparing with the linewidth measured from pristine powellite. Linewidth values of $\nu_1(A_g)$ from non-damaged regions of FIB sections are 0.2 to 0.6 cm^{-1} higher than that from pristine powellite bulk crystal (about 6.4 cm^{-1}), depending on the FIB process. It indicates that the Ga ion beam for FIB preparation can induce slight disorder effect on the sample. However, comparing with the linewidth broadening induced by Ar irradiations, the Ga beam effect is negligible. Maximum penetration depth of 30-KeV Ga ions (working condition) in powellite is around 90 nm (according to SRIM simulation).

d) Comparison of linewidth broadening of $\nu_1(A_g)$ and $\nu_3(E_g)$

Depth profiles of $\nu_3(E_g)$ linewidth in *c*-oriented irradiated powellite at 0.012, 0.12, 1.2 and 5.0 dpa are presented in Figure 4-17. For each *c*-oriented irradiated powellite, the evolution of the $\nu_3(E_g)$ linewidth in the expansion region of powellite behaviors quite the same as that of the $\nu_1(A_g)$, which decreases with depth. However, for the compression region of each irradiated powellite, the linewidth broadening of the $\nu_3(E_g)$ has some different features from that of the $\nu_1(A_g)$. A peak in the depth profile of $\nu_3(E_g)$ linewidth in the compression region of each irradiated powellite is observed instead of a plateau which is found in the $\nu_1(A_g)$ depth profile. This difference of $\nu_1(A_g)$ and $\nu_3(E_g)$ in linewidth broadening can be ascribed to the different response of Raman vibration modes to the lattice modification in powellite structure. Further detail about the change of properties of $\nu_1(A_g)$ and $\nu_3(E_g)$ modes due to structure modification will not be discussed here, since it is not the main purpose of the study.

Figure 4-24 shows the average linewidth of $\nu_1(A_g)$ and $\nu_3(E_g)$ of the compression region in function of dpa for *c*-oriented irradiated powellite. Initial linewidth of $\nu_3(E_g)$ mode from non-damaged bulk powellite crystal is very close to that of the $\nu_1(A_g)$ one, about 6.4 cm^{-1}. However, as irradiation increases, broadening of linewidth is more significant for $\nu_3(E_g)$ than for $\nu_1(A_g)$. Specially, for powellite with 5.0 dpa, linewidth of $\nu_3(E_g)$ has 1.6 times the $\nu_1(A_g)$ one. *The linewidth broadening is evidently more effective in $\nu_3(E_g)$ mode than in $\nu_1(A_g)$*. Considering the Grüneisen parameters (in Table 4-3) for $\nu_1(A_g)$ and $\nu_3(E_g)$, it is predictable that the $\nu_3(E_g)$ has more considerable response to the lattice change than what the $\nu_1(A_g)$ has due to the larger Grüneisen parameters of $\nu_3(E_g)$ mode. As can be seen in Figure 4-24, evolution behaviors of linewidth broadening due to irradiations are quite similar for $\nu_1(A_g)$ and $\nu_3(E_g)$ modes, which always tends to reach saturation at high dpa. It verifies the fact that the irradiation-induced disorder can be maintained in a certain level in powellite structure as dpa increase.

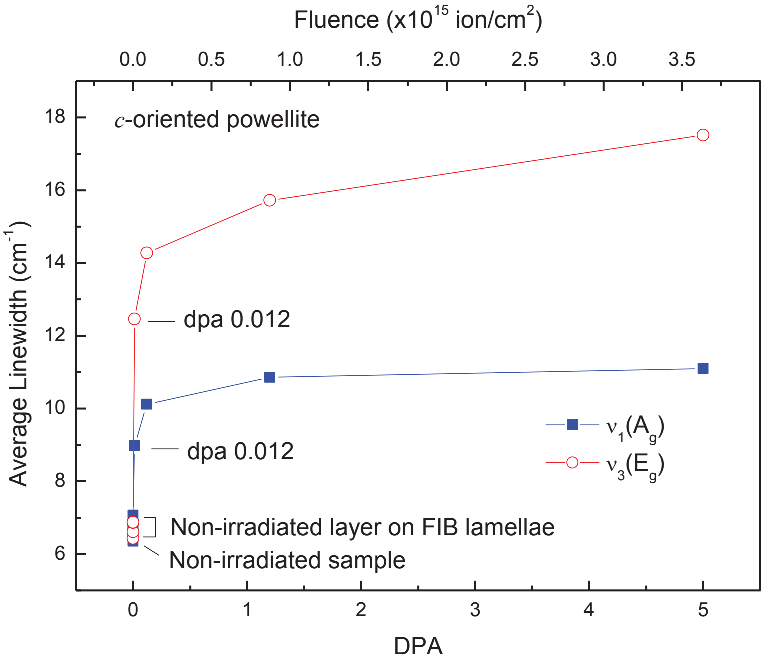

Figure 4-24: Evolution of $\nu_1(A_g)$ and $\nu_3(E_g)$ average linewidth with Ar irradiation dose (dpa) in the compression region of *c*-oriented irradiated powellite

Table 4-4: Several information about the irradiation-damaged layer in both *a*- and *c*-oriented irradiated powellite, including the estimated thickness of expansion (Exp.) and compression (Comp.) regions, the maximal peak position of $\nu_1(A_g)$ and $\nu_3(E_g)$ modes in the irradiation affected layers, as well as average linewidths of $\nu_1(A_g)$ and $\nu_3(E_g)$ modes in the compression regions

DPA	FIB Section	Region		Maximal frequency			Mean Linewidth	
		Exp. (μm)	Comp. (μm)	$\nu_1(A_g)$ (cm^{-1})	$\nu_3(E_g)$ (cm^{-1})	Depth (μm)	$\nu_1(A_g)$ (cm^{-1})	$\nu_3(E_g)$ (cm^{-1})
0.012	a	0.4	0.8	878.9	--	0.6	9.9	--
	c	0.4	0.8	879.3	794.4	0.6	9.0	12.5
0.120	a	0.8	0.9	879.0	--	1.2	10.1	--
	c	0.6	1.1	880.1	795.5	1.2	10.1	14.3
1.200	a	1.0	0.9	879.3	--	1.4	10.3	--
	c	0.8	1.1	879.8	795.8	1.4	10.9	15.7
5.000	a	1.2	1.1	879.1	--	1.8	11.3	--
	c	1.2	1.1	880.0	795.9	1.8	11.1	17.5

4.2.4.5 Combination of stress and disorder in irradiated powellite

To better illustrate the irradiation-induced stress and disorder in powellite structure, the peak position and the linewidth of $\nu_1(A_g)$ mode are plotted in function of both depth (0 to 5µm) and dpa (0.012, 0.12, 1.2 and 5.0), as shown in Figure 4-25 and Figure 4-26. Interpolation between two studied dpa values was used to obtain better images, which cannot be considered as real experimental data.

According to Figure 4-25 and Figure 4-26, the irradiation-affected layer grows in the depth direction with increasing dpa (from 0.012 to 5). The compressive-stressed layers (represented by the shift of $\nu_1(A_g)$ peak position towards higher frequency) propagates deeper and deeper as dpa increases, as indicated by the black arrow in Figure 4-25. Moreover, it is easy to see that the powellite structure endures more stress in *c*-orientation respecting to the larger peak shift.

Due to the fact that defects can migrate to the surface (defect sink), the most disordered structure always appears at the irradiated surface of powellite where the largest linewidth of $\nu_1(A_g)$ is observed, as shown in Figure 4-26. Linewidth beneath the surface is maintained in a certain range, which reveals an even structural disorder, agreeing with the predetermined flat dpa profile by SRIM (Chapter 2). Additionally, no significant evident anisotropic structural disorder is observed.

For powellite at each dpa, a release of compressive stress can be seen in the region above the compressed structure (indicated by the shift of $\nu_1(A_g)$ peak position towards lower frequency), in which an increase of structural disorder can also be recognized. Defect characterization using TEM was presented in the next section to further study the relation between the release of stress and the increase of structural disorder.

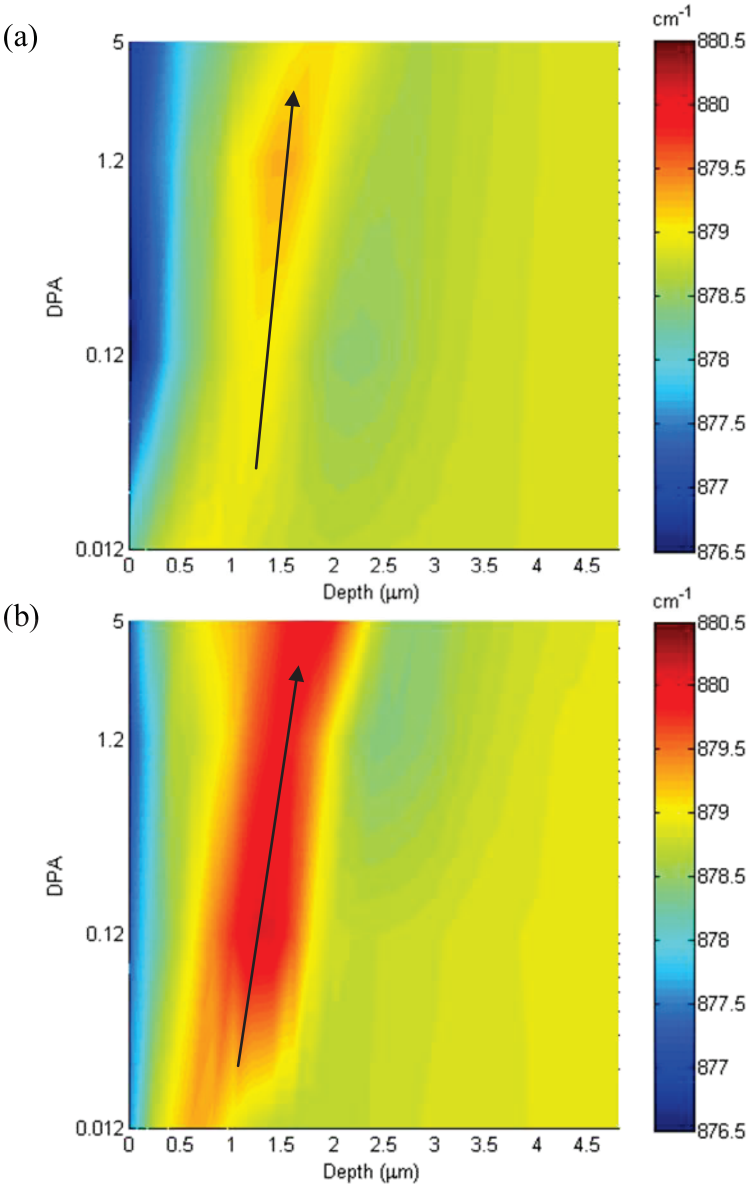

Figure 4-25: $\nu_1(A_g)$ peak position according to depth and dpa in *a*-oriented (a) and *c*-oriented (b) irradiated powellites; colorbars on the right side indicate the peak position of $\nu_1(A_g)$; black arrows indicate the evolution of stressed layer in the irradiated powllites

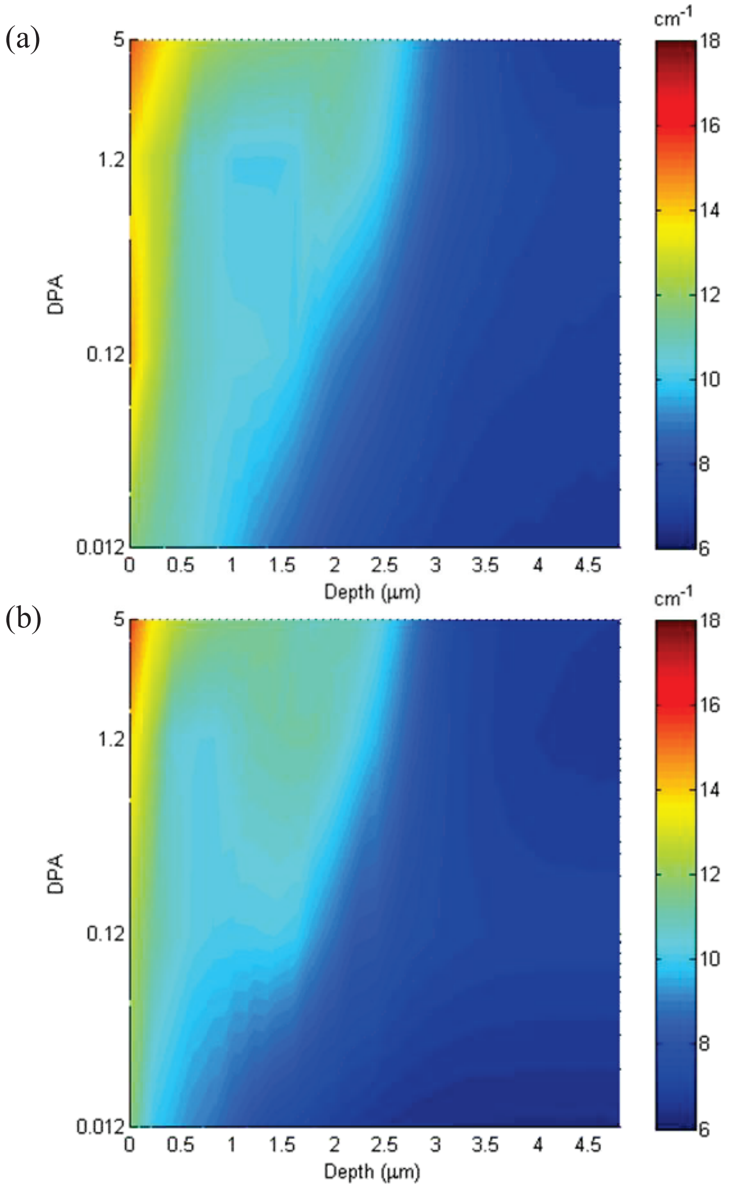

Figure 4-26: $\nu_1(A_g)$ linewidth according to depth and dpa in *a*-oriented (a) and *c*-oriented (b) irradiated powellites colorbars on the right side indicate the linewidht of $\nu_1(A_g)$

Summary of this subsection:

Several regions corresponding to different structural modification were defined in the irradiated-damaged layer of powellite single crystal according to the depth profile of $v_1(A_g)$ *peak position, including expansion region, compression region, and transition region. The depth of the compression region increases with increasing dpa (from 0.012 to 5.0). Anisotropic effect in the lattice volume change was observed along two crystallographic axes (a- and c-axes) by comparing the depth profile of* $v_1(A_g)$ *peak position. By determining the position shift of* $v_1(A_g)$ *peak, the irradiation-damaged layer is less compressed in the compression region and more expanded in the expansion region for powellite with a-oriented irradiation. Irradiation-induced compressive stresses in the powellite structure were determined by the shift of* $v_1(A_g)$ *and* $v_3(E_g)$ *peak positions, which shows that c-oriented irradiated powellite can endure more stress in the structure. Moreover, according to the estimated volume change, the expansion effect is more significant than the compression ones, which explains why swelling is always observed for each irradiated powellite. a-oriented irradiated powellites always have more expansion and less compression than the c-oriented ones under identical irradiation condition, which finally leads to the larger swelling. According to the linewidth of Raman* $v_1(A_g)$ *mode, the irradiation-induced disorder in powellite structure does not depend on crystal orientation. No significant anisotropic effect was found for the structural disorder in a- and c-oriented irradiated powellites. The most disordered structure was always found at the irradiated surface for each powellite sample due to the most broadened linewidth. However, the disorder in the compression region of irradiated powellite (0.12 to 5.0 dpa.) is quite constant since the linewidth reaches a plateau in this region. Although the structural disorder increases with irradiation level, the powellite structure still remains crystallized at 5.0 dpa. No amorphization was observed by Raman spectroscopy.*

4.3 Irradiation-induced lattice defects in powellite structure by TEM

The radiation-induced defects in crystalline phases have been studied for many years. One of the most important fundamental parameters affecting radiation damage in a material is the threshold displacement energy, which is the minimum kinetic energy necessary to displace an atom from its normal site. Point defects are therefore generated inside the lattice, which can migrate and be accumulated in the structure. The accumulation of point defects and evolution of microstructures under irradiation are controlled by the kinetic properties of the system. In this section, transmission electron microscope (TEM) was used to characterize the defects in the powellite structure induced by Ar irradiations and to correlate them with the spectroscopy data.

4.3.1 Ultra-thin FIB section for TEM

Ultra-thin FIB sections (about 100-nm thick) from *a*- and *c*-oriented irradiated powellites at 0.012 and 5.0 dpa were prepared for the TEM observations. Figure 4-27 and Figure 4-28 present respectively the conventional TEM bright-field images of the sections from *a*- and *c*-oriented irradiated powellites. The original surfaces of the irradiated powellites for TEM were protected by Pt coating (marked with red dash lines in the figures). Orientations of the FIB sections are shown in the figure.

Figure 4-27-(a) and (c) are TEM images at low magnification for *a*-oriented irradiated powellite sections at 0.012 and 5.0 dpa, respectively, while (b) and (d) are the corresponding high-magnified TEM images. First of all, *an evident defected layer induced by Ar irradiation can be observed below the irradiated surface.* However, the thicknesses of the defected layers are very different for low- and high-irradiated samples, with 1.6 μm in the 0.012-dpa powellite and 2.8 μm in the 5.0-dpa one.

Similar defected layers can be found in the *c*-oriented irradiated powellites, as shown in Figure 4-28. Figure 4-28-(a) and (c) are low-magnified TEM images of *c*-oriented irradiated powellite with 0.012 and 5.0 dpa, respectively, while (b) and (d) are the corresponding high-magnified ones. The thickness of the defected layer in 0.012-dpa sample is about 1.7 μm, while that in 5.0-dpa sample is about 2.5 μm.

Additionally, the long black curved bands on the pristine part of each FIB section are bend contours which is originate from the fact that crystal can become slightly bent as a result of internal strain. The change of orientations of the crystal planes due to structure bending can therefore make the Bragg equation[15] unfulfilled, resulting in occurrence of a bend contour as a dark band in the TEM image. For the pristine parts of the irradiated powellite FIB sections, bend contours do not represent a specific localized feature. They can shift to a new position in the TEM image when the TEM illumination is titled slightly.

The increase of the thickness of the defected layer with irradiation dose (0.012 to 5.0 dpa) provides the same result as what is shown by Raman mapping (Section 4.2). More importantly, *the features and the types of defects in the damaged layers are very different depending on the irradiation dose*, which can result from different modifications on the powellite structure and be revealed by the Raman spectra. Relation between the defected layers shown by TEM in irradiated powellites and the different regions estimated by Raman mapping will be discussed in the following subsection.

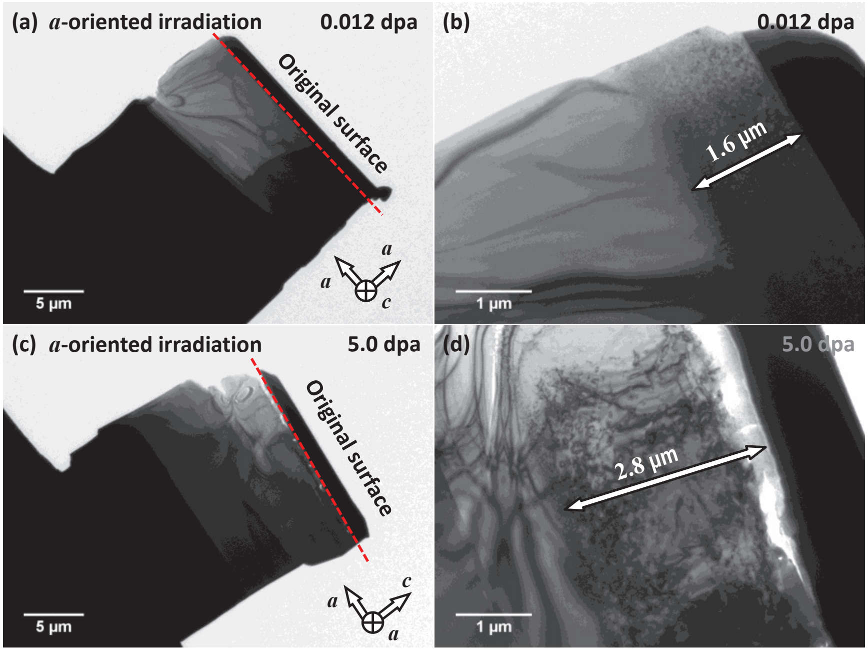

Figure 4-27: Conventional TEM bright-field images at different magnifications of ultra-thin FIB sections from *a*-oriented irradiated powellite at 0.012 dpa (a-b) and 5.0 dpa (c-d); original surface of the sample was protected by Pt coating layer (the very dark layer on top of the lamellae), indicating in the figures with red dash lines

---

[15] $n\,\lambda = 2\,d\,\sin\theta_i$; n is the order of the reflection; θ_i is the angle between the incident electron beam and the atomic planes (with a particular set of Miller indices) of spacing d in the crystal

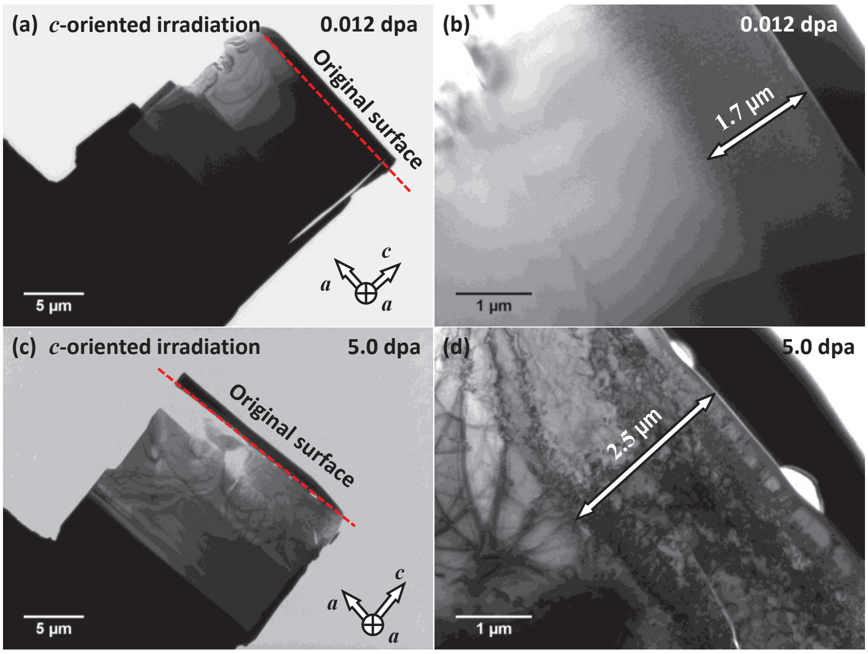

Figure 4-28: Conventional TEM bright-field images at different magnifications of ultra-thin FIB sections from *c*-oriented irradiated powellite at 0.012 dpa (a-b) and 5.0 dpa (c-d); original surface of the sample was protected by Pt coating layer (the very dark layer on top of the lamellae), indicating in the figures with red dash lines

4.3.2 Irradiation-induced defects in powellite single crystals

In this subsection, irradiation-induced defects in powellite single crystal are discussed in detail through high-magnified TEM images. A comparison between the TEM images and the Raman mapping ($\nu_1(A_g)$ and $\nu_3(E_g)$ modes) of irradiated powellites (at 0.012 and 5.0 dpa) is proposed and discussed to further investigate the modification of structural properties.

4.3.2.1 Irradiation-induced defects in low-dpa powellite (0.012 dpa)

Figure 4-29 and Figure 4-30 show the high magnified TEM bright-field and dark-field images of the FIB sections from *a*- and *c*-oriented irradiated powellite with 0.012 dpa, respectively. All the bright-field images were collected in zone axis condition, in order to gain a strong contrast. Accordingly, for *a*-oriented irradiated powellite, the zone axis is [001] (*c*-axis of the powellite structure) with the dark-field image collected from the (200) diffraction spot; whereas, for the *c*-oriented one, the zone axis is [010] (*a*-axis of the powellite structure) with the dark-field image from the (101) spot. Figure 4-31 presents the corresponding electron diffraction patterns of the irradiated-damaged layer of powellites.

First of all, *the main irradiation-induced damage in low-dpa powellite single crystal are point defect clusters* which distribute homogeneously in the damaged layer, according to the TEM bright-field images in Figure 4-29 and Figure 4-30. Both bright-field and dark-field images confirm the same range of irradiation-damaged layer in powellites.

There is no significant anisotropy in damage depth between the *a*- and *c*-oriented irradiated samples (1.6 μm and 1.7 μm on average, respectively). It is worth noting that, instead of a sharp interface, the transition from irradiated-damaged layer to the pristine structure is accompanied with a gradual decrease in defect density, indicating a gradual retrieval of powellite structure. This can be called “dose effect”. In addition, for the *c*-oriented irradiated sample, a narrow bright region (about 0.5-μm thick) appearing at the bottom of the damaged layer in the dark-field image ((101) spot) can be ascribed to the bending of crystal planes (bend contours), which introduces changes in diffraction condition and creates contrast in the image.

As stated previously, Raman spectroscopy provides information of medium-range order structure properties. It is interesting and important to compare the TEM images and the Raman mapping, in order to further interpret the irradiation-induced damage in powellite. Figure 4-32 and Figure 4-33 show the comparisons between Raman mapping on $\nu_1(A_g)$ mode (peak area, linewidth, and peak position) and the TEM images of *a*- and *c*-oriented irradiated powellite at 0.012 dpa, respectively.

According to Figure 4-32 and Figure 4-33, it is convinced that the irradiation-induced defected layers in powellite (TEM images) can be revealed clearly by Raman mapping, including a decrease in peak area, a broadening in linewidth, and a shift in peak position. However, for low-dpa powellites, the sub-layers shown by peak position and peak ratio mapping which have different structure modifications (i.e. expansion and compression) cannot be represented directly by TEM images.

Based on the depth profiles of $\nu_1(A_g)$ peak position, the total thicknesses of affected regions are about 2 μm for both *a*- and *c*-oriented irradiated powellite at 0.012 dpa (Subsection 4.2.4). Taking into account the spatial resolution (~0.8 μm) of Raman measurements, *the ranges of the irradiation-damaged layer given by TEM are in agreement with that shown by Raman measurements.*

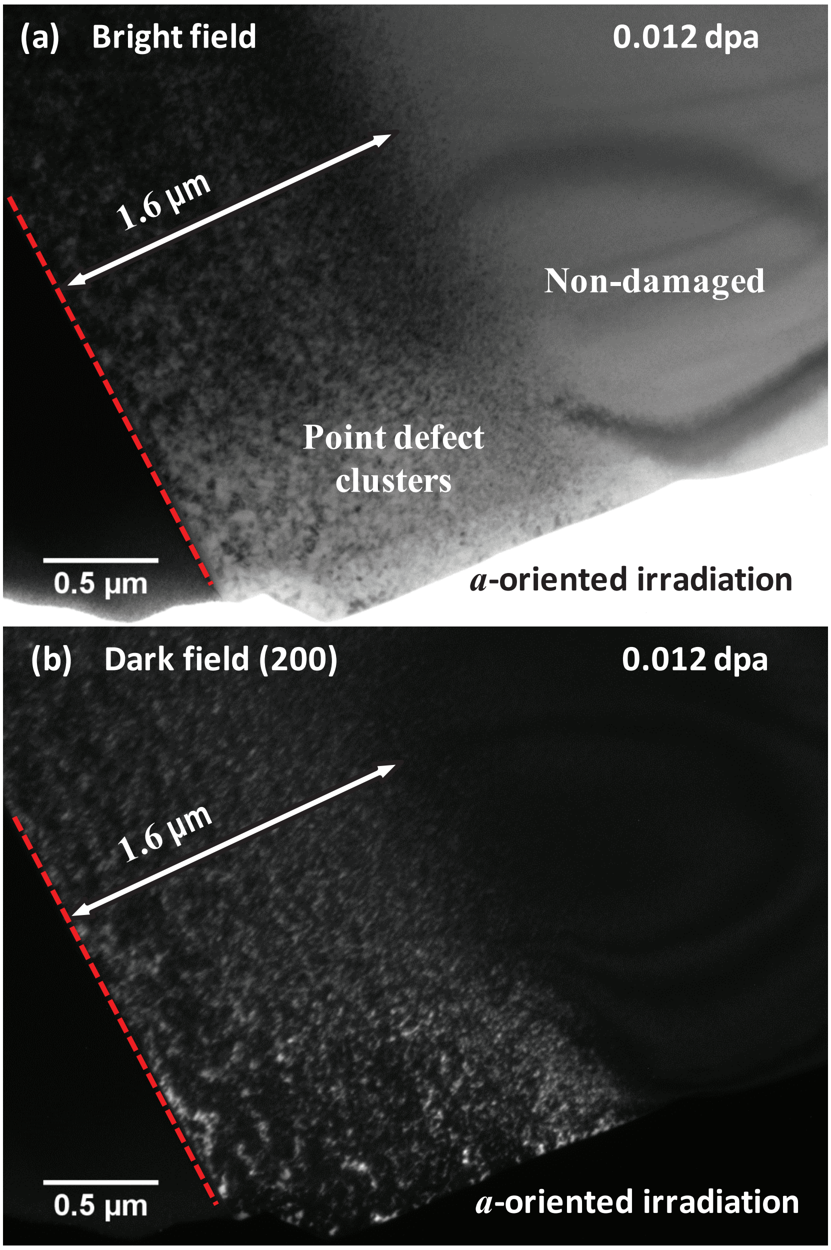

Figure 4-29: High magnified conventional TEM bright-field (a) and dark-field (b) images of FIB sections from *a*-oriented irradiated powellite with 0.012 dpa; zone axis is [001]; the bright-field image is collected from the central spot while the dark-field image is collected from the (200) spot; red dash lines indicate the original irradiated surface

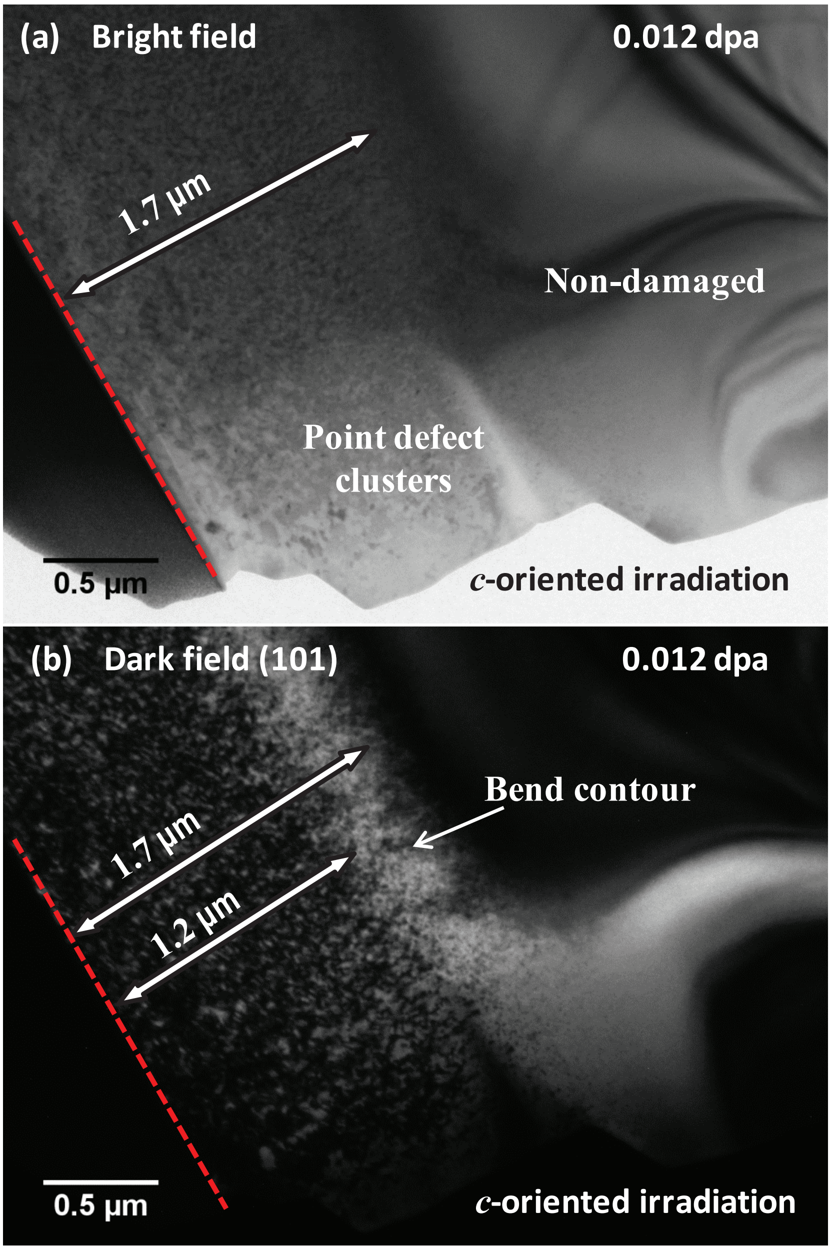

Figure 4-30: High magnified conventional TEM bright-field (a) and dark-field (b) images of FIB sections from *c*-oriented irradiated powellite with 0.012 dpa; zone axis is [010]; the bright-field image is collected from the central spot while the dark-field image is collected from the (200) spot; red dash lines indicate the original irradiated surface

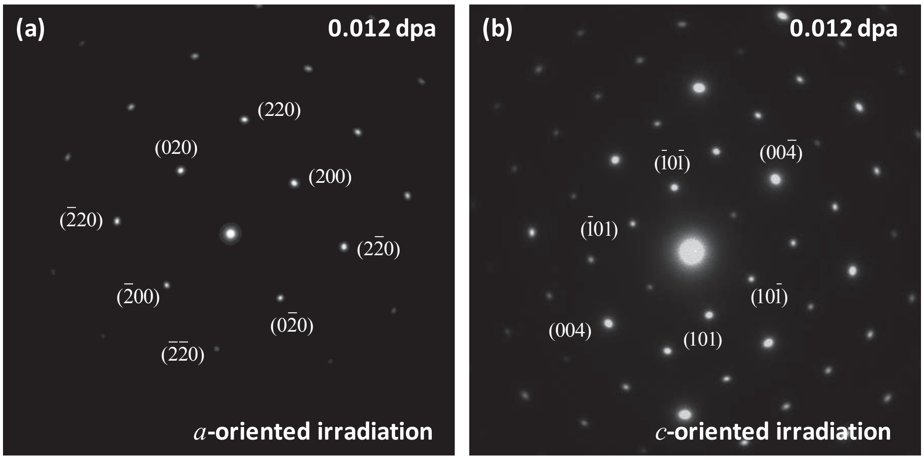

Figure 4-31: Electron diffraction pattern (200 kV) of the irradiated-damaged layer of *a*- and *c*-oriented irradiated powellites at 0.012 dpa; (camera length is 20 cm)

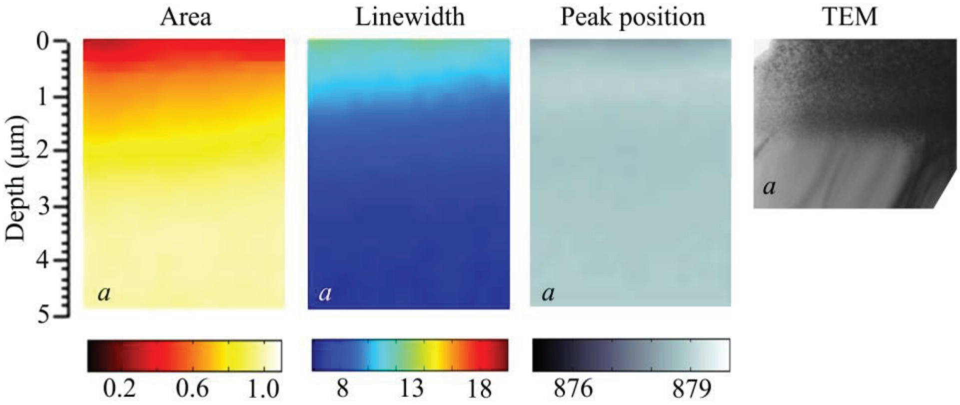

Figure 4-32: Comparison between Raman mapping on $\nu_1(A_g)$ mode (peak area, linewidth, and peak position) and TEM image of *a*-oriented irradiated powellite with 0.012 dpa

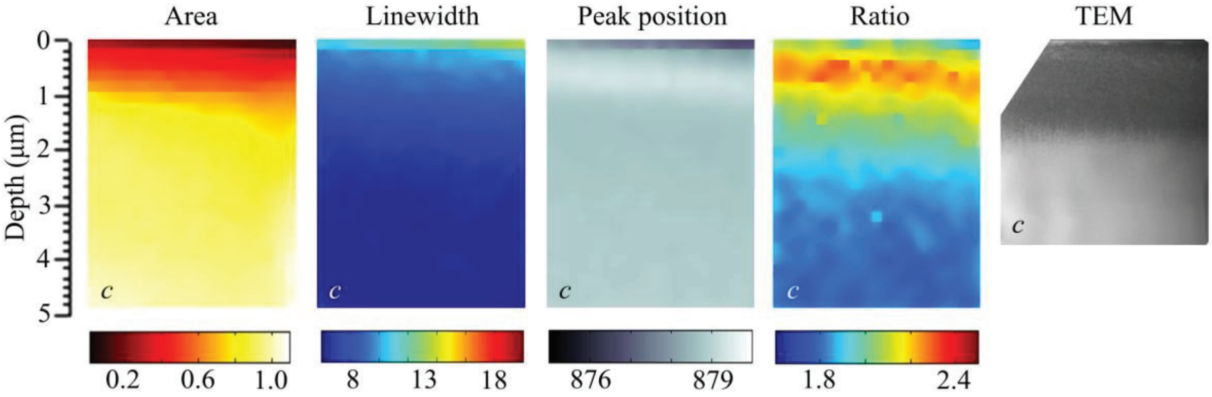

Figure 4-33: Comparison between Raman mapping on $\nu_1(A_g)$ mode (peak area, linewidth, peak position, and peak area ratio of $\nu_1(A_g)$ and $\nu_3(E_g)$) and TEM image of *c*-oriented irradiated powellite with 0.012 dpa

4.3.2.2 Irradiation-induced defects in high-dpa powellite (5.0 dpa)

Figure 4-34 and Figure 4-35 show the high magnified TEM bright-field and dark-field images of the FIB sections from *a*- and *c*-oriented irradiated powellite with 5.0 dpa, respectively. The imaging conditions are the same as those for low-dpa (0.012) samples. Electron diffraction patterns of the irradiated-damaged layer of powellites at 5.0 dpa are presented in Figure 4-36. Figure 4-37 and Figure 4-38 show the comparisons between Raman mapping on $\nu_1(A_g)$ mode (peak area, linewidth, and peak position) and the TEM images of *a*- and *c*-oriented irradiated powellite at 5.0 dpa, respectively.

According to the TEM images, the contrast produced by the local bending of powellite crystal planes shows that dislocations were generated in the irradiation- damaged layers after very high-fluence Ar implantations. Different from the previous case of low-dpa sample, *the main irradiation-induced damages in high-dpa powellite single crystal are dislocations*, indicating an increase in structural damage. Both the bright-field and dark-field images show the same range of irradiation-damaged layer in powellites. *The thickness of the irradiation-damaged layer shown by TEM is coherent with that detected by Raman mapping* (Figure 4-37).

As shown in Figure 4-34, the total defected layer is about 2.8 μm in thickness beneath the original surface for *a*-oriented irradiated powellite. It can be inferred that the damage level of the powellite structure varies with depth since the distribution and the concentration of dislocation in the defected layer are not homogeneous. Several specific regions can be estimated and distinguished according to the TEM images in Figure 4-34. The same as the low-dpa case, evident dose effect can be observed between the pristine part and the irradiation-damaged layer of powellite, following an evolution from non-damaged structure to *point defect clusters* in a very narrow range (marked as “A” in Figure 4-34, about 0.3 μm thick). In the neighboring narrow region (marked as “B”, about 0.4 μm thick) on the border, small and concentrated *dislocation loops* begin to appear in the powellite structure, representing an increasing damage. The increasing damage in the powellite structure from region A to B is also revealed by the Raman mapping (and profiles, Figure 4-17), which exhibits a gradual linewidth broadening in $\nu_1(A_g)$ mode due to the increasing structural disorder.

By comparison, the number of dislocations decreases in the middle of the defected layer (marked as “C”, about 1.0 μm thick), whereas in the region that is marked as “D” (about 0.7 μm thick), the number of dislocations increases again, consisting of small *dislocation* *networks*. Considering the Raman mapping, the observed linewidth of $\nu_1(A_g)$ mode reaches a plateau (Figure 4-17) in region C, which suggests that the structural disorder in this region is maintained in a certain level. The powellite structure becomes more disordered respecting to the more broadened linewidth in region D than that in region C.

Moreover, a very thin region (marked as “E”, about 0.4 μm thick) with very low contrast in the bright-field image can be seen on the surface of *a*-oriented irradiated powellite. However, many crystallized domain in short-range order (tens of nanometers) can be seen in the dark-field images in Figure 4-34, which indicates that the structure in region E becomes a state of so-called *mosaicity* [17, 18]. Mosaicity refers to crystal which is composed of very small mosaic crystal domains. Mosaicity is a long-range disorder without amorphization. It is confirmed that the mosaic region is the most damaged structure in irradiated powellite, from where the Raman spectra have the most broadened linewidth and weakest intensity, as shown in Figure 4-37.

Similar regions can be defined on the *c*-oriented irradiated powellite at 5.0 dpa, as shown in Figure 4-35. According to the Raman mapping, the linewidth profiles of $\nu_1(A_g)$ mode are more or less the same for both *a*- and *c*-oriented irradiated powellite with 5.0 dpa (Figure 4-22), indicating a similar evolution of structural disorder in the irradiation-damaged layers. In this case, there is no evident difference in structural damage between the two orientations.

It is important to point out that the powellite structure does not reach amorphous state (up to 5.0 dpa), which are both confirmed by Raman spectra and TEM diffraction patterns (Figure 4-36). No crystalline-to-amorphous transformation is found in the damaged layer.

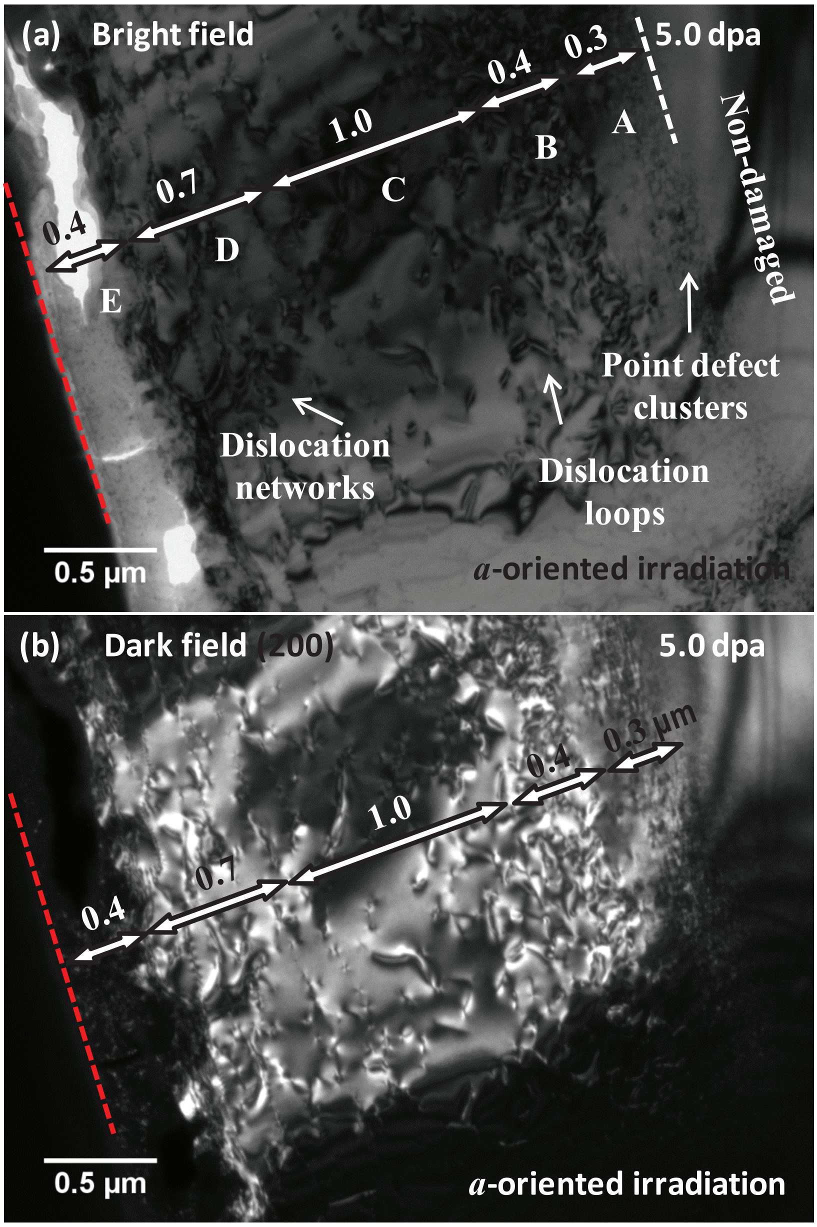

Figure 4-34: High magnified conventional TEM bright-field (a) and dark-field (b) images of FIB sections from *a*-oriented irradiated powellite with 5.0 dpa; zone axis is [001]; the bright-field image is collected from the central spot while the dark-field image is collected from the (200) spot; red dash lines indicate the original irradiated surface

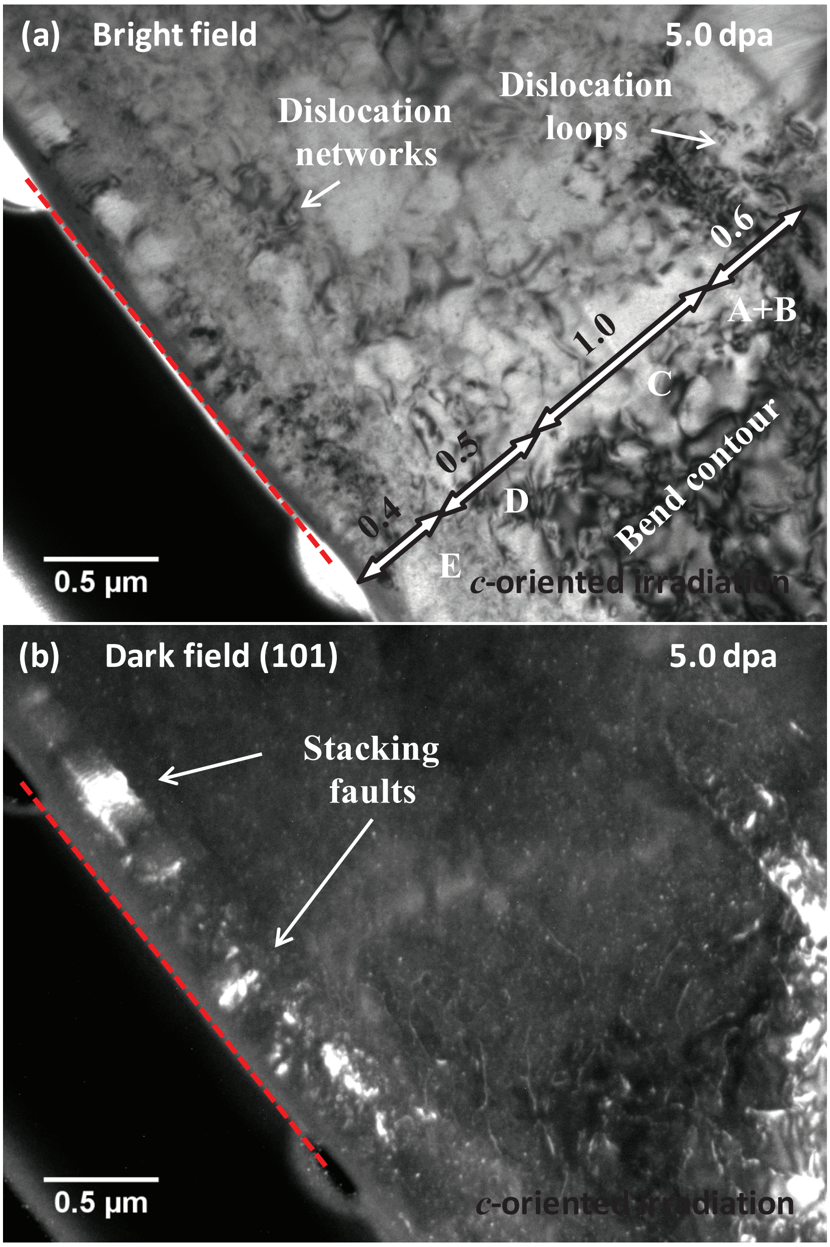

Figure 4-35: High magnified conventional TEM bright-field (a) and dark-field (b) images of FIB sections from *c*-oriented irradiated powellite with 5.0 dpa; zone axis is [010]; the bright-field image is collected from the central spot while the dark-field image is collected from the (101) spot; red dash lines indicate the original irradiated surface

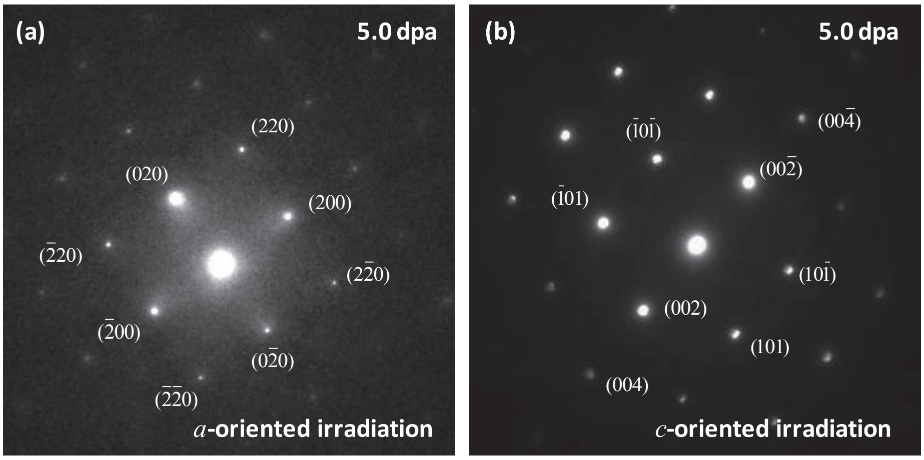

Figure 4-36: Electron diffraction pattern (200 kV) of the irradiated-damaged layer of *a*- and *c*-oriented irradiated powellites at 5.0 dpa; (camera length is 20 cm)

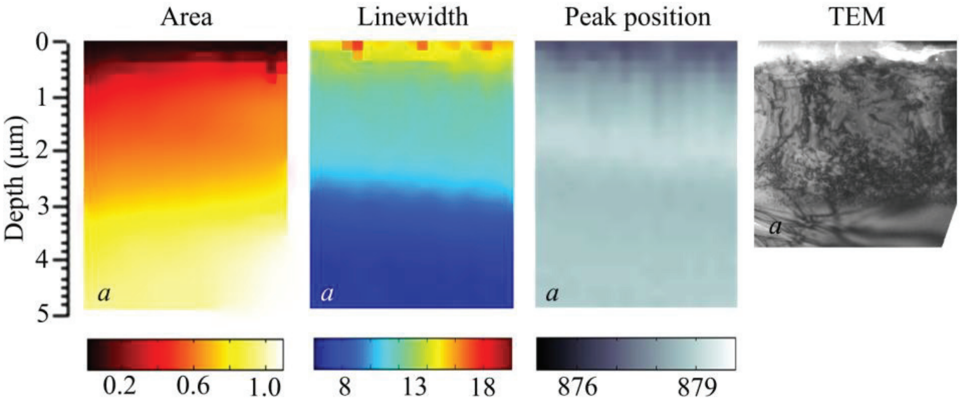

Figure 4-37: Comparison between Raman mapping on $\nu_1(A_g)$ mode (peak area, linewidth, and peak position) and TEM image of *a*-oriented irradiated powellite with 5.0 dpa

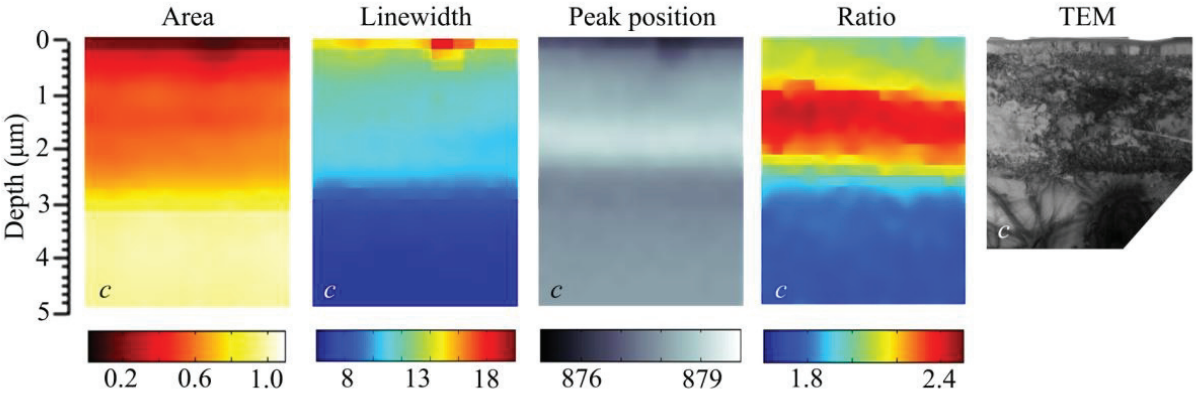

Figure 4-38: Comparison between Raman mapping on $\nu_1(A_g)$ mode (peak area, linewidth, peak position, and peak area ratio of $\nu_1(A_g)$ and $\nu_3(E_g)$) and TEM image of *c*-oriented irradiated powellite with 5.0 dpa

4.3.2.3 *Evolution of defects in the irradiated powellite with increasing irradiation fluence (dpa)*

A multi-step damage accumulation model was elaborated and developed by J. Jagielski [16, 19-21] to reproduce the damage accumulation behaviors observed in ion-irradiated crystals. Each stage is described by a simple accumulation of disorder. A new stage occurs when the current structure of the matrix is no longer characterized by the lowest free energy. Transformations are thus triggered by the destabilization of a given structure [20]. Here, *a two-step accumulation* (Figure 4-39 [20]) is proposed to interpret the evolution of powellite structure with increasing irradiation fluence (dpa) in this study.

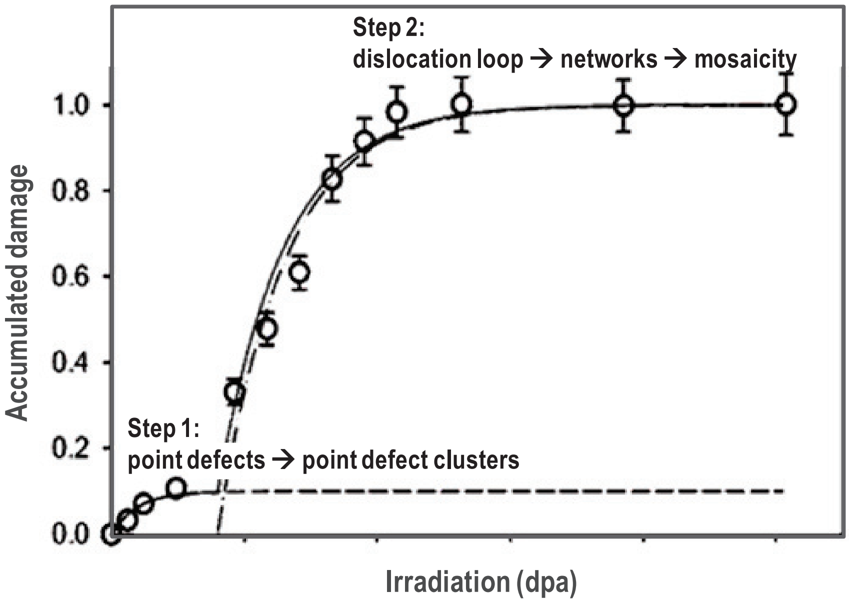

Figure 4-39: SiC irradiated by 160-keV Cs ions (two-step damage accumulation) [20]

At first, *point defects* (Frenkel pairs) are formed in unperturbed crystalline matrix due to collision between the implanted ion and the atoms in the lattice. At low irradiation fluence, point defects cluster are generated in the structure due to the accumulation of point defects. The interstitial atoms are likely to migrate to defect sinks (essentially the crystal surface), leaving vacancies in the damaged layer. The accumulation of vacancies leads to the formation of free volume within the crystal structure, resulting in the generation of high compressive stress. The surface of the crystal begins to swell in order to adapt the stress since it is not constrained by the bulk. Due to the fact that the crystal structure cannot indefinitely support continuously increasing stresses, *dislocations* (see the TEM images of 5.0-dpa powellite) are formed at high fluence to release the stress, which leads to the second step of damage accumulation in powellite. In the second step, the final state of accumulation of dislocation is *mosaicity* which is a structure with crystallized domain in short-range order. *Powellite does not reach amorphization*. The mosaicity appearing at the irradiated surface for 5.0-dpa powellite indicates the most disordered structure in the sample, which is consistent with the fact that the most broadened Raman linewidth were observed at the surface. Therefore, the evolution of powellite structure with increasing irradiation dose is proposed here according to the model, which follows from crystalline structure to crystalline structure with point defects, then to crystalline structure with dislocations, and finally to mosaicity (at 5.0 dpa).

As a combination of results from Raman and TEM, a relation among irradiation induced disorder, stress and defects in powellite is presented in Figure 4-40 (based on Figure 4-25 and Figure 4-26). As can be see, powellite structure is disordered in the region where point defects and defect clusters are formed. Meanwhile, compressive stress is generated in this corresponding region. A release of stress in powellite can be found in the region where dislocation forms.

It has to be pointed out that the damaged depths in powellite with different dpa are not always 3 μm. The characterizations of the damage depth by both Raman and TEM give consistent results which shows that the damaged layer in 5.0-dpa powellite is approximately 3 μm (2.8 μm and 2.5 μm for *a*- and *c*-oriented irradiated powellite, respectively), whereas that in 0.012-dpa one is actually much less than 3 μm (1.6μm and 1.7 μm for *a*- and *c*-oriented irradiated powellite, respectively). It is quite interesting to know why there is no damage in the depth range of 1.6 to 3 μm in 0.012-dpa powellite. It cannot be excluded that there are some errors of SRIM simulation on irradiation in single crystal or some addition effects due to multi-energy implantation (0.9, 2, 3, 5, and 7 MeV). However, some other possibilities should also be considered for the interpretation. According to the calculation of stopping power in Figure 2-21, the damage in powellite is mainly caused by electronic energy loss. For irradiation with 2-, 3-, 5-, and 7-MeV energy, the nuclear energy loss effect in powellite is very small; whereas, for 0.9-MeV irradiation, the nuclear energy loss is comparable with electronic energy loss. In the case of 0.012 dpa, the fluence of Ar-ion beam with each energy is very low (Table 2-8). The damage due to nuclear energy loss would be too small to contribute significantly to the modification of the crystal structure. By comparison, in the case of 5.0 dpa, very high fluences of Ar ions were performed on powellite. The nuclear energy loss can no longer be negligible. To figure out clearly the reason behind this phenomenon, more experiments and analyses are required, for example, characterizing the Ar deposition in the multi-energy irradiated powellite, performing single-energy irradiations for comparison, calculating the electronic stopping power at different depth of powellite, conducting TEM measurements on the other irradiated powellites (between 0.012 and 5.0 dpa) to find out at which dpa the structure is trigged to the second step, etc.

Moreover if the actual damaged depths are taken into account, some revisions have to be performed on the calculation of the percentages of powellite swelling (Table 4-5). It is surprising to find out that the percentages of powellite swelling for very low dpa (0.012) are not very different from that for high dpa (5.0), in spite of the extremely different defect types found in these two samples. It is suggested that point defect clusters and perhaps punctual defects (refers to vacancies, interstitial atoms) formed in powellite at very low dpa has a predominant contribution to swelling. By comparison, dislocations formed in powellite only help to release the excessive high compressive stress in the structure but do not have very significant contribution to the swelling. To further study, high resolved TEM could be useful for the characterization of local structure properties and of lattice parameters, which can provide more detail information of the irradiation-induced damage and modification in powellite.

Table 4-5: Percentages of swelling in *a*- and *c*-oriented irradiated powellite based on swelling measurement and TEM observation

DPA	Swelling (nm)	Damaged depth from TEM (μm)	Swelling (%)
a-oriented			
0.012	33	1.6	2.1
5.0	64	2.8	2.3
c-oriented			
0.012	23	1.7	1.4
5.0	43	2.5	1.7

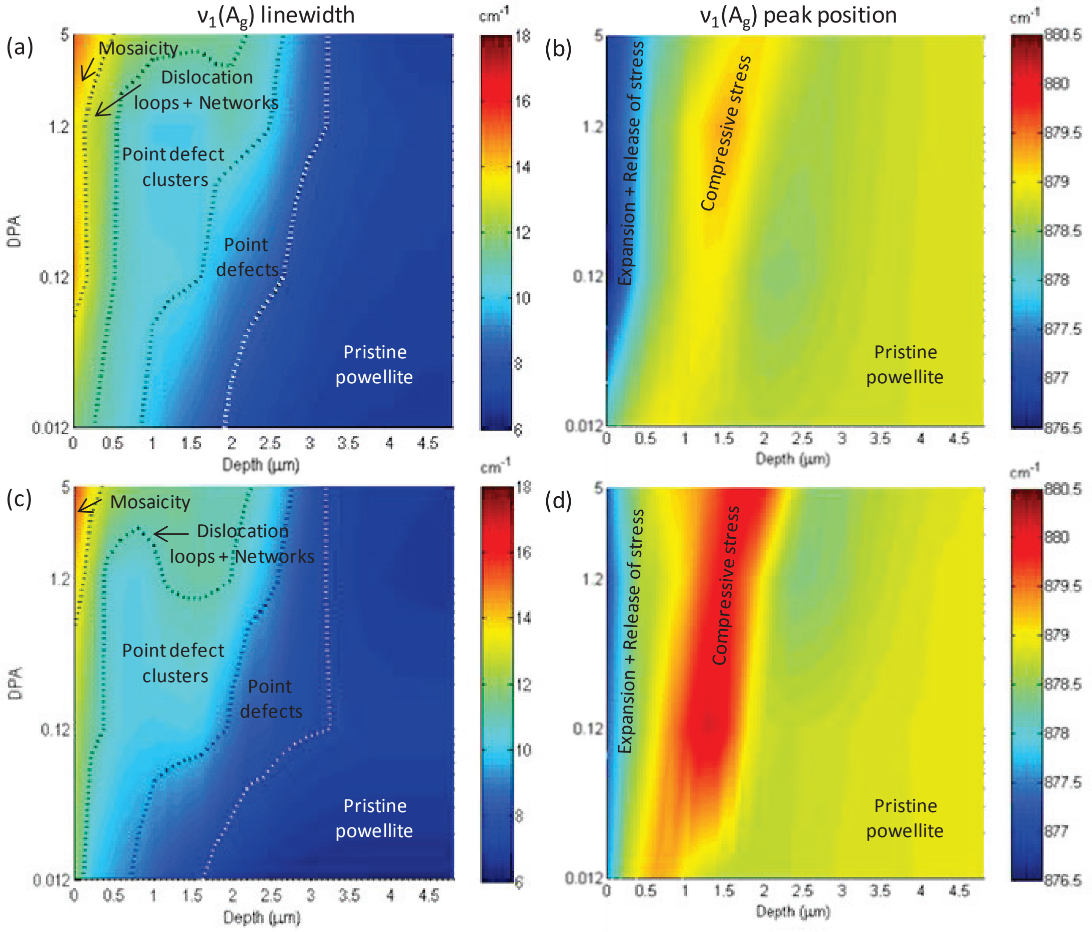

Figure 4-40: Relation among irradiation induced disorder, stress and defects in powellite; Raman $\nu_1(A_g)$ linewidth and peak position in function of depth and dpa for *a*-oriented (a-b) and *c*-oriented (c-d) irradiated powellites; dash lines are contours

Summary of this subsection:

TEM was used to characterize the defects in the powellite structure induced by Ar irradiations. For low-dpa (0.012) powellites, the main irradiation-induced damages are point defect clusters; while for high-dpa (5.0) ones, the main damages become dislocations. The ranges of the irradiation-damaged layer given by TEM are in agreement with that shown by Raman measurements (1.6 µm and 2.8 µm for a-oriented irradiated powellite at 0.012 and 5.0, respectively; 1.7 µm and 2.5 µm for c-oriented irradiated powellite at 0.012 and 5.0, respectively). Mosaicity appearing at the irradiated surface for 5.0-dpa powellite indicates the most disordered structure in the sample, which is consistent with the fact that the most broadened Raman linewidth were observed at the surface. A two-step damage accumulation is proposed to interpret the evolution of powellite structure with increasing irradiation dpa. It is confirmed by TEM that powellite does not reach amorphization within the studied dpa range.

4.4 Irradiation-induced modification of local structural environment by luminescent properties of Eu^{3+}

In this section, emissions[16] of Eu^{3+}: $^5D_0$ → $^7F_1$ transitions were used to briefly investigate the structure local environment change in the irradiation-damaged layer of powellite at 0.012 and 5.0 dpa.

4.4.1 Eu^{3+} sites in the studied pristine powellite structure

In a perfect powellite structure, Eu^{3+} ions substitute the Ca^{2+} site which has a S_4 point symmetry. The studied powellite single crystal is doped with 2 mol% Eu, 0.1 mol% Nd, and 2.1 mol% Na. Due to the influence of the codoping Na^+ (as compensator) and Nd^+ ions as well as the lattice defects generated during crystal growth, the lattice environment around Eu^{3+} is slightly disordered which leads to lower site symmetry, such as C_{2v} [22, 23]. For pristine powellite samples, the presence of C_{2v} sites in the structure can be proved by selectively exciting the Eu^{3+}: $^7F_0$ → $^5D_0$ transition which is generally forbidden under S_4 symmetry but allowed for the C_{2v} one. Figure 4-41 shows the emission spectra of Eu^{3+}: $^5D_0$ → $^7F_1$ under three main selected excitations that found in the studied pristine powellite at 77 K, including 577.8, 579.3, and 579.7 nm in wavelength.

Since neither the $^5D_0$ nor the $^7F_0$ levels of Eu^{3+} is split by the crystal field ($J = 0$), the detected number of $^7F_0$ → $^5D_0$ transitions corresponds to the number of C_{2v} sites in the powellite structure [24]. For the studied pristine powellite, *three main C_{2v} sites were found based on site-selective excitation* (Site 1 to 3, Table 4-6). The $^7F_1$ level of Eu^{3+} splits into two sub-Stark levels under S_4 symmetry, whereas it is completely unfolded ($2J+1$) under C_{2v} symmetry, resulting in three sub-Stark levels [25, 26]. By selectively exciting each C_{2v} sites ($^7F_0$ → $^5D_0$), the corresponding $^5D_0$ → $^7F_1$ transitions were observed. The three sub-Stark levels of $^5D_0$ → $^7F_1$ for each C_{2v} site are listed in Table 4-6 according to the emission spectra in Figure 4-41. An additional peak at 584.7 nm was observed when Site 3 was excited. This can be ascribed to energy transfer between two different C_{2v} sites (Site 1 and 3). The energy diagram (Figure 4-42) of $^7F_0$, $^7F_1$, and $^5D_0$ for each C_{2v} site can be figured out by calculating the energy difference between excited states and the ground state through emission wavelength.

---

[16] The emission spectra of Eu^{3+}: $^5D_0$ → $^7F_{0-4}$ is presented in Subsection 1.3.1.3

Schematic diagram of Eu environment in powellite structure is shown in Figure 4-43. It is reasonable to consider that, substitutions of Na for the first, the second, and the third nearest neighboring Ca sites of Eu are most likely to affect the Eu environment, resulting in a reduce of site symmetry (from S_4 to C_{2v}).

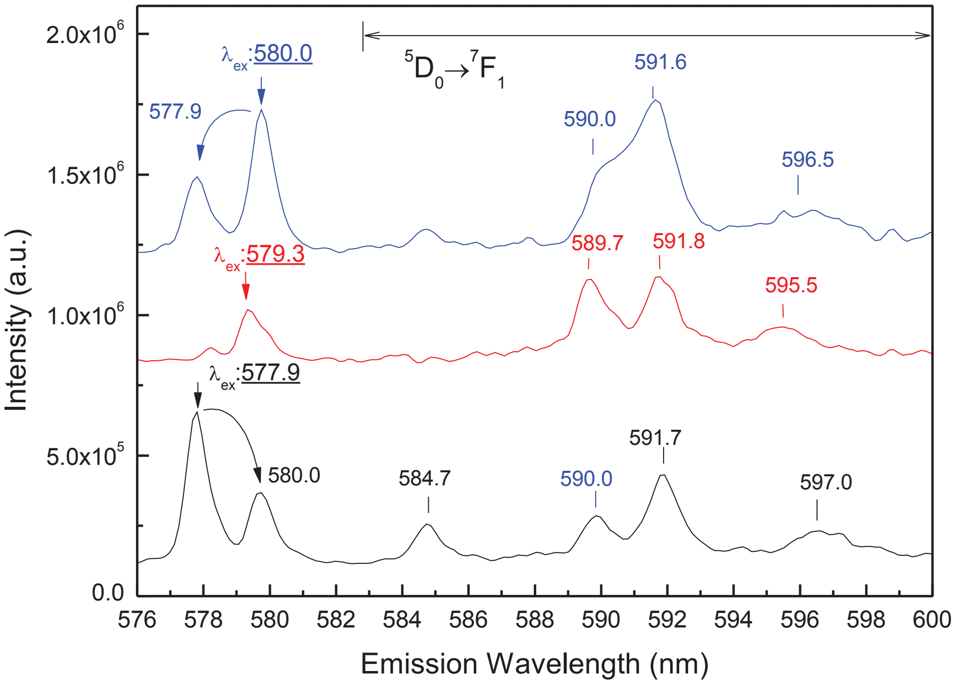

Figure 4-41: Emission spectra of Eu^{3+}: $^5D_0$ → $^7F_{0,1}$ in the pristine powellite under selected excitation (underlined) of 579.7 (Site 1), 579.3 (Site 2), and 577.8 (Site 3) nm at 77 K

Table 4-6: Three main C_{2v} sites and their corresponding Eu^{3+}: $^5D_0$ → $^7F_1$ transition in the studied pristine powellite structure

Symmetry	Selective excitation (nm)	Emission(nm)		
C_{2v}	$^5F_0$ → $^7D_0$	$^5D_0$ → $^7F_1$		
Site 1	580.0	590.0	591.6	596.5
Site 2	579.3	589.7	591.8	595.5
Site 3	577.9	584.7	591.7	597.0

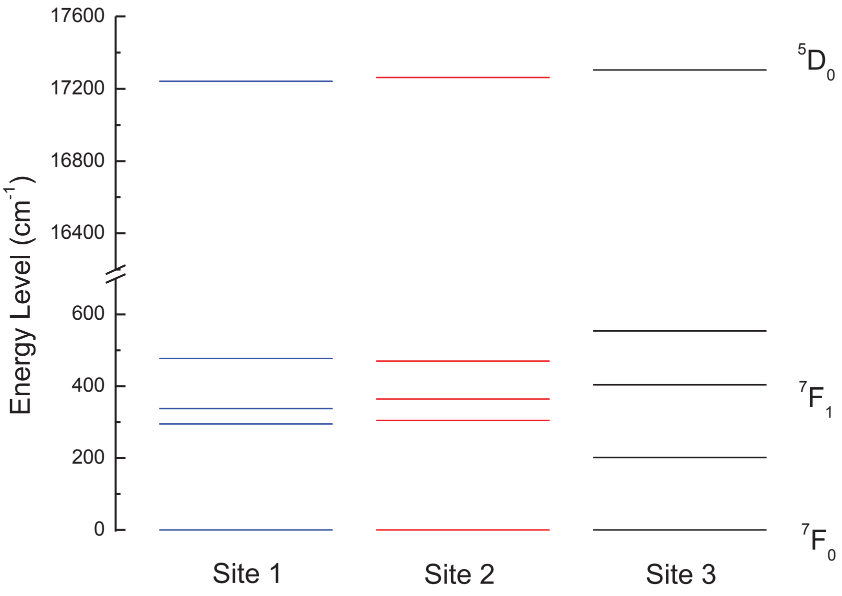

Figure 4-42: Energy levels of Eu^{3+} $^7F_0$, $^7F_1$, and $^5D_0$ for each C_{2v} site in the pristine powellite

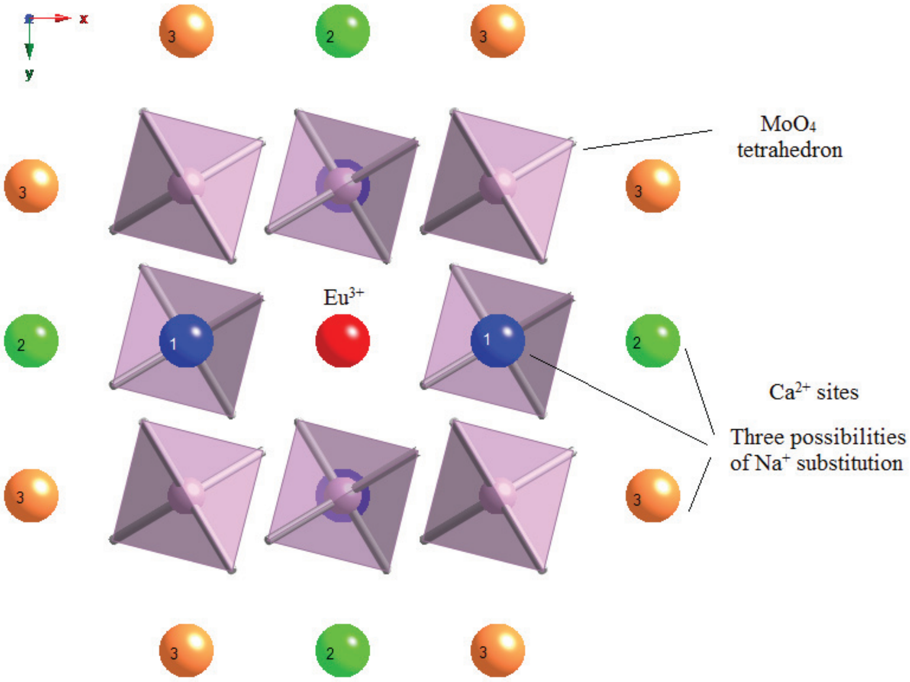

Figure 4-43: Schematic diagram of Eu (central red atom) environment in powellite structure (view from [001]); x and y axes are identical to the two *a*-axes of powellite; the numbers on the atoms indicate the first, the second, and the third nearest neighboring Ca sites of Eu

Figure 4-44 shows the polarized emission spectra of Eu^{3+}: $^5D_0$ → $^7F_{0,\ 1}$ in pristine powellite under 532 nm CW excitation at room temperature (300 K). α, σ, and π on the figure refer to different polarized spectra[17] which help to separate the transitions from $^5D_0$ to different sub-Stark levels of $^7F_1$ (according to the selection rules). Eu^{3+} in both S_4 and C_{2v} sites can be excited from the ground state to $^5D_1$ by using a 532-nm laser. Accordingly, the resulted emission spectrum is contributed by the emission from Eu^{3+} in all the sites in the sample. *Seven different emission peaks were observed within the* Eu^{3+}*:* $^5D_0$ → $^7F_1$ *range.*

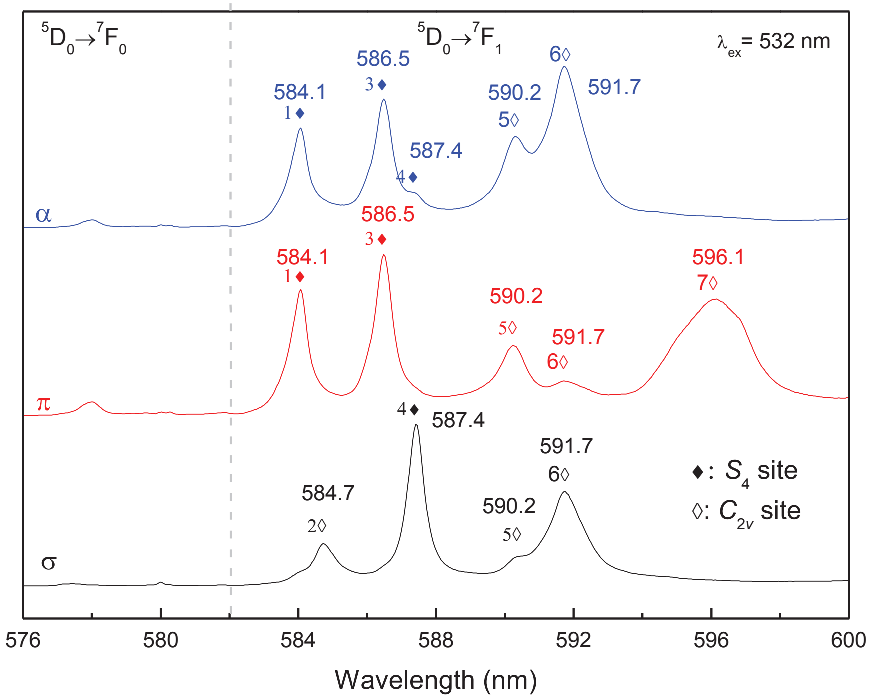

Figure 4-44: Polarized steady-state emission spectra of Eu^{3+}: $^5D_0$ →$^7F_{J\ (J = 0,\ 1)}$ in powellite under continuous 532 nm excitation at 300 K (♦: S_4 site; ◊: C_{2v} site); α, σ, and π refer to different polarized spectra

Eu^{3+} in S_4 sites cannot be excited by the $^7F_0$ → $^5D_0$ site-selective excitation since this transition is forbidden under S_4 symmetry. Here, it is assumed that the emission peaks in the $^5D_0$ → $^7F_1$ range which was not detected by selective excitation can be assigned to S_4 sites (♦ for S_4 sites and ◊ for C_{2v} sites in Figure 4-44). It is difficult to distinguish different S_4 sites if more than two S_4 sites exist simultaneously in the sample. More experiments are required for further investigation. Based on the assignment of different sites, the intensity

---

[17] For powellite,
α-spectrum: emission propagates along c-axis with polarization along a-axis
σ-spectrum: emission propagates along a-axis with polarization along a-axis
π-spectrum: emission propagates along a-axis with polarization along c-axis

ratio of different emission peaks in the $^5D_0 \rightarrow {}^7F_1$ range is calculated to follow the change of S_4 and C_{2v} sites in irradiated powellites (Subsection 4.4.2).

4.4.2 Luminescence properties of Eu³⁺ in irradiated powellites

Luminescent mapping of irradiated powellite were conducted on the FIB sections (the same as for Raman measurements) with a continuous 473-nm laser. The *c*-oriented irradiated powellite at 0.012 and 5.0 dpa are used as examples for discussion, since all 7 emission peaks in the $^5D_0 \rightarrow {}^7F_1$ range are available to observe in this orientation.

Figure 4-45 and Figure 4-46 are emissions of Eu^{3+}: $^5D_0 \rightarrow {}^7F_{0,1}$ transitions at different depth of FIB section from *c*-oriented irradiated powellite at 0.012 and 5.0 dpa, respectively. The emission peaks were assigned to different symmetry (S_4 and C_{2v}) based on the analysis in Subsection 4.4.1. Moreover, the luminescence spectra were fit with 7 Gaussian profiles which correspond to the 7 emission peaks in the $^5D_0 \rightarrow {}^7F_1$ range, in order to compare the ratio of peak areas which were assigned to the two symmetries.

First of all, *quenching* of Eu^{3+} luminescence was observed due to defected structure in powellite. An image of the irradiated sample under UV lamp (254 nm) in Appendix A.11 gives a direct view of this quenching effect. As shown in Figure 4-45 and Figure 4-46, the quenching effect on 5.0-dpa powellite is much more significant than the low-dpa (0.012) one since the structure is more damaged by Ar irradiation. As already been seen by Raman and TEM, the most damaged structure appears on the irradiated surface.

Ratio of peak areas between the main C_{2v} peaks (the 5th to the 7th peaks on the Figure 4-45 and Figure 4-46) and the S_4 peak at 584.1 nm (1st) are shown in Figure 4-47. Since the emission peaks in $^5D_0 \rightarrow {}^7F_1$ range can be assigned either S_4 or C_{2v} symmetry, the change in area ratio between S_4 peak and C_{2v} peak can provide information about the change in number of a specific site.

From Figure 4-47, the area ratios of the 6th peak and the 7th peak to the S_4 peak increase in the irradiation-damaged layer of the low-dpa (0.012) powellite, whereas they reduce in the damaged layer of the high-dpa (5.0) sample. However, the ratio of the 5th peak to the 1st one always decreases (basically) at 0.012 and 5.0 dpa. According to TEM measurement in Section 4.3, the main damage in low-dpa (0.012) powellite is point defect cluster while that in high-dpa (5.0) powellite is dislocations. Therefore, it is suggested that, comparing with the S_4 site(s) represented by 1st peak, the C_{2v} site(s) represented by the 6th and 7th emission peaks increase when there are only point defect clusters in the structure. On the contrary, these sites decrease when dislocations are formed in the powellite structure. However, the C_{2v} site(s) represented by the 5th emission peak always reduce when the structure is damaged.

More experiments are required to further study the change in the ratio between different sites. Site-selective excitation is a suitable tool for this investigation. So far, it is not easy to perform site-selective excitation measurement on the studied irradiated powellite under confocal condition. This could be a prospect of studies in the next step.

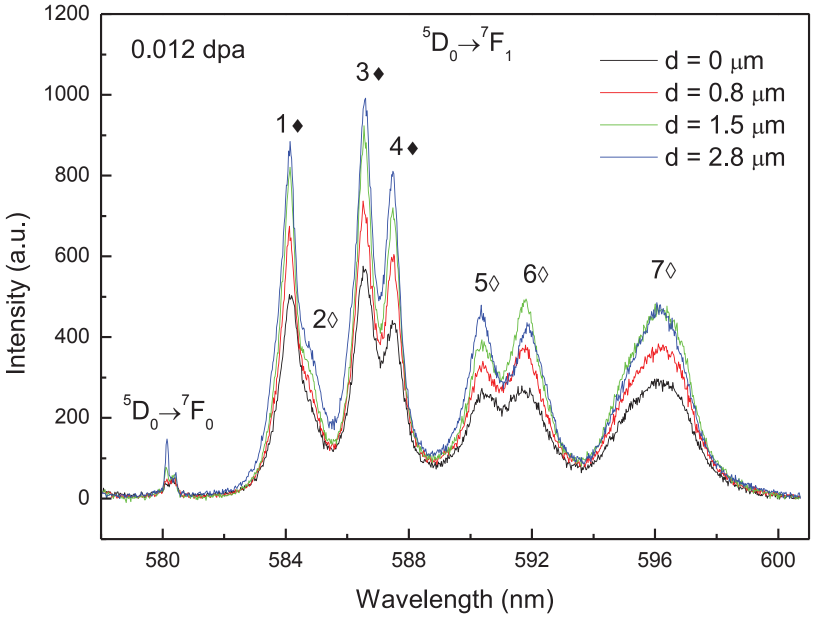

Figure 4-45: Steady-state emissions of Eu^{3+}: $^5D_0$ → $^7F_{0,1}$ transitions at different depth of FIB section from *c*-oriented irradiated powellite at 0.012 dpa (♦ for S_4 and ◊ for C_{2v}); Excitation 473 nm (continuous)

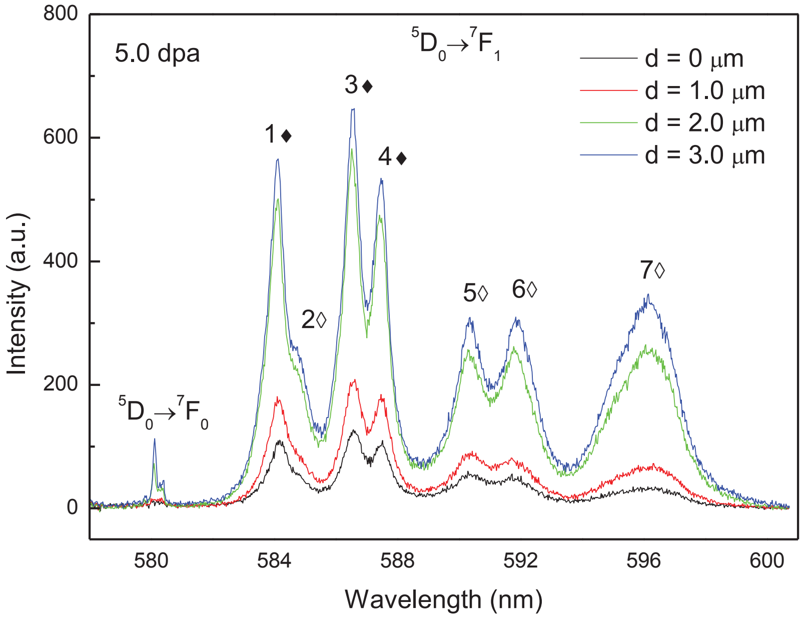

Figure 4-46: Steady-state emissions of Eu^{3+}: $^5D_0$ → $^7F_{0,1}$ transitions at different depth of FIB section from *c*-oriented irradiated powellite at 5.0 dpa (♦ for S_4 sites and ◊ for C_{2v} sites); Excitation 473 nm (continuous)

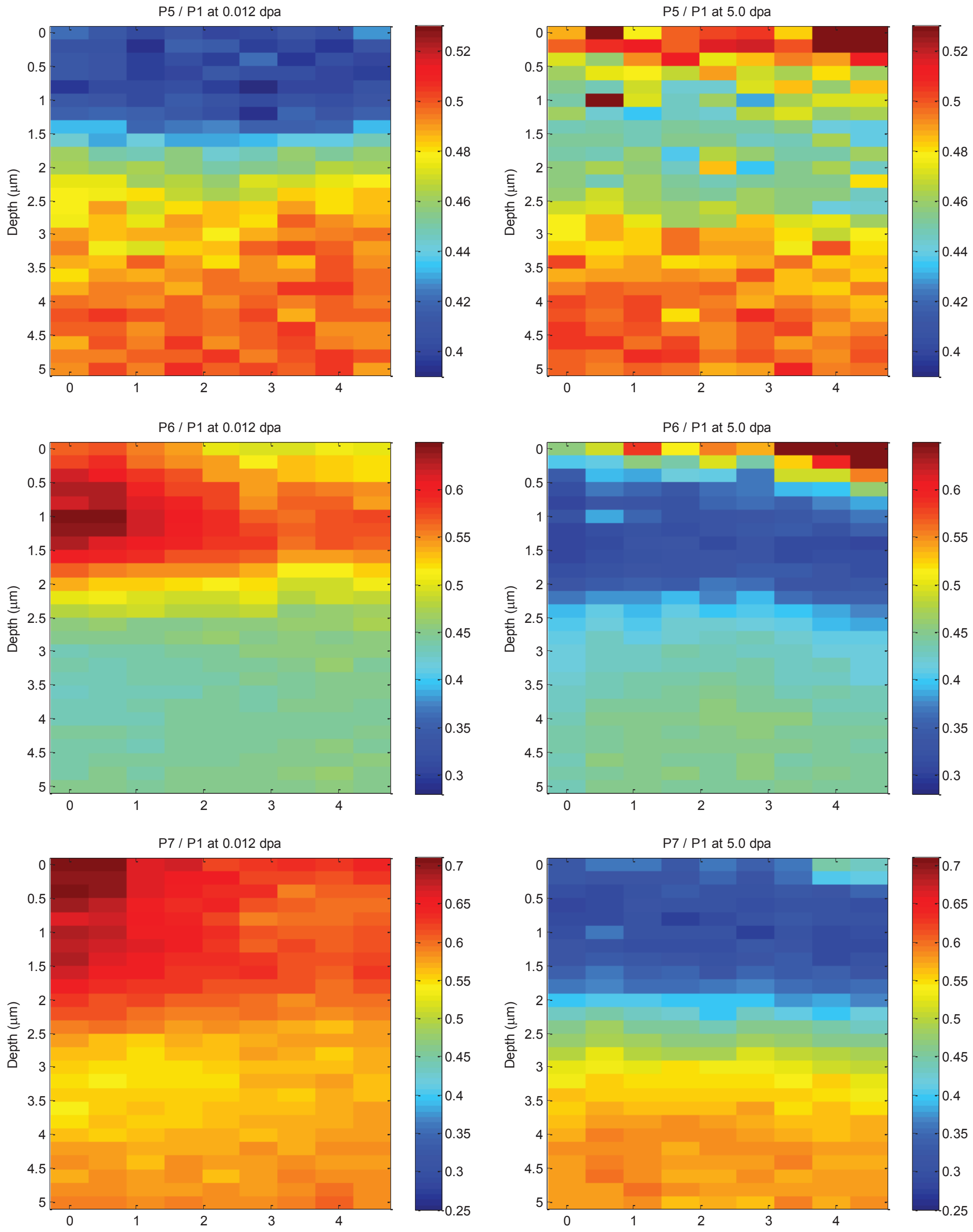

Figure 4-47: Ratio of peak areas between the main C_{2v} peaks (the 5th to the 7th peaks) and the S_4 peak at 584.1 nm (1st) for irradiated powellite at low (0.012) and high (5.0) dpa; the mapping steps 0.2 μm in depth direction and 0.5 μm in lateral direction;colorbars indicate the peak ratios

4.5 Conclusion

The macroscopic swelling of powellite after irradiation was determined by optical interferometry. The modifications of powellite structure in medium-range order due to irradiation were investigated by Raman spectroscopy. Irradiation-induced defects are characterized by using TEM. Finally, luminescent properties of Eu^{3+} were used to probe the change of local lattice environment in powellite structure.

Swelling was observed on the powellite surface after exposure under Ar irradiations. The irradiation-induced swelling of powellite crystal increases with dpa (from 0.012 to 1.2) at first and reaches saturation after 1.2 dpa. The swelling is more effective along *a*-axis than along *c*-axis of powellite crystal. The saturation values of swelling are 2.0 % along *a*-axis and 1.3 % along *c*-axis (over an irradiated thickness of 3-μm), respectively. The irradiation-induced unit-cell volume change of powellite single crystal was estimated based on the swelling along *a*- and *c*-axes, which shows a low saturation value of about 5.4 %. Stresses in the surrounded glass matrix induced by powellite swelling are higher in *a*-axis (maximum 1.96 GPa) than in the *c*-one (maximum 1.12 GPa). These moderate stresses are in the range of elastic region of borosilicate and can possibly be tolerated without inducing cracks.

A damaged layer in irradiated powellite was observed by Raman mapping, represented by decrease in Raman peak area, broadening in linewidth, and shift of peak position. The thickness of irradiation-damaged layer increases as the Ar irradiation dose rises from 0.012 to 1.2 dpa, which indicates an expansion of the affected layer in bulk powellite crystal. The thickness of the irradiation-damaged layer becomes constant (saturated) after 1.2 dpa.

The most disordered structure always appears on the irradiated surface of powellite due to the migration of irradiation-induced defects from the interior of the structure to the surface. Moreover, the irradiation-induced disorder in powellite does not depend on crystal orientation, namely, no significant anisotropic effect of irradiation- induced disorder.

Anisotropic effect in the lattice volume change was observed along two crystallographic axes (*a*- and *c*-axes) by comparing the depth profile of $\nu_1(A_g)$ peak position. Both expansion and compression of the structure exist in the irradiation-affected layer. The irradiation-damaged layer has less compression and more expansion for *a*-oriented irradiated powellite comparing with the *c*-one, which is positive correlated to the fact of more swelling in *a*-orientation. Irradiation can induce anisotropic compressive stress in powellite. It is shown that *c*-orientation of powellite can endure more stress in the structure than the *a*-one. The depth of the compressive-stressed region increases with increasing dpa (from 0.012 to 5.0). Particularly, for *a*-orientated irradiated powellite, delamination takes place close to the location where the maximum compressive stress is formed.

TEM was used to characterize the defects in the powellite structure induced by Ar irradiations. It is confirmed both by Raman and TEM that powellite does not reach amorphization within the studied dpa range. For low-dpa (0.012) powellites, the main irradiation-induced damages are point defect clusters; while for high-dpa (5.0) ones, the main damages become dislocations. The ranges of the irradiation-damaged layer given by TEM are in agreement with that shown by Raman measurements. The mosaicity appearing at the irradiated surface for 5.0-dpa powellite indicates the most disordered structure in the sample, which is consistent with the fact that the most broadened Raman linewidth were observed at the surface. A two-step damage accumulation is proposed to interpret the evolution of powellite structure under irradiation, which is basically consistent with the results of Raman and TEM. Evolution of the powellite structure with increasing irradiation dose follows from crystalline structure to point defects, then to dislocations, and finally to mosaicity (at 5.0 dpa). The formation of dislocation in powellite participates the release of excessive high compressive stress.

In addition, the quenching of Eu^{3+} emission also indicates the defect level of the irradiated powellites structure. Moreover, the change in ratio of C_{2v} sites and S_4 site(s) is related to different defect types in the damaged structure. For further study, site-selective excitation measurement on irradiated powellite under confocal condition could be useful to follow the modification of C_{2v} and S_4 sites in function of dpa.

Reference

1. Ewing, R.C., W.J. Weber, and F.W. Clinard Jr, *Radiation effects in nuclear waste forms for high-level radioactive waste.* Progress in Nuclear Energy, 1995. **29**(2): p. 63-127.
2. Weber, W.J., et al., *Radiation effects in crystalline ceramics for the immobilization of high-level nuclear waste and plutonium.* Journal of Materials Research, 1998. **13**(6): p. 1434-1484.
3. Weber, W.J., *Ingrowth of Lattice-Defects in Alpha Irradiated Uo2 Single-Crystals.* Journal of Nuclear Materials, 1981. **98**(1-2): p. 206-215.
4. Mendoza, C., *Caractérisation et comportement sous irradiation de phases powellites dopées terres rares: applications au comportement à long terme de matrices de confinement de déchets nucléaires*, 2010, Université Claude Bernard-Lyon I.
5. *Material Properties Database*, 2013: http://www.makeitfrom.com/material-data/?for=Borosilicate-Glass.
6. Chocron, S., et al., *Characterization of Borosilicate Glass Through Confined Compression Testing with Numerical Validation*, 2009, DTIC Document.
7. Li, P., Q. Peng, and Y. Li, *Dual-Mode Luminescent Colloidal Spheres from Monodisperse Rare-Earth Fluoride Nanocrystals.* Advanced Materials, 2009. **21**(19): p. 1945-1948.
8. Porto, S.P.S. and J.F. Scott, *Raman Spectra of Cawo4 Srwo4 Camoo4 and Srmoo4.* Physical Review, 1967. **157**(3): p. 716-719.
9. Hazen, R.M., L.W. Finger, and J.W.E. Mariathasan, *High-Pressure Crystal-Chemistry of Scheelite-Type Tungstates and Molybdates.* Journal of Physics and Chemistry of Solids, 1985. **46**(2): p. 253-263.
10. Liegeois.M and P. Tarte, *Vibrational Studies of Molybdates, Tungstates and Related Compounds .2. New Raman Data and Assignments for Scheelite-Type Compounds.* Spectrochimica Acta Part a-Molecular Spectroscopy, 1972. **A 28**(11): p. 2037-&.
11. Christofilos, D., G.A. Kourouklis, and S. Ves, *A high pressure Raman study of calcium molybdate.* Journal of Physics and Chemistry of Solids, 1995. **56**(8): p. 1125-1129.
12. Errandonea, D. and F.J. Manjón, *Pressure effects on the structural and electronic properties of ABX4 scintillating crystals.* Progress in Materials Science, 2008. **53**(4): p. 711-773.
13. Ferrari, A.C., *Raman spectroscopy of graphene and graphite: Disorder, electron–phonon coupling, doping and nonadiabatic effects.* Solid State Communications, 2007. **143**(1–2): p. 47-57.
14. Navarro-Contreras, H., et al., *Shallow to deep transformation of Se donors in GaSb under hydrostatic pressure.* Physical Review B, 1999. **59**(12): p. 8003-8007.
15. Senyshyn, A., et al., *Thermal properties of CaMoO4: Lattice dynamics and synchrotron powder diffraction studies.* Physical Review B, 2006. **73**(1).

16. Jagielski, J. and L. Thome, *Multi-step mechanism of damage accumulation in irradiated crystals.* Nuclear Instruments & Methods in Physics Research Section B-Beam Interactions with Materials and Atoms, 2008. **266**(8): p. 1212-1215.
17. Seydoux-Guillaume, A.M., et al., *An XRD, TEM and Raman study of experimentally annealed natural monazite.* Physics and Chemistry of Minerals, 2002. **29**(4): p. 240-253.
18. Weikusat, C., et al., *Raman study of apatite amorphised with swift heavy ions under various irradiation conditions.* Physics and Chemistry of Minerals, 2011. **38**(4): p. 293-303.
19. Jagielski, J. and L. Thome, *Accumulation of radiation damage in spinel crystals: Quantitative analysis and interpretation of RBS/C data.* Nuclear Instruments & Methods in Physics Research Section B-Beam Interactions with Materials and Atoms, 2007. **261**(1-2): p. 1155-1158.
20. Jagielski, J. and L. Thome, *Damage accumulation in ion-irradiated ceramics.* Vacuum, 2007. **81**(10): p. 1352-1356.
21. Jagielski, J., et al., *Analysis of the accumulation of radiation damage in selected crystals.* Nuclear Instruments & Methods in Physics Research Section B-Beam Interactions with Materials and Atoms, 2008. **266**(12-13): p. 2902-2905.
22. Binnemans, K. and C. GorllerWalrand, *Application of the Eu3+ ion for site symmetry determination.* Journal of Rare Earths, 1996. **14**(3): p. 173-180.
23. Schmidt, M., et al., *Characterization of powellite-based solid solutions by site-selective time resolved laser fluorescence spectroscopy.* Dalton Transactions, 2013. **42**(23): p. 8387-8393.
24. Huang, J., J. Loriers, and P. Porcher, *Spectroscopic properties of some Eu3+ doped scheelite-related rare earth sesquimolybdates and sesquitungstates.* Journal of Solid State Chemistry, 1983. **48**(3): p. 333-345.
25. Nazarov, M., et al., *Optical lines in europium–terbium double activated calcium tungstate phosphor.* Physics Letters A, 2004. **330**(3): p. 291-298.
26. Lempicki, A., H. Samelson, and C. Brecher, *The europium ion in octacoordinate crystal fields: Symmetry, potentential, and level splittings.* Journal of Molecular Spectroscopy, 1968. **27**(1): p. 375-401.

General conclusion

Fractionation of fission products in Mo-rich borosilicate glass-ceramic containing powellite ($CaMoO_4$) crystalline phase and the behavior of rare earth (Eu, Nd) doped powellite single crystal under irradiations were studied in this thesis.

According to the elemental analysis techniques (µLIBS, LA-ICP-MS, and EMPA), it is demonstrated that, by means of crystallization in borosilicate, Mo is easily trapped as $CaMoO_4$ which can also enrich REEs (surrogates of radioactive minor actinides) and Sr from the initial glass. About 55 % Mo and 10 % Ca of the initial glass are crystallized as powellite with an incorporation of 10 % Pr, 17 % La, and 26 % Sr. The similarity in effective ionic radii of Sr and REEs to Ca allows them to substitute the Ca site and be incorporated in powellite. On the contrary, Cs (another radioactive source) completely remains in the residual glass due to the mismatch of ionic radii.

The ability of powellite to incorporate Sr and REEs can be improved by increasing the crystallization in borosilicate. It is suggested that irradiation sources like Sr and minor actinides can be enriched using the Mo-rich powellite crystalline phase and be immobilized within a double-barrier environment. Accordingly, borosilicate glass-ceramic form provides a solution for both the Mo-storage problem arising from the UMo spent fuel and the reduction of matrix volume for accommodation of radioactive nuclear waste.

Swelling was observed on the powellite surface after exposure under Ar irradiations. The irradiation-induced swelling of powellite crystal increases with dpa (from 0.012 to 1.2) at first and reaches saturation after 1.2 dpa. The swelling is more effective along *a*-axis than along *c*-axis of powellite crystal. The saturation values of swelling are 2.0 % along *a*-axis and 1.3 % along *c*-axis (over an irradiated thickness of 3 µm), respectively. The irradiation-induced unit-cell volume change of powellite single crystal was estimated based on the swelling along *a*- and *c*-axes, which shows a low saturation value of about 5.4 %. Stresses in the surrounded glass matrix induced by powellite swelling are higher in *a*-axis (maximum 1.96 GPa) than in the *c*-one (maximum 1.12 GPa). These moderate stresses are in the range of elastic region of borosilicate and can possibly be tolerated without inducing cracks.

A damaged layer in irradiated powellite was observed by Raman mapping, represented by decrease in Raman peak area, broadening in linewidth, and shift of peak position. The thickness of irradiation-damaged layer increases as the Ar irradiation dose rises from 0.012 to 1.2 dpa, which indicates an expansion of the affected layer in bulk powellite crystal. The thickness of the irradiation-damaged layer becomes constant (saturated) after 1.2 dpa.

The most disordered structure always appears on the irradiated surface of powellite due to the migration of irradiation-induced defects from the interior of the structure to the surface. Moreover, the irradiation-induced disorder in powellite does not depend on crystal orientation, namely, no significant anisotropic effect of irradiation- induced disorder.

Anisotropic effect in the lattice volume change was observed along two crystallographic axes (*a*- and *c*-axes) by comparing the depth profile of $\nu_1(A_g)$ peak position. Both expansion and compression of the structure exist in the irradiation-affected layer. The irradiation-damaged layer has less compression and more expansion for *a*-oriented irradiated powellite comparing with the *c*-one, which is positive correlated to the fact of more swelling in *a*-orientation. Irradiation can induce anisotropic compressive stress in powellite. It is shown that *c*-orientation of powellite can endure more stress in the structure than the *a*-one. The depth of the compressive-stressed region increases with increasing dpa (from 0.012 to 5.0). Particularly, for *a*-orientated irradiated powellite, delamination takes place close to the location where the maximum compressive stress is formed.

TEM was used to characterize the defects in the powellite structure induced by Ar irradiations. It is confirmed both by Raman and TEM that powellite does not reach amorphization within the studied dpa range. For low-dpa (0.012) powellites, the main irradiation-induced damages are point defect clusters; while for high-dpa (5.0) ones, the main damages become dislocations. The ranges of the irradiation-damaged layer given by TEM are in agreement with that shown by Raman measurements. The mosaicity appearing at the irradiated surface for 5.0-dpa powellite indicates the most disordered structure in the sample, which is consistent with the fact that the most broadened Raman linewidth were observed at the surface. A two-step damage accumulation is proposed to interpret the evolution of powellite structure under irradiation, which is basically consistent with the results of Raman and TEM. Evolution of the powellite structure with increasing irradiation dose follows from crystalline structure to point defects, then to dislocations, and finally to mosaicity (at 5.0 dpa). The formation of dislocation in powellite participates the release of excessive high compressive stress.

In addition, the quenching of Eu^{3+} emission also indicates the defect level of the irradiated powellites structure. Moreover, the change in ratio of C_{2v} sites and S_4 site(s) is related to different defect types in the damaged structure. For further study, site-selective excitation measurement on irradiated powellite under confocal condition could be useful to follow the modification of C_{2v} and S_4 sites in function of dpa.

It is no doubt that there are still some phenomena which are not clearly understood. More experiments and analyses should be performed to answer the unsolved questions. For example, single-energy irradiation can be conducted on powellite to have a simplified reference for multi-energy irradiation; high resolved TEM could be useful for the characterization of local structure properties and of lattice parameters, which can provide more detail information of the irradiation-induced damage and modification in powellite; characterization of the Ar deposition in the multi-energy irradiated powellite would be helpful to explain why the damage depth for 0.012-dpa powellite is much less than the predetermined 3 μm; TEM measurements on the other irradiated powellites (between 0.012 and 5.0 dpa) are required to find out at which dpa the structure is trigged from point defect clusters to dislocation, etc.

Finally, based on all this study, it is inferred that the crystallization of $CaMoO_4$ can efficiently trap Mo and enrich the α-decay source (REEs/MA), resulting in a depletion in the residual glass. The volume of glass matrix for the vitrification of fission products can therefore be reduced. It is shown that μLIBS can be employed in future for the elemental analysis of nuclear materials, especially, for the detection of low-concentration elements (like Eu). The anisotropic swelling of powellite induces only moderate stress on the borosilicate glass matrix. It is expected that this moderate stress in borosilicate can be well maintained and less likely to induce crack. Most importantly, powellite resists strongly to irradiation. The structural evolution of powellite under irradiation becomes saturated after 1.2 dpa which is equal to a 2 000-year self-irradiation from α-decay. It is inferred that, powellite reaches a stable state after 2 000 years. As a conclusion, Mo-rich borosilicate containing powellite crystallites can provide an efficient double-barrier to immobilize the α-decay source and can be considered as a potential nuclear waste form for long-term storage.

List of figures

List of tables

List of publications

Wang, X., Motto-Ros, V., Panczer, G., De Ligny, D., Yu, J., Benoit, J. M., Dussossoy, J. L., Peuget, S., *Mapping of rare earth elements in nuclear waste glass–ceramic using micro laser-induced breakdown spectroscopy*. Spectrochimica Acta Part B: Atomic Spectroscopy, 2013. 87(0): p. 139-146.

Panczer G., De Ligny D., Mendoza C., Gaft M., Seydoux-Guillaume A-M., **Wang X.** (2012) *Raman and fluorescence,* in: *Applications of Raman Spectroscopy to Earth Sciences and Cultural Heritage* (J. Dubessy & F. Rull, editors). EMU Notes Book in Mineralogy Series, (J. Dubessy & F. Rull, editors). 12, chapter 2, 1–22.

Motto-Ros, V., Sancey, L., **Wang, X**. C., Ma, Q. L., Lux, F., Bai, X. S., Panczer, G., Tillement, O., Yu, J., *Mapping nanoparticles injected into a biological tissue using laser-induced breakdown spectroscopy*. Spectrochimica Acta Part B: Atomic Spectroscopy, 2013. 87(0): p. 168-174.

Motto-Ros V., Ma Q. L., Gregoire S., Lei W. Q., **Wang X. C.**, Pelascini F., Surma F., Detalle V., Yu J., *Dual-wavelength differential spectroscopic imaging for diagnostics of laser-induced plasma.* Spectrochimica Acta Part B-atomic Spectroscopy, vol. 74-75, p. 11-17 (2012)

Motto-Ros V., Sancey L., Ma Q. L., Lux F., Bai X. S., **Wang X. C.**, YU J., Panczer G., Tillement O., *Mapping of native inorganic elements and injected nanoparticles in a biological organ with laser-induced plasma.* Applied Physics Letters, vol. 101, p. 223702 (2012)

YU J., Ma Q. L., Motto-Ros V., Lei W. Q., **Wang X. C.**, Bai X. S., *Generation and expansion of laser-induced plasma as a spectroscopic emission source.* Frontiers of Physics, vol. 7, p. 649 (2012)

Grégoire S., Motto-Ros V., Ma Q. L., Lei W. Q., **Wang X. C**., Pelascini F., Surma F., Detalle V., Yu J. *Correlation between native bonds in a polymeric material and molecular emissions from the laser-induced plasma observed with space and time resolved imaging*. Spectrochimica Acta Part B-atomic Spectroscopy, vol. 74-75, p. 31-37 (2012)

Ma Q. L., Motto-Ros V., Lei W. Q., **Wang X. C.,** Boueri M., Laye F., Zeng C. Q., Sausy M., Wartelle A., Bai X. S., Zheng L. J., Zeng H. P., Baudelet M., Yu J., *Characteristics of Laser-Induced Plasma as a Spectroscopic Light Emission Source*. 17th International Conference On Atomic Processes In Plasmas (ICAPiP), vol. 1438, p. 243-248 (2012)

J. Jagielski, G. Gawlik, I. Jozwik-Biala, G. Panczer, N. Moncoffre, **X. Wang,** R. Ratajczak, M. Swirkowicz, L. Thomé, *Luminescence analysis of damage accumulation: case study of calcium Molybdate.* Nuclear Instruments and Methods in Physics Research Section B: Beam Interactions with Materials and Atoms. (*Submitted*)

A: Appendix

A.1 Estimation of the equivalent fluence for multi-energy irradiation

Based on the induced atom displacements (D_{atom}, vacancies/A/ion) given by SRIM, dpa can be calculated depending on determined fluence of the ion beam (ψ, ion/cm^2), as shown in the following equation.

$$\mathrm{dpa} = \frac{10^8 \times \sum_{i=1}^{5} \left(D_{\mathrm{atom}\ i} \times \psi_i \right)}{\frac{\rho}{M} \times N_{\mathrm{A}} \times Z}$$

Five implantations with different energies (7, 5, 3, 2, and 0.9 MeV) were performed successively on powellite to reach each required dpa. Here, $D_{\mathrm{atom}\ i}$ and ψ_i are the atom displacements and the fluence for the i^{th} implantation. ρ (g/cm^3) and M (g/mol) are respectively the density and the molar mass of $CaMoO_4$, while N_{A} is the Avogadro constant and Z is the number of atoms in one $CaMoO_4$ molecular unit. For $CaMoO_4$, $\rho = 4.26$ g/cm^3, $M = 200.02$ g/mol, $Z = 6$ and $N_{\mathrm{A}} = 6.02\times10^{23}$. The equivalent fluence of each multi-energy irradiation can be calculation by transforming the above equation, as shown below:

$$\Rightarrow \quad \overline{\psi} = \frac{\overline{\mathrm{dpa}} \times \frac{\rho}{M} \times N_{\mathrm{A}} \times Z}{10^8 \times D_{\mathrm{atom}}}$$

A.2 Full-range LIBS spectrum of the initial Mo-rich borosilicate glass

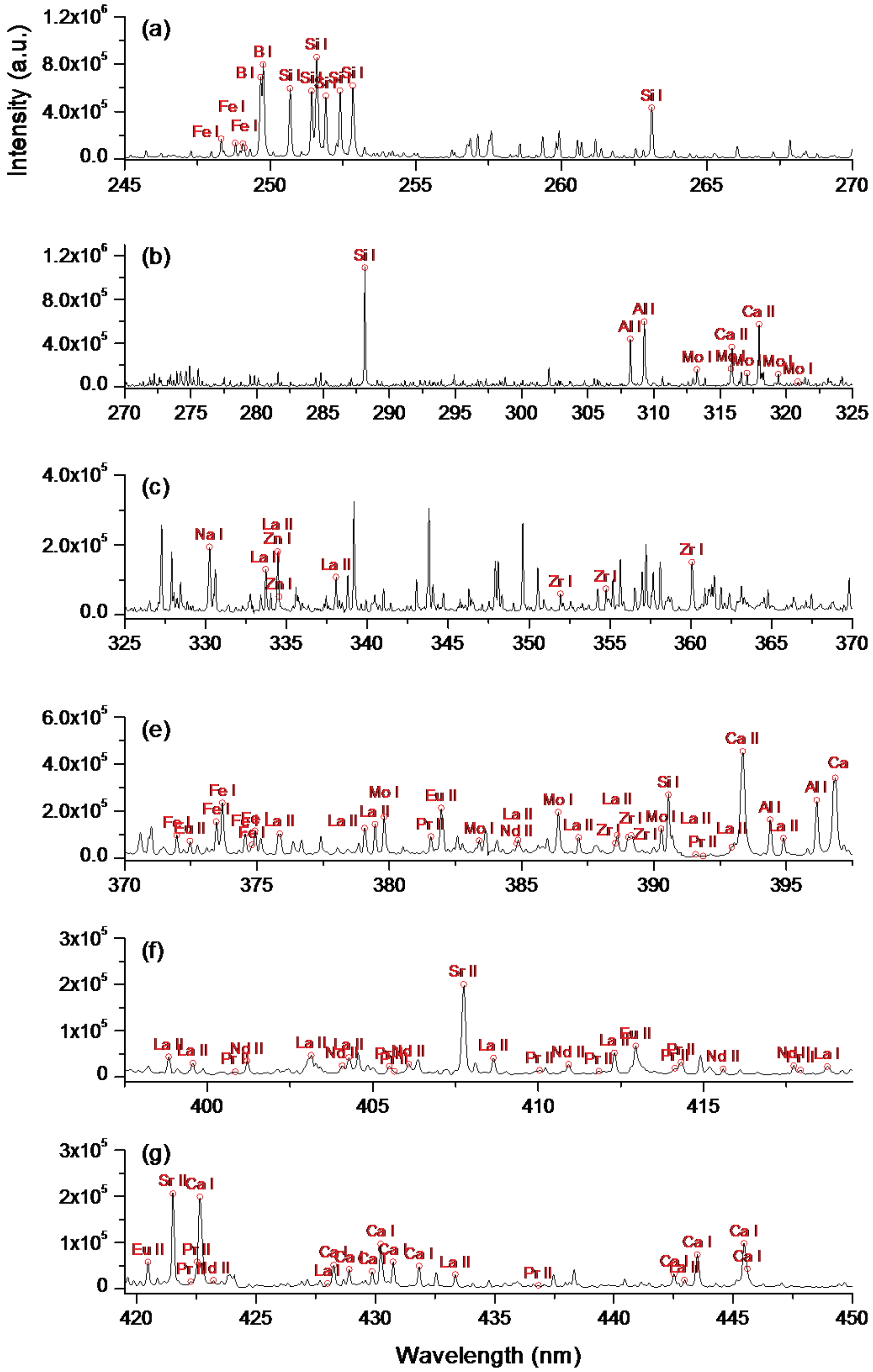

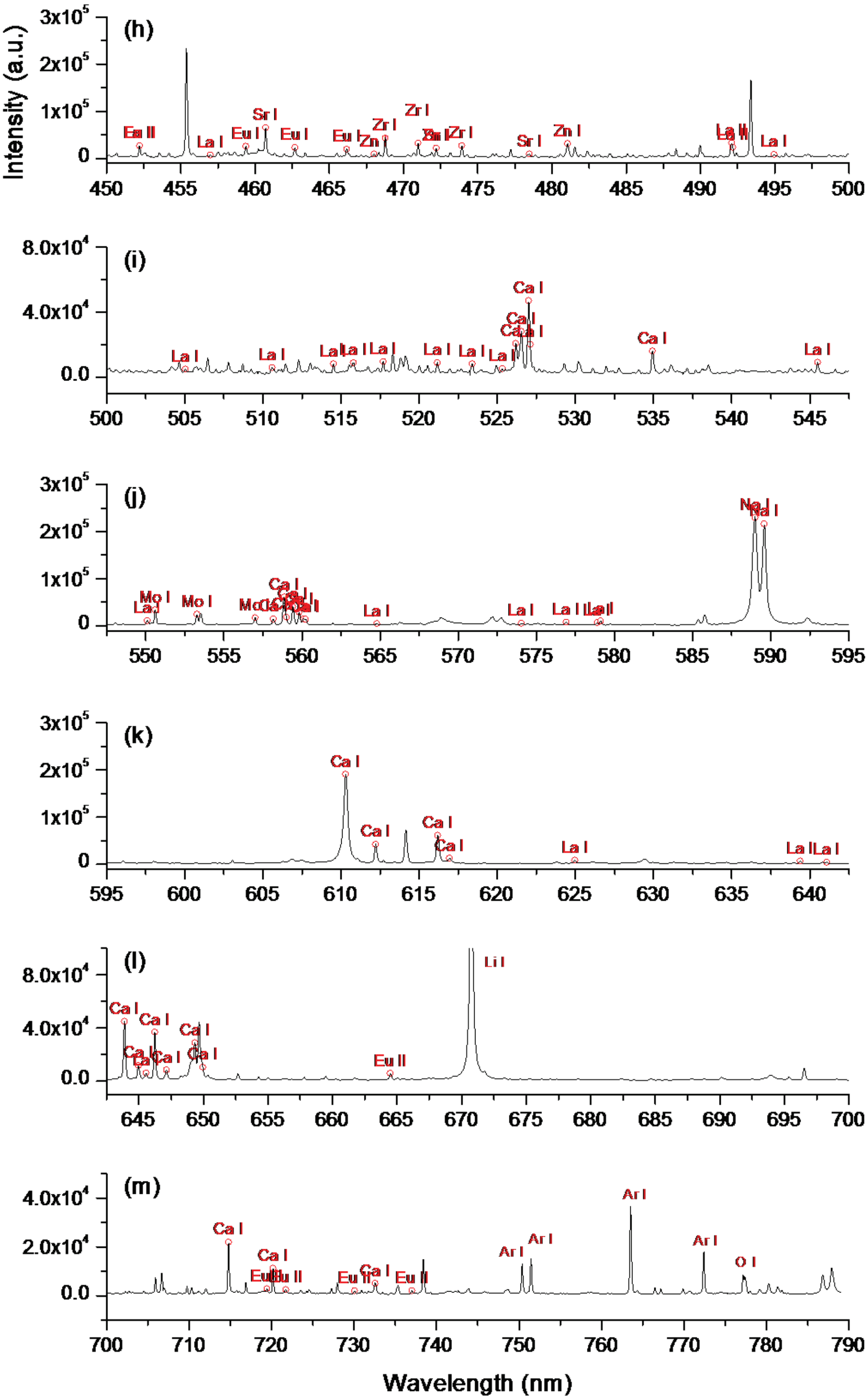

Figure A-1: Full-range LIBS spectrum (averaged from 100 spectra) of the initial Mo-rich borosilicate glass (the SM synthetic analogue); lines were identified according to the NIST database; excitation: 266nm; laser energy: 18 mJ; gate delay: 2 µs; gate width: 8 µs; accumulation times: 1; gain: 100; ambient gas: Ar

A.3 Correlation of LIBS spectral lines in two different spectra ranges

Section 3.1 in this manuscript shows the multi-element mapping on the Mo-rich borosilicate glass-ceramic sample by μLIBS. The data which were used to construct the multi-element maps were recorded in a spectral range of 364 to 396 nm. As we know, it is less likely to detect all the elements of the sample in one short spectral range (about 34 nm in length for Shamrock 303i with high-resolution grating). Sometimes the spectral range has to be changed in order to focus on specific elements. It is therefore necessary to figure out the possibility of multi-element mapping by perform multiple scanning with different spectral ranges on the same sample area.

During the optimization of the μLIBS setup, mapping was also conducted and realized in some other spectral range beside the 364-to-396-nm one, as shown in Figure A-2 and Figure A-3 (Spectral lines which were used for mapping are listed in Table A-1). In this experiment, two scans were performed on the same area successively in two different spectral ranges (403-to-436-nm range and 301-to-335-nm range). The maps obtain by the first and the second scans are quite consistent according to Figure A-3.

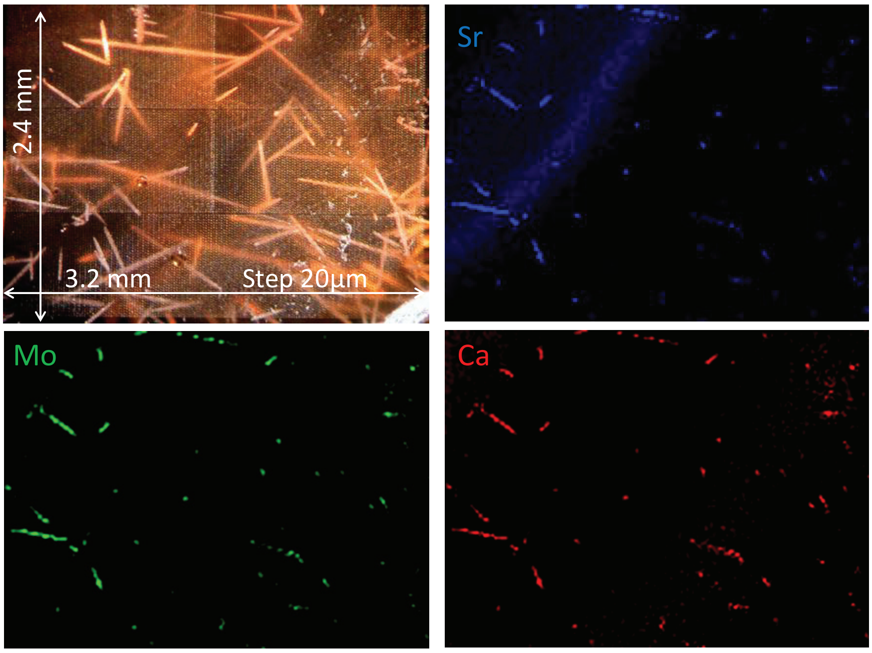

Figure A-2: μLIBS mapping of Mo, Ca, and Sr on the Mo-rich borosilicate glass-ceramic sample in the spectral range of 403 to 436 nm; the figure on the upper left corner is an optical microscope image of the mapping area; interpolation was used for imaging without losing spatial resolution

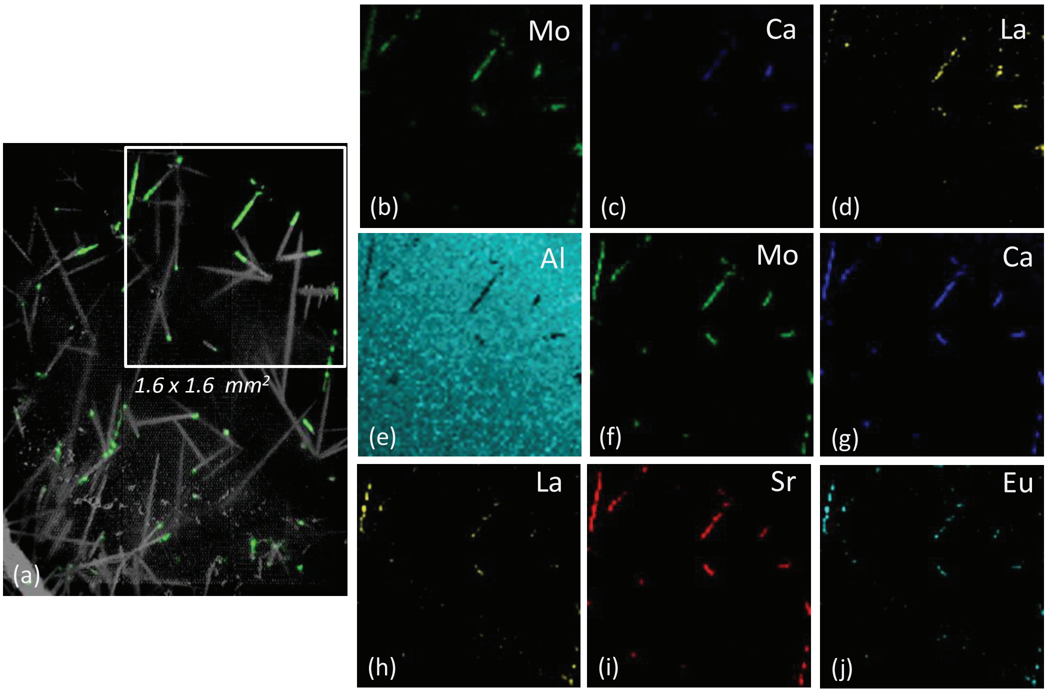

Figure A-3: (a) an optical microscope image Mo-rich borosilicate glass-ceramic; the green color on the image indicates the crystallites which are exposed on the sample surface; the white square indicates the zoom area of multi-element mapping; (b-f) µLIBS mapping of Mo, Ca, La, and Al in the spectral range of 301 to 335 nm; (g-k) µLIBS mapping of Mo, Ca, La, Sr, and Eu in the spectral range of 403 to 436 nm

Table A-1: Spectral lines which were used for mapping in Figure A-2 and Figure A-3

	Figure A-2 and A-3-(g-k)	Figure A-3-(b-f)
Lines (nm)	Range: 403 to 436 nm	Range: 301 to 335 nm
Mo	Mo I 414.3	Mo I 317.0
Ca	Ca I 428.9	Ca II 315.8
Sr	Sr I 421.5	
La	La II 408.6	La II 333.7
Eu	Eu II 412.9	
Al		Al I 309.0

The line intensity correlation in the same spectral range is shown in Figure A-4 (for the range of 403 to 436 nm) and Figure A-5 (for the range of 301 to 335 nm). The line intensity correlation in different spectral ranges is shown in Figure A-6. The linear correlation of Ca and Mo line intensity in two spectral ranges suggests the validity of µLIBS mapping by multiple scanning the same sample surface.

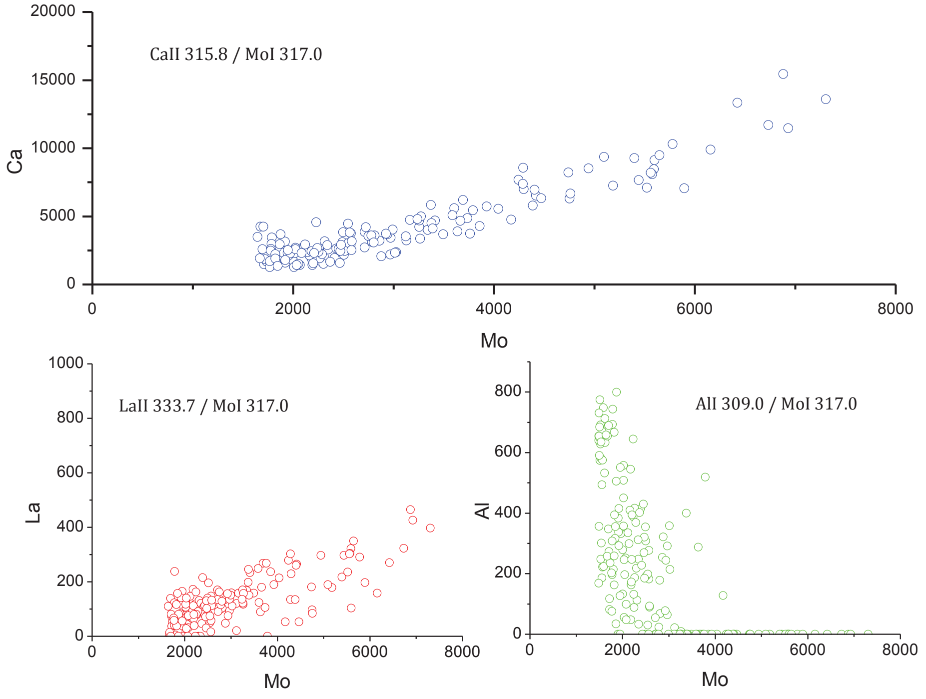

Figure A-4: Line intensity correlation between Mo I 317.0 nm line and the lines of other species in 301 to 335 nm spectral range for the Mo-rich borosilicate glass-ceramic sample

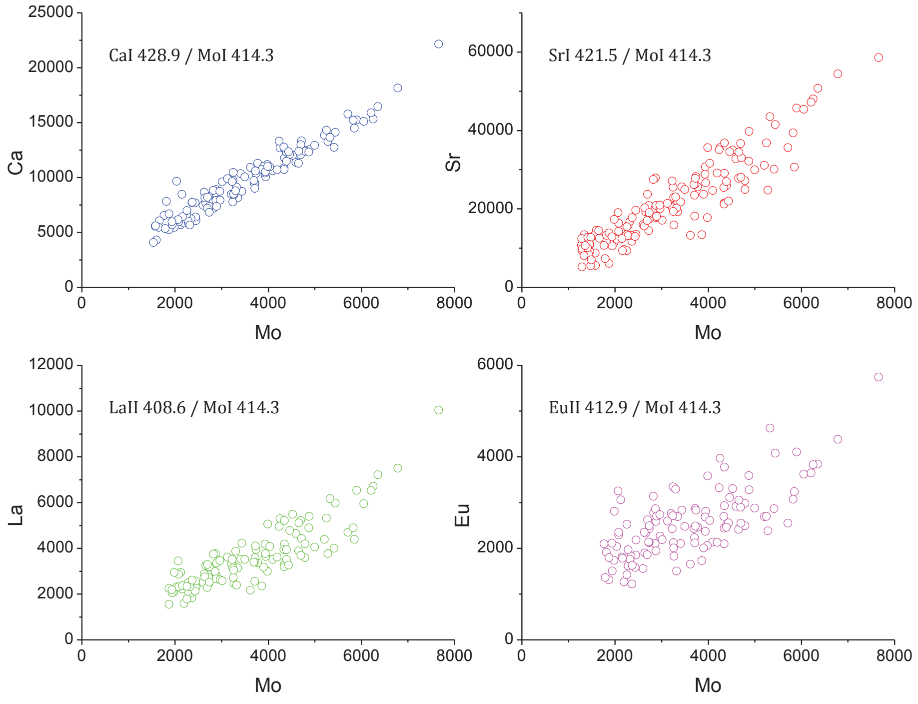

Figure A-5: Line intensity correlation between Mo I 414.3 nm line and the lines of other species in 403 to 436 nm spectral range for the Mo-rich borosilicate glass-ceramic sample

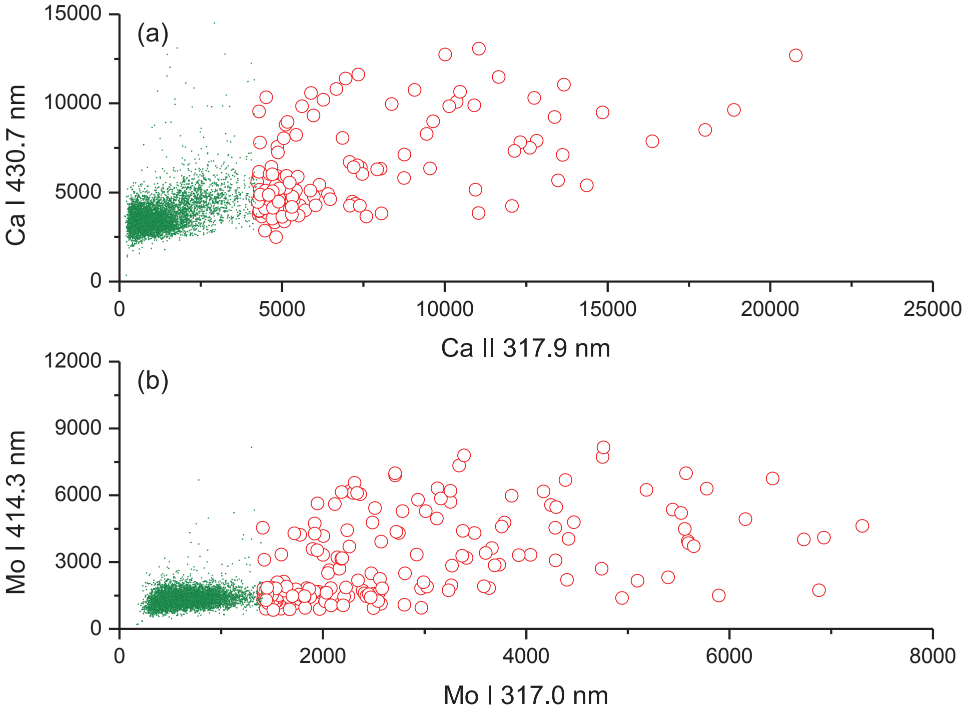

Figure A-6: Line intensity correlation between two spectral ranges (red hollow circle); (a) Ca I 430.7 nm (403 to 436 nm range) and Ca II 317.9 nm (301 to 335 nm range); (b) Mo I 414.3 nm (403 to 436 nm range) and Mo I 317.0 nm (301 to 335 nm range); the green points on the figure are noise

A.4 Principal component analysis (PCA) on the μLIBS mapping data of Mo-rich borosilicate glass-ceramic

1) The intensity maps of all the elements are rearranged to get a data matrix (D_0) as below. I_{iEj} (i = 1 to n; E_j= Al, Ca …, Mo, j = 1 to n) is the intensity of element E at the position P_i.

$$D_0 = \begin{array}{c} P_1 \\ P_2 \\ \vdots \\ P_m \end{array} \begin{bmatrix} I_{1Al} & I_{1Ca} & \cdots & I_{1Mo} \\ I_{2Al} & I_{2Ca} & \cdots & I_{2Mo} \\ \vdots & \vdots & \ddots & \vdots \\ I_{mAl} & I_{mCa} & \cdots & I_{mMo} \end{bmatrix}_{m\times n}.$$

2) Calculate the average ($\bar{I}_j$) of each column and subtract $\bar{I}_j$ from D_0 to get a new data matrix D_1.

$$\bar{I}_j = \frac{\sum_{i=1}^{m} I_{i,Ej}}{m}$$

$$D_1 = \begin{bmatrix} I_{1Al} - \bar{I}_1 & I_{1Ca} - \bar{I}_2 & \cdots & I_{1Mo} - \bar{I}_n \\ I_{2Al} - \bar{I}_1 & I_{2Ca} - \bar{I}_2 & \cdots & I_{2Mo} - \bar{I}_n \\ \vdots & \vdots & \ddots & \vdots \\ I_{mAl} - \bar{I}_1 & I_{mCa} - \bar{I}_2 & \cdots & I_{mMo} - \bar{I}_n \end{bmatrix}_{m\times n}$$

3) Third, calculate the covalent matrix of each column in D_1.

$$C_1 = \begin{bmatrix} Cov(L_1, L_1) & Cov(L_1, L_2) & \cdots & Cov(L_1, L_n) \\ Cov(L_2, L_1) & Cov(L_2, L_2) & \cdots & Cov(L_2, L_n) \\ \vdots & \vdots & \ddots & \vdots \\ Cov(L_n, L_1) & Cov(L_n, L_2) & \cdots & Cov(L_n, L_n) \end{bmatrix}_{n\times n}$$

where,

$$L_j = \begin{bmatrix} I_{1Ej} - \bar{I}_j \\ \vdots \\ I_{mEj} - \bar{I}_j \end{bmatrix}$$

4) Calculate the eigenvalues and their corresponding eigenvectors of the covalent matrix C_1.

$$EigVal = \left[EigValue_1 \quad EigValue_2 \quad \cdots \quad EigValue_n \right]$$

$$\begin{bmatrix} EigVec_{11} \\ \vdots \\ EigVec_{1n} \end{bmatrix} \begin{bmatrix} EigVec_{21} \\ \vdots \\ EigVec_{2n} \end{bmatrix} \cdots \begin{bmatrix} EigVec_{n1} \\ \vdots \\ EigVec_{nn} \end{bmatrix}$$

5) Sort descendingly the eigenvalues of the covalent matrix C_1 (from max to min). Then sort the eigenvectors according to the eigenvalues.

$$EigVal = \left[EigValue_{1'} \quad EigValue_{2'} \quad \cdots \quad EigValue_{n'} \right]$$

$$\begin{bmatrix} EigVec_{1'1} \\ \vdots \\ EigVec_{1'n} \end{bmatrix} \begin{bmatrix} EigVec_{2'1} \\ \vdots \\ EigVec_{2'n} \end{bmatrix} \cdots \begin{bmatrix} EigVec_{n'1} \\ \vdots \\ EigVec_{n'n} \end{bmatrix}$$

$$T = \begin{bmatrix} EigVec_{1'1} & EigVec_{2'1} & \cdots & EigVec_{n'1} \\ \vdots & \vdots & \ddots & \vdots \\ EigVec_{1'n} & EigVec_{2'n} & \cdots & EigVec_{n'n} \end{bmatrix}_{n \times n}$$

6) Calculate the loading weight (PC_i%, j = 1 to n) of each eigenvalue.

$$SumEig = \left(\sum_{j=1}^{n} \left(EigValue_{j'} \right)^2 \right)^{\frac{1}{2}}$$

$$WEig = \left[\frac{EigValue_{1'}}{SumEig} \quad \frac{EigValue_{2'}}{SumEig} \quad \cdots \quad \frac{EigValue_{n'}}{SumEig} \right]$$

Namely,

$$WEig = \left[PC_1\% \quad PC_2\% \quad \cdots \quad PC_n\% \right]$$

$$PC_j\% = \frac{EigValue_{j'}}{SumEig}$$

7) Multiply each eigvector by its corresponding weight of the eigenvalue.

$$\begin{bmatrix} PC_1\%\times EigVector_{1'1} \\ \vdots \\ PC_1\%\times EigVector_{1'n} \end{bmatrix} \begin{bmatrix} PC_2\%\times EigVector_{2'1} \\ \vdots \\ PC_2\%\times EigVector_{2'n} \end{bmatrix} \cdots \begin{bmatrix} PC_n\%\times EigVector_{n'1} \\ \vdots \\ PC_n\%\times EigVector_{n'n} \end{bmatrix}$$

$$Coor_j = \begin{bmatrix} PC_j\%\times EigVector_{j'1} & \cdots & PC_i\%\times EigVector_{j'n} \end{bmatrix}$$

Here, ($Coor_1$, $Coor_2$) shows the correlation of the first two important eigenvectors, which gives the coordination of each element in the $PC1$-$PC2$ space (Figure 3-7).

8) Data transformation: $D_1 \times T$

$$\begin{bmatrix} I_{1Al}-\bar{I}_1 & I_{1Ca}-\bar{I}_2 & \cdots & I_{1Mo}-\bar{I}_n \\ \vdots & \vdots & \ddots & \vdots \\ I_{mAl}-\bar{I}_1 & I_{mCa}-\bar{I}_2 & \cdots & I_{mMo}-\bar{I}_n \end{bmatrix} \times \begin{bmatrix} EigVec_{1'1} & EigVec_{2'1} & \cdots & EigVec_{n'1} \\ \vdots & \vdots & \ddots & \vdots \\ EigVec_{1'n} & EigVec_{2'n} & \cdots & EigVec_{n'n} \end{bmatrix}$$

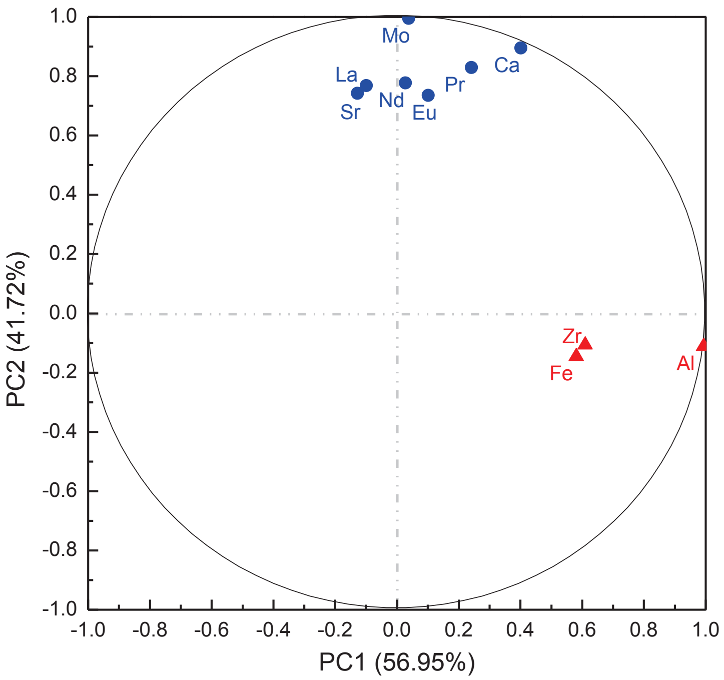

Figure 3-7: Correlation of all the species shown in with PCA; PC1 and PC2 represent respectively the performance of glassy and crystalline phases

A.5 Calculation of element fraction in the powellite crystalline phase and the residual glass

The atom concentration of element E in the initial glass, $C(E_i)$, is equal to the sum of its concentration in each individual phase times the respective phase fraction.

$$C(E_i) = x_c C(E_c) + x_g C(E_g)$$

$$\begin{bmatrix} C(\mathrm{Al}_i) \\ \vdots \\ C(\mathrm{Zr}_i) \end{bmatrix} = x_c \begin{bmatrix} C(\mathrm{Al}_c) \\ \vdots \\ C(\mathrm{Zr}_c) \end{bmatrix} + x_g \begin{bmatrix} C(\mathrm{Al}_g) \\ \vdots \\ C(\mathrm{Zr}_g) \end{bmatrix}.$$

$$\begin{bmatrix} C(\mathrm{Al}_i) \\ \vdots \\ C(\mathrm{Zr}_i) \end{bmatrix} = \begin{bmatrix} C(\mathrm{Al}_c) & C(\mathrm{Al}_g) \\ \vdots & \vdots \\ C(\mathrm{Zr}_c) & C(\mathrm{Zr}_g) \end{bmatrix} \begin{pmatrix} x_c \\ x_g \end{pmatrix}$$

Here, $C(E_i)$, $C(E_c)$, and $C(E_g)$ are one-dimensional vector constituted by the known atom concentration (determined by EMPA) of each element in the initial glass, the crystalline phase, and the residual glass, respectively. x_c and x_g are respectively the phase fractions of the crystal and the residual glass, which can be determined by the following equations[1]:

$$M_i = \begin{bmatrix} C(\mathrm{Al}_i) \\ \vdots \\ C(\mathrm{Zr}_i) \end{bmatrix}, \quad M_f = \begin{bmatrix} C(\mathrm{Al}_c) & C(\mathrm{Al}_g) \\ \vdots & \vdots \\ C(\mathrm{Zr}_c) & C(\mathrm{Zr}_g) \end{bmatrix}$$

$$\begin{pmatrix} x_c \\ x_g \end{pmatrix} = \left(M_f^{\mathrm{T}} M_f \right)^{-1} M_f^{\mathrm{T}} M_i$$

---

[1] Albarède, Francis. *Introduction to geochemical modeling*. Cambridge University Press, 1996.

A.6 Estimation of stress in the glass matrix induced by the swelling of the powellite crystal

According to Hooke's law, relationship between stress σ and strain ε is:

$$\sigma = -c\varepsilon$$

In continuum mechanics, c is four-order tensor, usually called stiffness tensor or elastic tensor. It can be considered that borosilicate glass is isotropic material. For isotropic material, the relationship between σ and ε tensors is:

$$\begin{bmatrix} \sigma_{11} \\ \sigma_{22} \\ \sigma_{33} \\ \sigma_{23} \\ \sigma_{31} \\ \sigma_{12} \end{bmatrix} = \begin{bmatrix} 2\mu+\lambda & \lambda & \lambda & 0 & 0 & 0 \\ \lambda & 2\mu+\lambda & \lambda & 0 & 0 & 0 \\ \lambda & \lambda & 2\mu+\lambda & 0 & 0 & 0 \\ 0 & 0 & 0 & \mu & 0 & 0 \\ 0 & 0 & 0 & 0 & \mu & 0 \\ 0 & 0 & 0 & 0 & 0 & \mu \end{bmatrix} \begin{bmatrix} \varepsilon_{11} \\ \varepsilon_{22} \\ \varepsilon_{33} \\ 2\varepsilon_{23} \\ 2\varepsilon_{31} \\ 2\varepsilon_{12} \end{bmatrix}$$

or

$$\begin{bmatrix} \varepsilon_{11} \\ \varepsilon_{22} \\ \varepsilon_{33} \\ 2\varepsilon_{23} \\ 2\varepsilon_{31} \\ 2\varepsilon_{12} \end{bmatrix} = \frac{1}{E} \begin{bmatrix} 1 & -v & -v & 0 & 0 & 0 \\ -v & 1 & -v & 0 & 0 & 0 \\ -v & -v & 1 & 0 & 0 & 0 \\ 0 & 0 & 0 & 2(1+v) & 0 & 0 \\ 0 & 0 & 0 & 0 & 2(1+v) & 0 \\ 0 & 0 & 0 & 0 & 0 & 2(1+v) \end{bmatrix} \begin{bmatrix} \sigma_{11} \\ \sigma_{22} \\ \sigma_{33} \\ \sigma_{23} \\ \sigma_{31} \\ \sigma_{12} \end{bmatrix}$$

Here, $\lambda = K - \frac{2}{3}G$; $\mu = G$; λ and μ are Lamé constants; K is bulk modulus; G is shear modulus; E is the Young's modulus; v is the Poisson ratio.

For powellite the relationship between σ and ε tensors is:

$$\begin{bmatrix} \sigma_{11} \\ \sigma_{22} \\ \sigma_{33} \\ \sigma_{23} \\ \sigma_{31} \\ \sigma_{12} \end{bmatrix} = \begin{bmatrix} C_{11} & C_{12} & C_{13} & 0 & 0 & C_{16} \\ C_{21} & C_{22} & 0 & 0 & 0 & 0 \\ C_{31} & 0 & C_{33} & 0 & 0 & 0 \\ 0 & 0 & 0 & C_{44} & 0 & 0 \\ 0 & 0 & 0 & 0 & 0 & 0 \\ C_{61} & 0 & 0 & 0 & 0 & C_{66} \end{bmatrix} \begin{bmatrix} \varepsilon_{11} \\ \varepsilon_{22} \\ \varepsilon_{33} \\ 2\varepsilon_{23} \\ 2\varepsilon_{31} \\ 2\varepsilon_{12} \end{bmatrix}$$

Table A-2: Mineral data of borosilicate glass[2] and powellite[3]; λ and μ are calculated from K and G.

	Modulus (GPa)			Lamé constants		Density (g/cm^3)	Poisson's ratio
	Bulk	Shear	Young's				
	K	G	E	λ	μ	ρ	v
Borosilicate	35-45	31-40	63-81	16.3	35.5	2.23-2.51	0.2-0.206
Powellite	81.0	39.9					

Table A-3: Components of the stiffness tensors of borosilicate and powellite[3]

	C_{11}	C_{33}	C_{44}	C_{66}	C_{12}	C_{13}	C_{16}
Borosilicate	87.3	--	35.5	--	16.3	--	--
Powellite	144	127	36.8	45.8	65	47	-13.5

Mineral data of borosilicate and powellite are listed in Table A-2 and Table A-3. Δa and Δc are respectively the absolute swelling of powellite crystal in a- and c-axes which were observed by optical interferometry. In the Mo-rich borosilicate glass-ceramic, powellite crystallites are constrained by the surrounded glass matrix. The swelling is therefore confined. $\Delta x_c|_a$ and $\Delta x_g|_a$ are the absolute change of length of crystallite and the surrounded glass in a-axis. $\Delta x_c|_c$ and $\Delta x_g|_c$ are the absolute change of length of crystallite and the surrounded glass in c-axis. Δx_c and Δx_g should satisfy the following relation:

$$(\Delta x_c + \Delta x_g)\Big|_a = \Delta a\,,\ \ (\Delta x_c + \Delta x_g)\Big|_c = \Delta c$$

Moreover, ratio of Δx_c and Δx_g can be roughly estimated by the elasticity coefficient (components of the stiffness tensors) of the crystal and the glass in the corresponding orientation. C_{c11} and C_{g11} are the elasticity components of the stiffness tensors in a-axis for the crystal and the glass respectively. Accordingly, $\Delta x_c/\Delta x_g$ in a-axis is proportional to C_{g11}/C_{c11}, and the same for $\Delta x_c/\Delta x_g$ in c-axis.

$$\left.\frac{\Delta x_c}{\Delta x_g}\right|_a \sim \frac{C_{g11}}{C_{c11}}\,,\ \ \left.\frac{\Delta x_c}{\Delta x_g}\right|_c \sim \frac{C_{g33}}{C_{c33}}$$

---

[2] *Material Properties Database*, 2013, http://www.makeitfrom.com/

[3] Bass, Jay D. "Elasticity of minerals, glasses, and melts" *AGU Reference Shelf* 2 (1995): 45-63.

ε_{c11} and ε_{c33} are respectively the strains of powellite crystallite in the glass matrix along the two crystal axes. It can be estimated as below:

$$\varepsilon_{c11} \sim \frac{\Delta a}{3\mu m} \times \frac{C_{g11}}{C_{g11}+C_{c11}}, \quad \varepsilon_{c33} \sim \frac{\Delta c}{3\mu m} \times \frac{C_{g33}}{C_{g33}+C_{c33}}$$

The stress generated in the glass matrix (σ_{g11} and σ_{g33}) to confine the powellite crystallite should be equivalent to the strain induced stress (σ_{c11} and σ_{c33}) in powellite. They follows:

$$\sigma_{c11} = (C_{c11}+C_{c12})\varepsilon_{c11} + C_{c13}\varepsilon_{c33}, \quad \sigma_{c33} = C_{c31}\varepsilon_{c11} + C_{c33}\varepsilon_{c33}$$

$$\sigma_{c11} = \sigma_{g11} = \sigma_{11}, \quad \sigma_{c33} = \sigma_{g33} = \sigma_{33}$$

The shear strain in powellite is ignored ($\varepsilon_{c12} \sim 0$). σ_{g11} and σ_{g33} can be figured out by substituting the ε_{c11} and ε_{c33} values into the equations above. Table A-4 shows the estimation of strain and stress in the glass matrix.

Table A-4: Absolute swelling (Δa and Δc) and the strain (ε_{c11} and ε_{c33}) of the powellite crystal, as well as the stress (σ_{11} and σ_{33}) in the surrounding glass matrix

dpa	Δa (nm)	ε_{c11}	σ_{11} (GPa)	Δc nm	ε_{c33}	σ_{33} (GPa)
0.012	33.1	4.16E-03	1.02	22.9	3.11E-03	0.59
0.06	50.3	6.33E-03	1.53	32.1	4.36E-03	0.85
0.6	58.9	7.41E-03	1.79	37.8	5.13E-03	1.00
1.2	63.6	8.00E-03	1.94	41.3	5.61E-03	1.09
5	64.0	8.05E-03	1.96	42.9	5.83E-03	1.12

A.7 Determination of Raman spatial resolution

In optics, the Airy disk[4] (or Airy disc) and Airy pattern are descriptions of the best focused spot of light that a perfect lens with a circular aperture can make, limited by the diffraction of light. The spatial extent of the laser focus can be derived from the formula of an Airy disk of light (as shown below), which predicts the lateral (or horizontal) spatial resolution (Δx) of the laser-based optical analyses (e.g. confocal Raman).

$$\Delta x = 1.22\lambda / \mathrm{NA}$$

Here, λ is the incident laser wavelength and NA is the numerical aperture of the objective. Accordingly, the lateral resolution of laser beam is independent of the measured object.

Contrary to the lateral resolution, the axial (or depth) resolution (Δz) depends on the refractive index n of the measured materials[5]:

$$\Delta z = 2n\lambda / \mathrm{NA}^2$$

For powellite crystal, the refractive index is about 2. Thus, Δz is about $4\lambda/\mathrm{NA}^2$. According to the two formulas above, the calculated lateral and depth resolutions of 633-nm laser with a NA-0.95 objective are respectively 0.8 μm and 2.8 μm. In this case, the lateral resolution is much better than the depth one.

The axial and lateral spatial resolution can also be determined by measuring the intensity profile of the signal along the axial and lateral direction, respectively. When the focus of the laser beam is approaching the sample, a progressive increase in the recorded signal can be observed, as shown in Figure A-7 and Figure A-8. The estimated spatial resolution is the spatial interval between the two positions where 20% and 80% of the maximal intensity are observed. For homogeneous samples, the inflection point on the signal intensity profile corresponds to the border of the sample.

---

[4] http://en.wikipedia.org/wiki/Airy_disk

[5] http://www.optics.rochester.edu/workgroups/novotny/courses/OPT463/resolution.pdf

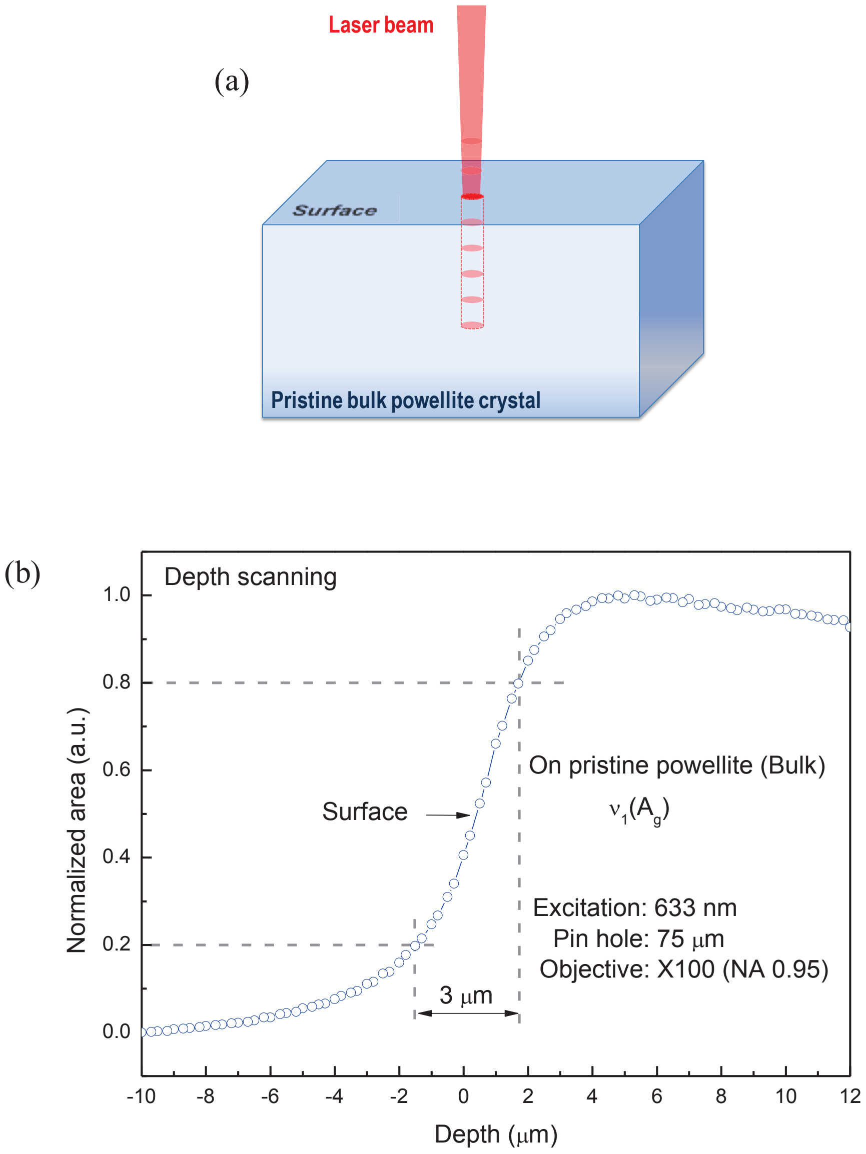

Figure A-7: (a) Schematic diagram of the Raman depth profile measurement on pristine bulk powellite crystal; (b) Depth profile of the $\nu_1(A_g)$ peak area of pristine bulk powellite crystal; the estimated depth resolution (20% to 80%) is 3 µm (By formula $4\lambda/NA^2$, the calculated depth resolution of 633-nm laser with a NA-0.95 objective is 2.8 µm.); the inflection point corresponds to the sample surface

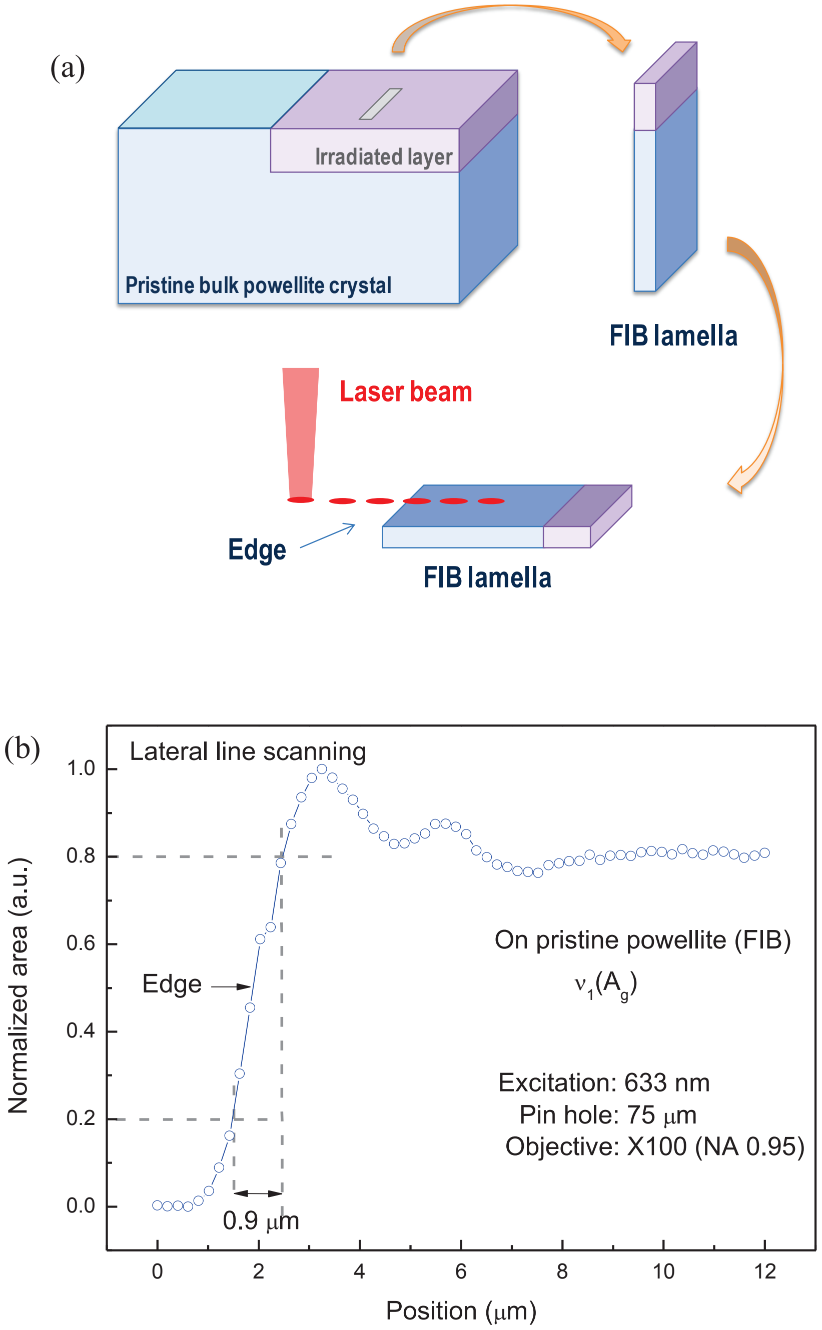

Figure A-8: (a) Schematic diagram of the Raman horizontal profile measurement on the FIB section of pristine powellite crystal; (b) Line profile of the $\nu_1(A_g)$ peak area of pristine powellite crystal FIB section; laser scanning was performed horizontally on the FIB section; the estimated depth resolution (20% to 80%) is 0.9 µm (By formula 1.22λ/NA, the calculated depth resolution of 633-nm laser with a NA-0.95 objective is 0.8 µm.); the inflection point corresponds to the edge of the FIB section; a much better spatial resolution can be obtain in this case comparing with the one in Figure A-7

A.8 Raman measurements on irradiated bulk powellite crystal

According to the explanation in Section A.4, depth resolution of the Raman characterization becomes very crucial when performing analyses perpendicular to the irradiated surface. Real analyzed volume can exceed the thickness of irradiated layer, from which spectrum is mixed by information from the non-irradiated layer just below the irradiated one. Figure A-9 to Figure A-14 show some examples of Raman measurements on *a*- and *c*-oriented irradiated bulk powellites. As can be seen, the Raman linewidth observed in this case is much less than the one observed in FIB sections. The fluctuation of the Raman linewidth in the irradiated area of *a*-oriented powellite is due to the delamination (see Figure 4-6) of the sample.

Figure A-15 shows a comparison of $\nu_1(A_g)$ depth profiles in linewidth and peak intensity between irradiated (1.2 dpa) and non-irradiated bulk powellite crystal. For the irradiated sample, the evolution of Raman intensity is significantly different from the pristine one when the focus of the laser beam moves from the exterior to the interior of the sample. The border of the irradiated sample is therefore difficult to define from the Raman intensity profile.

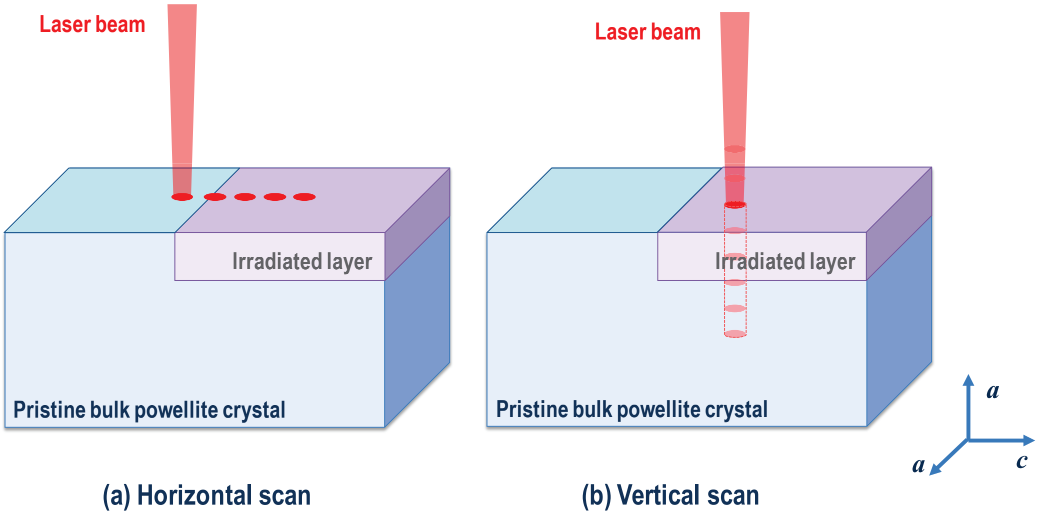

Figure A-9: Schematic diagram of the Raman horizontal (a) and depth (b) profiles measurement on *a*-oriented irradiated bulk powellite crystal

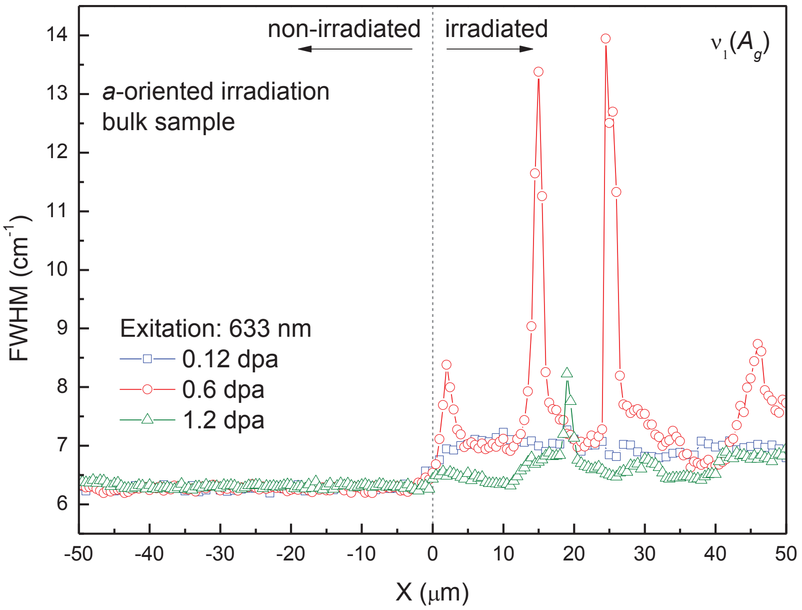

Figure A-10: Horizontal profile of the $\nu_1(A_g)$ linewidth of a-oriented irradiated bulk powellite crystal (0.12, 0.6 and 1.2 dpa); the laser beam scanned horizontally on the sample surface from the non-irradiated area to the irradiated area (Figure A-9-(a))

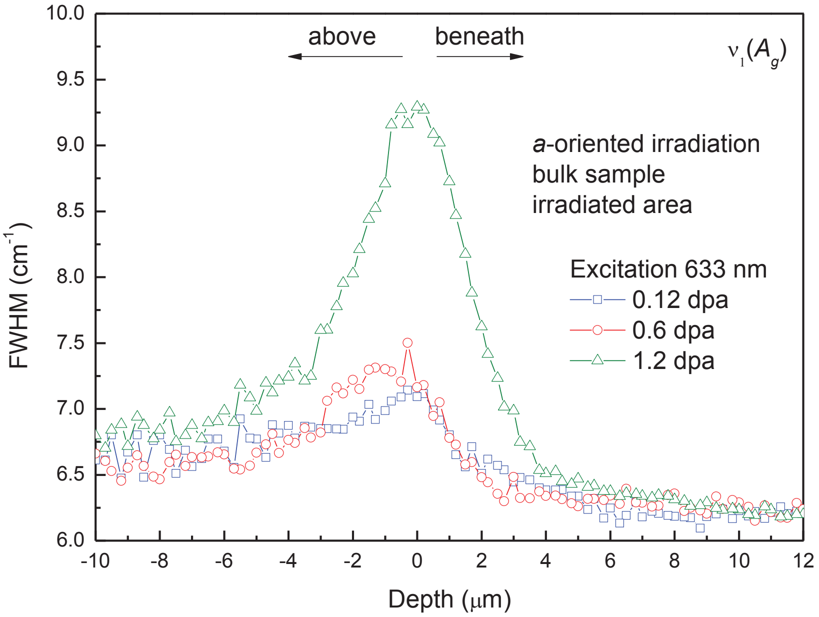

Figure A-11: Depth profile of the $\nu_1(A_g)$ linewidth of *a*-oriented irradiated bulk powellite crystal (0.12, 0.6 and 1.2 dpa); the laser beam scanned vertically from the exterior to the interior of the sample (Figure A-9-(b))

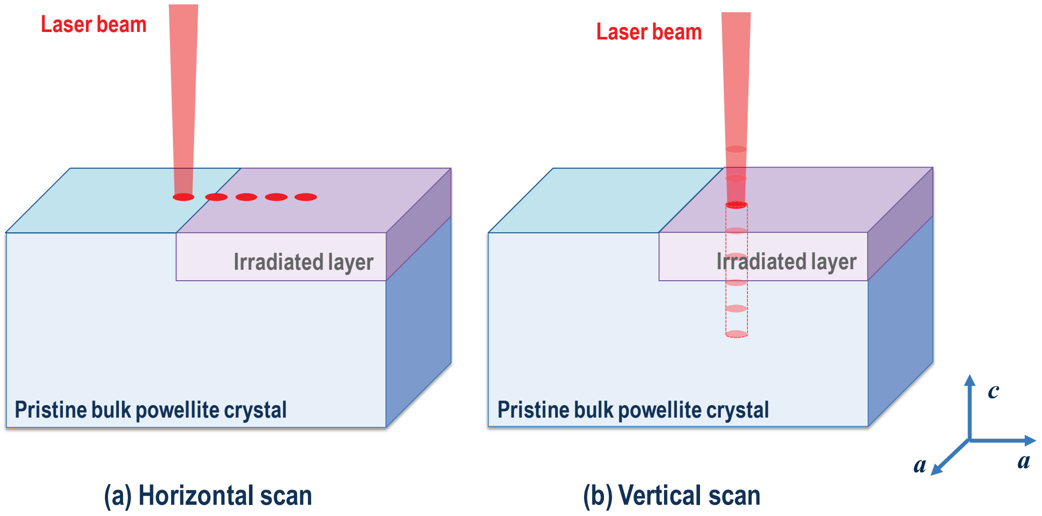

Figure A-12: Schematic diagram of the Raman horizontal (a) and depth (b) profiles measurement on *c*-oriented irradiated bulk powellite crystal

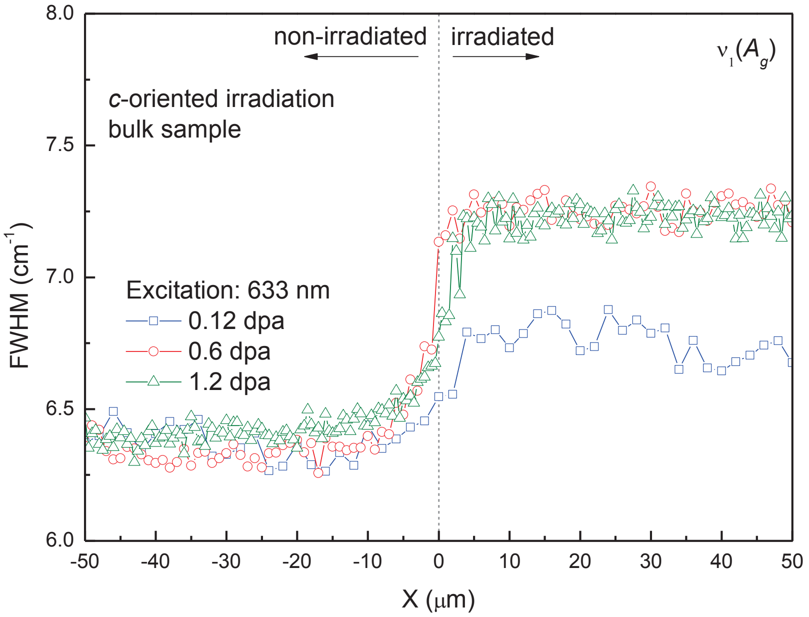

Figure A-13: Horizontal profile of the $\nu_1(A_g)$ linewidth of *c*-oriented irradiated bulk powellite crystal (0.12, 0.6 and 1.2 dpa); the laser beam scanned horizontally on the sample surface from the non-irradiated area to the irradiated area (Figure A-12-(a))

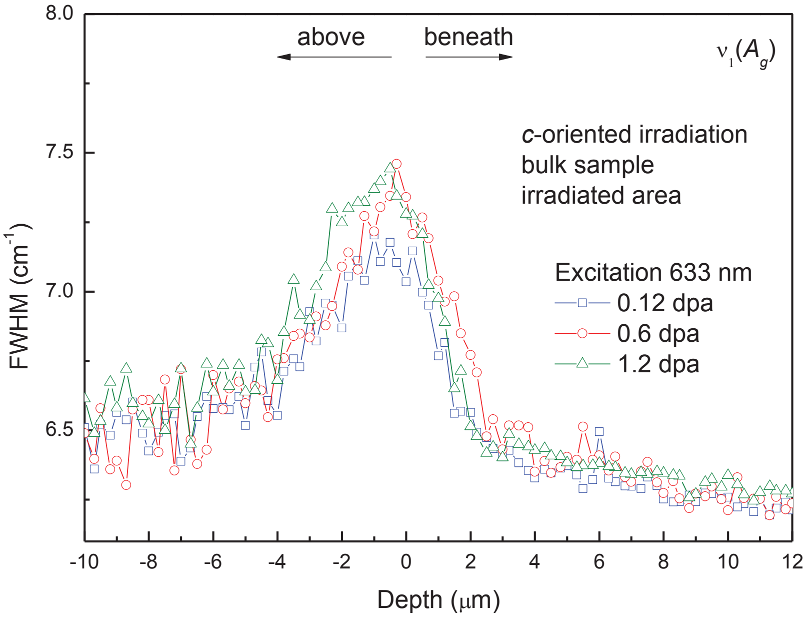

Figure A-14: Depth profile of the $\nu_1(A_g)$ linewidth of *c*-oriented irradiated bulk powellite crystal (0.12, 0.6 and 1.2 dpa); the laser beam scanned vertically from the exterior to the interior of the sample (Figure A-12-(b))

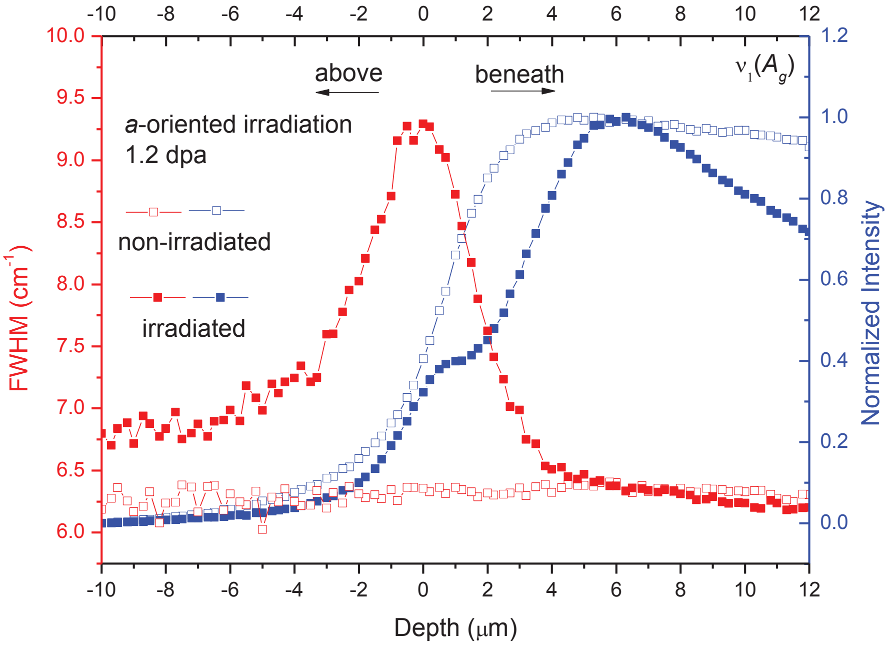

Figure A-15: A comparison of $\nu_1(A_g)$ depth profiles in linewidth and peak intensity between irradiated (1.2 dpa) and non-irradiated bulk powellite crystal; excitation 633 nm

A.9 *Determination of the edge of Raman mapping*

Figure A-17 shows the line profiles in peak area, peak position and linewidth of $\nu_1(A_g)$ Raman mode of pristine powellite and irradiated powellite. For pristine FIB sample, an inflection point on the peak area (intensity) profile can be found easily when the laser scans from the void zone to the sample surface due to the fact that the size of the laser beam is not zero. Hence, it is possible to record Raman signal when the laser beam is close to the border of the sample but still focus in void. In this case, the Raman signal is very low and noisy. When fitting the Raman spectra recorded in void with Labspec 5 software, the software gives some inaccurate values on peak position and linewidth. Therefore, a fluctuation of the profiles of peak position and linewidth can be found in the void. It can be considered that the position where the inflection point of the area profile locates is the edge (border) of the pristine FIB section. However, for irradiated sample, the evolution of peak area from void zone to sample zone is much more complicated than that in the pristine case. Due to the irradiation-induced damage, the peak intensity decrease a lot in the damaged structure (which locates in the border of the FIB section). Moreover, the evolution of peak area insider irradiated sample depends on the structural damage. In this case, it is quite difficult to define the inflection point on the area profile. Therefore, in this manuscript, the turning point on the area profile is considered to be the border of the FIB section (pink dash line in Figure A-17).

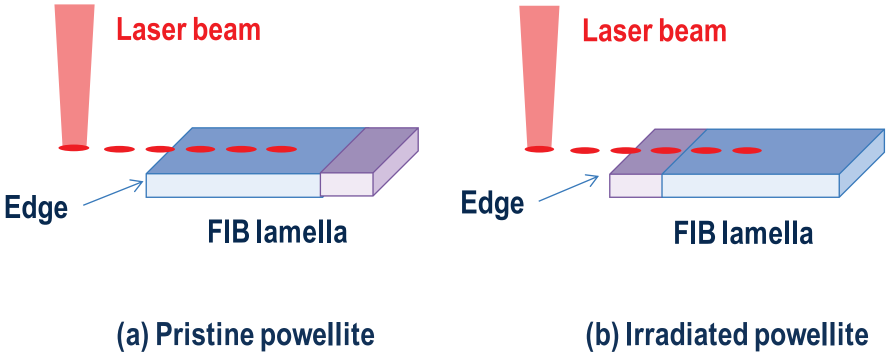

Figure A-16: Schematic diagram of the Raman horizontal profile measurement on the FIB section of pristine (a) and irradiated (b) powellite crystal;

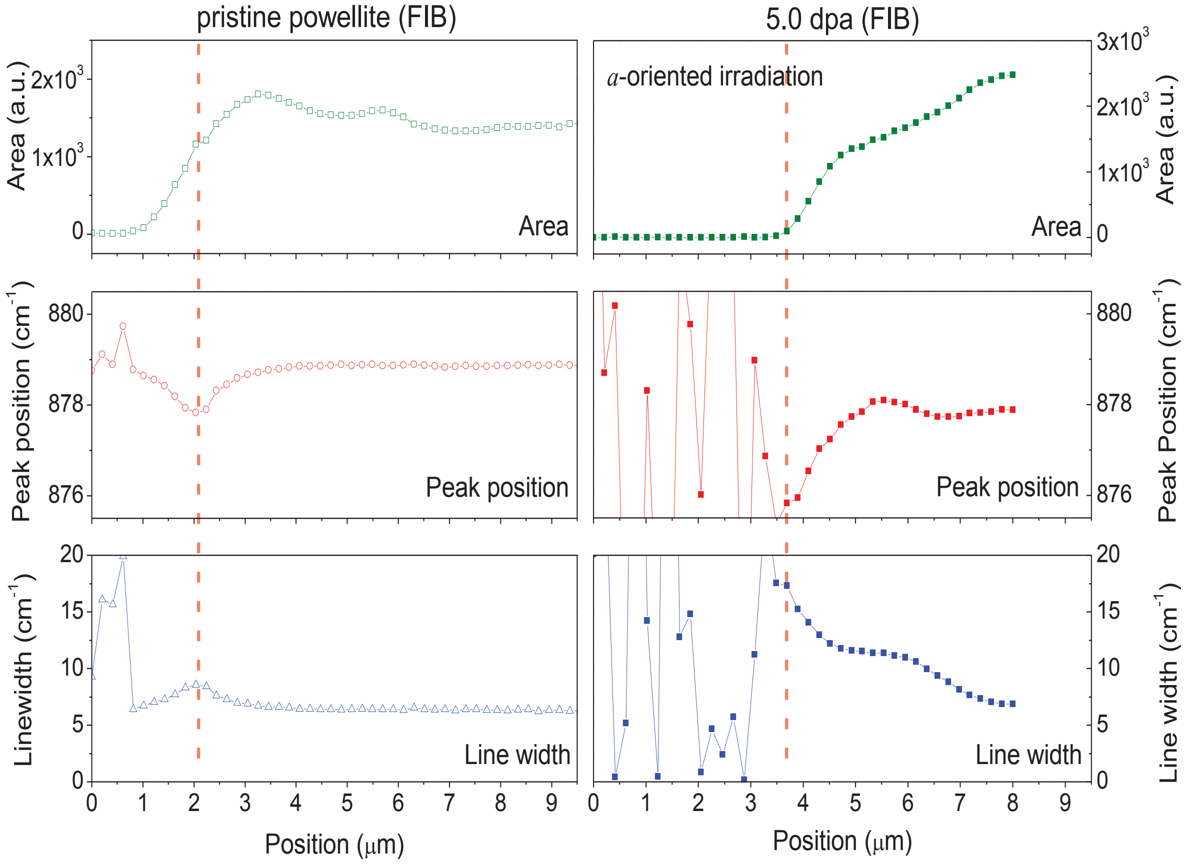

Figure A-17: Horizontal profiles in peak area, peak position and linewidth of $\nu_1(A_g)$ Raman mode of pristine powellite (left colume) and irradiated powellite (right colume); the pink dash line in the figure indicates the edge of the FIB section; excitation 633 nm

A.10 Laser-induced structural modification on irradiated powellite crystal during measurement

It has to be noted that shot-wavelength laser can induce some damages or recovery on the irradiated powellite during experiments. For all the powellite FIB sections, a 633-nm laser with low energy was first used to conduct Raman mapping. After the Raman measurements, a 473-nm laser was used to record Eu^{3+} emission. However, it is found that the 473-nm laser induced some structural modifications in the irradiated powellite. As shown in Figure A-18 and Figure A-19, the profiles (with 633-nm laser) of Raman linewidth and peak position of the irradiated FIB section change significantly after the exposure of FIB samples under a 473-nm laser. Due to the absorption of laser energy during measurement, the structure of powellite is possible to be more or less modified. The absorption coefficient of powellite around 633 nm is very small comparing to the one around 473 nm. Therefore, the 633-nm laser has much less impact on the sample when using as a Raman excitation. This phenomenon has to be carefully taken into account during the selection of Raman or luminescent excitation source.

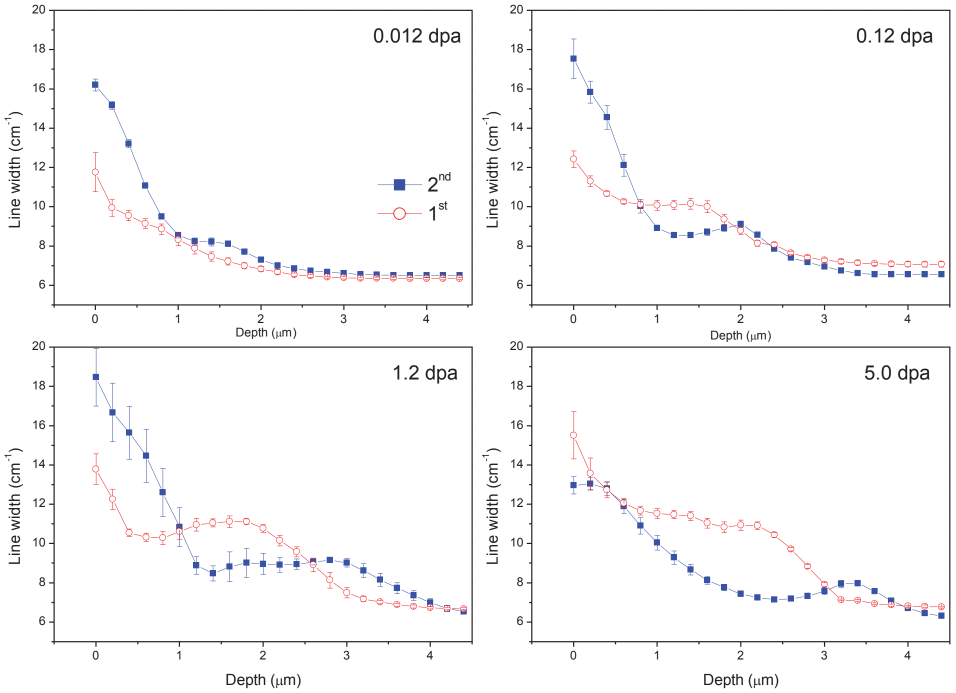

Figure A-18: Raman linewidth profile of the irradiated FIB section before (1st) and after (2nd) the exposure under 473-nm laser; Raman excitation: 633-nm laser

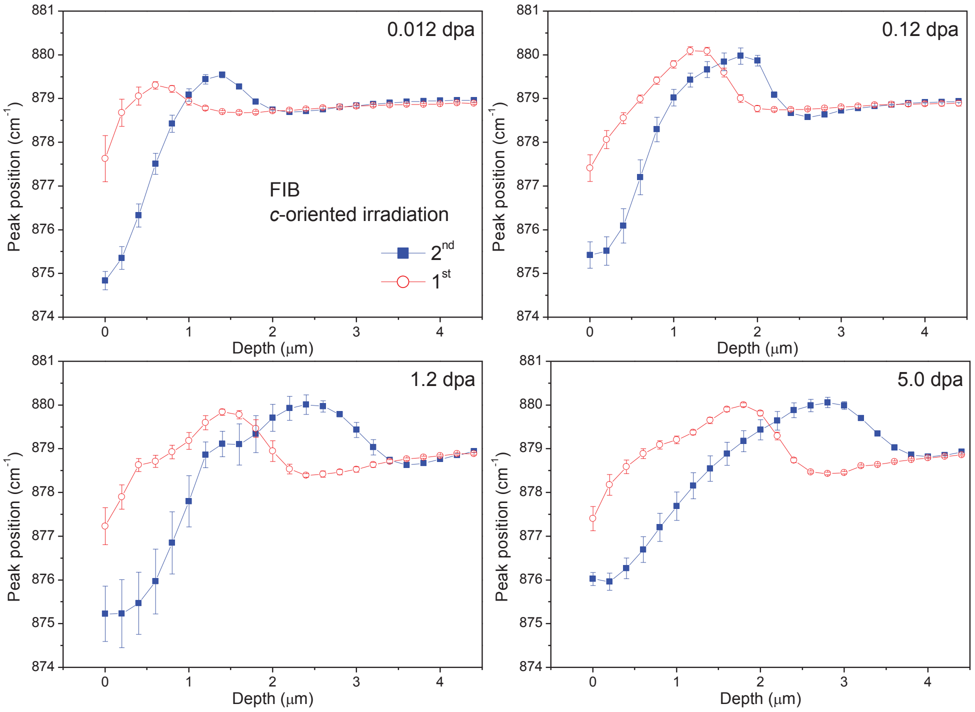

Figure A-19: Raman peak-position profile of the irradiated FIB section before (1st) and after (2nd) the exposure under 473-nm laser; Raman excitation: 633-nm laser

A.11 Quenching of Eu^{3+} in powellite after irradiation

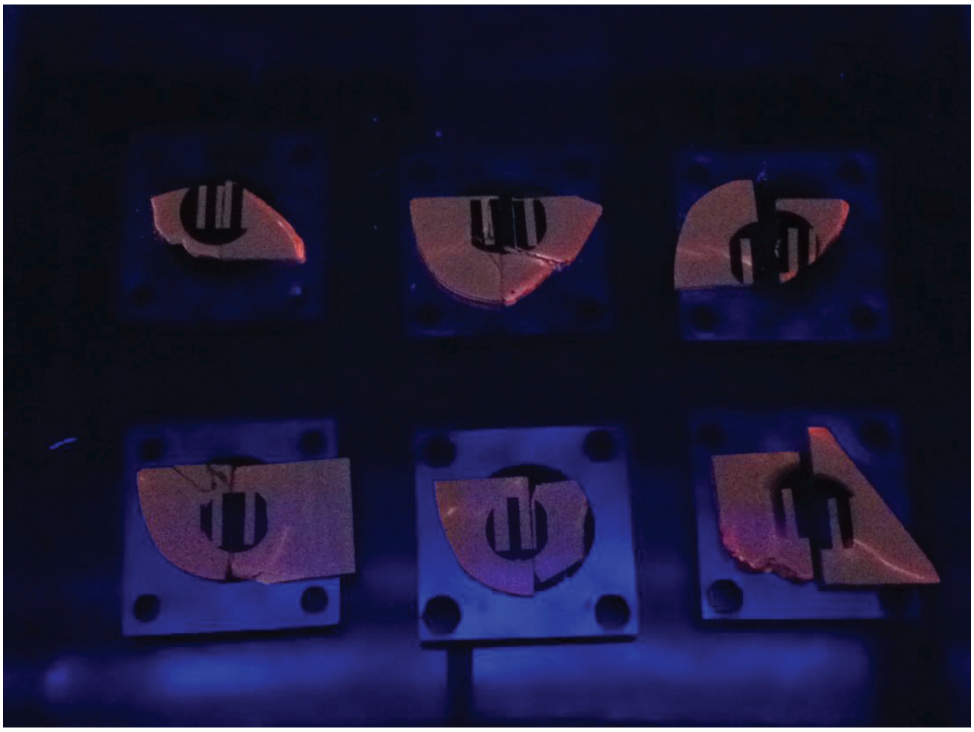

Figure A-20: Irradiated powellite under UV lamp (254 nm); the red emission corresponds to Eu^{3+} in powellite; the dark areas on the samples (which were not covered by Al masks during experiment) correspond to quenching of Eu^{3+} after irradiation